BEYOND THE STANDARD MODEL: COMPOSITE HIGGS AND DARK MATTER

A Dissertation

Presented to the Faculty of the Graduate School

of Cornell University

in Partial Fulfillment of the Requirements for the Degree of

Doctor of Philosophy

by

Ofri Telem

August 2019

© 2019 Ofri Telem

ALL RIGHTS RESERVED

BEYOND THE STANDARD MODEL: COMPOSITE HIGGS AND DARK MATTER

Ofri Telem, Ph.D.

Cornell University 2019

The Standard Model (SM) of particles and interactions provides some of the most extensively tested predictions in science. However, it does not adequately describe quantum gravity, and does not contain a suitable candidate for Dark Matter. Furthermore, the UV sensitivity of the SM Higgs sector suggests that new states beyond the SM might exist at energies not far above the weak scale. This dissertation explores potential scenarios for physics beyond the SM, either in a dark sector or linked to the Higgs sector of the SM.

The first part of this work includes two novel classes of composite Higgs models, with far reaching phenomenological consequences. In the first of these, an adjustable tree-level Higgs quartic coupling, allows for a significant reduction in the tuning of the Higgs potential. The quartic in this model originates from the dimensional reduction of a 6D theory, and is the first example of a holographic composite Higgs model with a tree-level quartic. In the second novel class of composite Higgs models, the top and gauge partners responsible for cutting off the Higgs quadratic divergences form a continuum. A concrete example is presented, based on a warped extra dimension with a linear dilaton, where this finite gap appears naturally. Spectral densities are derived for this model, as well as the full Higgs potential for a phenomenologically viable benchmark point, with percent level tuning. The continuum top and gauge partners in this model evade all resonance searches at the LHC and yield qualitatively different

collider signals.

The second part of this work features two different classes of models for an extended dark sector that undergoes either confinement or bound states formation. It is shown how each of these mechanisms could lead to vast modifications of early universe dynamics, as well as unique signals today. In the first of these, the relic abundance of heavy stable particles charged under a confining gauge group is depleted by a second stage of annihilations near the deconfinement temperature. This mechanism can be used to construct ultra-heavy dark-matter models with masses above the naive unitarity bound. The second contribution is Self-Destructing Dark Matter (SDDM), a new class of dark matter models which are detectable in large neutrino detectors. In this class of models, a component of dark matter can transition from a long-lived state to a short-lived one by scattering off of a nucleus or an electron in the Earth. The short-lived state then decays to SM particles, generating a dark matter signal with a visible energy of order the dark matter mass rather than just its recoil.

BIOGRAPHICAL SKETCH

Ofri Telem was born in Israel on July 20th, 1989, and grew up in the town of Modi'in. At age 15, he attended the Israel Art and Science Academy in Jerusalem, where he majored in Physics, Mathematics, Computer Science and Philosophy. At age 18, he enlisted in the Israel Defense Forces (IDF), serving in Talpiot, the IDF's elite technological training program. As part of the training, he completed a bachelor's degree in Physics and Mathematics at the Hebrew University, Jerusalem.

Towards the end of his military training in 2010, Ofri met Laura, the love of his life, on a "Birthright Israel" trip, and the two lived together in Israel until moving to the US in 2016. Ofri and Laura were married in 2015, and are expecting their first child.

In the years 2010-2016, Ofri served as an R&D officer in the IDF, and was granted the rank of Major. During his service, Ofri completed a Master's degree in Physics at the Technion - Israel Institute of Technology, under the supervision and mentorship of Professor Yael Shadmi. Ofri is particularly indebted to Professor Shadmi for introducing him to the world of High Energy Physics. Together with his close friend and collaborator Dr. Michael Geller, Ofri published the first Composite Higgs UV completion of the Twin Higgs model, which was the first in a wave of renewed interest in the Twin Higgs model.

In the fall of 2016, Ofri started his graduate studies at Cornell University, under the supervision and mentorship of Professor Csaba Csáki. Professor Csáki provided Ofri with endless support, ideas, care and guidance, and Ofri considers him a lifelong mentor. In the fall, after the birth of his first child, Ofri will continue his work in theoretical High Energy Physics as a postdoctoral researcher at the University of California, Berkeley.

To my loved ones, and the one to come.

ACKNOWLEDGEMENTS

Before jumping into the physics, I would like to thank my parents, Tali and Itiel, and my sister Liri. Moving to a different country to pursue your dream is an extremely hard thing, especially for a tight-knit family like ours. Ima, Aba and Liri, I love you and miss you every day.

Laura, my love and my soulmate. Having you by my side makes everything better. Thank you for listening to me talk about dark matter before we've even had coffee.

And now to physics. Throughout my short career so far in High Energy Physics, I've had the immense luck and pleasure to have three extraordinary particle physicists guide my path.

The first is Michael Geller, my first (and hopefully lifelong) collaborator. From Michael I learned that ideas need to be sharp and crystal clear, and that good physicists are ones who are brutally honest with themselves. Another thing that I learned from Michael is that you need to know what to expect from a calculation ahead of time - otherwise the result is just some random output from a black box. I thank Michael for being my scientific older brother, with whom I can share any idea that I have, and get laser focused feedback.

The second particle physicist who guides my path is Yael Shadmi. I did my Master's degree under her supervision at the Technion in the years 2012-2015, and enjoyed her wisdom. I learned from Yael how to write physics papers, and especially how to galvanize a physics idea and attack it from every possible angle, until it reaches maturity. Several times I rushed ahead in my eagerness to push a project forward, only to come full circle to Yael's original understanding of the physics. I thank Yael for helping me become a more mature physicist.

Last, but not least, I would like to thank Csaba Csáki, my mentor. In Csaba I

found a deep thinker, who is on the path to a better understanding of Quantum Field Theory. It's hard to summarize everything that I learned from Csaba, but if I have to name one thing, it would be to dare to ask the big questions. It's very tempting to get carried away by scientific fads, or to get lost in some technocratic number crunching. Csaba reminds me time and again that there are still so many wonderful things to understand better - be it instantons, monopoles, dualities or any other mind blowing concept, and that even people like me, who are no Ken Wilson, can maybe one day discover something truly deep. I am indebted to Csaba for bringing me to Cornell and giving me all the support in the world. I couldn't have asked for a better advisor.

I have many other thanks to give, so from now on I will have to make it shorter...

I thank Julia Thom-Levy and Maxim Perelstein for being on my committee, and also thank Maxim for many interesting physics discussions. Yuval, toda for all the fun ideas that we had together and for being there when I need a little bit of home away from home. Thank you to my dear collaborators Csaba Csáki, Yael Shadmi, Michael Geller, Sal Lombardo, Gabe Lee, Sho Iwamoto, Seung Lee, Roni Harnik, Yue Zhang, and Andi Weiler. I am also grateful to a host of other particle physicist with whom I've had the pleasure to talk physics. The list is far from exhaustive, and I am sorry if I forgot anyone: Nima Arkani-Hamed, John Terning, Yuri Shirman, Jay Hubisz, Liam McAllister, Tom Hartman, Eric Kuflic, Yonit Hochberg, Tomer Volansky, Gilad Perez, Yevgeny Kats, Nathaniel Craig, David Curtin, Jonathan Feng, Jeff Dror, Jack Collins, Hari Ramani, Oren Slone, Gustavo Marques-Tavares, Yushin Tsai, Kim Berghaus, Shaouly Bar-Shalom, Gad Eilam, Yaniv Weiss, Eitan Gozani, Yoav Afik, and many more.

I would like to express my gratitude to the UMD physics department for

their hospitality and their support. I was honored and grateful for the opportunity to talk to Raman Sundrum, Zackaria Chacko, Kaustubh Agashe, and Anson Hook.

To the physics department at UC Berkeley - I am eager and excited to start working together. I thank Hitoshi Murayama, Lawrence Hall, Zoltan Ligeti, Yasunori Nomura and Christian Bauer for the opportunity. See you soon!

Thank you to the power trio - Jeff Dror, Sal Lombardo, and Jack Collins. You guys are the best. Thank you to all the friends that I've had at Cornell - on the the post-doc side, Sungwoo Hong, Matt Klimek, Edgar Shagoulian, and Kartik Prabhu. On the student side, thank you to Ibrahim Shehzad, Gowri Kurup, Mehmet Demirtas, Amir Tajdini, Nima Afkhami-Jeddi, Wee-Hao Ng, Yu-Dai Tsai, Mijo Ghosh, Dnyanesh Kulkarni, Gebreile Rigo and Cem Eröncel. It was a pleasure to rant to you about American idiosyncrasies in our little model UN. Not that I managed to keep the rants to myself when around my other friends - ma man Cody Duell, Naomi Gendler, Dante Iozzo (ok Canadian), Mike Matty, Éamonn O'Shea (ok Irish), and Geoff Fatin. A special thanks to Katerina Malysheva and Kacey Bray Acquilano for their support along the way.

Many thanks to the organizers of TASI 2016, GGI 2017, Pheno 2017-2018, MITP 2017, JHU workshop Budapest 2017, and for the hospitality of the Technion - Israel Institute of Technology, the Weizmann Institute, and the University of Toronto.

TABLE OF CONTENTS

LIST OF TABLES

LIST OF FIGURES

CHAPTER 1

INTRODUCTION

The Standard Model (SM) of particles and interactions provides some of the most extensively tested predictions in science. As of the end of 2018, the LHC has collected close to $70\,\text{fb}^{-1}$ of data at 13 TeV. The analysis of close to $40\,\text{fb}^{-1}$ of this data by the ATLAS and CMS collaborations yielded no apparent significant deviation from the Standard Model [1]. Similarly, experiments at the intensity frontier such as LHCb [2], Belle II [3] and BaBar [4] provide extremely high-precision tests of the SM and its parameters, the most recent being the measurement of CP violation in the charm system [5] which is consistent with the SM value.

In spite of the tremendous success of the SM, it is not viewed as a complete theory of Nature, but rather as an Effective Field Theory (EFT). This is because it does not provide a quantum description of gravity. By naive dimensional analysis, gravity is expected to start exhibiting its quantum nature at energies no higher than the Planck scale $M_{\text{P}} \sim 10^{19}\,\text{GeV}$. This means that the cutoff Λ of the SM is smaller than the Planck scale $\Lambda \leq M_{\text{P}}$. Since this upper bound is much higher than any terrestrial scattering experiment one could imagine, it is useful to ask if there are any hints that physics beyond the SM might exist at energies hierarchically lower than the Planck scale. The answer to that is that we cannot know for sure, but there are good reasons to believe that this is the case.

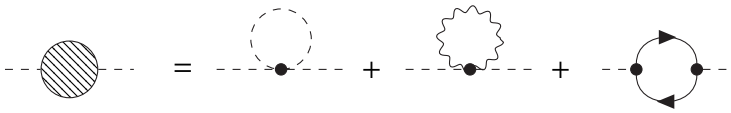

Figure 1.1: The one loop corrections to the Higgs mass parameter in the SM. All three diagrams are quadratically divergent, leading to the hierarchy problem.

1.1 The Higgs Hierarchy Problem

The first hint that new physics might be linked to the TeV scale comes from the Higgs sector of the SM. This is the famous "Higgs Hierarchy Problem" (for excellent reviews, see [6, 7]). It stems from the UV sensitivity of the effective potential for the SM Higgs boson. This potential is given by

$$V_{\text{eff}}(H) \;=\; -\mu^2 H^2 \;+\; \lambda H^4 \,, \tag{1.1}$$

where μ is the Higgs quadratic coupling and λ is the Higgs quartic coupling. One way to see the UV sensitivity of the Higgs potential is in *old fashioned renormalization*, i.e. by calculating the one loop radiative corrections to the Higgs potential due to top quark and gauge boson loops (see Fig. 1.1).

The SM 1-loop renormalized quadratic is quadratically divergent:

$$\mu^2|_{\text{ren.}} \;=\; \mu^2|_{\text{bare}} \;+\; \frac{\Lambda^2}{32\pi^2}\left[-6y_t^2 + \frac{1}{4}\left(9g^2 + 3g'^2\right) + 6\lambda\right], \tag{1.2}$$

where g, g' are the SU(2) and U(1) gauge couplings and y_t is the top Yukawa coupling. Note that Λ in this calculation is just a stand-in for the energy scale of some unknown new physics states that cuts off the quadratic divergence. The measured Higgs mass $m_H = 125\,\text{GeV}$ and Higgs VEV $v = 246\,\text{GeV}$ fix the renormalized values to be $\mu^2|_{\text{ren.}} = 87\,\text{GeV}$, $\lambda|_{\text{ren.}} = 1/8$, and so to have $\Lambda \gg \text{TeV}$, the bare value and the cutoff have to be extremely fine-tuned.

A more modern formulation of the UV sensitivity of the SM Higgs potential is in terms of Wilsonian renormalization. In this language, the parameters of the Higgs potential are energy dependent, and their values at the cutoff Λ are fixed by coarse graining over some underlying UV theory. Below Λ, the values of $\mu(E)$, $\lambda(E)$ flow according to the SM Renormalization group equations (RGE), and the quadratic divergence Eq. 1.2 manifests itself as extreme sensitivity of the resulting μ(TeV) to the RGE boundary conditions at Λ. The higher Λ is, the higher the sensitivity, such that if $\Lambda \sim M_P$, we need $\mu(\Lambda)$ to be tuned to an accuracy of 10^{-18} to reproduce the observed μ(TeV). From an RGE perspective, this is because the Higgs quadratic is a relevant parameter, unlike all other parameters in the SM which are either marginal or irrelevant.

1.2 Models Motivated by Higgs Naturalness

One way out of the Hierarchy problem is if the cutoff Λ for the SM is low, and if there's an underlying symmetry which protects the Higgs potential from UV sensitivity above Λ. This class of models is often called "natural solutions" to the Hierarchy problem, since they seek to minimize the tuning of parameters in the Higgs potential. Most of these models involve new states at Λ that contribute radiative corrections to the Higgs potential which exactly cancel the quadratic divergences due to the SM top quark and gauge bosons. The cancellation is exact by virtue of the imposed UV symmetry.

There are currently two classes of natural solutions to the Hierarchy problem:

- *Supersymmetry*

In Supersymmetry (SUSY)[1] the SM is embedded in a UV theory with fermion $\leftrightarrow$ boson symmetry. In an exactly supersymmetric theory, every particle has a supersymmetric partner of opposite spin, and scalars like the Higgs are protected from quadratic divergences by the chiral symmetry that they inherit from their supersymmetric partner. In particular, the top quark quadratic correction to the Higgs potential is exactly canceled by the contribution of the stop, the scalar supersymmetric partner of the top. An analogous cancellation happens for the gauge quadratic correction. To accommodate the SM as a low energy EFT, SUSY has to be explicitly broken by giving $\gtrsim$ TeV masses to all of the superpartners. This means that the SM Higgs potential is sensitive to the physics at the scale of the SUSY breaking masses, but not to higher scales where the superpartners enter.

- *Composite Higgs*

  In composite Higgs (CH) models [9–15], the Higgs is not a fundamental particle, but is rather a composite particle of some strong dynamics, which confines at a scale Λ above the TeV scale. This mechanism is inspired by the hadrons in QCD, which are insensitive to UV physics above the confinement scale Λ, simply because at high energies they separate into their constituents. In most realistic composite Higgs models, the Higgs is not just a composite, but is also a pseudo-Nambu-Goldstone boson (pNGB) of some global UV symmetry, which is broken by the confining dynamics. In the QCD analogy, this would make the Higgs similar to pions, which are the pNGBs of chiral symmetry breaking. As a pNGB, the effective cutoff in the Higgs potential is suppressed by an $O(10)$ with respect to the confinement scale Λ, allowing for a natural parametric separation between the mass of the Higgs and the strong dynamics at Λ. This is crucial for

[1] See [8] for a classic review of Supersymmetry.

realistic models, as the strong dynamics scale Λ is severely constrained by flavor and electroweak constraints.

In addition to natural models, there is a growing interest in recent years in Anthropic and dynamical solutions to the Higgs Hierarchy problem, among them relaxion-type models [16] and N-naturalness [17], as well as some initial ideas concerning UV-IR mixing [18].

1.3 Dark Matter

Dark Matter (DM) is our first and foremost indication for physics beyond the Standard Model. In the past decade, there has been an overwhelming accumulation of evidence for the existence of DM from galaxy rotation curves, weak lensing of clusters, the bullet cluster, and signals from the early universe. These early universe signals, such as the Cosmic Microwave Background radiation (CMB), Baryon Acoustic Oscillations (BAO), cosmic shear, and type Ia supernovae, allow for precision measurements of DM properties. For example, both late time and early universe signals allow us to establish that dark matter is a gravitationally interacting, cold matter, which interacts at most weakly with itself and with the SM.

The above properties are reflected in the standard cosmological model, ΛCDM, which describes the entire cosmological history of the universe based on the dynamics of DM, baryonic matter, and the cosmological constant. The average matter density in the universe Ω_m, a key parameter in ΛCDM, is extremely well measured by the CMB data from the Planck collaboration, consistently with BAO and cosmic shear data. This a triumph to the cold DM paradigm and its

experimental observation. However, there are some cosmological indications that ΛCDM is incomplete, most notably in the tension between the value of the Hubble constant measured from supernova data and from the CMB [19]. Additionally, data at the galactic scale hints at some level of self-interaction among DM particles. This collection of observations is known collectively as "small scale problems" [20].

From the particle physics side, the challenge that DM poses is clear. The SM has no DM candidate, and so there is a world encompassing effort to probe the possible particle nature of DM. Since DM is by definition weakly interacting with the SM, this means that the scarcity of DM interactions has to be overcome with large and/or extremely sensitive detectors, long detection timescales, and good background rejection. As we currently have almost no priors for what the mass of DM might be[1], the searches for DM are extremely diverse, ranging from tabletop precision experiments, through electron/nuclear recoil experiments, and all the way to collider searches and indirect detection in telescopes.

Finally, there is a growing interest in recent years in generic dark sectors that contain more than just one DM particle. This a-priori reasonable possibility gives rise to very rich early universe dynamics and novel detection possibilities. This work focuses on two such scenarios, both involving the possibility of bound state formation in the dark sector.

[1]There are some general bounds like the the Tremaine-Gunn [21] bound on fermionic DM or the fuzzy DM bound [22] on ultralight bosons. However the leave a good 90 orders of magnitude leeway for what the mass of DM might be.

1.4 Reader's Guide

This work comprises of two parts: one dedicated to novel classes of composite Higgs models (chapters 2-4), and one dedicated to DM and the surprising implications of bound state formation in the dark sector (chapters 5-7).

Chapter 2 provides an introduction to composite Higgs model building and phenomenology. In chapter 3 we present a novel class of composite Higgs models with a tree-level Higgs quartic coupling, originating from a 6D geometry. This chapter is based on the work done in [23], in collaboration with Csaba Csáki and Michael Geller. Chapter 4 demonstrates a unique class of composite Higgs models that lack any new particles beyond the SM, and instead predict the existence of continuum states that don't show up as resonances. This chapter is based on [24], which was done in collaboration with Csaba Csáki, Gabriel Lee, Seung Lee, and Salvator Lombardo.

Part 2 starts with an introduction to DM physics in chapter 5, followed by a study of Quarkonium formation in a strongly interacting dark sector in chapter 6. This is based on work done in [25], in collaboration with Michael Geller, Sho Iwamoto, Gabriel Lee, and Yael Shadmi. Finally, in chapter 7 we present an outside-the-box idea for how DM could "self-destruct" in detectors, leading to very unusual signals in neutrino detectors. This is based on work done in [26], in collaboration with Yuval Grossman, Roni Harnik, and Yue Zhang.

CHAPTER 2

REVIEW OF COMPOSITE HIGGS

In the upcoming chapters we will focus on novel variants of (pNGB-) composite Higgs models with non-standard phenomenology. To this end, we review standard composite Higgs models with a pNGB Higgs[2].

In composite Higgs models, the UV theory consists of some particles charged under an asymptotically free gauge theory, for example SU(N). At a scale $\Lambda \sim 10$ TeV the strong dynamics confines, generating composite fermions and vectors. Additionally, the UV theory respects a global symmetry G, which is broken by the strong dynamics to a subgroup H. The scale associated with this breaking is $f \sim \Lambda/4\pi$. By Goldstone's theorem, the effective theory below Λ must contain massless (in our case composite) "pions" transforming non-linearly in the coset G/H, similarly to the chiral Lagrangian in QCD. To identify these pions with the SM Higgs, we embed the SM $\mathrm{SU(2)_I \times U(1)_Y}$ gauge symmetry in G, such that the pions are in the complex $\mathbf{2}_{1/2}$ doublet of $\mathrm{SU(2)}_I \times \mathrm{U(1)}_Y$.

The gauging of only $\mathrm{SU(2)_I \times U(1)_Y}$ explicitly breaks the original G global symmetry, and so the Higgs is no longer an exact NGB but rather a *pseudo*-NGB. In particular, it gets a 1-loop potential (also called a Coleman-Weinberg potential [31]) from radiative corrections of the $\mathrm{SU(2)_I \times U(1)_Y}$ gauge bosons. In addition to the SM gauge bosons, we also have a whole G-adjoint worth of massive composite vectors. As we will see later, the strong dynamics tends to generate a whole infinite tower of such composite vectors, whose mass gap is $\sim f$, the scale of G/H breaking. This tower of composite vectors plays an important role in keeping the Higgs potential insensitive to UV physics above

[2]For reviews of composite Higgs, see [27–30].

the scale $\sim f$.

To demonstrate the above construction, let us focus on a concrete model - the classic CH model of [32]. In this model G = SO(5) × $U(1)_X$, while H = SO(4) × $U(1)_X$. The number of generators of SO(5) is $\frac{5\cdot4}{2}$ = 10, while the SO(4) has $\frac{4\cdot3}{2}$ = 6 generators. This leaves 4 pNGBs in the coset SO(5)/SO(4). Gauging $SU(2)_I \times U(1)_Y \subset SO(5) \times U(1)_X$, it's easy to check that these pNGBs indeed form the complex $\mathbf{2}_{1/2}$ doublet of $SU(2)_I \times U(1)_Y$: the composite Higgs doublet.

Consequently, the spectrum of scalars/vectors before electroweak symmetry breaking (EWSB) comprises the four massless SM gauge bosons in $SU(2)_I \times U(1)_Y$, a (massless at tree level) Higgs doublet, and a tower of SO(5)×$U(1)_X$ composite vectors whose masses start at $\sim f$. The potential for the pNGB Higgs is zero at tree level, but arises radiatively from loops of the gauge bosons, which are cut at the scale $\sim f$ by the radiative contribution of the massive vector towers.

Finally, we have not addressed the SM $SU(3)_C$ gauge symmetry, since it is implicitly assumed to exist in both the elementary and the composite sectors. In particular, the composite quarks transform in the fundamental of this $SU(3)_C$, and there is a tower of composite gluons in the spectrum.

2.1 The Electroweak Gauge Boson sector

Here we describe the gauge sector of composite Higgs models using the classical SO(5)/SO(4) composite Higgs as a prototype. First, we make the choice of global symmetry in the strong sector to be SO(5)×$U(1)_X$, which is broken by the

confining dynamics to $SO(4) \times U_X$. The pNGB Higgs is in the coset SO(5)/SO(4), and transforms as $(\mathbf{2}, \mathbf{2})$ under $SU(2)_L \times SU(2)_R = SO(4)$.

Once the symmetry breaking pattern SO(5)/SO(4) is fixed, the form of the effective gauge boson action below the scale $\sim f$ is uniquely fixed by the Coleman-Callan-Wess-Zumino formalism (CCWZ) [33]. This formalism dictates the unique way to write an effective action which realizes the $SO(4) \times U(1)_X$ symmetry linearly, and the full $SO(5) \times U(1)_X$ *non-linearly*. To do this we define the pNGB matrix

$$U = e^{i \frac{\sqrt{2}}{f} h^a T^a} , \tag{2.1}$$

where T_a are the generators in SO(5)/SO(4), as well as the SO(5) vector

$$\Sigma = U\,(0,0,0,0,f)^T = \frac{\sin\frac{h}{f}}{f}\left(h_1, h_2, h_3, h_4, h\cot\frac{h}{f}\right)^T , \tag{2.2}$$

where $h \equiv \sqrt{h_a h^a}$. The effective action for the SM gauge bosons is then given by

$$\mathcal{L}_{\text{gauge}} = \frac{1}{2}\left(D_\mu \Sigma\right)^\dagger \left(D^\mu \Sigma\right) , \tag{2.3}$$

where D_μ is the $SU(2)_I \times U(1)_Y$ gauge covariant derivative, including momentum dependent form factors that represent the integrated out tower of composite vectors.

Expanding Eq. 2.3 in the SM gauge fields and the complex Higgs doublet H we arrive at

$$\begin{aligned}\mathcal{L}_{\text{gauge}} = \frac{1}{2} P_T^{\mu\nu} \Bigg[&\left(\Pi_0^X\left(p^2\right) + \Pi_0\left(p^2\right) + \frac{\sin^2\frac{h}{f}}{4}\Pi_1\left(p^2\right)\right) B_\mu B_\nu + \\ &+ \left(\Pi_0\left(p^2\right) + \frac{\sin^2\frac{h}{f}}{4}\Pi_1\left(p^2\right)\right) W_\mu^a W_\nu^a + 2\sin^2\frac{h}{f}\Pi_1\left(p^2\right) H^\dagger T_L^a Y H W_\mu^a B_\nu \Bigg] ,\end{aligned} \tag{2.4}$$

where $P_T^{\mu\nu} = \left(\eta_{\mu\nu} - \frac{p^\mu p^\nu}{p^2}\right)$ is the transverse projection operator, and $\Pi_{0,1}\left(p^2\right)$, $\Pi_0^X\left(p^2\right)$ are momentum dependent form factors from integrating out the tower of composite vectors at $\sim f$ such that [27],

$$\begin{aligned} \Pi_0(0) &= 0 = \Pi_0^X(0) \;,\; \Pi_1(0) = f \\ \frac{1}{g^2} &= -\Pi_0'(0) \;,\; \frac{1}{g'^2} = -\left[\Pi_0'(0) + \Pi_0^{X'}(0)\right] . \end{aligned} \tag{2.5}$$

Note that the form factors $\Pi_{0,1}\left(p^2\right)$, $\Pi_0^X\left(p^2\right)$ encode the details *confining dynamics* and so cannot be determined by the group theoretical considerations that we applied so far. In Sec. 2.4 we will show how to generate them from a warped 5D model of the confining dynamics.

From the effective gauge Lagrangian Eq. 2.4 we can calculate the 1-loop potential of the pNGB Higgs, using the *Coleman-Weinberg* formula:

$$V_{\text{gauge}}(h) = \frac{9}{2}\int \frac{d^4p}{(2\pi)^4} \log\left[1 + \frac{1}{4}\frac{\Pi_1\left(p^2\right)}{\Pi_0\left(p^2\right)}\sin^2\frac{h}{f}\right] . \tag{2.6}$$

The momentum integral is damped for $p^2 \gtrsim f^2$ due to the confining dynamics encoded in the form factors $\Pi_{0,1}\left(p^2\right)$. Interestingly, the potential generated by the gauge bosons is always positive, and so we always need a negative contribution from the fermions to trigger EWSB.

2.2 Partial Compositeness

To incorporate the SM fermions into composite Higgs models, we need a way to make them couple to the composite Higgs. For that, the fermion multiplets have to "feel" the G/H breaking, and so naturally they must be linked to the composite fermions generated below Λ. This seems problematic, since the SM

fermions are chiral while the composite fermions are vectorlike. Moreover, the SM fermions don't come in full G multiplets.

The solution is to consider *partially*-composite fermions. In this scenario, the composite fermions come in complete vectorlike G multiplets $Q_{L,R}$, $T_{L,R}$, $B_{L,R}$. While the strong dynamics generates entire towers of these multiplets, in this part we will only keep the lightest state in each tower, whose mass is at $\sim f$. In addition, we introduce an elementary sector with the SM gauge symmetry $\mathrm{SU(2)_I}\times\mathrm{U(1)_Y}$ and fermions q_L, t_R, b_R in the usual SM representations $\mathbf{2}_{\frac{1}{6}}$, $\mathbf{1}_{\frac{2}{3}}$, $\mathbf{1}_{-\frac{1}{3}}$. We implicitly take these quarks to be in the fundamental of $\mathrm{SU(3)_C}$.

The essence of the partial compositeness mechanism [34–37] is the introduction of linear mixing between the elementary and composite sectors:

$$f\lambda_q\,\bar{q}_L\hat{Q}_R \;+\; f\lambda_t\,\bar{t}_R\hat{T}_L \;+\; f\lambda_b\,\bar{b}_R\hat{B}_L\,, \tag{2.7}$$

where $\hat{Q}_R$, $\hat{T}_L$, $\hat{B}_L$ are the parts of Q_R, T_L, B_L that have the same quantum numbers as q_L, t_R, b_R. Since the elementary quarks are chiral, in the mass basis we get chiral fermions with SM quantum numbers, which are a mixture of elementary and composite fermions. These are the *partially composite* SM quarks, and they have and a Yukawa coupling to the Higgs through their composite components.

Since the mixing terms in Eq. 2.7 only involves parts of the G multiplets, they constitute a source of explicit breaking of G, which provides an additional radiative contribution to the Higgs potential. This time, the contribution is from the quarks, and most importantly the top, which has the largest elementary-composite mixing. The top radiative contribution is cut at the scale $\sim f$ by the contribution of the tower of vectorlike composite fermions in full G-multiplets. This the pNGB composite-Higgs model at work: both the radiative corrections of the top and the gauge bosons are cut at $\sim f$ by the corresponding tower of

composite fermions and vectors.

Finally, note that in this part we've only talked about partially composite quarks, but an analogous construction can be made for the SM leptons.

2.3 The Top Sector

To get the low energy effective action for the top sector below the scale $\sim f$, we first need to choose $SO(5) \times U(1)_X$ representations for the composite fermion towers Q_L, T_R, B_R [1]. In the classic CH$_4$ [32], the fermion representations were $Q_L(\mathbf{4})_{\frac{1}{3}}$, $T_R(\mathbf{4})_{\frac{1}{3}}$, $B_R(\mathbf{4})_{\frac{1}{3}}$, while in the more realistic models [38, 39], the fermion multiplets were $Q_L(\mathbf{5})_{-\frac{2}{3}}$, $T_R(\mathbf{5})_{-\frac{2}{3}}$, $B_R(\mathbf{10})_{-\frac{2}{3}}$. For simplicity, we will focus on the former, following [27].

As in the gauge sector, the effective action is completely determined by the CCWZ formalism up to form factors that encode the confining dynamics:

$$\begin{aligned}\mathcal{L}_{\text{top}} \;=\; & \sum_{\Psi=Q_L,\,T_R,\,B_R} \bar{\Psi} \not{p} \left[\Pi_0^{\Psi}(p) + \Pi_1^{\Psi}(p)\,\Gamma^i \Sigma_i\right] \Psi \;+\; \bar{Q}_L \left[M_0^T(p) + M_1^T(p)\,\Gamma^i \Sigma_i\right] T_R \;+ \\ & \bar{Q}_L \left[M_0^B(p) + M_1^B(p)\,\Gamma^i \Sigma_i\right] B_R\,, \end{aligned} \tag{2.8}$$

where Γ^i are the gamma matrices for SO(5) and $\Pi_{0,1}^{Q,T,B}(p)$, $M_{0,1}^{Q,T,B}(p)$ are form factors that encode the composite dynamics and cannot be determined by group theory alone. Expanding Σ and keeping only the SM fermions q_L, t_R[2] we arrive at

$$\begin{aligned}\mathcal{L} \;=\; & \bar{q}_L \not{p} \left(\Pi_0^Q(p) + \Pi_1^Q(p) \cos\frac{h}{f}\right) q_L \;+\; \bar{t}_R \not{p} \left(\Pi_0^T(p) - \Pi_1^T(p) \cos\frac{h}{f}\right) t_R \;+ \\ & + \sin\frac{h}{f}\, M_1^T(p)\, \bar{q}_L \hat{H}^c t_R + \text{h.c.} \end{aligned} \tag{2.9}$$

[1] Q_R, T_L, B_L will be in the conjugate representations to allow for vectorlike masses.
[2] we neglect the bottom quark for the purpose of calculating the Higgs potential

We can now calculate the Coleman-Weinberg potential for the pNGB Higgs that arises from the top quark:

$$V_{\text{top}}(h) \;\approx\; 6\int \frac{d^4p}{(2\pi)^4}\left\{F_1\left(p^2\right)\cos\frac{h}{f} - F_2\left(p^2\right)\sin^2\frac{h}{f}\right\} \tag{2.10}$$

where

$$\begin{aligned} F_1\left(p^2\right) &\equiv \frac{\Pi_1^T}{\Pi_0^T} - 2\frac{\Pi_1^Q}{\Pi_0^Q} \\ F_2\left(p^2\right) &\equiv \frac{\left(M_1^T\right)^2}{(-p^2)\left(\Pi_0^Q + \Pi_1^Q\right)\left(\Pi_0^T - \Pi_1^T\right)}\,. \end{aligned} \tag{2.11}$$

Similarly to the integral in the gauge sector, $F_{1,2}\left(p^2\right)$ are also damped at $p \gtrsim f$, yielding a Higgs potential which is insensitive to UV physics above this scale.

2.4 5D Realization

As mentioned above, the Coleman-Weinberg potential of pNGB Higgs is generated at the 1-loop level from the radiative corrections of the SM top quark and gauge bosons. These corrections are cut at the G/H breaking scale by the towers of massive vectors and vectorlike quarks. The cancellation at $\sim f$ makes sense from a symmetry perspective, since the Higgs is a pNGB of G/H. However, to demonstrate the finiteness of the Higgs potential explicitly and calculate it, we need some way to model this infinite tower of composite states. One way is to use Weinberg sum rules [40, 41] to demonstrate the finiteness of the potential, and then approximate the Coleman-Weinberg potential by truncating the tower of composites.

An alternative way, inspired by the AdS/CFT correspondence [42], is to

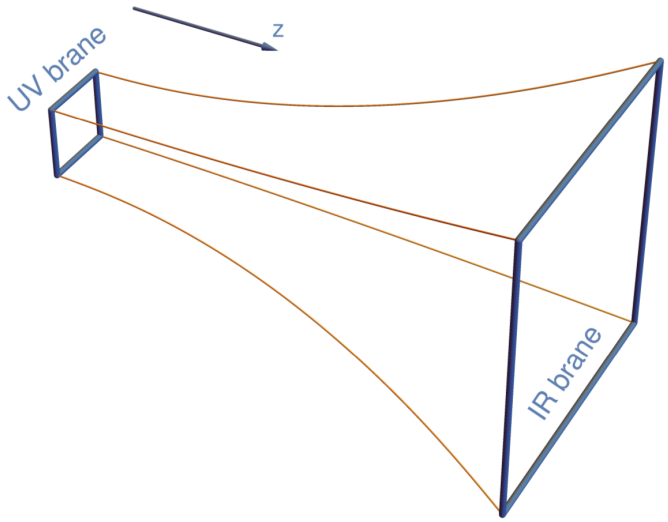

Figure 2.1: A sketch of the Randall-Sundrum geometry. The expanding lines from the UV brane to the IR brane are just an illustration of the z dependent factor $a(z)$ which scales all distances as we move from the UV to the IR. Reproduced from [30].

model the confining dynamics in a warped 5D geometry[1]. Consider a slice of AdS_5 space, parametrized by the Poincaré coordinates $x_{1,2,3,4} \in [-\infty, \infty)$ and $x_5 \equiv z \in [R, R']$, and the metric

$$ds^2 \;=\; a(z)^2 \left[dx^\mu dx_\mu - dz^2\right], \tag{2.12}$$

where $a(z) \equiv \left(\frac{R}{z}\right)$, and $R \sim M_P^{-1}$, $R' \sim \text{TeV}^{-1}$. In the full AdS_5 we have $z \in [0, \infty)$, while here we only consider a slice, bound between a 3-*brane* at $z = R$ (UV brane) and a 3-brane at $z = R'$ (IR brane). This is the famous Randall-Sundrum geometry [44], whose stabilization was considered in [45]. A sketch of this geometry is shown in Fig. 2.4

To model the confining dynamics in our composite Higgs model, we will consider bulk fields in this geometry [36,46], and extract their Green's functions by solving their bulk Equations of Motion (EOM), subject to boundary condi-

[1]For applications for QCD, see [43]

tions on the UV and IR branes. These Green's functions serve to construct a 4D effective action involving the partially composite SM fields below the confinement scale.

For example, let us model the interaction of a single elementary Weyl fermion with a confining strong sector that gives rise to a tower of composite vectorlike fermions [47]. The 5D action for a bulk fermion in RS is [48]:

$$S_5 \;=\; \int d^5x\, a(z)^4 \left\{ -i\bar{\chi}\bar{\sigma}^\mu \partial_\mu \chi \;-\; i\psi\sigma^\mu \partial_\mu \bar{\psi} \;+\; \frac{1}{2}\left(\psi \overleftrightarrow{\partial_z} \chi - \bar{\chi} \overleftrightarrow{\partial_z} \bar{\psi}\right) \;+\; \frac{c}{z}(\psi\chi + \overline{\chi}\overline{\psi}) \right\}, \tag{2.13}$$

where χ, ψ are the left and right chiralities of the bulk *Dirac* fermion, and c is the bulk mass. The bulk solutions for χ, ψ are $\chi = \chi(x)\, f_\chi(z)$, $\psi = \psi(x)\, f_\psi(z)$, where $f_{\chi,\psi}(z)$ satisfy the EOM:

$$\begin{aligned} f'_\chi(z) \;-\; \frac{2-c}{z}\, f_\chi(z) \quad &= \quad\;\; p\, f_\psi(z) \\ f'_\psi(z) \;-\; \frac{2+c}{z}\, f_\psi(z) \quad &= \quad -\, p\, f_\chi(z)\,, \end{aligned} \tag{2.14}$$

subject to the IR Dirichlet boundary condition $f_\psi(R') = 0$. To model the strong dynamics coupling to an elementary left handed Weyl fermion, we demand $f_\chi(R) = 1$, (left-handed source). The Green's function for the CFT operator mixing with the elementary fermion is given by

$$\langle \mathcal{O}_{\rm R} \mathcal{O}_{\rm R} \rangle \;=\; \bar{\lim}_{R\to 0} \frac{f_\psi(R)}{p}\,, \tag{2.15}$$

while the Green's function for the left handed fermion after integrating out the strong sector is

$$G\left(p^2\right) \;=\; \bar{\lim}_{R\to 0} \frac{1}{p f_\psi(R)} \;\approx\; \frac{4^c}{(p^2)^{c+\frac{1}{2}}} \frac{\Gamma\left(\frac{1}{2}+c\right)}{\Gamma\left(\frac{1}{2}-c\right)} \frac{J_{c-\frac{1}{2}}(pR')}{J_{\frac{1}{2}-c}(pR')}\,. \tag{2.16}$$

The 4D effective action for the LH Weyl fermion is then

$$S_{\text{4D eff.}} \;=\; -\, i\overline{\chi}\, \not{p}\, \Pi\left(p^2\right) \chi\,, \tag{2.17}$$

with $\Pi\left(p^2\right) \equiv \left[p^2 G\left(p^2\right)\right]^{-1}$. This is the 4D action describing a single Weyl fermion, whose 2-point function encodes an entire tower of composite vectorlike fermions that were integrated out below the confinement scale $\Lambda \sim R'^{-1}$. The Green's function $G(p^2)$ has poles at discrete values of the four momentum p, corresponding to the tower of composite vectorlike fermions that we integrated out. There is also a pole at $p = 0$ corresponding to the partially composite chiral "zero mode" χ.

It is useful to plot $f_{\chi,\psi}(z)$ for $p = m_n$ where the m_n are the poles of $G(p^2)$. The functions $f^n_{\chi,\psi}(z) \equiv f_{\chi,\psi}(z)|_{p=m_n}$ are called Kaluza-Klein (KK) profiles, and they form the eigenbasis of solutions to the bulk Dirac operator subject to the boundary conditions $f_\psi(R) = f_\psi(R') = 0$. In fact, we could have gotten a 4D effective action by expanding the bulk fields in the action Eq. 2.13 in this eigenbasis and then integrating over $z \in [R, R']$. This is called a KK expansion, and it is useful when calculating the production and decay rates of composite particles, as well as their contribution to flavor violation. For the purpose of calculating the Higgs potential, we prefer the use of Green's functions, since they make the UV finiteness of the potential more apparent.

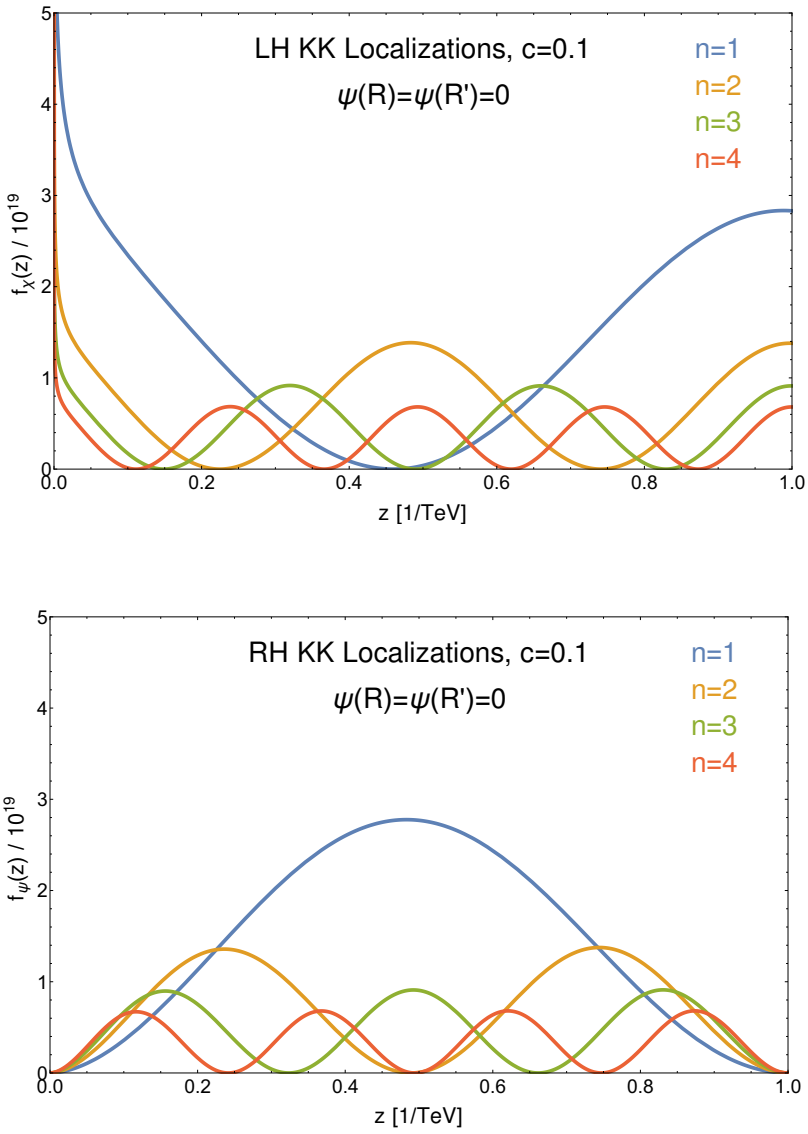

Figure 2.2: Localizations of first few fermion KK modes in RS, for $c = 0.1$ and Dirichlet boundary conditions for ψ on both branes. Top panel: $f_\chi^n(z)$. Bottom panel: $f_\psi^n(z)$. The number of zeros for each profile is exactly n.

In Fig. 2.2 we plot the *localization* $\left[\left(\frac{R}{z}\right)^2 f_\chi^n(z)\right]^2$ for the first few KK profiles, for $c = 0.1$. Note that the number of zeros for each mode is exactly its index n - this is equivalent to potential-well eigenfunctions in QM. Finally, we comment on the KK profile for the zero mode $m_0 = 0$. Going back to Eq. 2.14 and solving for

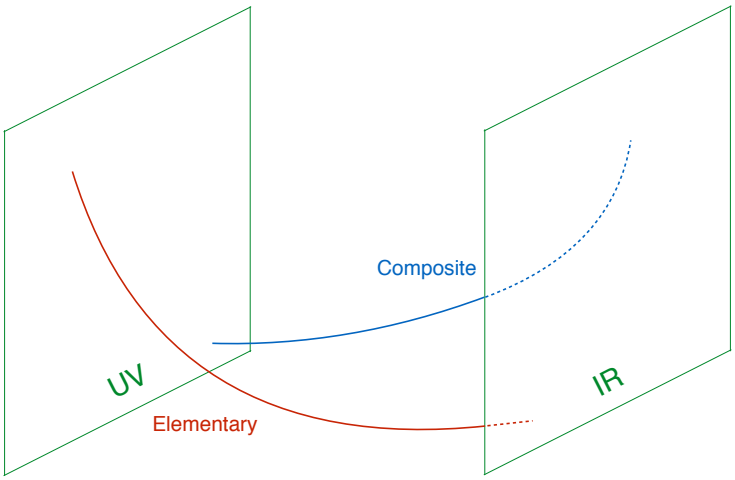

Figure 2.3: The localization of the zero mode for $c > 0$ (blue) and $c < 0$ (red). These correspond to a mostly composite or mostly elementary LH fermion in the 4D EFT, respectively. Reproduced from [30].

$f_{\chi,\psi}(z)$ with $f_\psi(R) = f_\psi(R') = 0$, we see that the solution has to be of the form

$$f_\chi(z) \sim \left(\frac{z}{R}\right)^{2-c} , \quad f_\psi(z) = 0 . \tag{2.18}$$

this is a reflection of the fact that the zero mode is chiral - and exists only for the left handed chirality as anticipated. Interestingly, the zero mode localization depends on the sign of c: for $c > 0$, the localization grows in the IR ($z \to R'$), and we say that the zero mode is IR localized - which correspond to a "mostly composite" partially composite fermion in the 4D EFT. Conversely, for $c < 0$, the localization grows in the UV ($z \to R$), and we say that the zero mode is UV localized - which correspond to a "mostly elementary" partially composite fermion in the 4D EFT. This is illustrated in Fig. 2.4.

2.4.1 4D Interpretation

Analogously to the AdS/CFT correspondence, the z coordinate in the RS geometry represents RGE flow, where the UV brane corresponds to $E \sim M_P$ and the IR brane to $E \sim O(\text{TeV})$. The asymptotically free strong sector is approximately conformal and thus is well captured by the bulk of AdS_5. However, the theory ultimately breaks conformal invariance in the IR and flows to a gapped theory with a tower of composite excitations. This is captured by the IR brane cutting off the z coordinate at $R' \sim \text{TeV}^{-1}$, ultimately giving rise to a tower of massive particles in the 4D effective action for every bulk field the theory. The UV brane, on the other hand, represents external deformations to the strong sector, suppressed by powers of the Planck scale. These deformations are the sources for the explicit breaking of the global symmetry G of the strong sector, which eventually lead to the SM gauge group and partially composite fermions below the confinement scale $\Lambda \sim R'^{-1}$. The deformations a for LH source are relevant for $c < \frac{1}{2}$, since the anomalous dimension of the RH operator coupling to the source is $d_{O_R} = 2 + c$ (see [47]).

2.4.2 Gauge-Higgs Unification

So far we've shown how to model the confining dynamics by considering bulk fields in the RS geometry and extracting Green's functions. However, we have not yet shown how to model the breaking of the global symmetry G into H by this confining dynamics. This is a crucial ingredient if we want the Higgs to be a pNGB. The way to model this breaking in called *Gauge-Higgs Unification*

(GHU)[1].

In GHU, we consider a *gauge* symmetry G in the bulk of our RS geometry. This is dual to the *global* symmetry G in the 4D picture. The G gauge bosons propagate in the bulk, and are given boundary conditions on the UV and IR branes. Each bulk gauge boson has a 4D component A_μ with $\mu = 1, 2, 3, 4$ and an extra component A_5, which gets opposite boundary conditions to A_μ due to orbifold parity. The A_5 for the generators in the G/H coset plays a very important role in our mechanism - it's what gives rise to the pNGB Higgs in the effective 4D action.

On the IR brane, the G symmetry is broken to the H subgroup by giving Dirichlet boundary conditions to the A_μ in the G/H coset. Similarly, the symmetry is reduced on the UV brane to the SM gauge symmetry $SU(2)_I \times U(1)_Y$. The 4D effective spectrum only has massless modes for fields that have Neumann boundary conditions on both branes. Here, as before, we've neglected to mention to mention $SU(3)_C$, which exists both in the bulk and on the two branes.

We will demonstrate this construction in the classic SO(5)/SO(4) model of [32]. In this model, there is a total of 11 bulk gauge bosons in $SO(5) \times U(1)_X$. To account for the symmetry breaking on the two branes we give the gauge bosons

[1]Originally introduced in [49,50]. For more recent incarnations, see [51–57]

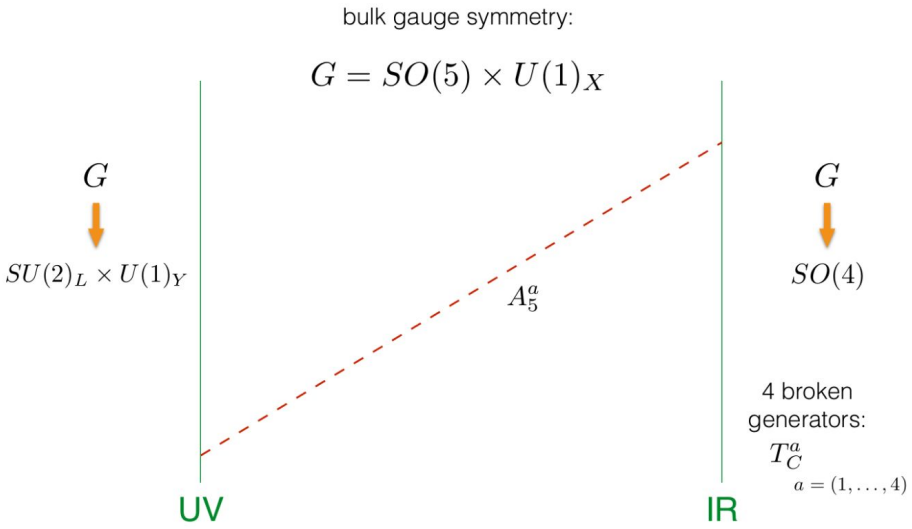

Figure 2.4: The 5D setup for SO(5)/SO(4) composite Higgs. Reproduced from [30].

the following boundary conditions[1]:

$$
\begin{aligned}
&\underline{\text{On the UV brane}} \\
&\quad \text{Gauge bosons in } \mathrm{SU(2)_I \times U(1)_Y}: \qquad A_\mu\,(+)\,,\; A_5\,(-) \\
&\quad \text{Gauge bosons in } \frac{\mathrm{SO(5) \times U(1)_X}}{\mathrm{SU(2)_I \times U(1)_Y}}: \qquad A_\mu\,(-)\,,\; A_5\,(+) \\
&\underline{\text{On the IR brane}} \\
&\quad \text{Gauge bosons in } \mathrm{SO(4) \times U(1)_X}: \qquad A_\mu\,(+)\,,\; A_5\,(-) \\
&\quad \text{Gauge bosons in } \frac{\mathrm{SO(5)}}{\mathrm{SO(4)}}: \qquad A_\mu\,(-)\,,\; A_5\,(+)
\end{aligned}
\tag{2.19}
$$

The above symmetry assignments and boundary conditions are depicted in Fig. 2.4.2.

The only thing that remains is to connect the UV and IR brane boundary conditions, i.e. determine the misalignment of the $\mathrm{SU(2)_I \times U(1)_Y}$ and the $\mathrm{SO(4) \times U(1)_X}$ within $\mathrm{SO(5) \times U(1)_X}$. This relative misalignment is determined by the

[1] "+" means Neumann and "-" means Dirichlet.

Wilson line [9, 32, 58, 59]:

$$U \;=\; e^{ig_5 \int_R^{R'} \langle A_5^a \rangle T^a \, dz}\,, \tag{2.20}$$

where g_5 is the 5D gauge coupling, T^a are the four generators in SO(5)/SO(4) and $\left\langle A_5^a \right\rangle$ is the VEV. Note that the Wilson line is nothing but the 5D realization of the pNGB matrix Eq. 2.1.

If $\left\langle A_5^a \right\rangle = 0$ there is no misalignment and $\mathrm{SU(2)_I \times U(1)_Y} \subset \mathrm{SO(4) \times U(1)_X}$, and so the boundary conditions are given as follows:

- 4 gauge bosons in $\mathrm{SU(2)_I \times U(1)_Y}$: $\quad A_\mu\,(++)\,,\; A_5\,(--)$
- 4 gauge bosons in SO(5)/SO(4): $\quad A_\mu\,(--)\,,\; A_5\,(++)$
- 3 gauge bosons in $\frac{\mathrm{SO(4)\times U(1)_X}}{\mathrm{SU(2)_I \times U(1)_Y}}$: $\quad A_\mu\,(-+)\,,\; A_5\,(+-)$

This means that the 4D effective theory has 4 massless $\mathrm{SU(2)_I \times U(1)_Y}$ gauge bosons and a complex Higgs doublet from the A_5 of G/H.

If $\left\langle A_5^a \right\rangle \neq 0$, $\mathrm{SU(2)_I \times U(1)_Y}$ is no longer contained in $\mathrm{SO(4) \times U(1)_X}$, and we need to apply the boundary conditions Eq. 2.19 for the fields $A_{\mu,5}$ on the UV brane and for the fields $U\,A_{\mu,5}\,U^{-1}$ on the IR brane. In this case we have

- SM photon in $[\mathrm{SU(2)_I \times U(1)_Y}] \cap [\mathrm{SO(4) \times U(1)_X}]$: $\quad A_\mu\,(++)\,,\; A_5\,(--)$
- SM $W^\pm$, Z in $[\mathrm{SU(2)_I \times U(1)_Y}] \cap \left[\frac{\mathrm{SO(5)}}{\mathrm{SO(4)}}\right]$: $\quad A_\mu\,(+-)\,,\; A_5\,(-+)$
- 1 gauge boson in $\left[\frac{\mathrm{SO(5)\times U(1)_X}}{\mathrm{SU(2)_I \times U(1)_Y}}\right] \cap \left[\frac{\mathrm{SO(5)}}{\mathrm{SO(4)}}\right]$: $\quad A_\mu\,(--)\,,\; A_5\,(++)$
- 6 gauge bosons in $\left[\frac{\mathrm{SO(5)\times U(1)_X}}{\mathrm{SU(2)_I \times U(1)_Y}}\right] \cap [\mathrm{SO(4) \times U(1)_X}]$: $\quad A_\mu\,(-+)\,,\; A_5\,(+-)$

Consequently, the 4D effective theory has 1 massless photon, 3 massive SM vectors $W^\pm$, Z, and a single real scalar - the physical Higgs. This is the 5D manifestation of the Higgs mechanism [32, 50, 58].

The form factors in Eq. 2.4 are extracted from our 5D model by applying the BC Eq. 2.19 for the VEV-rotated fields $U\,A_{\mu,5}\,U^{-1}$, and extracting the Green's functions in a similar way to Sec. 2.4. To extract the form factors in the top sector, we can introduce bulk fermions and apply UV and IR BC for their Higgs-rotated fields as well. We will not dwell into the details of this calculation, as it was covered many times in the literature [32, 38, 39, 59–62].

2.5 The Higgs Potential

Summing up the contributions of the gauge and top contributions to the Higgs potential in the CH_4 model, we arrive at the total Higgs potential

$$V_{\rm tot}(h) \;\approx\; \alpha\,\cos\frac{h}{f} - \beta\sin^2\frac{h}{f}\,, \tag{2.21}$$

where

$$\begin{aligned}\alpha &\equiv 6\int\frac{d^4p}{(2\pi)^4}\,F_1\left(q^2\right)\\ \beta &\equiv \int\frac{d^4p}{(2\pi)^4}\left\{6F_2\left(q^2\right) - \frac{9}{8}\frac{\Pi_1\left(p^2\right)}{\Pi_0\left(p^2\right)}\right\}.\end{aligned} \tag{2.22}$$

The coefficients α and β are of order f^4 and are completely calculable using the form factors extracted from warped 5D. By minimizing the potential Eq. 2.21 with respect to h, we can extract the Higgs mass and VEV:

$$\frac{v^2}{f^2} \;=\; 1-\left(\frac{\alpha}{2\beta}\right)^2 \quad,\quad m_h^2 \;=\; \frac{2\beta v^2}{f^4}\,. \tag{2.23}$$

A simple NDA for β gives

$$\beta \;=\; \frac{3}{8\pi^2}y_t^2\,f^2\,m_*^2\,, \tag{2.24}$$

where m_* is an effective $O(f)$ mass scale that is directly calculable from Eq. 2.22 using the 5D form factors. This gives

$$m_h^2 \;=\; \frac{3y_t^2}{4\pi^2}\,\xi\, m_*^2\,, \tag{2.25}$$

where $\xi \equiv \frac{v^2}{f^2}$. Electroweak precision constraints require $\xi \lesssim 0.1$, and so we can accommodate a 125 GeV Higgs if $m_* \gtrsim 2$ TeV.

The fine tuning required in this model was estimated in [63] to be $\frac{m_t^2}{m_*^2} \sim 1\%$, characteristic of what they define as "double-tuned models". Other CH models of this category are the CH_5 and CH_{10} [64], while the tuning in CH_{14} [41, 65] is only $\sim \xi \sim 10\%$.

2.6 Phenomenology

Here we briefly review the current and future bounds on CH models. These involve:

- *Higgs couplings*:

  In SO(5)/SO(4) CH, the Higgs-gauge boson term in the effective Lagrangian is given by

  $$\mathcal{L}_{hVV} \;=\; P_T^{\mu\nu}\,\frac{M_V^2}{v^2}\,f^2\sin^2\!\left(\frac{h}{f}\right)V_\mu V_\nu\,, \tag{2.26}$$

  where $V = W, Z$ and $v^2 \equiv f^2\sin^2(\langle h\rangle/f)$, as can be seen by expanding Eq. 2.4. Expanding around $h = \langle h\rangle$, we have

  $$\mathcal{L}_{hVV} \;=\; P_T^{\mu\nu}\,\frac{M_V^2}{v^2}\left[v^2 + 2v\sqrt{1-\xi}h + (1-2\xi)h^2 + \ldots\right]V_\mu V_\nu\,. \tag{2.27}$$

Consequently, the hVV and $hhVV$ couplings in CH models deviate from their SM values by

$$g_{hVV} = g_{hVV}^{\rm SM}\,\sqrt{1-\xi}\quad,\quad g_{hhVV} = g_{hhVV}^{\rm SM}\,(1-2\xi)\,, \tag{2.28}$$

with similar representation dependent deviations for $g_{ht\bar{t}}$. The projected bounds on g_{hZZ} and $g_{ht\bar{t}}$ from future lepton colliders (CPEC, FCC-ee, ILC) is of order 0.8% and 5%, respectively, providing projected bounds [66] of $\xi \lesssim 3\cdot 10^{-3}$, which could imply extensive tuning.

- *Electroweak precision*:

  Electroweak precision bounds from LEP are usually formulated in terms of the Peskin-Takeuchi parameters S and T [67]. In CH models with custodial symmetry in the Higgs sector (for example all SO(5)/SO(4) models), there is no tree level deviation in the T parameter due to the exchange of composite vector resonances. The S parameter gets a contribution [32, 64, 68]

  $$S \;=\; 4\pi\,(2.08)\left(\frac{v}{m_\rho}\right)^2\,, \tag{2.29}$$

  where m_ρ is the effective mass gap of the composite vector tower. An additional correction to the S and T parameters comes from the deviation in the Higgs-gauge boson couplings [69]:

  $$\begin{aligned}\Delta S &= \frac{1}{12\pi}\,\xi\,\log\left(\frac{4\pi f}{m_h}\right)\\ \Delta T &= -\,\frac{3\sec^2\theta_W}{16\pi}\,\xi\,\log\left(\frac{4\pi f}{m_h}\right).\end{aligned} \tag{2.30}$$

  The LEP bounds on S, T then imply that $m_\rho > 3\,\text{TeV}$ and that $\xi \leq 0.1$ for $m_\rho \sim 3.5$ [27].

- *Flavor*:

  The flavor bounds on models with partial compositeness (and no flavor

symmetry) were studied in [39,70]. The leading bound was from the contribution of the tower of composite gluons to tree level Flavor Changing Neutral Currents (FCNCs), and specifically the C_{4K} operator. Interestingly, models with partial compositeness enjoy some level of protection from FCNCs due to an alignment mechanism called RS-GIM [37], which lowers the bound on heavy vector resonances from $\Lambda_{\rm GUT}$ to $m_\rho \sim O(30\,\text{TeV})$. This is still and order of magnitude above the TeV scale, and so natural CH models with $m_\rho \sim 3.5\,\text{TeV}$ require flavor symmetry.

- *Direct top and gauge partner searches*:

  Finally, the LHC has put direct lower bounds on the masses of heavy vector resonances and vectorlike top partners. The current bounds on vectorlike top partners are of order $1.2\,\text{TeV} @ 36\,\text{fb}^{-1}$, where the exact limits depend on the charge of the top partner and its branching ratios [71–75]. The combined ATLAS bounds on heavy vector resonances are of order $3 - 4\,\text{TeV} @ 36\,\text{fb}^{-1}$, depending on the channel [76–79], comparable to the bound from electroweak precision.

CHAPTER 3

A TREE LEVEL QUARTIC FROM 6D COMPOSITE HIGGS

BEYOND THE STANDARD MODEL: COMPOSITE HIGGS AND DARK MATTER

Ofri Telem, Ph.D.

Cornell University 2019

We present a new class of composite Higgs models where an adjustable tree-level Higgs quartic coupling allows for a significant reduction in the tuning of the Higgs potential. Our 5D warped space implementation is the first example of a holographic composite Higgs model with a tree-level quartic. It is inspired by a 6D model where the quartic originates from the $\mathrm{Tr}[A_5, A_6]^2$ term of the gauge field strength, the same model that led to the original little Higgs construction of Arkani-Hamed, Cohen, and Georgi. Beyond the reduction of the tuning and the standard composite Higgs signatures, the model predicts a doubling of the KK states with relatively small splittings as well as a Higgs sector with two doublets in the decoupling limit.

3.1 Introduction

The origin of the Higgs potential and its stabilization is one of the key mysteries posed by the standard model (SM) of particle physics. An exciting possibility for explaining the dynamics behind electroweak symmetry breaking (EWSB) is that the Higgs boson itself is composite [9, 13, 14], due to an additional strong interaction at scales about a decade or two above the weak scale. While this idea is intriguing, it does not work without additional structure: in order to reduce the scale of the Higgs mass well below the new strong coupling scale, one also needs to assume that the Higgs is a pseudo-Nambu-Goldstone boson (pNGB) of a global symmetry broken at a scale f, giving rise to pNGB composite Higgs models. There are two basic types of these: little Higgs (LH) models [80, 81] which were very popular in the early 2000s and (holographic) composite Higgs (CH) models [32, 58, 64, 82], the simplest of which is the so called Minimal Composite Higgs Model (MCHM). For reviews see [27–30]. In both cases the essential ingredient for the 1-loop cancellation of the quadratic divergences is collective symmetry breaking [81], in which no single explicit breaking term breaks the global symmetry completely, and the divergences in the Higgs potential are softened. Most LH models contain a tree-level collective quartic (and a loop-induced finite or at most log divergent quadratic term), resulting in completely natural EWSB with no tuning. However, since the size of the quartic is determined by the same parameters as the quadratic, these models predict a heavy Higgs boson well above the observed 125 GeV mass. Holographic composite Higgs models have a loop-induced quartic and therefore predict the correct size of the Higgs mass. This, however, comes at a cost of a $(v/f)^2$ tuning [39] in the Higgs potential. Additionally, the top partners in these models tend to be at

least as heavy as 1.5 – 2 TeV and thus not immediately discoverable at the LHC.

The tuning in holographic composite Higgs models could clearly be reduced if a tree-level but adjustable quartic were present.[1] This realization has inspired us to revisit the original little Higgs model [80], formulated as a 6D gauge theory where two Higgses correspond to two Wilson loops going around the fifth and sixth dimensions and the collective quartic arises from the field strength term $\mathrm{Tr}[A_5, A_6]^2$.

The aim of this work is to implement the ideas of [80] within the holographic approach where the extra dimension is warped. For this purpose, we construct a 6D model on an $AdS_5 \times S_1$ background where the quartic is generated similarly to [80] and the Higgs can be interpreted as a composite pNGB. We discuss the essential aspects of the 6D model and then quickly zoom in on a simple and transparent formulation in terms of a warped 5D model, where only the sixth dimension has been deconstructed. The resulting Higgs sector is a CP-conserving two Higgs doublet model (2HDM) in the decoupling limit with a tree-level, MSSM-like quartic. As we will see, this quartic can be adjusted to fit the observed value without extra tuning.

In its warped 5D version it provides the first example of a composite Higgs model with a tree-level Higgs quartic coupling in which the only source of tuning is related to the reduction of the Higgs mass parameter. Moreover, the top partners in this model can be light and discoverable at the LHC. It turns out to be a relatively simple model which captures almost all the essential elements of the 6D theory (as well as the original model of [80]).

[1] For an alternative recent approach towards reducing the tuning in the Higgs potential for CH models see [83].

The chapter is organized as follows: Sec. 3.2 contains an explanation of the reduction of the tuning in the Higgs potential due to the presence of the adjustable Higgs quartic. In Sec. 3.3 we present the essential ingredients of the 6D theory and the structure of the zero modes. Sec. 3.4 contains the warped 5D model, which is the main new result of this work. We provide the matter content along with the structure of the Higgs potential and a mechanism for lifting the flat direction in the tree-level potential in Sec. 3.5. The matching onto generic 2HDM models is contained in Sec. 3.6, and the basic elements of the expected phenomenology in Sec. 3.7. We conclude in Sec. 3.8.

3.2 Motivations for a Quartic from 6D

The first implementation of the little Higgs idea [80] was based on a deconstructed [84] 6D gauge theory. The aim was to construct a composite Higgs model where a large tree-level quartic could result in a fully natural electroweak symmetry breaking (EWSB) Higgs potential. The extra dimensional components A_5, A_6 of the gauge field can have the right quantum numbers to be identified with the Higgs. Compactification of the extra dimension can provide physical irreducible Wilson lines in the extra dimension which have all the properties of a pNGB in 4D (see also [85]). The quartic arises from the field strength term:

$$\mathrm{Tr}[A_5, A_6]^2 \in F_{56}F_{56}. \tag{3.1}$$

In the deconstructed version, this corresponds to a plaquette operator.

Before explaining the details of the full 6D construction (as well as the simple warped 5D version), we would like to explain how the presence of such a tree-

level quartic could help alleviate the tuning in composite Higgs models[1]. The Higgs potential in CH models with a loop-induced quartic is parametrized as

$$V(h) = \frac{3g_t^2 M_\Psi^2}{16\pi^2}\left(-ah^2 + \frac{b}{2}\frac{h^4}{f^2}\right) \tag{3.2}$$

where g_t is the SM coupling, $M_\Psi = g_\Psi f$ is the top partner mass, and a and b are (at most) $O(1)$ numbers. The coefficients a and b can be smaller than 1 (at the price of tuning various terms against each other) but can not be bigger than $O(1)$. The tuning is then quantified by

$$\Delta = \frac{1}{ab}\,. \tag{3.3}$$

The origin of the v^2/f^2 tuning is easy to see: since both the quadratic and quartic terms are loop-induced by the same dynamics, the minimum of the potential is when $\frac{v^2}{f^2} = \frac{a}{b}$, which for $b \sim 1$ gives the "irreducible" tuning of composite Higgs models $\Delta = \frac{1}{ab} = \frac{f^2}{v^2} \gtrsim 9$. The lower bound on this tuning follows from electroweak precision and Higgs coupling constraints, which imply that that $\frac{f}{v} \gtrsim 3$. A more detailed analysis of the tuning yields

$$\Delta \simeq 8\, y_t \left(\frac{g_\Psi}{1.8}\right)^2 \left(\frac{f/v}{3}\right)^2 \gtrsim 8\, y_t\,, \tag{3.4}$$

since $g_\Psi > 1.8$ is required to get a large enough loop-induced quartic.

An additional (adjustable) tree-level quartic significantly changes the picture, reducing the previously "irreducible" $\frac{f}{v}$ tuning. The reason is that the coupling g_Ψ setting overall magnitude of the loop-induced Higgs potential can be taken smaller, while the adjustable contribution ensures that $\lambda = 0.13$. In this case the dominant bound on the tuning is no longer the indirect bound Eq. (3.4) but rather the direct bound on the top partner mass from direct searches at the LHC,

$$\Delta \simeq 5.5\, y_t \left(\frac{M_\Psi}{1100\ \text{GeV}}\right)^2 \gtrsim 5.5\, y_t\,. \tag{3.5}$$

[1]For a detailed analysis of the tuning in CH models, see [63].

This is parametrically weaker than the bound in the conventional CH. Moreover, Eq. 3.5 implies that top partners should lie just around the corner, well within the reach of the LHC.

The reduction of the bounds on tuning in twin Higgs type models [61, 62, 86–93] is even more impressive. One can show that twin Higgs models with an additional source of quartic will remain natural (no tuning required) even after the end of the high luminosity 13 TeV run of the LHC. Similar ideas have been discussed in [94, 95].

3.3 The 6D Composite Higgs Model

In the following section we present a warped model with a collective tree-level quartic for the pNGB Higgs. This model can either be written in six dimensions or deconstructed into lower dimensional models. As we will see in the next section, the simplest and most useful representation of this model is as a warped 5D model with two sites in the bulk representing the sixth dimension. To motivate this construction, we first review the essential features of the full 6D theory.

The 6D model is defined on an interval of $AdS_5 \times S_1/Z_2 \times Z_2$ with metric

$$ds^2 = \left(\frac{R}{z}\right)^2 (dx^2 - dz^2) - dy^2 \tag{3.6}$$

where the $R < z < R'$ coordinate parametrizes the warped direction of AdS_5 and $0 < y < R_y$ parametrizes the S_1 direction. The geometry along with the boundary conditions is illustrated in Fig. 3.1. At $z = R$ and $z = R'$ there are UV and IR 4-branes, and at $y = 0$ and $y = R_y$ there are other 4-branes, denoted Down and Up.

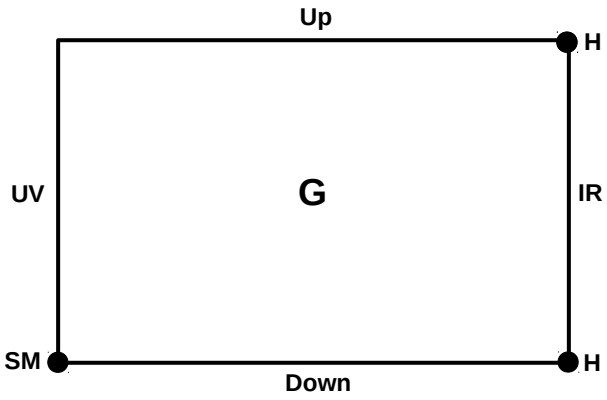

Figure 3.1: A sketch of the layout of the 6D model. The rectangle represents the two extra dimensions, the horizontal corresponding to the warped extra dimension, the vertical to the extra flat segment of the 6th dimension. The 3-branes in the 3 corners represent the symmetry breaking pattern at those locations, necessary to obtain the appropriate pattern of Higgs fields and couplings.

Furthermore, there are 3-branes at the four 'corners' UV-Down, UV-Up, IR-Up, and IR-Down.

The bulk gauge symmetry of the model is G (usually chosen to be $SO(5)$ to incorporate custodial symmetry), broken to an H subgroup ($SO(4)$ in the simplest model) on the IR-Up, and IR-Down 3+1 branes. This setting is a direct extension of the standard CH construction of a bulk G in AdS_5 broken to H on the IR brane. The two IR symmetry breaking points in our case correspond to two sets of G/H pNGBs instead of just a single one in the standard CH. Additionally, the bulk symmetry on the UV-Down corner to the SM $SU(2) \times U(1)$. This is analogous to the UV breaking in the standard CH, which ensures that only the SM gauge bosons remain light.

In a similar way to 5D gauge-Higgs unification, the Higgses in our setting

arise as the two Wilson lines connecting the UV-down corner where the G symmetry is broken with the two IR symmetry breaking points. To calculate the Higgs potential, we start from the 6D Maxwell action

$$\mathcal{S} = -\frac{1}{4g_6^2}\int d^4x dz dy\ \sqrt{g} F^a_{MN} F^{a;MN}\ . \tag{3.7}$$

Choosing a bulk Lorentz gauge ($\partial^M A^a_M = 0$), we find the bulk equations of motion for $A^a_{z,y}$ simplify to:

$$\partial_z\left(\frac{R^3}{z^3}F^a_{zy}\right) = 0\ ,\ \partial_y\left(\frac{R^3}{z^3}F^a_{zy}\right) = 0\,. \tag{3.8}$$

By integrating the bulk action by parts, we can also obtain the boundary conditions:

$$F^a_{zy}\,|_{UV,\,IR,\,UP,\,DN} = 0\ ,\ F^a_{\mu z}\,|_{UV,\,IR} = 0\ ,\ F^a_{\mu y}\,|_{UP,\,DN} = 0\ . \tag{3.9}$$

We would like to emphasize that these BC are valid at generic points on the 4-branes, but not on the 3-branes at the UV-Down, IR-Up, and IR-Down corners in the corners, where the BC are modified for the broken generators. In the Lorentz gauge the generic BC can be rewritten as:

$$F^a_{zy}\,|_{UV,\,IR,\,UP,\,DN} = 0\ ,\ A^a_z\,|_{UV,\,IR} = 0\ ,\ A^a_y\,|_{UP,\,DN} = 0. \tag{3.10}$$

Together with the bulk EOMs these BCs can only be satisfied if $F^a_{zy} = 0$ throughout the entire bulk. The vanishing of $F^a_{zy} \equiv \left(\partial_y A^a_z - \partial_z A^a_y\right)$ allows us to define a bulk potential F^a so that $A^a_z = \partial_z F^a$, $A^a_y = \partial_y F^a$. The potential F^a satisfies the warped version of a 2D Laplace equation, and will be the main object of interest for us. This potential also has a distinct physical meaning: after fixing an integration constant, this potential is exactly the log of the Wilson line from the UV-Down 3-brane to any other point in the bulk.

The problem of finding zero modes for A_z and A_y is thus reduced to solving the warped Laplace equation on a rectangle with Dirichlet boundary conditions

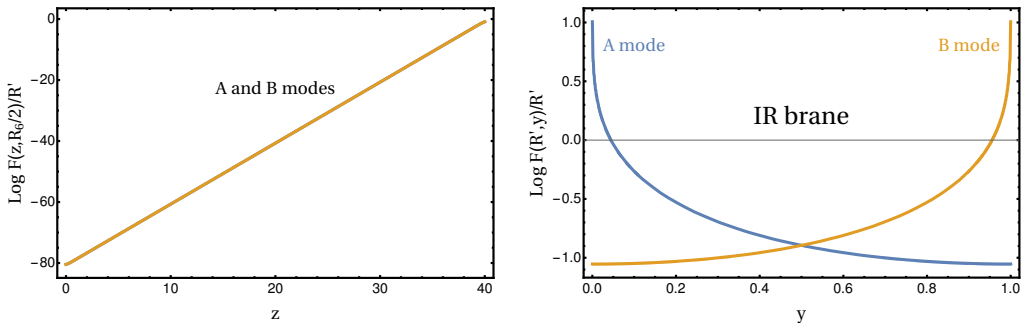

Figure 3.2: Slices of the 6D zero modes. (a): z-slice at $y = R_6/2$ as a function of z, illustrating that both are IR localized. (b) y-slice of the IR 4-brane $z = R'$. Here the modes differ: mode A is localized close to the IR-Down corner, while mode B is localized close to the IR-Up corner.

everywhere but the three gauge symmetry breaking points on the UV-Down, IR-Up, and IR-Down corners. We have obtained the full solution to this problem via Fourier transforms. The solution is a linear combination of two zero modes $A, B = 1, 2$:

$$F^i(z, y, x) = F_A(z, y)\, h_A^i(x) \;+\; F_B(z, y)\, h_B^i(x), \tag{3.11}$$

where F_A are the extra dimensional wave functions and h_A^i are two 4D doublet modes. Both of these are IR localized, F_A is localized in the IR-Up corner and F_B is localized in the IR-Down corner. The index i above stands for the $SU(2)_L$ doublet embedded in the adjoint of $SO(5)$ as usual, and will be suppressed in the following. We present slices of the zero modes obtained from solving the 2D Laplace equation in Fig. 3.2. We can see that indeed both modes are IR localized, and peak at two different corners on the IR brane.

3.4 A 5D Model Holographic Composite Higgs Model with a Tree-level Quartic

In this section we present the key result of this work: a warped 5D composite Higgs model with a non-vanishing tree-level quartic for the Higgses. It is based on the 6D model outlined in the previous section, by deconstructing the flat sixth dimension as a two-site model, while the warped fifth dimension is kept unchanged. For previous attempts at warped UV completions of LH models see [96, 97]. The background is the standard AdS_5 metric in the 5D bulk

$$ds^2 = \frac{R^2}{z^2}\left(dx^2 - dz^2\right) \tag{3.12}$$

and the bulk Lagrangian looks like a two-site model: the bulk gauge symmetry is $SO(5)^u \times SO(5)^d$, where $i = u, d$ are the two sites mimicking the effect of the 6th dimension. The bulk symmetry is broken on the IR brane to $SO(4)^u \times SO(4)^d$ and on the UV brane in $SO(5)^u \times [SU(2)_L \times U(1)_Y]^d_{SM}$. In addition, the $SO(5)^u \times SO(5)^d$ symmetry is broken in the bulk to the diagonal $SO(5)_V$, with the original $SO(5)^u \times SO(5)^d$ realized nonlinearly via a bulk link field $U = e^{i\frac{\sqrt{2}}{f_6}\pi^a T^a}$. The π^a's play the role of the 6th component of the 6D $SO(5)$ gauge fields A_y. The decay constant f_6 is taken to be a constant along the 5th dimension, and is roughly of the order of the inverse AdS curvature $1/R$. This model is illustrated in Fig. 3.3.

Next we will explicitly show that this model contains two scalar zero modes with IR localized profiles. The bulk action for this model includes the gauge kinetic terms and the covariant derivative of the link field:

$$S = \int d^4x dz \sqrt{g}\left(-\frac{1}{4}F_{MN}F^{MN} + \frac{f_6^2}{4}\left(D^M U\right)^\dagger D_M U\right), \tag{3.13}$$

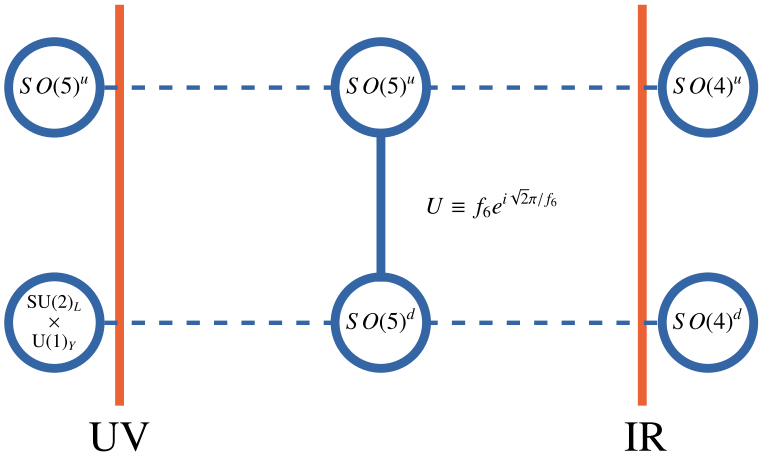

Figure 3.3: A sketch of the main elements of our deconstructed 5d model. The two sites in the bulk represent the $SO(5)^u \times SO(5)^d$, broken on the IR into $SO(4)^u \times SO(4)^d$ and on the UV into $SO(5)^u \times [SU(2)_L \times U(1)_Y]^d_{SM}$. The bulk link corresponds to the breaking of $SO(5)^u \times SO(5)^d$ into the diagonal $SO(5)_V$ with a constant VEV in the bulk.

where the covariant derivatives are

$$D_\mu U = \left(\frac{\sqrt{2}}{f_6}\partial_\mu \pi - g_5 A^{(A)}_\mu\right) + ..., \quad D_z U = -\left(\frac{\sqrt{2}}{f_6}\partial_z \pi - g_5 A^{(A)}_z - i\frac{\sqrt{2}g_5}{f_6}\left[A^u_z, \pi\right]\right) + ... \tag{3.14}$$

and $A^{(A)}_{\mu,z} \equiv A^u_{\mu,z} - A^d_{\mu,z}$, $A^{(V)}_{\mu,z} \equiv A^u_{\mu,z} + A^d_{\mu,z}$, while the ellipses stand for higher order commutator terms and terms negligible in the limit $R \ll R'$. The scalar zero modes live in a linear combination of π and $A^{u,d}_z$. We will use the Lorentz gauge $\partial_\mu A^\mu = 0$, with the additional gauge fixing $A^{(A)}_0 = 0$. The vector combination A^V_z corresponds to an unbroken bulk symmetry, and so the part of the zero mode contained in the corresponding fifth component must be of the usual form $A^V_z \sim z$. Substituting the π variation in the axial part of the A_0 variation, we obtain the equation for the zero mode as well as the relation between A_z and π components

of the zero mode:

$$\begin{aligned} \frac{z^3}{R^3}\partial_z\left[\frac{R}{z}\,\partial_z\pi\right] - g_5^2 f_6^2\,\pi &= 0 \\ \partial_z\pi \;-\; \frac{g_5 f_6}{\sqrt{2}} A_z^{(A)} &= 0\,. \end{aligned} \tag{3.15}$$

We choose the UV boundary condition to be $A_z^u|_{UV} = 0$. We do not need to specify an IR boundary condition for the A_zs: the reason is that in the gauge we chose there is no boundary localized term involving A_z, thus one does not need to consider the boundary variation of these fields. This is in accordance with our expectations from the fact that the A_z equations of motion are effectively first order, hence one BC should be sufficient. The space of zero mode solutions is two dimensional, spanned by modes A and B satisfying:

$$\begin{aligned} \text{A mode} \;&:\quad A_z^d|_{IR} = 0 \\ \text{B mode} \;&:\quad A_z^u|_{IR} = 0\,. \end{aligned} \tag{3.16}$$

The two solutions to the EOM are:

$$\begin{aligned} \pi(z,x)_{A/B} &= \frac{g_5 f_6}{2\sqrt{2}}\left[\pm\frac{1}{1+\alpha}\left(\frac{R}{R'}\right)^{\alpha}\left(\frac{z}{R}\right)^{1+\alpha} + \frac{1}{1-\alpha}\left(\frac{R}{R'}\right)\left(\frac{z}{R}\right)^{1-\alpha}\right] h_{A/B}(x) \\ A_z^u(z,x)_{A/B} &= \frac{1}{2R}\left\{\frac{z}{R'} + \left[\pm\left(\frac{R}{R'}\right)^{\alpha}\left(\frac{z}{R}\right)^{\alpha} + \left(\frac{R}{R'}\right)\left(\frac{z}{R}\right)^{-\alpha}\right]\right\} h_{A/B}(x) \\ A_z^d(z,x)_{A/B} &= \frac{1}{2R}\left\{\frac{z}{R'} - \left[\pm\left(\frac{R}{R'}\right)^{\alpha}\left(\frac{z}{R}\right)^{\alpha} + \left(\frac{R}{R'}\right)\left(\frac{z}{R}\right)^{-\alpha}\right]\right\} h_{A/B}(x)\,, \end{aligned} \tag{3.17}$$

where $\alpha = \sqrt{1 + g_5^2 f_6^2 R^2}$ and $h_A(x)$ and $h_B(x)$ are the two canonically normalized 4D modes. The $\pm$ mean a "+" for the A mode and a "−" for the B mode.

In the $g_5 f_6 R = g_* f_6 R^{3/2} \equiv \theta_6 \ll 1$ limit, which is necessary to obtain a quartic smaller than $O(1)$ (see Sec. 3.4.1), the profiles far from the UV brane ($z \gg R$) are:

$$\begin{aligned} \text{A Mode} \;&:\quad A_z^u(z) = \frac{1}{R}\frac{z}{R'}\,h_A(x)\,,\; A_z^d(z) = O(\theta_6^2)\,h_A(x)\,,\; \pi(z) = O(\theta_6)\,h_A(x) \\ \text{B Mode} \;&:\quad A_z^u(z) = O(\theta_6^2)\,h_B(x)\,,\; A_z^d(z) = \frac{1}{R}\frac{z}{R'}\,h_B(x)\,,\; \pi(z) = O(\theta_6)\,h_B(x) \end{aligned} \tag{3.18}$$

This can be understood as the limit of no bulk breaking, in which the two modes simply correspond to the pNGBs of the two separate SO(5)/SO(4) cosets. It is then sensible to define the pNGB matrices:

$$\Sigma^u = \exp\left(ig_6 \int_R^{R'} A_z^u dz\right) \equiv e^{ih_u/f} \ , \ \Sigma^d = \exp\left(ig_6 \int_R^{R'} A_z^d dz\right) \equiv e^{ih_d/f} \tag{3.19}$$

These matrices restore the two $SO(5)$ symmetries by rotating the IR vacua that break $SO(5)$ into $SO(4)$. In the limit $\theta_6 \ll 1$:

$$h_u \approx h_A \ , \ h_d \approx h_B \, . \tag{3.20}$$

Since we need to work in this limit for any realistic model building, from now on we identify $h_{A,B}$ with $h_{u,d}$.

3.4.1 The tree-level quartic

We can now evaluate the quartic scalar coupling by substituting the zero modes in the commutator term of Eq. (3.14):

$$\mathcal{L}_\lambda \quad = \quad \lambda \, \mathrm{Tr}\left[h_A, h_B\right]^2 \approx \lambda \, \mathrm{Tr}\left[h_u, h_d\right]^2 \tag{3.21}$$

with

$$\lambda \quad = \quad g_5^2 \int dz \left(\frac{R}{z}\right)^3 \left[\pi_A \, A^V_{z,B} - \pi_B \, A^V_{z,A}\right]^2 . \tag{3.22}$$

Plugging in the profiles and working in the limit $R'/R \to \infty$, we get:

$$\lambda \quad = \quad g_5^2 \frac{g_5^2 f_6^2 R}{4(1+\alpha)^3} \sim \frac{1}{4} g_*^2 \, \theta_6^2 \, . \tag{3.23}$$

where the last result is in the limit that the scale of the bulk breaking is small, i.e. $\theta_6 \ll 1$. This choice is necessary to get a quartic which is smaller than $O(1)$, and as promised, also justifies the identification Eq. (3.20).

The quartic has the following structure:

$$\lambda\,[h_u, h_d]^2 = \lambda\left(h_1^\dagger h_1 - h_2^\dagger h_2\right)^2 + \lambda\ \mathrm{tr}\left(h_1 h_1^\dagger - h_2 h_2^\dagger\right)^2\ , \tag{3.24}$$

where we have adopted the definitions of [80]:

$$h_1 = \frac{1}{\sqrt{2}}\left(h_u + i h_d\right)\ ,\ h_2 = \frac{1}{\sqrt{2}}\left(h_u - i h_d\right)\ . \tag{3.25}$$

This quartic has a flat direction for h_u or h_d, which corresponds to $h_1 = \pm h_2$. In Sec. 3.5.3 we will discuss how these flat directions are lifted radiatively by the SM top and its partners.

3.4.2 The 4D interpretation

The warped 5D picture makes it easier to identify the 4D dual to our model based on the rules of the AdS/CFT correspondence [42, 98, 99]. As in the standard CH, this dual is a strongly interacting theory which is close to conformal in the UV but confines in the IR. Above the confinement scale there is a global symmetry $G \times G$ (the bulk symmetry in the 5D picture), and the IR condensate breaks it to $H \times H$ with two sets of G/H pNGBs.

To better understand the CFT dual to the $G \times G \to G$ breaking in the bulk we have to specify the origin of this breaking. We take this origin to be a scalar in the bi-fundamental of $G \times G$ which gets a bulk VEV. The generic profile of this scalar is:

$$U(z)\ =\ f_6\left[\left(\frac{z}{R}\right)^{-\epsilon} + b\left(\frac{z}{R'}\right)^{4+\epsilon}\right], \tag{3.26}$$

with $\epsilon = \sqrt{4 + m^2/k^2} - 2$. The coefficient b is determined by the IR boundary conditions and is generically $\sim \mathcal{O}\left(\frac{R^\epsilon}{R'^\epsilon}\right)$. By choosing the bulk mass of the scalar

to be small, we can have $\epsilon \approx 0$ and $b \sim \mathcal{O}(1)$, so that

$$U(z) \;\approx\; f_6 \left[1 + b\left(\frac{z}{R'}\right)^4\right], \tag{3.27}$$

Which is well approximated by a constant VEV f_6 in the bulk and slightly larger VEV $f_6' \;=\; f_6\;(1+b)$ on the IR brane. The presence of $G\times G \to G$ breaking on the IR brane does not spoil the collective breaking in our scenario, as we elaborate towards the end of this section.

Using the AdS/CFT dictionary, this configuration corresponds to a source $\mathcal{J}_{G\times G}$ coupled to an operator $\mathcal{O}_{G\times G}$ that transforms as a bi-fundamental of the global $G \times G$:

$$\Delta\mathcal{L} \;=\; \mathcal{J}_{G\times G}\,\mathcal{O}_{G\times G}\,. \tag{3.28}$$

The magnitude of the source is f_6, while its dimension is $-\epsilon \;\approx\; 0$ and the dimension of the operator is $4+\epsilon \approx 4$. The source explicitly breaks $G \times G$ to the diagonal, and also triggers a VEV for the operator [99]:

$$\langle \mathcal{O}_{G\times G}\rangle \;=\; (4+2\epsilon)\;\frac{b f_6}{R'^{4+\epsilon}}\,, \tag{3.29}$$

Due to the explicit $G \times G \;\to\; G$ breaking from the source, the $G \times G/H \times H$ pNGBs get a tree-level potential. Remarkably, this tree-level potential consists only of a commutator-squared term, and in particular does not include tree-level masses for the pNGBs. This is a demonstration of the 'collective' nature of our potential.

In addition to the effect of the explicit $G \times G$ breaking, one might worry that the VEV $\langle \mathcal{O}_{G\times G}\rangle$ (dual to the $G\times G$ breaking on the IR brane) could generate a tree level mass to the axial PNGB, spoiling our collective breaking. This is indeed true, but is an artifact of representing the six dimension with only two sites

in the bulk. Indeed, in the full 6D model the two G/H breakings are physically separated along the 6th dimension, and the tree level mass for the axial PNGB is exponentially suppresses. This effect would have been captured in a 5D model with more sites in the bulk. For that reason, we did not include any $G \times G$ breaking on the IR brane in our 5D model from section 3.4.

3.5 The SM field content

So far we have only considered the scalar modes and their tree-level quartic (while also introducing the SM gauge fields). In this picture, the 4D gauge fields correspond to the zero modes of the surviving diagonal subgroup of the bulk gauge symmetry:

$$A_\mu^{SM} = A_\mu^u + A_\mu^d. \tag{3.30}$$

These are the $SU(3) \times SU(2) \times U(1)_Y$ gauge fields, which have Neumann BC on both branes and no bulk mass.

The scalar sector consists of two pNGB Higgs scalars which in the $\theta_6 \ll 1$ limit are the $h_{u,d}$ of $SO(5)^{u,d}/SO(4)^{u,d}$. However, the $h_{u,d}$ basis is not the physical basis for our Higgses, as we will see from the radiatively generated contribution. Instead, we work in the $h_{1,2}$ basis of Eq. (3.24), with the quartic given by Eq. (3.25).

Next we introduce the SM fermion matter content into this theory. Presently we do not specify the light fermion representations, as there are many different possibilities. The exact choice will definitely be relevant for flavor physics, but its effect on the Higgs potential is negligible. In the following we will only focus on the top sector and its contribution to the Higgs potential. To be consistent

with the LHC results on Higgs couplings, we require one Higgs to be SM-like, while the other one should be heavy. We achieve this by arranging for the top to couple only to h_1 so that the top loop gives a negative mass term for h_1, while h_2 is lifted by the other members of the top's $SO(5)$ multiplet.

3.5.1 The top sector

The simplest choice for the top sector is to embed t_L in a multiplet T_L transforming as a $(\mathbf{5},\mathbf{1}) + (\mathbf{1},\mathbf{5})$ of $SO(5) \times SO(5)$, while t_R is a singlet localized on the IR brane. This is summarized in Tab. 3.1. In terms of two component spinors, the bulk fermion T_L can be written as

$$T_L = \begin{pmatrix} \chi_L^u & \chi_L^d \\ \bar{\psi}_L^u & \bar{\psi}_L^d \end{pmatrix}, \tag{3.31}$$

where $\chi^{u,d}, \psi^{u,d}$ are 2-component Weyl spinors. We impose a Z_4 symmetry on the fermion sector in the bulk and on the U field:

$$\begin{aligned} Z_4: \qquad & T_L^u \to -T_L^d \qquad T_L^d \to T_L^u \\ & U \to U^\dagger \, (\pi \to -\pi) \ . \end{aligned} \tag{3.32}$$

As we will see, this Z_4 symmetry ensures that the top couples only to h_1, which is important for a realistic Higgs potential. The 5D Lagrangian for T_L can be written as

$$\begin{aligned} \mathcal{L}_{T_L} \ = \ & \left[i\bar{\chi}_L \bar{\sigma}^\mu D_\mu \chi_L + i\psi_L \sigma^\mu D_\mu \bar{\psi}_L + \frac{1}{2}\left(\psi_L \overleftrightarrow{D_z} \chi_L - \bar{\chi}_L \overleftrightarrow{D_z} \bar{\psi}_L \right) + \frac{c_L}{z} \left(\psi_L \chi_L + \bar{\chi}_L \bar{\psi}_L \right) \right]^{u,d} + \\ & \frac{y_6 \theta_6}{2z} \left(i\psi_L^d \, U^\dagger \chi_L^u - i\psi_L^u \, U \chi_L^d + i\bar{\chi}_L^d \, U^\dagger \, \bar{\psi}_L^u - i\bar{\chi}_L^u \, U \, \bar{\psi}_L^d \right), \end{aligned} \tag{3.33}$$

where y_6 is a $O(1)$ coupling of the link field. The first line is just the standard 5D warped fermion Lagrangian, while the second line includes the fermion cou-

plings to the link field which stand for their coupling to A_6 in the full 6D Lagrangian. The bulk masses for both multiplets are assumed to be equal. This arises naturally in the 6D picture and can be thought of as a $u \leftrightarrow d$ Z_2 symmetry that is preserved in the bulk and on the IR brane (while broken in the UV).

Field	$SO(5)^u$	$SO(5)^d$
$(\chi_L, \bar{\psi}_L)^u$	$\square$	**1**
$(\chi_L, \bar{\psi}_L)^d$	**1**	$\square$
t_R	**1**	**1**
U	$\square$	$\bar{\square}$

Table 3.1: Representations of the 5D Model Top Sector

The A_z VEV is set to zero by a gauge rotation [59], with the A_z Wilson line entering in the IR boundary condition. Rotating to the bulk mass basis, we have

$$\mathcal{L}_{T_L} = \left[i\bar{\chi}_L \bar{\sigma}^\mu \partial_\mu \chi_L + i\psi_L \sigma^\mu \partial_\mu \bar{\psi}_L + \frac{1}{2}\left(\psi_L \overleftrightarrow{\partial_z} \chi_L\right) + \frac{c_L \pm y_6\theta_6}{z}\psi_L\chi_L \right]^{0,1}, \quad (3.34)$$

where $\psi_L^{0,1} = \frac{1}{\sqrt{2}}\left(\psi_L^u \pm i\psi_L^d\right), \chi_L^{0,1} = \frac{1}{\sqrt{2}}\left(\chi_L^u \pm i\chi_L^d\right)$.

We see that the full T_L bulk multiplet splits into two bulk fermions with masses $c_L \pm y_6\theta_6$. On the IR brane we will always take the same BC for the up and down fermions, while on the UV the BC may be different. To understand how this works, take for example the following BC for a bulk fermion:

$$\tilde{\chi}_L^u : (-,+)\,,\ \tilde{\chi}_L^d : (+,+)\,, \quad (3.35)$$

where the tilde serves to remind us that the boundary conditions are for the Wilson line rotated fields

$$\tilde{\chi}_L^u = \chi_L^u\,\Sigma^u\,,\ \tilde{\chi}_L^d = \chi_L^d\,\Sigma^d\,, \quad (3.36)$$

and $\Sigma^{u,d}$ are the usual pNGB matrices given by Eq. (3.19). In terms of the two combinations in the bulk mass basis $\tilde{\psi}^{0,1}_l$ this corresponds to:

$$\begin{aligned} \tilde{\psi}^0_L(R) = \tilde{\psi}^1_L(R) \quad &, \quad \tilde{\chi}^0_L(R) = -\tilde{\chi}^1_L(R) \\ \tilde{\psi}^0_L(R') = \quad 0 \quad &, \quad \tilde{\psi}^1_L(R') = \quad 0 \quad . \end{aligned} \tag{3.37}$$

These boundary conditions result in a single zero mode that lives both in the 0 and 1 parts of the multiplet:

$$\chi^{0,1}_L(z,x) \sim \left(\frac{z}{R}\right)^{c_L \pm y_6 \theta_6} t_L(x) \ . \tag{3.38}$$

Note that the combination χ^0 with the higher bulk mass rises faster towards the IR, and so the dominant contribution to the Higgs potential comes from that combination. In the following calculation of the Higgs potential we will neglect the χ^1 contribution, and comment on it in the end of section 3.6.

On the IR brane, the singlets of $SO(4) \times SO(4)$ in the T_L multiplet can couple to t_R. Formally, these couplings can be written in terms of the spurions that break the $SO(5)$s into $SO(4)$s, denoted as $S_{u,d} = (0,0,0,0,1)$. The IR Lagrangian is given by:

$$L_{IR} = \mu \bar{\chi}^u_L \Sigma^u S_u t_R + \mu \bar{\chi}^d_L \Sigma^d S_d t_R + h.c. \tag{3.39}$$

with the projections of the *pNGB* matrices written explicitly as

$$\Sigma^{u,d} S_{u,d} = \frac{\sin\left(\frac{h^{u,d}}{f}\right)}{h^{u,d}} \left[h^{u,d}_1, h^{u,d}_2, h^{u,d}_3, h^{u,d}_4, h^{u,d} \cot\left(\frac{h^{u,d}}{f}\right) \right]^T \ , \ h^{u,d} = \sqrt{h^{u,d}_a h^{u,d}_a}. \tag{3.40}$$

We have also assumed that the IR masses respect the $u \leftrightarrow d$ symmetry (similarly to the bulk masses).

3.5.2 The top contribution to the Higgs potential

The 4D effective Lagrangian for the top zero mode can be obtained from Eq. (3.39) by inserting the bulk profile of Eq. (3.38) evaluated on the IR brane. The profile on the IR brane is dominated by the combination $T_L^0 = \frac{1}{\sqrt{2}}\left(T_L^u + iT_L^d\right)$ of the two bulk multiplets, and so on the IR brane

$$\chi_L^d \simeq i\chi_L^0 \, , \, \chi_L^u \simeq \chi_L^0 \tag{3.41}$$

The 4D Lagrangian for the top is then:

$$\mathcal{L}_{\text{top}} = \frac{y_t f}{\sqrt{2}} \bar{\chi}_L^0 \left(\Sigma^u S_u + i\Sigma^d S_d\right) t_R \tag{3.42}$$

where

$$\bar{\chi}_L^0 = \frac{1}{\sqrt{2}}\left(-i\bar{b}_L, \bar{b}_L, i\bar{t}_L, \bar{t}_L, 0\right) . \tag{3.43}$$

Substituting these definitions and expanding to second order in the Higgs doublets $h_{1,2}$, where

$$h_{1,2} = \frac{1}{2}\begin{pmatrix} ih_3^u + h_4^u \pm i\left(\, ih_3^d + h_4^d\right) \\ -ih_1^u + h_2^u \pm i\left(-ih_1^d + h_2^d\right) \end{pmatrix}, \tag{3.44}$$

we get the effective Yukawa coupling of the top:

$$\mathcal{L}_{\text{eff}} = y_t \, h_1 \, \bar{t}_L t_R. \tag{3.45}$$

We see that the top couples only to h_1, so that it contributes a $-\frac{3y_t^2 M_{KK}^2}{16\pi^2} h_1 h_1^\dagger$ to the 2HDM potential, generating a negative quadratic term in the h_1 direction.

3.5.3 Lifting the flat direction

To lift the flat direction we must have a sizable positive mass term of h_2. To do that, we break down the contribution of the top partners to the Higgs potential.

The top partners populate the T_L multiplet, which is the $(\mathbf{5},\mathbf{1})+(\mathbf{1},\mathbf{5})$ of $SO(5)\times SO(5)$. As before, we separate T_L into the linear combinations:

$$T_L^{0,1} = \frac{1}{\sqrt{2}}\left(T_L^u \pm iT_L^d\right) , \tag{3.46}$$

These multiplets couple to t_R through the pNGB matrices:

$$\mathcal{L}_{\text{top+topKK}} = \frac{y_t f}{\sqrt{2}}\bar{\chi}^{0,1}\left(\Sigma^u S_u \pm i\Sigma^d S_d\right)t_R + h.c. \tag{3.47}$$

where $\chi^{0,1}$ are the left handed Weyl fermions in the Dirac fermions $T_L^{0,1}$.

The total contribution to the Higgs potential from complete multiplets T_L^0 and T_L^1 has to be zero, because their linear combinations T_L^u, T_L^d form complete $SO(5)\times SO(5)$ multiplets. Furthermore, even the individual contributions of complete multiplets T_L^0 and T_L^1 are separately zero. Indeed, the Coleman Weinberg potential depends on $T_L^{0,1}$ through

$$\left|\frac{y_t f}{\sqrt{2}}\left(\Sigma^u S_u \pm i\Sigma^d S_d\right)\right|^2 = y_t^2 f^2 , \tag{3.48}$$

which is independent of $h_{1,2}$. Since our zero modes live mostly in T_L^0 and all the other modes are at M_{KK}, we can now ignore the complete multiplet T_L^1 and focus only on the T_L^0 contribution, which is cut at M_{KK}.

The top partners in T_L^0 are:

$$T_L^0 = \frac{1}{\sqrt{2}}\left(0,0,-i\tilde{t}_d^0,\tilde{t}_d^0,t_s^0\right) . \tag{3.49}$$

Here t_d^0 is part of an electroweak doublet and t_s^0 is an electroweak singlet. Their couplings to the Higgs in Eq. (3.47) can be explicitly written as:

$$\mathcal{L}_{\text{top partners}} = y_t\tilde{t}_{dL}^0 h_2^\dagger t_R + y_t\tilde{t}_{sL}^0\left(f-\frac{h_1^2}{2f}-\frac{h_2^2}{2f}\right)t_R + M_d\tilde{t}_{dL}^0 t_{dR}^0 + M_s\tilde{t}_{sL}^0 t_{sR}^0 , \tag{3.50}$$

while the Higgs potential contribution of this sector is

$$V(h_1,h_2) = -\frac{3y_t^2M_s^2}{16\pi^2}h_1h_1^\dagger + \frac{3y_t^2\left(M_d^2-M_s^2\right)}{16\pi^2}h_2h_2^\dagger . \tag{3.51}$$

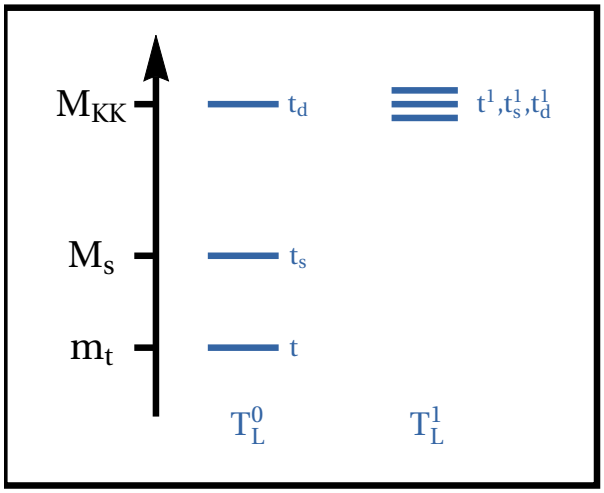

Figure 3.4: The top partner spectrum in our model.

The top partner spectrum of our model is shown in Fig. 3.4. We see that M_s acts effectively as a cutoff for the h_1 mass term, while both the doublet and the singlet contribute to h_2 with opposite signs. For $M_d > M_s$, we get a positive mass for h_2, lifting the flat direction as required. A simple way to achieve this is to take t^0_{sL} as a zero mode as well, and marry it in the bulk and on the IR to a similar right handed fermion in a new multiplet. The b.c. for the top multiplet are thus taken as:

$$\begin{aligned}
(t_L, b_L) \quad &: \quad \tilde{\chi}^u_L : (-,+)\ ,\ \tilde{\chi}^d_L : (+,+) \\
(t_{dL}, b_{dL}) \quad &: \quad \tilde{\chi}^u_L : (-,+)\ ,\ \tilde{\chi}^d_L : (-,+) \\
s_L \quad &: \quad \tilde{\chi}^u_L : (-,+)\ ,\ \tilde{\chi}^d_L : (+,+),
\end{aligned} \tag{3.52}$$

where the b.c. are given for the left-handed Weyl fermion and the b.c. are flipped for the opposite chirality. The new multiplet S_R is also in a $(\mathbf{5},\mathbf{1}) + (\mathbf{1},\mathbf{5})$ of $SO(5) \times SO(5)$. Its boundary conditions are different from those of T_L, as only

the singlets of $SO(4) \times SO(4)$ have BC similar to the top

$$\tilde{\chi}^u_S : (-,+)\,,\ \tilde{\chi}^d_S : (+,+)\,, \tag{3.53}$$

while the rest have $(-,+)$ BC for both up and down components. This means that the zero mode, which we denote s^0_R, exactly mirrors t^0_{sL} and can marry it in the bulk and on the IR. The bulk mass of the multiplet is chosen such that zero mode is localized sufficiently far from the UV so that $M_s \lesssim M_{kk}$. We also choose the mixing of the two multiplets to obey the full $SO(5)\times SO(5)$ symmetry so that a new contribution to the Higgs potential is not generated. The 4D Lagrangian is then exactly Eq. (3.50) with M_s being a free parameter. With our choice of $M_s < M_d \sim M_{KK}$, the total radiative Higgs potential is

$$V(h_1, h_2) = -\frac{3y_t^2 M_s^2}{16\pi^2} h_1 h_1^\dagger + \frac{3y_t^2 M_{KK}^2}{16\pi^2} h_2 h_2^\dagger\,. \tag{3.54}$$

This potential lifts the h_2 mass to the KK scale, so that:

$$m_{h_2} = \frac{M_{KK}}{M_s} m_{h1} \approx \frac{M_{KK}}{\sqrt{2}M_s} m_h \tag{3.55}$$

where m_h is the measured mass of the SM Higgs (which corresponds to h_1 in our scenario).

3.6 The 2HDM Potential

In this section we present the Higgs potential in our model. As we will see, this is a 2HDM potential in the decoupling limit[1]. The h_1 doublet will serve as the SM Higgs, coupling with approximately SM magnitudes to the W and Z gauge bosons and to the top and bottom sector, while h_2 will be heavy.

[1]For another example of a CH model with a 2HDM scalar sector, see [100].

3.6.1 Mass terms and quartic

The SM-like h_1 gets a negative quadratic term via top loops

$$m_{h_1}^2 \sim -\frac{3y_t^2 M_s^2}{16\pi^2}\,, \tag{3.56}$$

while the positive quadratic term of the second Higgs is

$$m_{h_2} \sim \frac{M_{KK}}{M_s} m_{h_1}\,, \tag{3.57}$$

as explained above. Additionally, there is a small $h_1 h_2$ mixing from the subdominant mode with bulk mass $c - \Delta c$, which we have neglected previously. Including this mode, we get a fermion Lagrangian of the form of Eq. (3.50) with the following corrections:

$$h_1 \to h_1 + \epsilon h_2\,,\ h_2 \to h_2 + \epsilon h_1\,, \tag{3.58}$$

where $\epsilon \sim \left(\frac{R}{R'}\right)^{2\Delta c} \sim \frac{1}{40}$ is the mixing angle of the subdominant combination in the top zero mode. The resulting correction to the 2HDM potential is subdominant except for a possibly important mixing term $-m_{12}^2\, h_1 h_2$ which was neglected in Eq. (3.54). We estimate this term to be

$$m_{12}^2 \sim \epsilon m_{h_2}^2\,. \tag{3.59}$$

The only tree-level part of the 2HDM potential is the quartic term

$$\lambda\left(h_1^\dagger h_1 - h_2^\dagger h_2\right)^2 + \lambda\ \mathrm{tr}\left(h_1 h_1^\dagger - h_2 h_2^\dagger\right)^2\,, \tag{3.60}$$

with λ given by Eq. (3.23).

3.6.2 Matching to the general 2HDM potential

The general 2HDM Lagrangian [101, 102] is

$$\begin{aligned}\mathcal{L}_{h_{12}} &= m_{h_1}^2\, h_1^\dagger h_1 + m_{h_2}^2\, h_2^\dagger h_2 - m_{12}^2\left(h_1^\dagger h_2 + \text{h.c.}\right) + \\ &\quad + \frac{1}{2}\lambda_1\left(h_1^\dagger h_1\right)^2 + \frac{1}{2}\lambda_2\left(h_2^\dagger h_2\right)^2 + \lambda_3\left(h_1^\dagger h_1\right)\left(h_2^\dagger h_2\right) + \lambda_4\left(h_1^\dagger h_2\right)\left(h_2^\dagger h_1\right) \\ &\quad + \text{ other CP violating quartics}\,. \end{aligned} \tag{3.61}$$

Matching this to our case, we have $\lambda_1 = \lambda_2 = -2\lambda_3 = -2\lambda_4 = 4\lambda$, while the other CP violating quartics are zero - exactly the same as in the Higgs sector of the MSSM. Since $|m_{12}^2| < |m_{h_1}^2| < |m_{h_2}^2|$, we are in the decoupling limit with small $\tan\beta$. Indeed, minimizing the potential we get:

$$\tan\beta \sim \epsilon \sim \frac{1}{40}\,, \tag{3.62}$$

so that $m_A^2 = m_{H^\pm}^2 = m_{h_2}^2$. In the decoupling limit, we can just fit the quartic to its experimental value

$$\frac{1}{2}\, g_*^2\theta_6^2 = 2\lambda \approx 0.13\,. \tag{3.63}$$

For $g_* \gtrsim 3$ we get that the bulk $SO(5)\times SO(5)$ breaking parameter is $\theta_6 \sim 0.1$. The physical Higgs masses in the decoupling limit are just:

$$m_h \simeq m_{h_1}\ ,\ m_H \simeq m_{h_2}\,, \tag{3.64}$$

while the alignment angle is

$$\cos\left(\alpha-\beta\right) = \tan\beta\,\frac{m_h}{\sqrt{m_H^2 - m_h^2}}\,. \tag{3.65}$$

Since our $\cos\left(\alpha-\beta\right)$ is small, our decoupling limit leads to alignment: the vector bosons couple to h with SM-like magnitudes, while their coupling to H is suppressed. In other words, h is almost completely SM-like, while H is both heavy and inert up to $O(\frac{1}{40})$.

3.7 Phenomenological Consequences

The BSM phenomenology of our model can be largely divided into standard composite Higgs phenomenology, which implies all the generic features of composite Higgs models, and additional features which are specific to our model. The standard composite Higgs phenomenology has been covered extensively in the literature (see [27–30]), and here we only briefly summarize the main predictions:

- Fermionic top partners: New vector-like quarks that would appear in direct searches. In our model there is a light top partner - t_s^0 with SM quantum numbers $(\mathbf{3}, \mathbf{1}, 2/3)$, which is lighter than the rest of the KK states. This state cancels the top loop and so its mass is directly connected to the tuning. Current constraints are $M_s \gtrsim 1.1$ TeV [103, 104], which corresponds to a tuning of $O(20\%)$. We assume the rest of the top KK modes are much heavier: $M_{KK} > 3$ TeV.
- Gauge partners: Heavy new EW vectors that would appear as resonances at the LHC. The gauge partners also directly contribute to the tuning, and their mass has to be $M_V \gtrsim 2.5$ TeV. In this model we assume that the necessary $O(20\%)$ tuning in the Higgs sector is obtained via the cancellation of the top and gauge loops.
- Higgs data: Due to the pNGB nature of the Higgs, the coupling of the Higgs differ from the SM expectation by $O\left(\frac{v^2}{f^2}\right)$. This is also the main deviation in the Higgs signals in our model.
- EW precision data: In composite Higgs models with custodial protection, the dominant effect is on the S parameter due to tree-level mixing with the

gauge partners. At the loop level, the change in the Higgs coupling and the new top partners also have a measurable effect. This is true for our model as well.

- Flavor: The new composite states can mediate FCNC. These are suppressed if the SM fermions are partially composite, but the suppression is usually not sufficient for the composite Higgs to be the solution of the hierarchy problem. To avoid these constraints, CH models with various flavor symmetries have been considered [105–108]. Addressing these constraints is beyond the scope of this work, but it is plausible that similar symmetries can be implemented in our model for the same purpose.

The main non-standard features of our model are the doubled KK spectrum and the extended Higgs sector.

Double KK spectrum. All the KK modes in our model appear in both the up and down sites. The splitting between two such modes is $O(\theta_6 M_{KK}) \sim 300$ GeV for fermion KK modes and $O(\theta_6^2 M_{KK}) \sim 30$ GeV for vector KK modes. To obtain the measured quartic we require $\theta_6 \sim 0.1$. The small splitting between the modes is a clear prediction of our model.

Extended Higgs sector. The Higgs sector of our model is a 2HDM where the second doublet is almost inert. The mass of the second doublet depends on the ratio between the light top partner and the KK scale:

$$m_{h2} \sim \frac{M_{KK}}{\sqrt{2} M_S} m_h \tag{3.66}$$

For reasonable choice of parameters, we get $m_{h2} \sim 300 - 500$ GeV. The phenomenology of the states in this doublet depends on the embedding of the quarks in our model. If we assume that all the quarks couple to h_1 similarly

to the top, then the coupling to the second doublet are suppressed by the mixing which is $O(\frac{1}{40})$. This suppresses all single production processes for the scalar states in the second doublet. The charged Higgs can additionally be produced in pairs via an unsuppressed Drell-Yan process. Further analysis is required to obtain precise bounds and discovery potential for these states.

3.8 Conclusions

Composite Higgs models are among the most exciting viable extensions of the SM. One of the long-standing issues with such models is the tuning necessary to obtain a realistic Higgs potential with a 125 GeV Higgs mass. In this work we presented a novel class of models where this tuning can be reduced in the presence of a tree-level quartic for the Higgs. The model originates from a 6D orbifold producing two pNGB Higgs doublets which naturally obtain a collective quartic due to the 6D gauge interactions. The simplest and most useful implementation is based on its 5D two-site deconstructed version, where the bulk gauge group for the minimal model is $SO(5) \times SO(5)$, with a bulk link field breaking the group to the diagonal, in addition to boundary breakings ensuring the presence of the two light Higgs doublets. This is the first example of a holographic composite Higgs model with a tree-level quartic for the Higgs. Importantly, the magnitude of the quartic can be adjusted by dialing the parameters of the theory which can result in the SM quartic dominantly arising from the tree-level contribution. This in turn allows us to suppress all loop effects, leading to the reduction of the tuning. The main experimental consequence of such models (beyond the standard signals of composite Higgs models such as colored top partners, gauge partners, etc) is the doubling of the KK spectrum.

The splitting among the KK modes is related to the same parameters setting the magnitude of the quartic. We find that for a realistic model with reduced tuning, the splitting among the doubled KK states has to be relatively small (of order tens of GeV for the vector KK modes and hundreds of GeV for the fermionic KK modes). In addition, the Higgs sector has to contain two Higgs doublets, which must be in the decoupling limit in order to correctly reproduce the measured Higgs phenomenology. Finally, unlike the CH case, direct searches for fermionic top partners provide the most stringent bounds on naturalness in our model, and so we expect them to lie just around the corner within the LHC reach.

CHAPTER 4

CONTINUUM NATURALNESS

BEYOND THE STANDARD MODEL: COMPOSITE HIGGS AND DARK MATTER

Ofri Telem, Ph.D.

Cornell University 2019

We present a novel class of composite Higgs models in which the top and gauge partners responsible for cutting off the Higgs quadratic divergences form a continuum. The continuum states are characterized by their spectral densities, which should have a finite gap for realistic models. We present a concrete example based on a warped extra dimension with a linear dilaton, where this finite gap appears naturally. We derive the spectral densities in this model and calculate the full Higgs potential for a phenomenologically viable benchmark point, with percent level tuning. The continuum top and gauge partners in this model evade all resonance searches at the LHC and yield qualitatively different collider signals.

4.1 Introduction

The cornerstone of conventional solutions to the hierarchy problem, e.g. supersymmetry and composite Higgs (CH) [13, 27–30, 32, 80, 109, 110], is the existence of new states around the TeV scale. The role of these top and gauge partners is to cut off the quadratically divergent radiative corrections to the Higgs po-

tential from the top quark and gauge bosons. In recent years, searches at the LHC have placed the naturalness paradigm under pressure by setting significant lower bounds on the masses of top and gauge partners of about 1.2–1.4 TeV [71, 72, 111–114] and 2.2–2.5 TeV [78, 115, 116], respectively.

However, many of these searches assume that the top and gauge partners are particles that can be produced on-shell. In this work we introduce a new class of models in which the top and gauge partners are gapped *continuum* states [117–120], rather than ordinary *particles*.

The simplest example of a spectrum with gapped continuum modes is that obtained from the finite potential well in standard quantum mechanics (QM). While the bound states inside the well form a discrete set, the scattering states form a continuum with energies above the well. Another example is a strongly-interacting theory with a critical behavior in the IR that gives rise to a gapped continuum[1]. For example, it is believed that at the bottom of the conformal window of supersymmetric QCD, a gapped continuum can be generated by turning on a squark mass [119].

In this work we present a CH model in which continuum top and gauge partners arise as the composites of a strong sector with critical behavior in the IR. Inspired by the AdS/CFT correspondence [42] and holographic realizations of CH models [32, 58], our gapped continuum arises from a warped 5D geometry [44] with a linear dilaton [125–127]. The resulting Green's functions have a branch cut starting at a finite gap μ corresponding to the slope of the linear dilaton, indicating the emergence of a continuum.

Based on this linear dilaton geometry, we construct a fully realistic CH model

[1] For example, see [121–124].

with partial compositeness [34–37, 46] and gauge-Higgs unification [49–53, 57]. Similar to the standard warped 5D realizations of CH, our setting involves AdS_5 with a UV brane and an IR brane. However, in our case, the fifth dimension continues beyond the IR brane to infinity, with a dilaton rising in the deep IR [128–130]. The other ingredients of the model are identical to standard CH models: a bulk gauge symmetry $SO(5) \times U(1)$ broken to $SO(4) \times U(1)$ on the IR brane and to $SU(2)_L \times U(1)_Y$ on the UV brane; the A_5 of $SO(5)/SO(4)$ playing the role of the pseudo-Nambu-Goldstone (pNGB) Higgs; and the Standard Model (SM) fermions and their partners embedded in bulk $SO(5)$ representations.

The result is a realistic CH model in which the top and gauge partners are all continua, with no BSM resonances within the reach of the LHC. We demonstrate this by focusing on one point in our parameter space, for which we get a realistic Higgs potential (with 1% tuning) with gaps of about 1–2 TeV.

The chapter is structured as follows. In Section 4.2 we present the effective action for continuum states, and how the properties of the continua are encoded in their spectral densities. In Section 4.3 we show how to model gauge and fermion continua in a warped 5D geometry with a linear dilaton. We give an intuitive argument for the emergence of a gapped continuum from this geometry, based on an effective Schrödinger equation, and then calculate the continuum spectral densities in a procedure inspired by AdS/CFT. Using linear dilaton geometry, we construct a realistic CH model with gauge-Higgs unification and continuum top and gauge partners in Section 4.4. For the purpose of breaking the bulk $SO(5)$ symmetry, we introduce an IR brane. However, the fifth dimension continues beyond the IR brane to a region where the linear dilaton dominates and leads to the gapped continuum. The role of the Higgs is played as

usual by the A_5 of the $SO(5)/SO(4)$ generators, while the SM Yukawa couplings originate from the jump conditions for the bulk fields on the IR brane.

Our results are summarized in Section 4.5, while the detailed calculation of the gauge and fermion spectral densities is given in Section 4.6 (and in the appendices). To extract the fermion spectral densities, we solve the 5D inhomogeneous equations of motion (EOM) subject to the UV boundary conditions and the IR jump conditions. We account for the bulk VEV of the Higgs–A_5 by rotating it into the IR jump conditions as usual [59]. We diagonalize the resulting 20×20 fermionic Green's function matrix to obtain all of the fermionic spectral densities in our model. The gauge spectral densities are calculated in a similar manner.

In Section 4.7 we calculate the Coleman-Weinberg potential for the Higgs from the spectral densities of our benchmark point in parameter space. We obtain a fully realistic Higgs potential, consistent with electroweak precision bounds on v/f and with a tuning of 1%, compared to per mille level tuning in a corresponding composite Higgs model with the same IR scale R' and the same choice of bulk representations [63]. Finally, we comment on the phenomenology of continuum partners: the lack of resonances within the reach of the LHC, bounds from the running of α_s, and the way to calculate the pair-production cross section for continuum fermions. The phenomenology of continuum partners will be explored further in an upcoming work [131].

4.2 Effective Action for Continuum States

The essential ingredients of CH models are the tower of composite top and gauge partners. These states cancel the one-loop SM top and gauge contributions to the Higgs potential below the confinement scale of Λ, which we take to be about 2–3 TeV. The main new aspect of the model we present in this work is that the critical IR dynamics give rise to a *continuum* of top and gauge partners rather than a tower of ordinary particles. To study the phenomenology of such continuum top and gauge partners we need to first explain how to write an effective action for these states.

We will illustrate this by presenting the general effective action for a continuum Weyl fermion. We start with the Lagrangian for an ordinary massless Weyl fermion χ:

$$\mathcal{L}_\chi \;=\; -i\bar{\chi}\bar{\sigma}^\mu p_\mu \chi\,. \tag{4.1}$$

The two-point function in momentum space is simply the inverse of the bilinear term in Eq. 4.1,

$$\langle \bar{\chi}\chi \rangle \;=\; \frac{i}{\bar{\sigma}^\mu p_\mu} = \frac{i\sigma^\mu p_\mu}{p^2}\,. \tag{4.2}$$

The Lagrangian for a continuum Weyl fermion generalizes Eq. 4.1 by including a momentum-dependent form factor $G(p^2)$:

$$\mathcal{L}_\chi^{\text{cont.}} \;=\; -i\bar{\chi}\frac{\bar{\sigma}^\mu p_\mu}{p^2 G(p^2)}\chi\,, \tag{4.3}$$

from which we can extract the two point function

$$\langle \bar{\chi}\chi \rangle^{\text{cont}} \;=\; i\sigma^\mu p_\mu G(p^2)\,. \tag{4.4}$$

Clearly, in the limit $G(p^2) \to ip^{-2}$, the continuum fermion just reduces to the massless particle limit. In general, $G(p^2)$ is a complex function whose poles

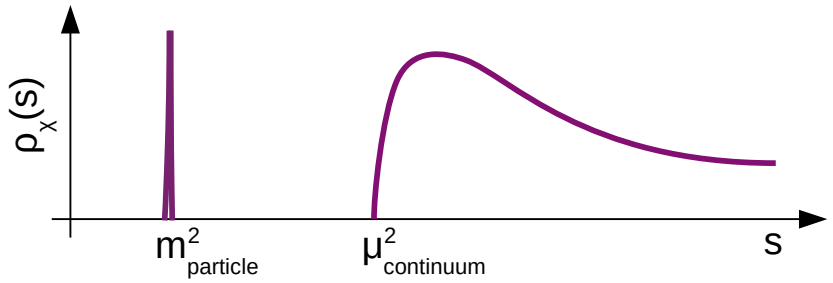

Figure 4.1: A cartoon of a typical fermionic spectral density. The delta function corresponds to a massive particle in the spectrum, while the continuous part indicates a fermion continuum.

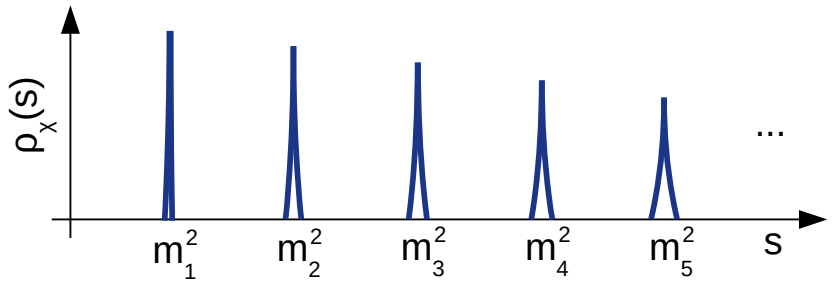

Figure 4.2: A cartoon of a typical fermionic spectral density in the case of an infinite tower of massive fermions (KK modes).

correspond to massive particles and whose branch cut corresponds to a continuum. This complex structure is easily captured by introducing the (real-valued) spectral density function $\rho(s)$, such that

$$G(p^2) \;=\; \int_0^\infty \frac{\rho(s)}{s - p^2 + i\epsilon}\, ds \;\;,\;\; \rho(s) = \frac{1}{\pi}\mathrm{Im}G(s)\,. \tag{4.5}$$

The spectral density contains all the relevant spectral information for the fermion χ, and is essentially the famous Källén-Lehmann spectral density [132, 133]. Its typical form is illustrated in Fig. 4.1, with the delta functions corresponding to massive particles and the continuous part encoding the fermion

continuum. For comparison, in Fig. 4.2, we show the spectral density for a tower of massive fermions, which, in the narrow width approximation, is just a sequence of delta functions. This is the typical KK spectrum obtained by putting a Weyl fermion in the bulk of 5D Randall-Sundrum geometry [44]. One can indeed think of the continuum as the merging of the spectral density of the KK modes as their separation goes to zero while their width remains finite.

4.3 Modeling the Continuum Dynamics with Linear Dilaton Geometry

The effective action presented in the previous section was completely generic in the sense that it did not assume a specific functional form for the spectral density $\rho(s)$. However, to say something meaningful about the continuum dynamics, we would like to find a model of the strong dynamics responsible for the emergence of continuum modes that allows us to calculate quantities below the strong scale. Inspired by the AdS/CFT duality, we seek to model the continuum dynamics in some weakly coupled, warped 5D geometry. We build on past work on how to model continuum dynamics. The authors of [120] showed, among other things, how a bulk Dirac fermion in AdS_5 is dual to a gapless Weyl fermion continuum, while in [134], a gapped supersymmetic continuum arose from a chiral superfield in AdS_5 with a bulk dependent mass. We will use a setup similar to the latter, albeit in a non-supersymmetric setting.

To correctly model the continuum dynamics, we consider Weyl fermions in a dilaton background[1]. In this background the 5D Lagrangian in the string frame

[1]For the stabilization of linear dilaton backgrounds, see [135] and references therein. As

is then

$$\mathcal{L}_S = e^{-2\Phi(z)} a_S^5(z) \left[a_S^{-1}(z) \mathcal{L}_{\text{kin}} + \frac{1}{R} \left(c + y\,\Phi(z) \right) \left(\psi\chi + \bar{\chi}\bar{\psi} \right) \right] , \tag{4.6}$$

where $z \in [0, \infty)$ is the coordinate of the fifth dimension, $a_S(z) = \frac{R}{z}$ is the AdS scale factor, $\Phi(z)$ is the dilaton profile, and y is a bulk Yukawa coupling between the dilaton and the bulk fermion. Later we will introduce a UV brane and cut off the space at $z = R$. The kinetic term is the standard kinetic term for a 5D Dirac fermion:

$$\mathcal{L}_{\text{kin}} \;=\; -i\bar{\chi}\bar{\sigma}^\mu p_\mu \chi \; - i\psi\sigma^\mu p_\mu \bar{\psi} \; + \; \frac{1}{2} \left(\psi \overleftrightarrow{\partial}_5 \chi - \bar{\chi} \overleftrightarrow{\partial}_5 \bar{\psi} \right) . \tag{4.7}$$

To conveniently extract the fermion EOM, we first move to the Einstein frame through the rescaling of the coordinates leading to $a(z) = a_S(z)\, e^{-\frac{2}{3}\Phi(z)}$, followed by a canonical renormalization of the fermions. The resulting Einstein frame Lagrangian is then

$$\mathcal{L}_E = a^4(z) \mathcal{L}_{\text{kin}} + a^5(z) \frac{\hat{c}(z)}{R} \left(\psi\chi + \bar{\chi}\bar{\psi} \right) , \tag{4.8}$$

where $\hat{c}(z) \equiv (c + y\Phi(z)) e^{\frac{2}{3}\Phi(z)}$. The fermion bulk EOM's are conveniently presented in a Schrödinger form [122]:

$$-\hat{\chi}''(z) + V_{\text{eff}}(z)\, \hat{\chi}(z) \;=\; p^2 \hat{\chi}(z) \, , \tag{4.9}$$

where $\hat{\chi}(z) = \left(\frac{R}{z} \right)^2 \chi(z)$ and the effective Schrödinger potential is

$$V_{\text{eff}}(z) = \frac{c(c+1) + y\Phi(z)(2c + y\Phi(z) + 1) - yz\Phi'(z)}{z^2} \, . \tag{4.10}$$

This equation has gapped continuum solutions (similar to scattering solutions in standard QM) when $V_{\text{eff}}(z \to \infty) = \text{const} > 0$. That clearly indicates that

we will elaborate below, our realistic model involves an IR brane stabilized by the usual Goldberger-Wise [45] mechanism, which in turn can set the boundary conditions for the linear dilaton, generating the IR scale μ.

$\Phi(z)$ has to be linear in z in the deep IR—a linear dilaton. For the linear dilaton $\Phi(z) = \mu(z - R)$ with $\mu \sim 1\,\text{TeV}$, $V_{\text{eff}}(z \to \infty) = y^2\mu^2$, and we expect a continuum beyond the gap $y\mu$. Indeed, the IR regular[1] bulk solutions are

$$\begin{aligned} \chi(z) &= A\, a^{-2}(z)\; W\left(-\frac{c\mu y}{\Delta}, c + \frac{1}{2}, 2\Delta z\right), \\ \psi(z) &= A\, a^{-2}(z)\; W\left(-\frac{c\mu y}{\Delta}, c - \frac{1}{2}, 2\Delta z\right)\frac{\mu y - \Delta}{p}, \end{aligned} \tag{4.11}$$

where $\Delta = \sqrt{y^2\mu^2 - p^2}$ and $W(a, b, z)$ is a Whittaker function. From these bulk solutions we can extract the left-handed (LH) source Green's function as

$$\langle O_{\text{R}} O_{\text{R}} \rangle = -\frac{(2\pi)^{-2c-1}\,(\mu y - \Delta)}{2\left(c + \frac{1}{2}\right)p^2}\,\frac{\Gamma(1-2c)}{\Gamma(1+2c)}\,\frac{\Gamma\left(1 + c\,\frac{\mu y + \Delta}{\Delta}\right)}{\Gamma\left(1 + c\frac{\mu y - \Delta}{\Delta}\right)}\,(2\Delta)^{2c}\,, \tag{4.12}$$

while the Green's function for χ is its (almost) inverse

$$G(p^2) = -\frac{(2\pi)^{2c-1}}{2\left(c - \frac{1}{2}\right)(\mu y - \Delta)}\,\frac{\Gamma(1+2c)}{\Gamma(1-2c)}\,\frac{\Gamma\left(1 + c\,\frac{\mu y - \Delta}{\Delta}\right)}{\Gamma\left(1 + c\frac{\mu y + \Delta}{\Delta}\right)}\,(2\Delta)^{-2c}\,. \tag{4.13}$$

The notation $\overline{\lim}$ indicates a regulated limit, i.e., the leading term regulated by powers of z. We've normalized our Green's function such that at $p \gg \mu$ it is identical with the Green's function for an ungapped fermionic unparticle [120]. For a right-handed (RH) source, we replace $\chi(z) \leftrightarrow \psi(z)$ and $y \leftrightarrow -y$. The Green's function, extracted from 5D, now serves as the momentum-dependent form factor of Eq. 4.3. It has a pole at $p^2 = 0$, indicating a massless zero mode. For $p \geq y\mu$, Δ goes imaginary and $G(p^2)$ has a branch cut corresponding to the continuum. The exact form of the spectral density depends on the bulk mass c, which we take in the range $0 \leq c < \frac{1}{2}$ to avoid poles from the gamma functions. The resulting spectral densities for select values in this range are shown in Fig. 4.3. Note also that following the case of pure AdS_5 [120], we can assign the LH source an

[1] As in standard AdS/CFT, we define the "IR regular" solution for Lorentzian AdS as the analytic continuation of the corresponding IR regular solution for Euclidean AdS. This is equivalent to choosing an outgoing wave boundary condition in Lorentzian AdS.

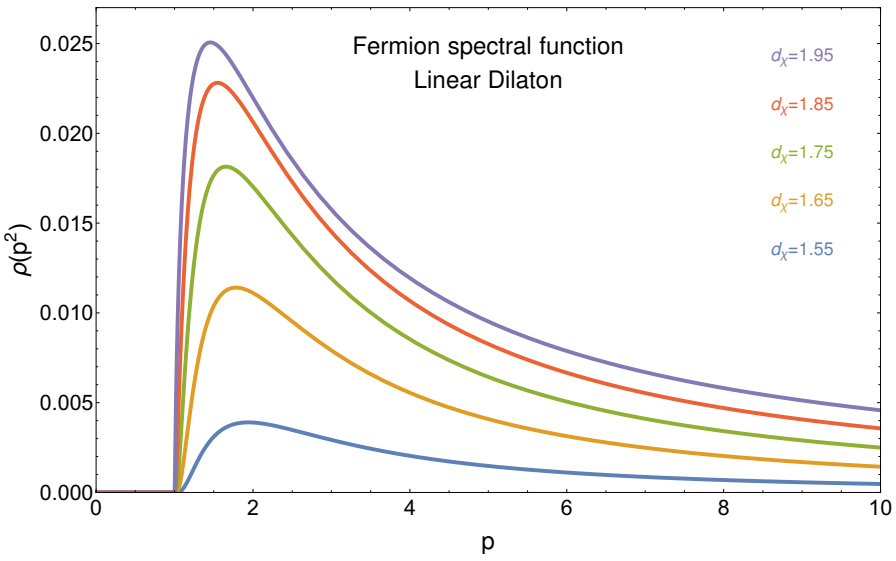

Figure 4.3: The spectral density for a continuum Weyl fermion modeled in a linear dilaton background. The anomalous dimension d_χ is linked to the bulk mass by the relation $d_\chi = 2 - c$. The dark black line is the spectral function for a single, massless particle LH fermion.

anomalous dimension $d_{O_R} = 2 + c$ in the range $2 \leq d_{O_R} \leq \frac{5}{2}$ [1]. This anomalous dimension governs the UV behavior of our spectral function, where it goes over to the fermionic unparticle spectral function. The corresponding anomalous dimension for the LH fermion is given by $d_\chi = 4 - d_{O_R} = 2 - c$.

We model the gauge continuum in a similar way to the fermion continuum, by considering gauge modes in the bulk of a linear dilaton geometry with $\Phi(z) = \mu(z - R)$. The Einstein frame Lagrangian is

$$\mathcal{L}_E = a(z)\, e^{-\frac{4}{3}\mu(z-R)} \left[\frac{1}{4} F^{MN} F_{MN} \right], \tag{4.14}$$

while the effective Schrödinger equation is

$$-\hat{A}''(z) + V_{\text{eff}}(z)\hat{A}(z) \;=\; p^2 \hat{A}(z)\,, \tag{4.15}$$

[1] For a RH source, the identification becomes $d_{O_L} = 2 - c$ and $3/2 \leq d_{O_R} \leq 2$.

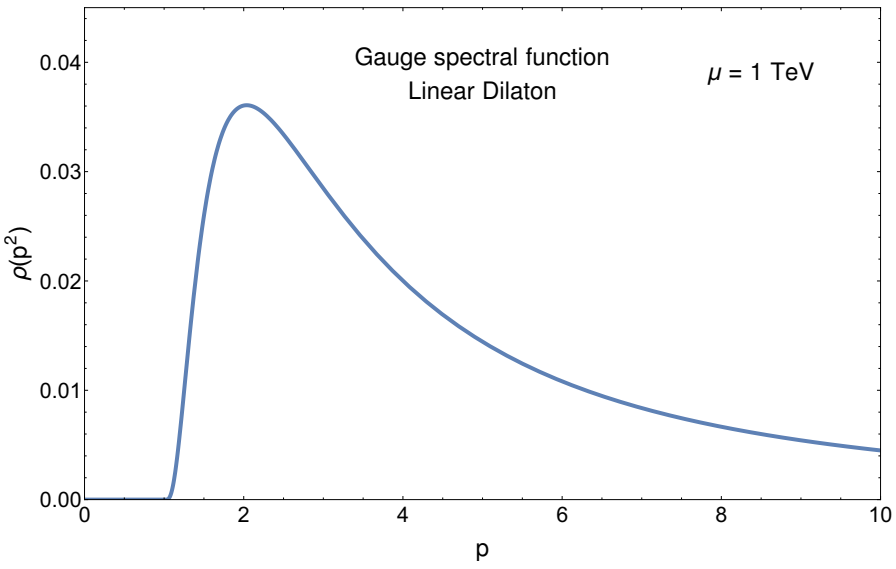

Figure 4.4: The spectral density for a continuum gauge boson in a linear dilaton background.

where $\hat{A}(z) = \sqrt{\frac{R}{z}}\, e^{-\mu(z-R)}\, A(z)$ and the effective Schrödinger potential is

$$V_{\text{eff}}(z) = \mu^2 + \frac{\mu}{z} + \frac{3}{4z^2}\,. \tag{4.16}$$

As in the fermion case, the potential in the deep IR goes to a constant, $V_{\text{eff}}(z \to \infty) = \mu^2$. Hence we expect a gauge continuum with a gap of μ. Indeed, the IR regular bulk solutions are

$$A(z) \;=\; A\,\sqrt{\frac{z}{R}}\, e^{\mu(z-R)}\, W\left(-\frac{\mu}{2\Delta}, 1; 2\Delta z\right), \tag{4.17}$$

with $\Delta = \sqrt{\mu^2 - p^2}$, and the Neumann Green's function has a pole at $p^2 = 0$ and a branch cut for $p^2 > \mu^2$ with the spectral density

$$\rho(s) \;=\; \frac{1}{\pi}\overline{\lim_{z\to 0}}\,\text{Im}\frac{A(z)}{A'(z)} = \frac{1}{2s}\left[\pi + i\psi\left(\frac{1}{2} + \frac{\mu}{2\Delta}\right) - i\psi\left(\frac{1}{2} - \frac{\mu}{2\Delta}\right)\right], \tag{4.18}$$

where $\psi(x)$ is the digamma function. The gauge spectral density is depicted in Fig. 4.4.

4.4 A Realistic Continuum Composite Higgs Model

In the two previous sections, we have shown how to model the fermion and gauge continua in a linear dilaton geometry. Here, we use them as building blocks in a full CH model, in which the continuum fermion and gauge modes play the role of top and gauge partners. In fact, our construction mirrors the existing CH models in its group theory, choice of representations, etc. The only modification is in the introduction of a linear dilaton geometry instead of the standard RS one.

Our extra dimensional geometry is depicted in Fig. 4.5. We consider AdS_5 regulated by a UV brane at $z = R$. In addition we introduce an IR brane at $z = R' \sim 1/\text{TeV}$, which is stabilized as usual by the Goldberger-Wise mechanism. The fifth dimension continues beyond the IR brane to $z \to \infty$. The IR brane has a double role in our model:

1. It provides the location for the breaking of the bulk gauge symmetry.
2. It is responsible for the generation of the IR scale $\mu \sim$ TeV, which is the slope of the linear dilaton. The dilaton profile is basically negligible up to distances close to the IR brane, where it has a boundary condition involving the IR scale μ. After the IR brane, the dilaton grows linearly with a slope μ. We are agnostic about the exact mechanism stabilizing the dilaton beyond the IR brane (see [135] and references therein for possibilities), but note that there is no tuning involved because the slope of the dilaton is related to its boundary condition on the IR brane. In other words, the solution to the hierarchy problem in our case is the usual Goldberger-Wise mechanism, or dimensional transmutation. The linear dilaton is merely a

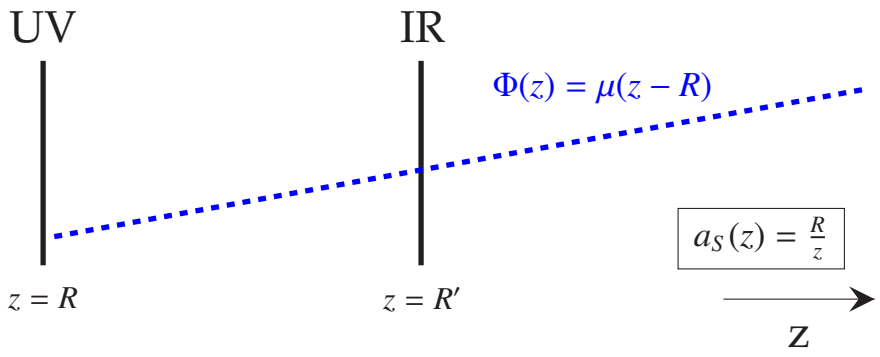

Figure 4.5: A sketch of our geometry in the string frame. The IR brane carries local fields that result in jump conditions for the bulk fields.

way to model a different confining dynamics which gives rise to composite continua.

The remaining details of our model are very similar to standard CH models [32,38,39,58]. We consider a $G = SO(5) \times U(1)_X$ gauge symmetry in the bulk of our geometry. This gauge symmetry is reduced to $SO(4) \times U(1)_X$ on the IR brane, by giving Dirichlet boundary conditions (B.C.) to the gauge fields corresponding to broken generators. On the UV brane, we break $SO(5) \times U(1)_X$ to the SM electroweak gauge symmetry $SU(2)_L \times U(1)_Y$, such that $Y = T_R^3 + X$. This choice of boundary conditions leads to a zero mode in the fifth component of the bulk gauge field, $A_5^{\hat{a}}$, with $\hat{a}$ denoting the generators in the coset G/H. The role of the pNGB Higgs boson is then played by the Wilson line from the UV to the IR brane, $ig_5 \int_R^{R'} A_5 \, dz$. It is interesting to note that this Wilson line between the two branes is the only gauge invariant Wilson line we can write, so there is no physical meaning to the A_5 profile beyond the IR brane. We can always account for the effect of the A_5 vacuum expectation value (VEV) by rotating it into the matching conditions on the IR brane.

In addition to the bulk gauge symmetry, we embed the SM fermions q_L, t_R, b_R in the bulk multiplets Q_L, T_R, B_R, transforming in the $\mathbf{5}_{\frac{2}{3}}$, $\mathbf{5}_{\frac{2}{3}}$, $\mathbf{10}_{\frac{2}{3}}$ representations of $SO(5) \times U(1)_X$, respectively. This is the same choice of bulk representations as [38, 39]. Under the subgroup $SU(2)_L \times U(1)_Y$, the bulk multiplets decompose as:

$$\begin{aligned}
Q_L(\mathbf{5})_{\frac{2}{3}} &\rightarrow q_L(\mathbf{2})_{\frac{1}{6}} + \tilde{q}_L(\mathbf{2})_{\frac{7}{6}} + y_L(\mathbf{1})_{\frac{2}{3}}\,, \\
T_R(\mathbf{5})_{\frac{2}{3}} &\rightarrow q_R(\mathbf{2})_{\frac{1}{6}} + \tilde{q}_R(\mathbf{2})_{\frac{7}{6}} + t_R(\mathbf{1})_{\frac{2}{3}}\,, \\
B_R(\mathbf{10})_{\frac{2}{3}} &\rightarrow q'_R(\mathbf{2})_{\frac{1}{6}} + \tilde{q}'_R(\mathbf{2})_{\frac{7}{6}} + x_R(\mathbf{3})_{\frac{2}{3}} + y_R(\mathbf{1})_{\frac{7}{6}} + \tilde{y}_R(\mathbf{1})_{\frac{1}{6}} + b_R(\mathbf{1})_{-\frac{1}{3}}\,.
\end{aligned} \tag{4.19}$$

Let χ and ψ be the LH and RH components of the bulk Dirac fermion appearing in Eq. (4.7). On the UV brane, the states χ_{q_L}, ψ_{t_R} and ψ_{b_R} get Neumann B.C., while all other states in χ_{Q_L}, ψ_{T_R} and ψ_{B_R} get Dirichlet B.C. On the IR brane, all of the states in χ_{Q_L}, ψ_{T_R} and ψ_{B_R} get Neumann B.C. Consequently, we have zero modes only for the SM states q_L, t_R and b_R. On the IR brane with induced metric g_{ind}, we can write the $SO(4) \times U(1)_X$ invariant mass terms:

$$S_{\text{IR}} = \int d^4x \, \sqrt{g_{\text{ind}}} \, \left[M_1 \, \bar{y}_L t_R + M_4 \, (\bar{q}_L q_R + \bar{\tilde{q}}_L \tilde{q}_R) + M_b \, (\bar{q}_L q'_R + \bar{\tilde{q}}_L \tilde{q}'_R) \right] . \tag{4.20}$$

These terms give rise to the SM Yukawa coupling in the 4D effective action. From the 5D point of view, these IR brane-localized terms provide the discontinuity (jump B.C.) resulting in quasi-IR brane-localized wave function profiles for the fermionic fields (albeit with support in the deep IR), but with large enough wave function overlap with the physical A_5 below the IR brane to obtain the correct top mass.

4.5 Summary of Results

In this section we present a concise summary of the results in our model. The details are fleshed out in the next sections and the appendices.

- *Overview*: We constructed a realistic CH model with continuum top partners. There are no fermionic KK resonances in the model. The continuum generically does contain broad peaks (of width $\sim$ TeV) that could be probed with non-resonant high p_T dilepton searches at a future 100 TeV collider. The only gauge particle resonances occur at energies well outside the reach of the LHC.
- *Model parameters*: We have only two additional parameters to the standard parameters of CH models: the dilaton slope μ and the fermion-dilaton Yukawa y. The other standard CH parameters are R and R', as well as the gauge parameters θ, r (see Sec. 4.6) and the fermion bulk and IR brane mass parameters c_Q, c_T, c_B, M_1, M_4 and M_b. We demonstrate a realistic SM spectrum and Higgs potential for the following benchmark point (BP) in parameter space:

$$\begin{gathered} R/R' = 10^{-16},\ 1/R' = 2.81 \text{ TeV},\ \mu = 1 \text{ TeV},\ y = 1.75, \\ r = 0.975,\ \sin\theta = 0.39, \\ c_Q = 0.2,\ c_T = -0.22,\ c_B = -0.03, \\ M_1 = 1.2,\ M_4 = 0,\ M_b = 0.017\,. \end{gathered} \tag{4.21}$$

  For this particular point in parameter space, all of the SM variables are correctly reproduced, except for the mass of the top quark, which is a bit too light (125 GeV instead of 140 GeV at 2 TeV). This is an artifact of our particular bulk fermion representations that also exists in standard

CH models [38, 39], and can be overcome by either changing to different bulk representations or choosing a slightly more tuned point in parameter space.

- *Continua:* In our specific point in parameter space, the gauge continuum starts at $\mu = 1$ TeV, while the fermion continuum starts at $y\mu = 1.75$ TeV. It is of course possible to find other points with larger gaps for the continua, at the cost of more tuning in the Higgs potential. The existence of the relatively low gauge continuum is phenomenologically viable due to the lack of s-channel resonances in our model, but the fermion continuum taken to be higher to avoid tension with LHC bounds. The spectral densities of the top and bottom are depicted in Fig. 4.6 and those of the W and Z in Fig. 4.7. The broad peaks in the fermion spectral densities at 5 TeV and 9 TeV originate in their IR brane masses (see Sec. 4.6.1). These broad peaks, of width ~ 1 TeV, could be probed at a future 100 TeV collider.

- *Higgs Potential:* As in standard CH models, the potential for the pNGB Higgs is radiatively generated. The radiative contributions of the top, W and Z in our model are balanced by the contribution of the fermion and gauge continua, which also couple to the pNGB Higgs. We get the correct Higgs potential at the cost of a standard 1% tuning, with $v/f = 0.3$, consistent with electroweak precision bounds [136]. This is to be compared with per mille level tuning in a corresponding composite Higgs model with the same IR scale R' and the same choice of bulk representations [63]. The Higgs potential in our model is depicted in Fig. 4.8.

- *Phenomenology:* Since there are practically no s-channel resonances in our model, the regular bounds on KK gauge bosons do not apply. This is the main feature of the continuum naturalness, which is illustrated in Fig. 4.9,

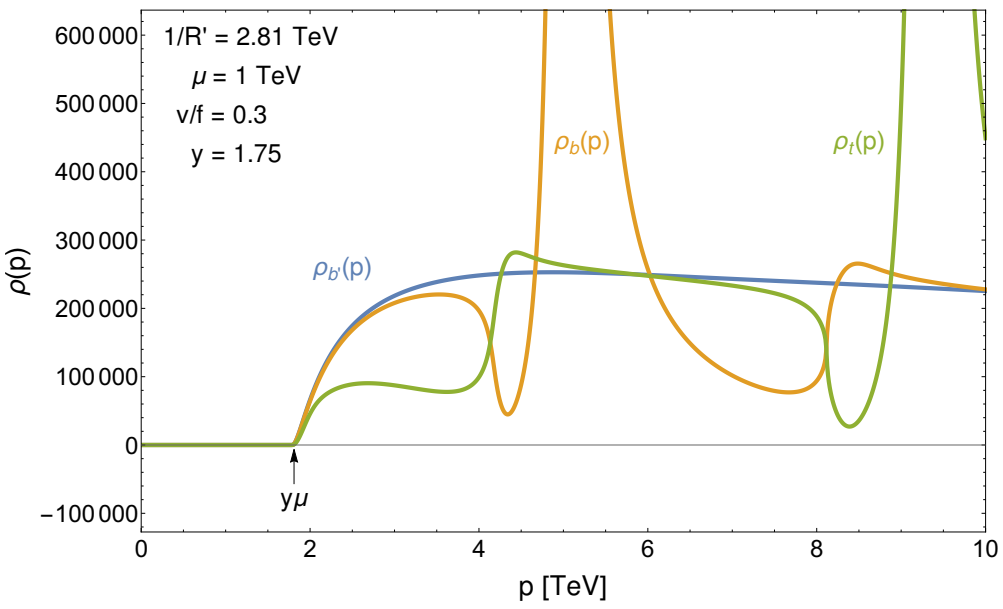

Figure 4.6: Top, bottom and b' spectral densities for $v/f = 0.3$ and parameter values from the BP in Eq. 4.21. The spectral function features broad peaks that could be probed at a future 100 TeV collider.

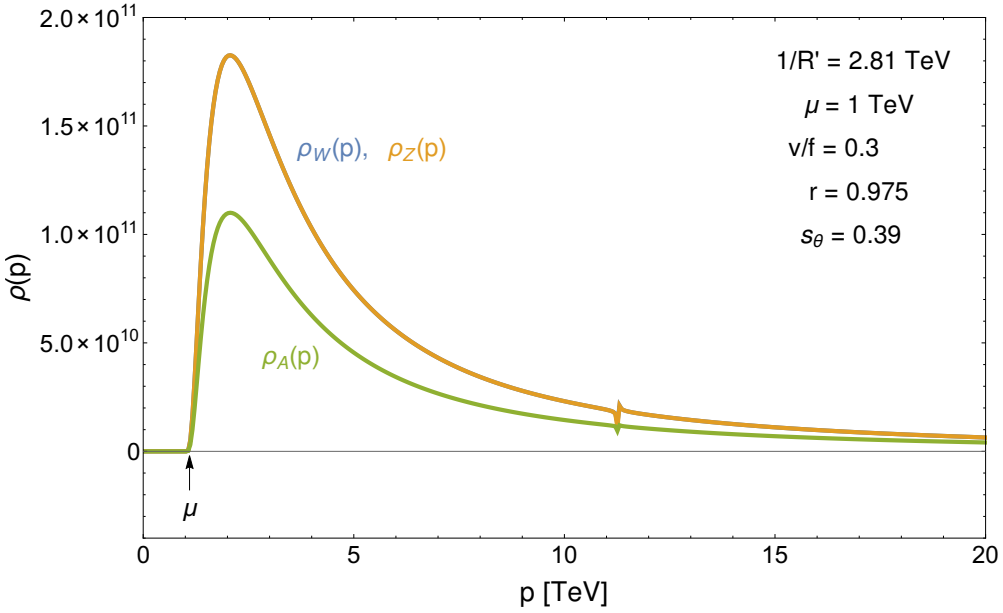

Figure 4.7: Gauge spectral density for $v/f = 0.3$ and parameter values from the BP in Eq. 4.21.

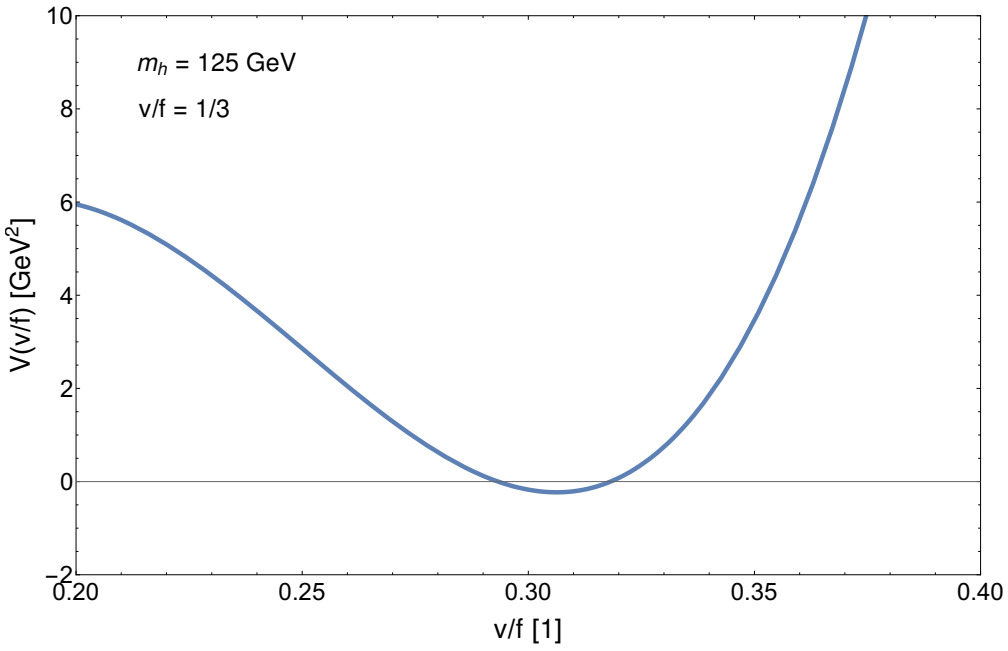

Figure 4.8: The Coleman-Weinberg potential in our model. The minimum is at $v/f = \sin(\langle h \rangle / f) = 0.3$ and the Higgs mass is reproduced.

where the partonic cross-section for $\sigma(q\bar{q} \to G^* \to t_R \bar{t}_R)$ in our model is compared to models with gauge KK resonances. We use G^* to denote the overall sum of the SM gluon, the tower of KK gluons in the RS case, and the gluon spectral density in the continuum case. Compared to the KK case, in the continuum case the spectral density tends to push the effect of new physics to the higher invariant mass regions where there is a larger PDF suppression, resulting in an overall suppression of the total cross section. To simplify the calculation we assume an IR brane localized t_R, which is in general a very good approximation in CH models.

A lower bound on the gap of the gauge continuum is obtained from the running of α_s in Sec. 7.6: the bound is $\mu \gtrsim 600\,\text{GeV}$. To correctly infer the LHC bounds on continuum top partners, we have to calculate their pair production cross-section, which we do in an upcoming work [131].

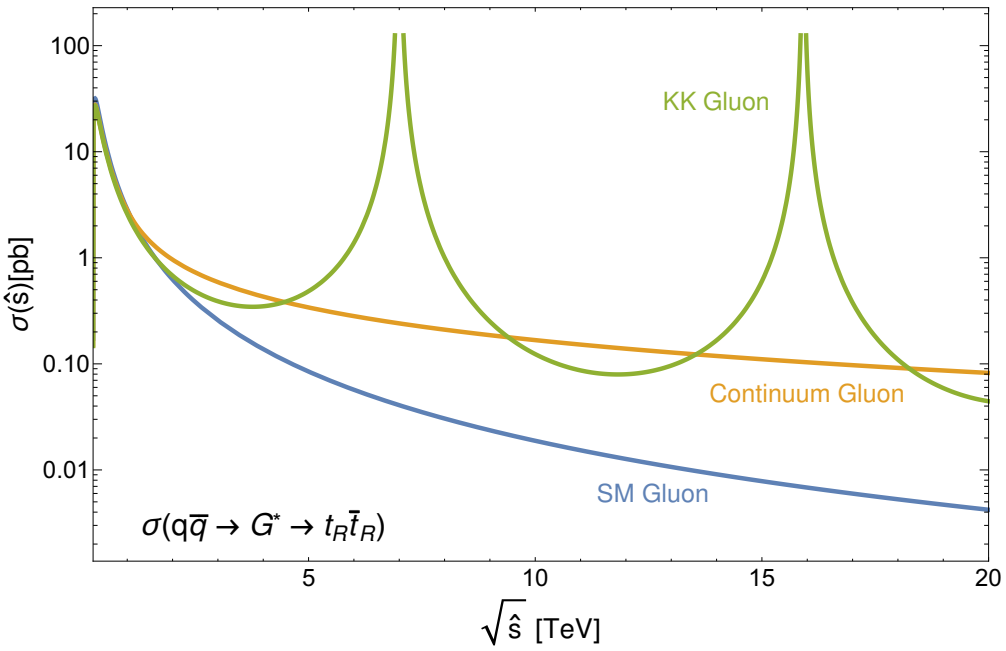

Figure 4.9: The partonic cross section $\sigma(q\bar{q} \to G^* \to t_R\bar{t}_R)$ in three simplified models: only SM gluon, with KK gluons, and with continuum gluons. While the presence of KK gluons leads to resonances in the partonic cross section, the continuum only leads to a smooth rise above the SM background.

4.6 Calculating Spectral Densities

In the following sections we give an overview of the calculations that lead to the results in Sec. 4.5. Some of the details are presented in the appendices. This section explains the basic ingredients used for obtaining the various spectral densities for the gauge and fermion states in our model, using methods similar to Sec. 4.3. The 4D Green's function is extracted as the UV limit of the 5D Green's function as

$$G(p^2) \;=\; \lim_{z,z' \to R} G(z, z'; p^2)\,, \tag{4.22}$$

where $G(z, z'; p^2)$ is the IR regular solution to the inhomogeneous EOM, which is schematically

$$\mathcal{D}_{g/f} G(z, z'; p^2) \;=\; \delta(z - z')\,, \tag{4.23}$$

subject to the UV B.C. and IR matching conditions. In the above equation, $\mathcal{D}_{g/f}$ is the relevant differential operator for the gauge bosons/fermions. The spectral densities are obtained from the Green's functions via $\rho(s) = \frac{1}{\pi}\mathrm{Im}\, G(s)$.

The homogeneous EOM for gauge fields is ∂_z

$$a_{\mathrm{eff}}(z)\, p^2 G \;+\; \partial_z \left[a_{\mathrm{eff}}(z)\, \partial_z G\right] \;= 0\,. \tag{4.24}$$

where $a_{\mathrm{eff}}(z) \equiv \left(\frac{R}{z}\right) e^{-2\mu(z-R)}$. The general solution to this equation is

$$G(z) \quad = \quad \left(\frac{z}{R}\right) e^{\mu(z-R)} \left[A\, M\left(-\frac{\mu}{2\Delta}, 1; 2\Delta z\right) \;+\; B\, W\left(-\frac{\mu}{2\Delta}, 1; 2\Delta z\right)\right], \tag{4.25}$$

where W and M are Whittaker functions, and A and B are coefficients. To find the gauge Green's functions, we have to solve the inhomogeneous version of Eq. 4.24, with $\delta(z - z')$ inserted on the right hand side, subject to the boundary conditions presented below.

UV Boundary Conditions

The UV B.C. are Neumann for $SU(2)_L \times U(1)_Y$ and Dirichlet for the other generators. In particular, we give Neumann B.C. for the hypercharge gauge boson B_μ defined as:

$$B_\mu = \sin\theta\, W_\mu^{3R} + \cos\theta\, X_\mu\,. \tag{4.26}$$

where W_μ^{3R} is the gauge boson corresponding to the T_R^3 generator of $SO(5)$ and the X_μ gauge boson of the $U(1)_X$. The angle θ is set to reproduce the correct

Weinberg angle θ_W. Similarly to [39], we also include a UV brane localized kinetic term for the $SU(2)_L$ gauge bosons, which changes their UV B.C. to

$$\partial_z G_{SU(2)_L} + C_{BKT}\, G_{SU(2)_L}|_{z=R} = 0 \tag{4.27}$$

where $C_{BKT} = r^2\, p^2 R \log R'/R$ and r is an $O(1)$ parameter adjusted to reproduce the correct right W mass for any value of g_5.

IR Matching Conditions

On the IR brane we have matching conditions, which are either

$$\Delta G|_{z=R'} = \Delta\partial_z G|_{z=R'} = 0 \tag{4.28}$$

for the generators of $SO(4)\times U(1)_X$ or

$$G|_{z=R'^-} = G|_{z=R'^+} = 0 \tag{4.29}$$

for the generators of $SO(5)/SO(4)$. Here and below, we use $G|_{z=R'^+}, G|_{z=R'^-}$ to denote the Green's function evaluated at $z \to R'$ from the right and left, respectively, and $\Delta G \equiv G|_{z=R'^+} - G|_{z=R'^-}$. We only select Green's functions that are regular in the deep IR, as described in Sec. 4.3.

Accounting for the VEV of the Higgs–A_5

As a final complication, note that we are generically looking for the Green's functions in the presence of a VEV for the Higgs–A_5. To account for the VEV, we use the well known technique of rotating the $\langle A_5\rangle$ into the IR boundary conditions. We do this by the bulk gauge transformation $A_\mu \to e^{ig\int_R^z \langle A_5\rangle dz'} A_\mu e^{-ig\int_R^z \langle A_5\rangle dz'}$ to the left of the IR brane and $A_\mu \to e^{ig_5\int_{R'}^z \langle A_5\rangle dz'} A_\mu e^{-ig_5\int_{R'}^z \langle A_5\rangle dz'}$ to the right of the IR

brane. This eliminates the bulk $\langle A_5 \rangle$, but changes the IR matching conditions for the $SO(4) \times U(1)_X$ fields to

$$G|_{z=R'^+} = U(h)\, G|_{z=R'^-}\, U(h)^{-1} \quad \partial_z G|_{z=R'^+} = U(h)\, \partial_z G|_{z=R'^-}\, U(h)^{-1}\,. \tag{4.30}$$

where $U(h) \equiv e^{ig_5 \int_R^{R'} \langle A_5 \rangle dz'} \equiv e^{ig_5 \frac{h}{f}}$. Note that the rotation to the right of the IR does not have any impact on the boundary conditions because the A_5 is pure gauge in this region.

Results

In Fig. 4.7 we present the gauge spectral density, for a Higgs VEV ratio $v/f = 0.3$. The spectral density is nonzero above the gap μ. Note the poles on top of the continuum at 11 TeV: these are the result of the IR brane Dirichlet B.C. for the generators of $SO(5)/SO(4)$, and are the only BSM poles that appear in our model. Since these are well beyond the reach of the LHC, we will not study them further in this work. In addition to the gauge boson continuum, our gauge boson Green's functions reproduce the SM W and Z masses and a massless photon: in Fig. 4.10, we show the inverse of the gauge boson Green's functions, which intersect zero exactly at the SM values.

4.6.1 Fermion Spectral Densities

The quadratic fermion Lagrangian is the one from Eq. 4.8, where each one of the bulk multiplets Q_L, T_R and B_R has a different bulk mass c_Q, c_T or c_B. The three multiplets have dilaton Yukawa couplings $y, -y, -y$. Note the flip in the sign of the dilaton Yukawa, required to get a zero mode in the ψ component of T_R, B_R.

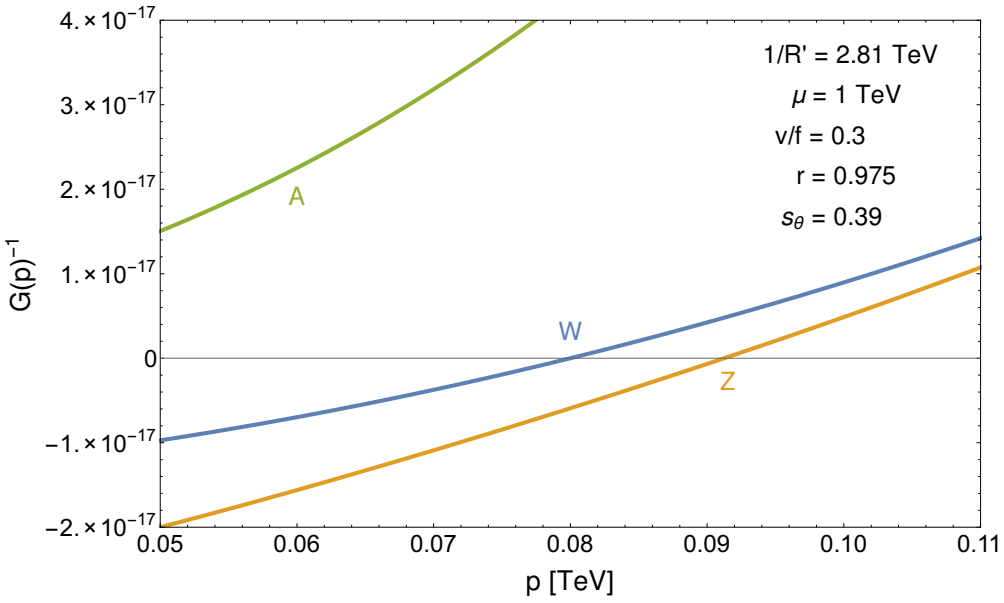

Figure 4.10: Inverse Green's function for the gauge bosons for $v/f = 0.3$. The zero modes are at m_W and m_Z.

The homogeneous EOM for Q_L are

$$\begin{aligned} -\mathcal{D}_f \chi_{Q_L} - \frac{\hat{c}_Q(z) a(z)}{R} \chi_{Q_L} + p\, \psi_{Q_L} &= 0\,, \\ \mathcal{D}_f \psi_{Q_L} - \frac{\hat{c}_Q(z) a(z)}{R} \psi_{Q_L} + p\, \chi_{Q_L} &= 0\,, \end{aligned} \tag{4.31}$$

where $\mathcal{D}_f f = \partial_z f + 2\frac{\partial_z a(z)}{a(z)} f$, $a(z) = \frac{R}{z} e^{-\frac{2}{3}\mu(z-R)}$ and $\hat{c}_Q(z) = (c_Q + \mu(z-R)) e^{\frac{2}{3}\mu(z-R)}$. The general solutions for Q_L are:

$$\begin{aligned} \chi_{Q_L}(z) &= a(z)^{-2} \left[A\, \hat{M}(c_Q, z) + B\, \hat{W}(c_Q, z) \right], \\ \psi_{Q_L}(z) &= a(z)^{-2} \left[A\, \alpha(c_Q, p)\, \hat{M}(c_Q, z) + B\, \beta(p)\, \hat{W}(c_Q, z) \right], \end{aligned} \tag{4.32}$$

with $\alpha(c_Q, p) \equiv \frac{4\left(\frac{1}{2} + c_Q - R\mu y\right)\Delta}{p}$, $\beta(p) \equiv \frac{\mu y - \Delta}{p}$ and $\Delta \equiv \sqrt{\mu^2 y^2 - p^2}$. The functions $\hat{W}(c_L, z)$, $\hat{M}(c_L, z)$ are defined as:

$$\begin{aligned} \hat{M}(c_Q, z) &= M\left(\frac{-\mu y\,(c_Q - \mu y R)}{\Delta}, \frac{1}{2} + c_Q - R\mu y, 2\Delta z \right), \\ \hat{W}(c_Q, z) &= W\left(\frac{-\mu y\,(c_Q - \mu y R)}{\Delta}, \frac{1}{2} + c_Q - R\mu y, 2\Delta z \right), \end{aligned} \tag{4.33}$$

where $M(a,b,z), W(a,b,z)$ are Whittaker functions. The homogeneous solution for T_R (B_R) is the same as the one for Q_L under $c_Q \to -c_{T(B)}$ and $\chi_{Q_L}, \psi_{Q_L} \to \psi_{T_R(B_R)}, \chi_{T_R(B_R)}$.

To find the Green's functions, we have to solve the inhomogeneous version of Eq. 4.31, inserting $\delta(z - z')$ on the right side of the first or second of these equation, depending on the Green's function. The full details of the calculation are presented in Appendix 4.B.

The fermionic Green's functions are subject to the boundary conditions given below.

UV Boundary Conditions

We assign UV brane Dirichlet B.C. to the following states:

$$\begin{aligned} Q_L &: \quad \psi_{q_L}, \chi_{\tilde{q}_L}, \chi_{y_L}\,, \\ T_R &: \quad \psi_{q_R}, \psi_{\tilde{q}_R}, \chi_{t_R}\,, \\ B_R &: \quad \psi_{q'_R}, \psi_{\tilde{q}'_R}, \psi_{x_R}, \psi_{y_R}, \psi_{\tilde{y}_R}, \chi_{b_R}\,. \end{aligned} \tag{4.34}$$

These boundary conditions reflect the fact that only q_L, q_R and b_R are partially composite and should have the SM fermions as zero modes.

IR Matching Conditions

Due to the masses $M_{1,4,b}$ on the IR brane (Eq. 4.20), we have the jump conditions relating $G^{\pm} = G|_{z=R'^{+}} \pm G|_{z=R'^{-}}$ for the different multiplets.

$$\begin{aligned} G^{-}_{t_R} &= \kappa M_1 G^{+}_{s_L}, \qquad G^{-}_{y_L} = \kappa M_1 G^{+}_{t_R}, \\ G^{-}_{a_R} &= \kappa M_4 G^{+}_{a_L}, \qquad G^{-}_{a_L} = \kappa M_4 G^{+}_{a_R} + \kappa M_b G^{+}_{a'_R}, \\ G^{-}_{a'_R} &= \kappa M_b G^{+}_{a_L}, \end{aligned} \tag{4.35}$$

where $a = q, \tilde{q}$ and the $\kappa = \mp 1$ is for the χ/ψ Green's function. We only select Green's functions that are regular in the deep IR, as described in Sec. 4.3.

Accounting for the VEV of the Higgs–A_5

Similarly to the gauge case, we can account for the VEV of the Higgs–A_5 by acting on the fermion with the Wilson line $U(h)$. The IR matching conditions remain the same as long as we modify the definition of $G^{\pm}$ to be

$$G^{\pm} = G|_{z=R'^{+}} \pm G^{h}|_{z=R'^{-}}, \tag{4.36}$$

where $G^h = U(h)G$ for Q_L, T_R in the **5** of $SO(5)$ and $G^h = U(h)\,G\,U(h)^{-1}$ for B_R in the **10** of $SO(5)$.

Results

Here we show the final results for the fermionic spectral densities for the parameter choices in Eq. 4.21. Since the bulk matter content of the full model is given by the representations **5** + **5** + **10**, we will end up with a 20×20 matrix for the Green's functions. Each entry of the matrix is a two-point function between

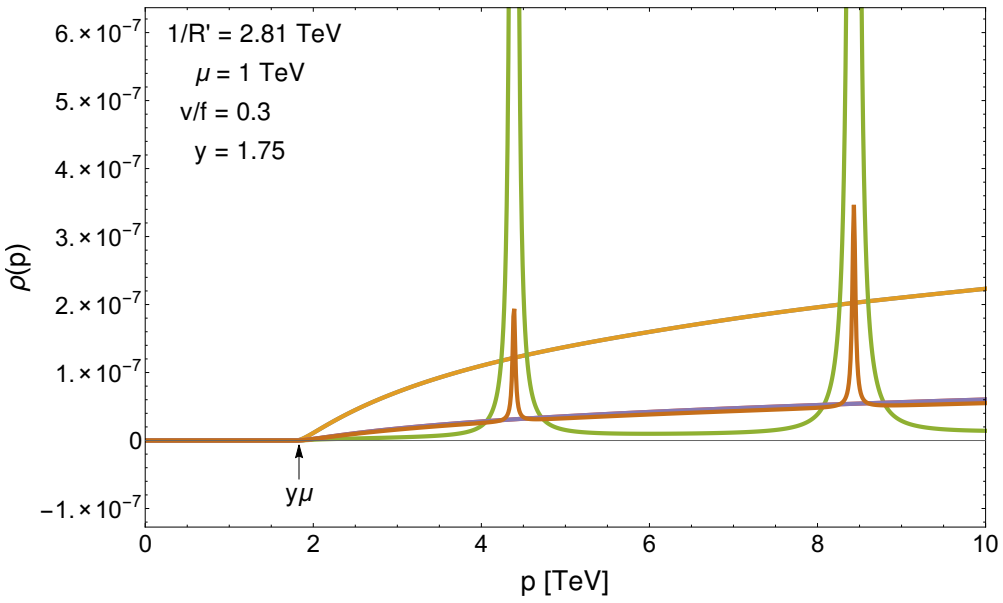

Figure 4.11: Spectral densities for additional exotic top partners.

a pair of fermions, and diagonalizing this yields the 20 fermionic spectral densities of our model. In Fig. 4.6 we can see the spectral densities for t, b and an exotic b'. All other spectral densities corresponding to states with other quantum numbers in the decomposition Eq. 4.19 are shown in Figs. 4.6, 4.11, and 4.12. Note that the difference in normalization between the different spectral densities stems from the difference in bulk mass between the three bulk multiplets, which leads to factors of $\left(\frac{R}{R'}\right)^{\Delta c}$ between the spectral densities depicted in the figures.

As stated before, some of the spectral functions feature broad peaks that can be probed at future colliders. The width of these peaks is a model dependent parameter which depends on the magnitude of the IR mass M_1. By choosing a slightly different point in parameter space with $M_1 = 2$, we can make these peaks as wide as 2 TeV. This effect is depicted in Fig 4.14 in a toy model with a single bulk fermion.

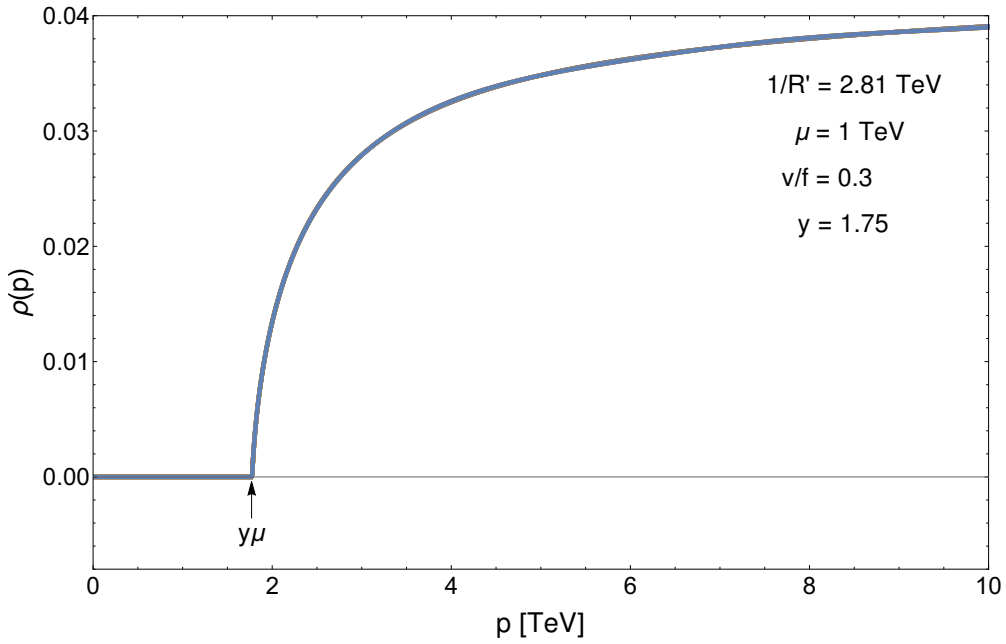

Figure 4.12: Spectral densities for the remaining top partner quantum numbers. The figure contains ten overlapping spectral densities corresponding to components that are continuous across the IR brane.

Without a Higgs VEV, four of the 20 fermions, $t_{L,R}$ and $b_{L,R}$, would have zero modes. The Higgs VEV lifts these to m_t and m_b, as shown in the inverse Green's functions for t, b and b' in Fig. 4.13.

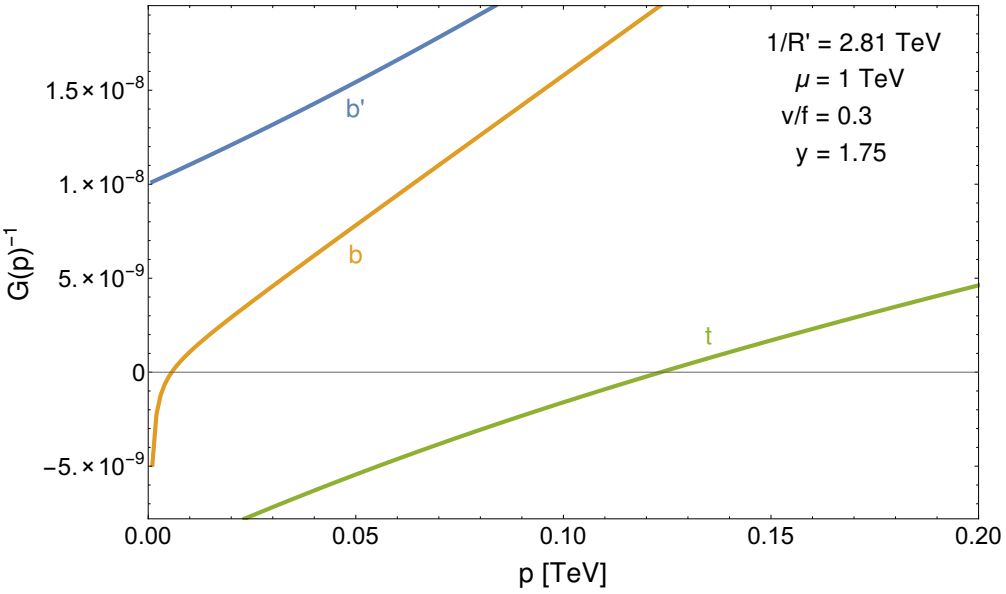

Figure 4.13: Top, bottom and b' inverse Green's functions. The zero modes of t and b are lifted in the presence of the Higgs VEV.

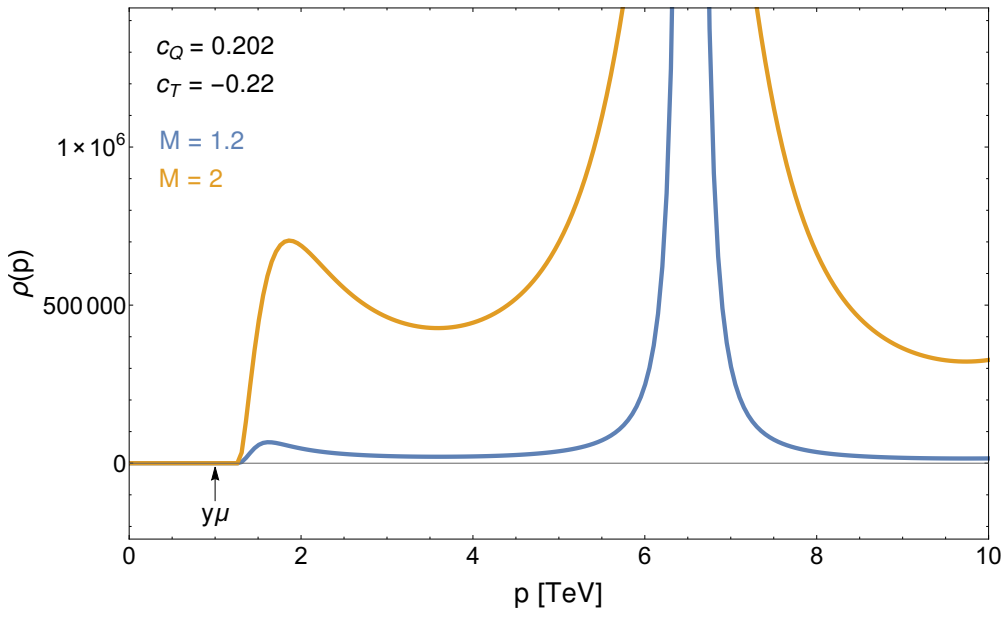

Figure 4.14: The effect of the IR mass on the width of a fermionic peak in a toy model with a single bulk fermion. By varying the IR mass, the peak could be made as wide as 2 TeV.

4.7 The Higgs Potential

Given all of the gauge and fermion Green's functions that we have calculated, it is straightforward to compute the Coleman-Weinberg potential for the Higgs using the formula [39]:

$$V(h) \;=\; \frac{3}{16\pi^2}\int dp\, p^3 \left[-4\sum_{j=1}^{20}\log G_{f_j}(ip) \;+\; \sum_{k=1}^{4}\log G_{g_k}(ip)\right], \tag{4.37}$$

where $G_{f_j}(p)$ and $G_{f_k}(p)$ are the eigenvalues of the fermion and gauge Green's function matrices, respectively. Note that these Green's functions are Higgs-dependent, hence their contribution to the Coleman-Weinberg potential. In Fig. 4.8 we plot the Coleman-Weinberg potential as a function of $\sin\langle h\rangle/f \equiv v/f$. There is a minimum at $v/f = 0.3$, and so the right Higgs VEV is obtained for $f = 820\,\text{GeV}$, which is consistent with electroweak precision bounds. By differentiating this twice, one can show that indeed $m_h = 125\,\text{GeV}$.

By varying the parameters of our model, we can estimate the tuning for the BP. We use the Barbieri-Giudice measure to quantify the tuning:

$$\text{tuning} \;=\; \left[\max_i \frac{d\log\, v}{d\log\, p_i}\right]^{-1}, \tag{4.38}$$

where $p_i \in \{R, R', \mu, r, \theta, y, c_Q, c_T, c_B, M_1, m_4, M_b\}$ are the fundamental parameters of the model. We obtain a tuning of 1% for the BP, with the strongest dependence being on c_Q and c_T as expected.

4.8 Comments on Phenomenology

The detailed study of continuum partner phenomenology will appear in a separate work [131]. Here, we will merely point out some of the main points regarding the phenomenology of continuum partners.

1. *No s-channel resonances at the LHC:* The unique feature of our continuum CH model is the lack of particle resonances within the reach of the LHC. This leads to vastly different phenomenology, in which the traditional searches for KK gauge bosons no longer apply, as well as all of the resonance-based top partner searches. To demonstrate this point, we present the partonic cross-section $\sigma(q\bar{q} \to G^* \to t_R\bar{t}_R)$, in three simplified models: only SM gluon, KK gluons, and continuum gluons. This cross section is given by

$$\sigma(\hat{s}) \;=\; \sigma(\hat{s})_{\rm SM} \times \hat{s}^2 \left|G(R,R';\hat{s})\right|^2 , \tag{4.39}$$

   where $G(R,R';\hat{s})$ is the UV to IR Green's function, calculated in a similar manner to Sec. 4.6. The results are depicted in Fig. 4.9.

2. *Bounds from the running of α_S:* The running of α_s in the presence of a colored gauge boson continuum provides an interesting bound on μ, the starting point of the gapped continuum. The running of the 4D gauge coupling is given by [39, 98, 137]

$$\frac{1}{g^2(Q)} = \frac{1}{g_5^2}\int_R^{1/Q} dz\, a(z) + \frac{1}{g_{\rm UV}^2} - \frac{b_{\rm UV}}{8\pi^2}\log\left(\frac{1}{RQ}\right), \tag{4.40}$$

   where $g_5^2 = g_*^2 R$, $g_{\rm UV}$ is the UV brane coupling, and $b_{\rm UV}$ is the one-loop beta function including effects for the zero modes on the UV brane. In our case, we localize all fields except for t_R on the UV brane, so $b_{\rm UV} = 22/3$.

There are determinations of α_s up to $Q \sim 1.42$ TeV from measurements of jets by CMS using $\sqrt{s} = 7$ TeV LHC data [138–141]. For a given value of μ_g, we choose the SM value for $\alpha_s(\mu_g)$. Evaluating Eq. (4.40) at two different scales $Q = \mu_g, 1.42$ TeV and taking the difference, we can determine the effect of the continuum on the running of α_s. Results with different UV-brane localized values of $\alpha_{\rm UV}$ are shown in Fig. 4.15: gluon continuum scales above $\mu = 600$–700 GeV are generically safe from the 1σ-high value of $\alpha_s(1.42\ \text{TeV})$. The value of $\alpha_{\rm UV} = 0.025$ corresponds to the limit $g_*^2 < (4\pi)^2$ from requiring perturbativity in the bulk.

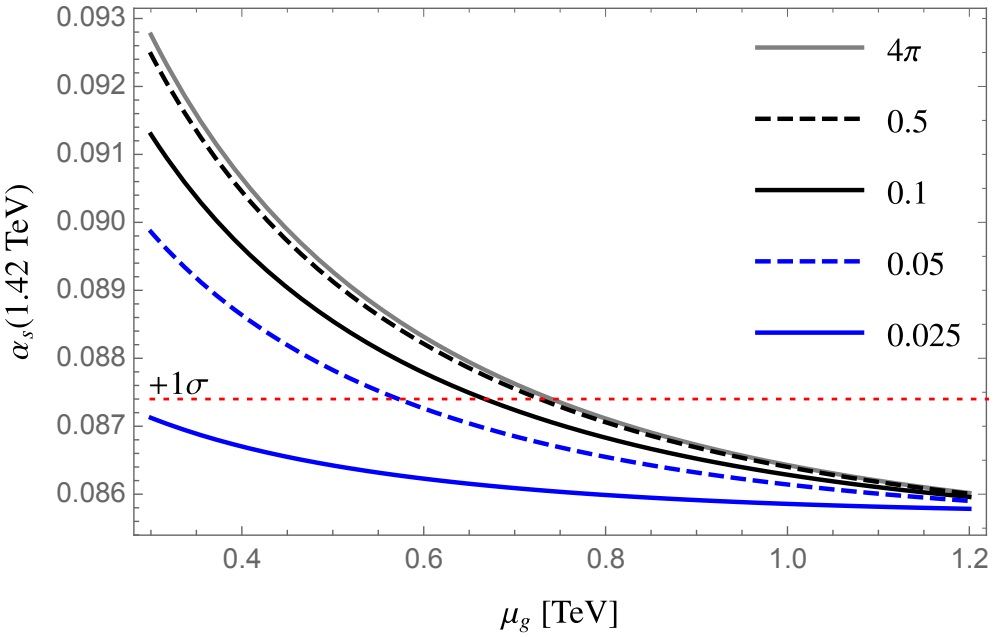

Figure 4.15: Bound from running α_s from the gluon continuum scale μ_g to $Q = 1.42$ TeV.

3. *Pair production of continuum top partners:* We expect the continuum top pair-production cross section to be parametrically smaller than the one for particle top partners. This is due to the smearing of the spectral density to higher energies, where PDF suppression dominates. This is also the case in the result of [120] for colored fermionic unparticles.

The full calculation of the pair-production cross section for continuum top partners is far from trivial, as it is unclear how to calculate the phase space factor for a pair of final-state continuum fermions. Inspired by the work of [119, 120], we can use the optical theorem to relate the pair-production cross section to the imaginary part of the diagram of the vacuum polarization with a continuum fermion loop, which we can calculate using dispersion relations. We leave the full calculation of the top partner pair production for future work [131].

Since we are not calculating the full cross section in this work, we chose a conservative point in parameter space with a continuum fermion gap of 1.75 TeV, with 1% tuning.

4.9 Conclusions

We presented a novel type of composite Higgs model, where all top and gauge partners form continua rather than being ordinary particles. Such top and gauge partners will evade all s-channel resonance searches and are expected to lead to unique experimental signatures. We showed how to obtain a realistic model of this sort from a warped extra dimension, where space continues beyond the IR brane. A linear dilaton dominates the deep IR region, corresponding to critical IR dynamics that produces a gapped continuum. We have shown how to calculate the full set of spectral densities for the fermion and gauge partners. Furthermore, we established a phenomenologically viable benchmark point, tuned at the percent level, with a realistic radiatively generated Higgs potential. The phenomenology of continuum partners, as well as the existing collider bounds on this model, will appear in an upcoming publication.

APPENDIX

4.A Gauge Boson Green's Functions

In this appendix we present the details necessary for evaluating the gauge boson spectral densities. We demonstrate our calculation in a simple toy model with a bulk $U(1) \times U(1)$ broken to $U(1)$ on the IR brane, where the role of the Higgs is played by the A_5 of the broken $U(1)$. In the bulk we have two gauge bosons, W_μ and W'_μ. W_μ corresponds to an unbroken direction (before the Higgs VEV) with the boundary conditions $(+,+)$ on the UV and IR branes, while W'_μ corresponds to a broken direction $(-,-)$. The Higgs VEV will mix these two fields. There are now four different Green's functions to solve for: $\langle W(z)W(z')\rangle$, $\langle W'(z)W(z')\rangle$, $\langle W(z)W'(z')\rangle$ and $\langle W'(z)W'(z')\rangle$, which we denote collectively by $G(z,z';p^2)_{ij}, i,j \in \{W,W'\}$.

To get each spectral density we need to first specify whether the source (the delta function) is in the W or the W' equation. This depends if we're looking for $W(z')$ or $W'(z')$ in the correlation function. In a shorthand notation, we will write

$$\mathcal{D}_g\, G(z,z';p^2)_{ij} \;=\; \delta_{ij}\,\delta(z-z')\,. \tag{4.41}$$

The gauge EOM is Eq. 4.24, with a general solution of the form Eq. 4.25. To solve for the Green's function, we divide our space into the domains $R \le z \le z'$, $z' \le z \le R'$ and $R' \le z$, where the coefficients are denoted $\overleftarrow{A}, \overleftarrow{B}, \overrightarrow{A}, \overrightarrow{B}$ and A^∞, B^∞, respectively. Our goal is then to find these coefficients, subject to the following jump/boundary conditions:

- UV BC:

$$\partial_z G_{Wj}|_{z=R} \;=\; G_{W'j}|_{z=R} \;=\; 0\,. \tag{4.42}$$

- Jump conditions at $z = z'$:

$$\begin{aligned} \Delta G_{Wj}|_{z=z'} \;&=\; \Delta G_{W'j}|_{z=z'} \;=\; 0\,, \\ \Delta\partial_z G_{ij}|_{z=z'} \;&=\; a(z)^{-1}\delta_{ij}\,. \end{aligned} \tag{4.43}$$

- Jump conditions at $z = R'$:

$$\begin{aligned} \Delta G_{Wj}|_{z=R'} \;&=\; \Delta\partial_z G_{Wj}|_{z=R'} \;=\; 0\,, \\ G_{W'j}|_{z=R'^-} \;&=\; G_{W'j}|_{z=R'_+} \;=\; 0\,. \end{aligned} \tag{4.44}$$

- Regularity of $G(z, z, p^2)$ at $z \to \infty$:

$$A^{\infty}_{Wj} = A^{\infty}_{W'j} = 0\,. \tag{4.45}$$

From these linear conditions we arrive at the Green's function matrix $G(z, z'; p^2)_{ij}$. We can of course diagonalize this matrix and define two spectral densities:

$$\rho(s)_{1,2} \;\equiv\; \lim_{z,z'\to R} \frac{1}{\pi}\mathrm{Im}\; G(z, z'; s)_{1,2}\,. \tag{4.46}$$

corresponding to the two eigenvalues of G_{ij}. Note, however, that in the present case $G_{W'W} = G_{W'W'} = 0$ by virtue of the UV Dirichlet BC, and also that $G_{WW'} = 0$ because the W and W' IR BC are completely decoupled. The situation is different once we consider a bulk $\langle A_5\rangle$ VEV rotating the two multiplets. In this case the IR BC is modified to:

$$\begin{aligned} \Delta\hat{G}_{Wj}|_{z=R'} \;&=\; \Delta\partial_z\hat{G}_{Wj}|_{z=R'} \;=\; 0\,, \\ \hat{G}_{W'j}|_{z=R'^-} \;&=\; \hat{G}_{W'j}|_{z=R'_+} \;=\; 0\,, \end{aligned} \tag{4.47}$$

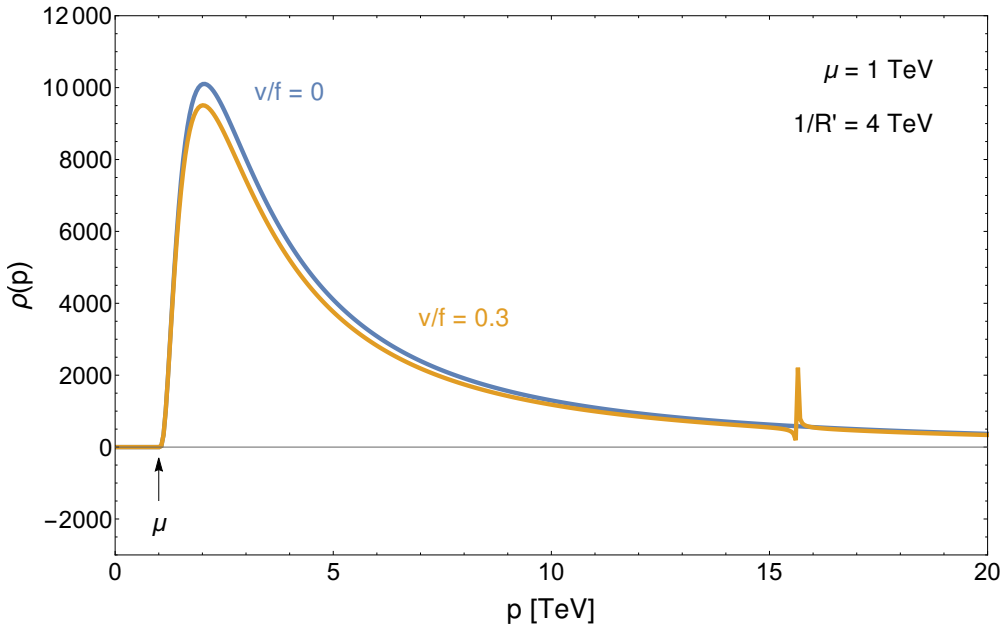

Figure 4.16: Spectral density for W/W' mix with $\mu = 1\,\text{TeV}$, $1/R' = 4\,\text{TeV}$.

with

$$\begin{aligned} \hat{G}_{Wj} &= \quad c_h\, G_{Wj} \;+\; s_h\, G_{W'j}\,, \\ \hat{G}_{W'j} &= -\, s_h\, G_{Wj} \;+\; c_h\, G_{W'j}\,, \end{aligned} \tag{4.48}$$

and $c_h = \cos\left(\langle h\rangle / f\right)$, $s_h = \sin\left(\langle h\rangle / f\right) \equiv v/f$. The resulting spectral density $\rho_1(p)$ is depicted in Fig. 4.16 ($\rho_2(p)$ is still zero by virtue of the Dirichlet BC for W'). Note that for $v/f \neq 0$, $\rho_1(p)$ acquired a pole on top of the branch cut. This is as expected: the pole originates from the W' component of the eigenstate 1, and W' has a Dirichlet BC at R'. We also note that the zero mode of eigenstate 1 is no longer massless since it acquires a mass from the Higgs. This is seen by determining where $1/G_1(p)$ vanishes, as shown in Fig. 4.17.

We are now ready to present the spectral densities for the gauge bosons of the realistic model. As previously explained, the bulk gauge symmetry $SO(5) \times U(1)_X$ is broken on the IR brane to $SO(4) \times U(1)_X$. We choose the following

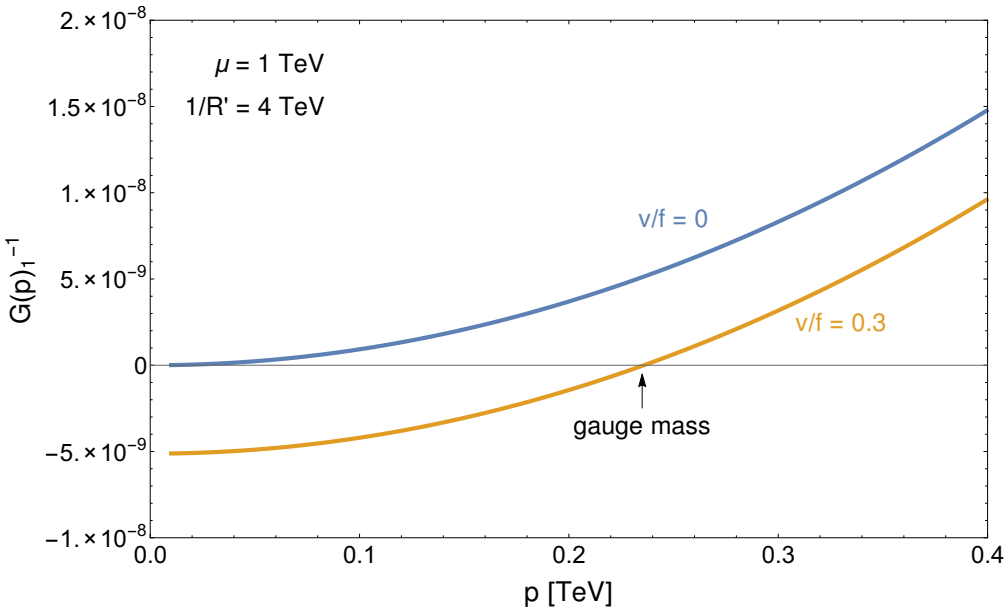

Figure 4.17: Inverse Green's function for W/W' mix with $\mu = 1$ TeV, $1/R' = 4$ TeV.

generators as a basis of $SO(5)$:

$$\begin{aligned} \left(T^a_{L,R}\right)_{ij} &= -\frac{i}{2}\left[\epsilon^{abc}\delta^b_i\delta^c_j \pm \left(\delta^a_i\delta^4_j - \delta^4_i\delta^a_j\right)\right], \\ \left(T^{\hat{a}}_C\right)_{ij} &= -\frac{i}{\sqrt{2}}\left[\left(\delta^{\hat{a}}_i\delta^5_j - \delta^5_i\delta^{\hat{a}}_j\right)\right], \end{aligned} \tag{4.49}$$

with $a \in \{1,2,3\}$ and $\hat{a} \in \{1,2,3,4\}$. The gauge bosons corresponding to the generators $T^a_{L,R}$ are continuous across the IR brane, while the ones corresponding to $T^{\hat{a}}_C$ get a Dirichlet BC. The Higgs emerges as the $4D$ component of $A_5^{C\hat{a}}$. To solve for the bulk profiles in the presence of a Higgs VEV, we use the trick of solving for $v = 0$ but with the IR BC rotated by the Higgs matrix:

$$U_h = e^{i g_5 \int_R^{R'} A_5(z) T^{C\hat{a}} h^{\hat{a}}(x)\, dz}. \tag{4.50}$$

The profile $A_5(z)$ is given by solving the bulk EOM:

$$\partial_z\left[a(z)A_5(z)\right] = 0. \tag{4.51}$$

and so $A_5(z) = N_5\, a^{-1}(z)$, with $N_5 = \left[\int_R^{R'} a^{-1}(z)dz\right]^{-1/2}$. We only integrate A_5 up to the IR brane because it is pure gauge beyond it. In other words, the only gauge invariant Wilson line for the A_5 is between the UV and IR branes.

Due to the SM gauge freedom, we are allowed to choose the Higgs VEV $\langle h\rangle$ to be in the $\hat{a} = 4$ direction. We then have:

$$U_h = e^{i\,T^{C\hat{4}}\langle h\rangle/f}\,, \tag{4.52}$$

where $f = g_5^{-1}\left[\int_R^{R'} a^{-1}(z)dz\right]^{-1/2}$. Substituting the expression for $T^{C\hat{4}}$, we get

$$U_h = \begin{pmatrix} 0 & 0 & 0 & 0 & 0 \\ 0 & 0 & 0 & 0 & 0 \\ 0 & 0 & 0 & 0 & 0 \\ 0 & 0 & 0 & \cos(\langle h\rangle/f) & \sin(\langle h\rangle/f) \\ 0 & 0 & 0 & -\sin(\langle h\rangle/f) & \cos(\langle h\rangle/f) \end{pmatrix}. \tag{4.53}$$

The components of the bulk $SO(5)$ gauge field are:

$$W_\mu = W_\mu^{\pm,3;L}\, T_L^{\pm,3} + W_\mu^{\pm,3;R}\, T_R^{\pm,3} + W_\mu^{\pm,\pm}\, T^{\pm\pm}\,, \tag{4.54}$$

where

$$\begin{aligned} T_{L,R}^{\pm} &= \frac{1}{\sqrt{2}}\left(T_{L,R}^1 \pm iT_{L,R}^2\right), \\ T^{\pm\mp} &= \frac{1}{\sqrt{2}}\left(T_C^3 \pm iT_C^4\right), \\ T^{\pm\pm} &= \frac{1}{\sqrt{2}}\left(T_C^1 \pm iT_C^2\right). \end{aligned} \tag{4.55}$$

There is an additional bulk $U(1)_X$ field that we denote by X_μ. The extra $U(1)_X$ is required to reproduce the correct hypercharge assignments for the SM fields [32].

The UV boundary conditions are then

$$\begin{aligned} W_\mu^{\pm;R}|_{z=R} &= W_\mu^{\pm,\pm}|_{z=R} = 0\,, \\ \partial_z W_\mu^{\pm,3;L} &+ C_k\, W_\mu^{\pm,3;L}|_{z=R} = 0\,, \\ c_\theta\, W_\mu^{3;R} &- s_\theta\, X_\mu|_{z=R} = 0\,, \\ \partial_z \left[s_\theta\, W_\mu^{3;R} + c_\theta\, X_\mu \right]|_{z=R} &= 0\,. \end{aligned} \tag{4.56}$$

Note that the above boundary conditions mix the gauge fields $W_\mu^{3;R}$ and X_μ with an angle θ as a result of a UV boundary kinetic term. A similar boundary kinetic term $C_k \equiv Rp^2r^2 \log R'/R$ is responsible for the mixed boundary conditions for $W_\mu^{\pm,3;L}$. This term is necessary to get the right $SU(2)_L$ gauge coupling for every value of the bulk coupling g_5. To account for the VEV of the Higgs–A_5, we rotate its effect into the IR jump conditions, which are now given are given in terms of the Higgs-rotated gauge fields:

$$\hat{W}_\mu = U_h\, W_\mu\, U_h^{-1}\,. \tag{4.57}$$

This multiplet is decomposed similarly to Eq. 4.54:

$$\hat{W}_\mu = \hat{W}_\mu^{\pm,3;L}\, T_L^{\pm,3} + \hat{W}_\mu^{\pm,3;R}\, T_R^{\pm,3} + \hat{W}_\mu^{\pm,\pm}\, T^{\pm\pm}\,. \tag{4.58}$$

The IR BC are then

$$\begin{aligned} \Delta\hat{W}_\mu^{\pm,3;L}|_{z=R'} &= \Delta\hat{W}_\mu^{\pm,3;R}|_{z=R'} = 0\,, \\ \hat{W}_\mu^{\pm,\pm}|_{z=R'} &= 0\,. \end{aligned} \tag{4.59}$$

The resulting gauge boson spectral densities and inverse Green's functions are presented in the main text in Figs. 4.7 and 4.10.

4.B Fermion Green's Functions

Next we explain how an A_5 (Higgs) VEV can give mass to two fermion zero modes. This is a standard result in Gauge-Higgs unification, and we demonstrate it here explicitly in the context of continuum CH. As a starting point, we take two bulk fermions $Q_L^{1,2}$ with equal bulk masses and dilaton Yukawas c_L, y and opposite UV boundary conditions, and two bulk fermions $Q_R^{1,2}$ with equal bulk masses and dilaton Yukawas $c_R, -y$ and opposite UV boundary conditions. In the context of warped CH models, $Q_L^{1,2}$ will represent two different quantum numbers within the same Q_L bulk multiplet that is in a large representation of the bulk gauge group, and likewise for $Q_R^{1,2}$. However, in this toy example we will not be concerned with the group theory aspects of the model. The UV boundary conditions are:

$$\psi_L^1|_{z=R} \;=\; \chi_L^2|_{z=R} \;=\; \psi_R^1|_{z=R} \;=\; \chi_R^2|_{z=R} \;=\; 0\,, \tag{4.60}$$

where $Q_L^{1,2} = \left(\chi_L^{1,2}, \psi_L^{1,2}\right)$ and $Q_L^{1,2} = \left(\chi_R^{1,2}, \psi_R^{1,2}\right)$. These boundary conditions, together with the assignment of $\pm y$ dilaton Yukawas and the demand for a regular solution in the deep IR, implies zero modes for χ_L^1 and ψ_R^2. As IR mass terms only couple (Q_L^1, Q_R^1), (Q_L^2, Q_R^2), they won't be enough to lift the zero modes χ_L^1 and ψ_R^2. As we will see below, only a non-zero VEV for the A_5-Higgs can rotate the multiplets and lift the two zero modes. To obtain the matrix of Green's functions we divide the problem into the same domains as in the gauge case, and solve for $\overleftarrow{A}_j, \overleftarrow{B}_j, \overrightarrow{A}_j, \overrightarrow{B}_j, A_j^\infty, B_j^\infty$, where this time i, j are joint indices in $\{1L, 2L, 1R, 2R\}$.

The boundary and jump conditions in this case are:

- UV BC:

$$G^\psi_{L1;j}|_{z=R} \;=\; G^\chi_{L2;j}|_{z=R} \;=\; G^\psi_{R1;j}|_{z=R} \;=\; G^\chi_{R2;j}|_{z=R} \;=\; 0\,. \tag{4.61}$$

- Jump conditions at $z = z'$:

$$\Delta G^{\psi}_{ij}|_{z=z'} \;=\; -\,\Delta G^{\chi}_{ij}|_{z=z'} \;=\; D_{ij}\, a(z')^{-4}\,. \tag{4.62}$$

- Jump conditions at $z = R'$: On the IR brane we turn on the masses $M_1\, \bar{Q}^1_L\, Q^1_R$ and $M_2\, \bar{Q}^2_L\, Q^2_R$, which give us the jump condition:

$$\begin{aligned} \Delta G^{\chi}_{ak;j}|_{z=R'} &= -\,M_k \left\langle G^{\chi}_{\bar{a}k;j} \right\rangle |_{z=R'} \\ \Delta G^{\psi}_{ak;j}|_{z=R'} &= \quad M_k \left\langle G^{\psi}_{\bar{a}k;j} \right\rangle |_{z=R'}\,, \end{aligned} \tag{4.63}$$

  where $j \in \{1L, 2L, 1R, 2R\}$, $a \in \{L, R\}$, and $k \in \{1, 2\}$.

- Regularity of $G(z, z; p^2)$ at $z \to \infty$: as before, $A^{\infty}_{ij} = 0$.

Note that we have yet to turn on a Higgs VEV mixing the 1 and 2 states. At this stage there are zero modes in χ^1_L and in ψ^2_R. The IR masses $M_{1,2}$ cannot change this fact, we can only lift the two zero modes with a mass that connects them to each other. This is impossible as long as the 1 and 2 BC are completely decoupled. This is not the case when a Higgs VEV is turned on. As usual, this VEV appears as a rotation of the IR jump conditions:

$$\begin{aligned} \hat{G}_{a1;j}|_{z=R'} &= \quad c_h\, G_{a1;j} \;+\; s_h\, G_{a2;j}\,, \\ \hat{G}_{a2;j}|_{z=R'} &= -\,s_h\, G_{a1;j} \;+\; c_h\, G_{a2;j}\,. \end{aligned} \tag{4.64}$$

The rotation is the same for G^{χ}_{ij} and G^{ψ}_{ij}. We now write the IR BC in Eq. 4.63 in terms of the *Higgs-rotated* Green's functions $\hat{G}_{ij}$.

Solving these conditions, we obtain the Green function G^h_{ij} with $G_{a1;j} = G^{\chi}_{a1;j}$, $G_{a2;j} = G^{\psi}_{a2;j}$. This matrix now has four eigenvalues $G^h(z, z'; p)_{1,2,3,4}$ with appropriate spectral densities $\rho^h(p)_{1,2,3,4}$. The label h is an explicit reminder that they depend on the Higgs VEV. In Fig. 4.18 we plot the spectral densities for $R' = (4\,\text{TeV})^{-1}$, $M_1 = 0.3$, $M_2 = 0$, $c_L = 0.3$ and $c_R = -0.1$, for $v/f = 0.3$. In Fig. 4.19

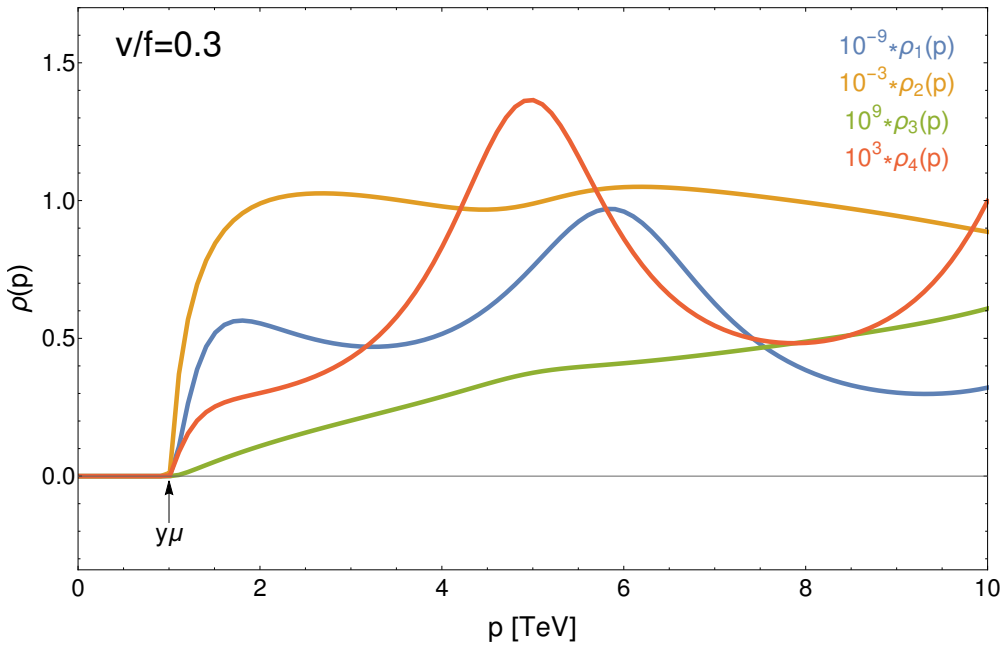

Figure 4.18: Spectral density for $c_L = 0.3$, $c_R = -0.1$, $M_1 = 0.3$, $M_2 = 0$.

we plot the inverse Green's functions for $v/f = 0, 0.3$, and show that there are non-trivial zeros for $v/f = 0.3$.

We are now ready to present the spectral densities for the top/bottom sector for the realistic model. We will choose the fermions to be embedded in the bulk multiplets Q_L, T_R and B_R in the $\mathbf{5}_{\frac{2}{3}}, \mathbf{5}_{\frac{2}{3}}$ and $\mathbf{10}_{\frac{2}{3}}$ of $SO(5) \times U(1)_X$. The SM gauge group $SU(2)_L$ is a subgroup of $SO(5)$, and the hypercharge is a combination of $U(1)_R \subset SO(5)$ and $U(1)_X$ defined by $Y = T_R^3 + X$. Under the subgroup $SU(2)_L \times U(1)_Y$, the bulk multiplets decompose as:

$$\begin{aligned}
Q_L(\mathbf{5})_{\frac{2}{3}} &\to q_L(\mathbf{2})_{\frac{1}{6}} + \tilde{q}_L(\mathbf{2})_{\frac{7}{6}} + y_L(\mathbf{1})_{\frac{2}{3}}\,, \\
T_R(\mathbf{5})_{\frac{2}{3}} &\to q_R(\mathbf{2})_{\frac{1}{6}} + \tilde{q}_R(\mathbf{2})_{\frac{7}{6}} + t_R(\mathbf{1})_{\frac{2}{3}}\,, \\
B_R(\mathbf{10})_{\frac{2}{3}} &\to q'_R(\mathbf{2})_{\frac{1}{6}} + \tilde{q}'_R(\mathbf{2})_{\frac{7}{6}} + x_R(\mathbf{3})_{\frac{2}{3}} + y_R(\mathbf{1})_{\frac{7}{6}} + \tilde{y}_R(\mathbf{1})_{\frac{1}{6}} + b_R(\mathbf{1})_{-\frac{1}{3}}\,.
\end{aligned} \tag{4.65}$$

We choose the UV BC such that only q_L, t_R and b_R have zero modes by assigning Neumann BC for $G^{\chi}_{q_L}$, $G^{\psi}_{q_R}$ and $G^{\psi}_{B_R}$, and Dirichlet BC for all the other $G^{\chi}_{Q_L}$, $G^{\psi}_{T_R}$

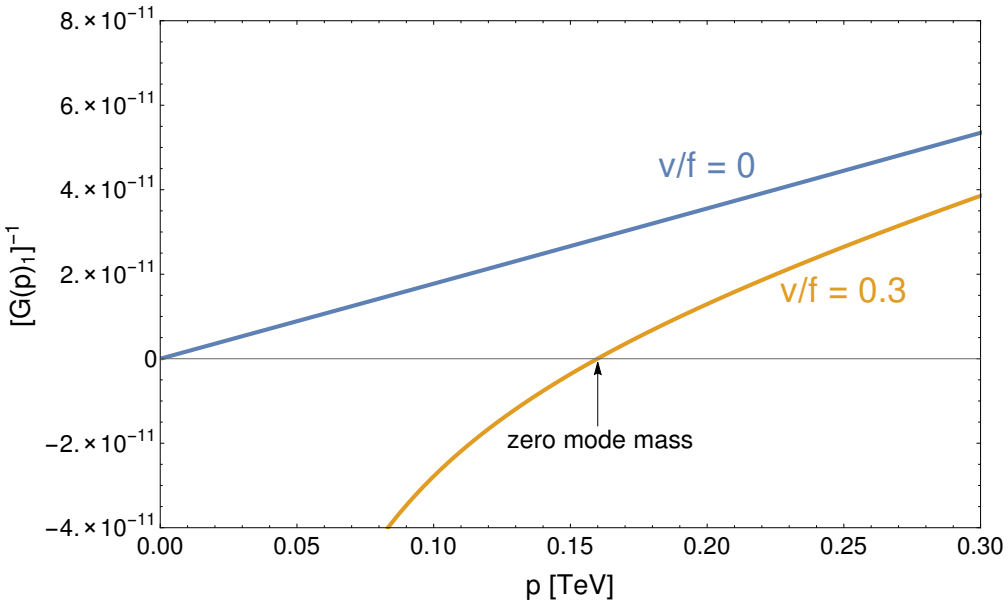

Figure 4.19: Inverse Green's function for $c_L = 0.3$, $c_R = -0.1$, $M_1 = 0.3$, $M_2 = 0$. The inverse Green's function gets a non-trivial zero for $v/f = 0.3$.

and $G^{\psi}_{B_R}$. The $SO(4) \times U(1)_X$ symmetry on the IR brane allows for three mass terms:

$$S_{\rm IR} = \int dx^4 \sqrt{g_{\rm ind}} \left[M_1 \bar{y}_L t_R + M_4 \left(\bar{q}_L q_R + \bar{\tilde{q}}_L \tilde{q}_R\right) + M_b \left(\bar{q}'_L q_R + \bar{\tilde{q}}'_L \tilde{q}_R\right) \right] . \quad (4.66)$$

These mass terms lead as usual to IR jump conditions which are for Q_L:

$$\begin{aligned}
\Delta G^{\chi}_{q_L,\tilde{q}_L;j}|_{z=R'} &= -M_4 \left\langle G^{\chi}_{q_R,\tilde{q}_R;j} \right\rangle - M_b \left\langle G^{\chi}_{q'_R,\tilde{q}'_R;j} \right\rangle |_{z=R'} , \\
\Delta G^{\psi}_{q_L,\tilde{q}_L;j}|_{z=R'} &= M_4 \left\langle G^{\psi}_{q_R,\tilde{q}_R;j} \right\rangle - M_b \left\langle G^{\psi}_{q'_R,\tilde{q}'_R;j} \right\rangle |_{z=R'} , \\
\Delta G^{\chi}_{y_L;j}|_{z=R'} &= -M_1 \left\langle G^{\chi}_{t_R;j} \right\rangle |_{z=R'} , \\
\Delta G^{\psi}_{y_L;j}|_{z=R'} &= M_1 \left\langle G^{\psi}_{t_R;j} \right\rangle |_{z=R'} .
\end{aligned} \quad (4.67)$$

For T_R they are:

$$\begin{aligned}
\Delta G^{\chi}_{q_R,\tilde{q}_R;j}|_{z=R'} &= -M_4 \left\langle G^{\chi}_{q_L,\tilde{q}_L;j} \right\rangle |_{z=R'} , \\
\Delta G^{\psi}_{q_R,\tilde{q}_R;j}|_{z=R'} &= M_4 \left\langle G^{\psi}_{q_L,\tilde{q}_L;j} \right\rangle |_{z=R'} , \\
\Delta G^{\chi}_{t_R;j}|_{z=R'} &= -M_1 \left\langle G^{\chi}_{s_L;j} \right\rangle |_{z=R'} , \\
\Delta G^{\psi}_{t_R;j}|_{z=R'} &= M_1 \left\langle G^{\psi}_{s_L;j} \right\rangle |_{z=R'} ,
\end{aligned} \tag{4.68}$$

and for B_R they are:

$$\begin{aligned}
\Delta G^{\chi}_{q'_R,\tilde{q}'_R;j}|_{z=R'} &= -M_b \left\langle G^{\chi}_{q_L,\tilde{q}_L;j} \right\rangle |_{z=R'} , \\
\Delta G^{\psi}_{q'_R,\tilde{q}'_R;j}|_{z=R'} &= M_b \left\langle G^{\psi}_{q_L,\tilde{q}_L;j} \right\rangle |_{z=R'} , \\
\Delta G^{\chi}_{x_R,y_R,\tilde{y}_R,b_R;j}|_{z=R'} &= 0 , \\
\Delta G^{\psi}_{x_R,y_R,\tilde{y}_R,b_R;j}|_{z=R'} &= 0 .
\end{aligned} \tag{4.69}$$

As usual, in the IR jump conditions, the fields to the left of the IR brane are really the Higgs-rotated fields:

$$\hat{G}_{Q_L} = U_h G_{Q_L} , \; \hat{G}_{T_R} = U_h G_{T_R} , \; \hat{G}_{B_R} = U_h G_{B_R} U_h^{-1} , \tag{4.70}$$

decomposed into their different components. The jump discontinuity due to IR localized mass terms results in quasi-IR brane-localized wave function profiles for the fermionic fields as noted at the end of Sec. 4.4.

CHAPTER 5

REVIEW OF DARK MATTER

5.1 Observations of Dark Matter

Dark Matter (DM) is our first and foremost indication for physics beyond the Standard Model. Though not yet observed in the lab, there is a plethora of observational evidence for the existence of DM, which we shall briefly review here, following [142] and [143]. This brief review is by no means exhaustive.

5.1.1 Rotation Curves

A Galactic rotation curve is a measurement of the radial rotation speed of virialized matter as a function of its distance from the center of the galaxy. The velocity is measured by spectrometry of atomic hydrogen, which extends well beyond the galaxy's stellar component. Current compendia of galactic rotation curves are given in [144, 145]. While the theoretical rotation curves due to baryonic matter only tend to decay as $v(r) \sim r^{-\frac{1}{2}}$, observational data indicates flat $v(r) \sim r^0$ rotation curves up to radii well beyond the maximal radius of the stellar component. This constituted the original observational evidence for the existence of a DM galactic halo [146]. In a DM halo with $\rho_{\rm DM}(r) \sim r^{-2}$, the rotation curve goes as

$$v(r) \sim \sqrt{\frac{4\pi G \int_0^r \rho(r)\, r^2\, dr}{r}} \sim r^0 \,, \tag{5.1}$$

as indicated by data.

5.1.2 Galaxy Clusters

The most striking evidence for DM at the cluster level is from the bullet cluster (1E 0657-56) [147–149]. This is a groundbreaking observation of two clusters colliding. While the DM components of these two clusters already crossed each other, the X-ray emitting baryonic plasma in them lags, due to dissipation. This results in an $8\,\sigma$ spatial offset between the center of mass of each cluster (as observed by weak lensing), and the observed location of the plasma in each cluster. Further indications for DM at the cluster level involve weak lensing studies of DM sub-halos in the Coma cluster using the Subaru telescope [150], as well as extensive weak lensing surveys using the Subaru Telescope and the Canada-France-Hawaii telescope (see [151] and references therein). Baryonic counterparts to weak lensing (showing that the baryonic mass is smaller than the total cluster mass) were presented in [152] as a direct indication of DM.

5.1.3 Cosmological Scales

Observations from the early universe allow us to put very stringent bounds on the parameters of the ΛCDM model, including Ω_{m}, the average comoving matter density in the universe (including DM), and σ_8, the present RMS matter fluctuation averaged over a sphere of radius $8h^{-1}$ Mpc. A summary plot of these stringent bounds in the $\Omega_{\mathrm{m}}-\sigma_8$ plane is shown in Fig. 5.1, reproduced from [143]. The bounds originate from cosmological-scale observations of the Cosmic Microwave Background Radiation (CMB), Baryonic Acoustic oscillations (BAO), and bounds from Large Scale Structure as observed by the Dark Energy Survey (DES).

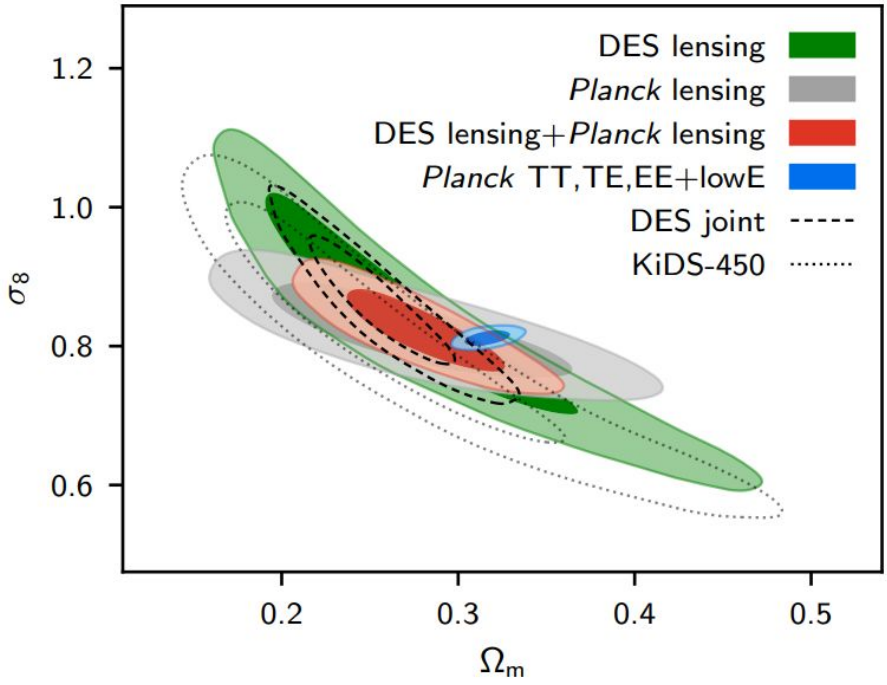

Figure 5.1: Λ*CDM* model 68% and 95% constraint contours on the matter-density parameter Ω_m and fluctuation amplitude σ_8. The bounds from DES lensing, Planck CMB lensing, and the joint lensing constraint are shown in green, grey, and red, respectively. The blue filled contour shows the independent constraint from the Planck CMB power spectra. Reproduced from [143].

Cosmic Microwave Background Radiation

The CMB is the approximately isotropic photon radiation from the early universe. CMB photons decoupled from matter following Hydrogen recombination, at a redshift of $z \sim 1100$. On average, the CMB fits very well to a blackbody spectrum with $T = 2.762^{\circ}$ K. However, the CMB has 10^{-5} anisotropies in the temperature, which can be expanded as

$$\frac{\delta T}{T}(\theta, \phi) = \sum_{\ell=2}^{+\infty} \sum_{m=-\ell}^{+\ell} a_{\ell m} Y_{\ell m}(\theta, \phi)\,, \tag{5.2}$$

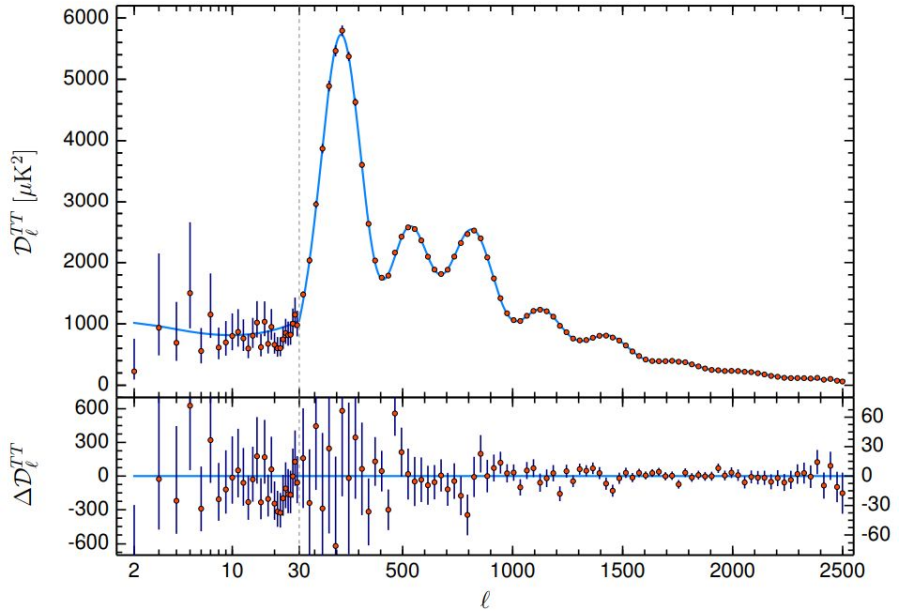

Figure 5.2: TT power spectrum as measured by the Plank Collaboration. The red dots are the measured spectrum and the blue line is the ΛCDM best fit prediction. Reproduced from [143].

where the $Y_{\ell m}(\theta, \phi)$ are spherical harmonics. The TT power spectrum D_ℓ is then defined as

$$D_\ell \equiv \frac{1}{2\pi} \sum_{m=-\ell}^{\ell} |a_{\ell m}|^2 \ . \tag{5.3}$$

The power spectrum has peaks due to DM-baryonic matter acoustic oscillations, whose position, height, and spacing of the peaks are extremely sensitive to cosmological parameters. Peaks with a similar sensitivity exist in the temperature-polarization (TE) and polarization-polarization (EE) power spectra. The Planck space observatory [143,153,154] provided the most precise measurement of the CMB power spectrum, which can be seen in Fig. 5.2.

Baryon Acoustic Oscillations

Baryon Acoustic Oscillations (BAO) are are peaks in the matter power spectrum inferred from galaxy surveys such as the Sloan Digital Sky Survey III [155] and the 6dF Galaxy Survey [156]. More specifically, BAO surveys measure the distance ratio

$$\frac{D_{\rm V}(z)}{r_{\rm s}\left(z_{\rm drag}\right)}\,, \tag{5.4}$$

at reshifts $0.1 \leq z \leq 0.7$. In the equation above, $r_{\rm s}\left(z_{\rm drag}\right)$ is the comoving sound horizon at the baryon drag epoch (when baryons became dynamically decoupled from the photons) and $D_{\rm V}(z)$ is a combination of the angular-diameter distance, $D_{\rm A}(z)$, and the Hubble parameter, $H(z)$. As for the CMB peaks, the height and position of BAO peaks are sensitive to cosmological parameters such as $\Omega_{\rm m}$ [157], and so they provide a complimentary bound to the CMB, as can be seen in Fig. 5.1.

Dark Energy Survey

The Dark Energy survey [158,159] provides complimentary bounds on $\Omega_{\rm m}$ from two types of measurements: cosmic shear and type Ia supernovae. Cosmic shear measures the correlated distortion of the light emitted from distant galaxies due to weak gravitational lensing by Large Scale Structure. The amplitude of the lensing signal is primarily sensitive to the normalization of the matter fluctuations, σ_8, and to the matter density $\Omega_{\rm m}$. Another very recent constraint on $\Omega_{\rm m}$ comes from the DES-SN survey [160], measuring the luminosity distance vs redshift of type Ia supernovae for $z < 1$. This allows for complementary constraints on $\Omega_{\rm m}$ through its impact on $H(z)$.

5.2 Early Universe Dynamics

Though we know from observations that DM exists, we still don't know much about its properties, beyond the fact that it interacts gravitationally, it is cold, and its other interactions with the SM are weak. In particular, there is no good DM candidate in the SM, and so we are lead to DM model building. Most DM models involve number changing interactions either between DM and SM particles or within the dark sector.

Consequently, the observed DM comoving density $\Omega_{\rm DM}$ is not a free parameter but rather a quantity that is set dynamically throughout the thermal history of the universe. The details of this dynamics depend on the particular DM model and its parameter space. Here we will elaborate on the popular thermal WIMP scenario, while for the plethora of other DM models we refer the reader to the excellent reviews [161–163]. A handful of these models and their relevant mass scales is given in Fig. 5.3.

Weakly interacting massive particle (WIMP) DM is a simple class of models that involves $2 \leftrightarrow 2$ number changing interactions between the DM and SM [165]. We assuming a DM particle of mass $m_{\rm DM}$ that was initially in thermal equilibrium with the SM through the number changing interactions

$$\mathrm{DM\,DM} \leftrightarrow \mathrm{SM}\,\overline{\mathrm{SM}}\,, \tag{5.5}$$

where SM/$\overline{\rm SM}$ is a stand in for one or more SM particles and their antiparticle, for example $e^{\pm}$. At temperatures $T \gg m_{\rm DM}$, the DM is relativistic, and so its number density is given by $n_{\rm DM} = AgT^3$, where $A = \frac{\zeta(3)}{\pi^2}\left(\frac{3}{4}\right)$ for bosons (fermions) and g is the number of degrees of freedom (d.o.f) per DM particle. When the temperature of the universe drops below m, the SM particles in the

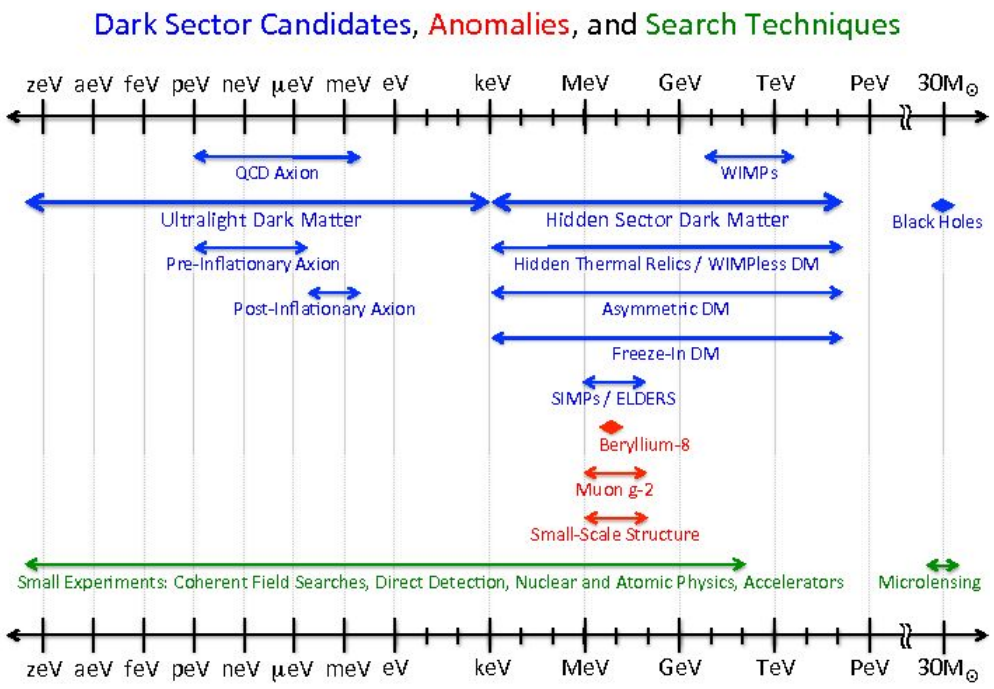

Figure 5.3: Mass ranges for different DM Models. Reproduced from [164]

plasma no longer have enough energy to pair produce DM, and so the process SM $\overline{\text{SM}}$ $\rightarrow$ DM DM stops. Now, the DM number density drops like that of a non-relativistic particle:

$$n_{\text{DM}} \approx n^{\text{eq}}(T) = g \left(\frac{m_{\text{DM}} T}{2\pi}\right)^{3/2} e^{-m_{\text{DM}}/T} . \tag{5.6}$$

The depletion in the number density of DM does not continue indefinitely, since at some temperature $T^* \approx m_{\text{DM}}/10$, the rate for the process DM DM $\rightarrow$ SM $\overline{\text{SM}}$ becomes smaller than the expansion rate of the universe given by the Hubble parameter $H(T)$. This happens when

$$n_{\text{DM}} \langle \sigma v_{\text{DM}} \rangle = H(T^*) , \tag{5.7}$$

where σ is the cross section for DM DM $\rightarrow$ SM $\overline{\text{SM}}$ and $\langle \sigma v_{\text{DM}} \rangle$ ia a thermal average at temperature T^*. Below this temperature, the comoving number density is constant, and we say that the DM is "frozen-out". The observed Ω_{DM} to

day is then

$$\Omega_{\rm DM}\, h^2 \;=\; h^2\, \frac{m_{\rm DM}\, s_{\rm today}}{\rho_{\rm crit}\, s(T^*)}\, n^*_{\rm DM} \;=\; \frac{10^{-9}\,{\rm GeV}^{-2}}{\langle \sigma\, v_{\rm DM}\rangle}\,, \tag{5.8}$$

and so to get the correct DM relic abundance we need

$$\langle \sigma\, v_{\rm DM}\rangle \;\approx\; 10^{-9}\,{\rm GeV}^{-2} \;=\; 10^{-26}\,{\rm cm}^3/{\rm s}\,, \tag{5.9}$$

which is a typical thermally averaged $2 \leftrightarrow 2$ cross section for a 1 TeV weakly coupled DM particle. This coincidence was dubbed "the WIMP miracle", and was the driving force behind an extensive DM search program in the past two decades.

5.3 Dark Matter Searches

5.3.1 Direct Detection

Direct detection is the effort to probe DM by searching for DM-SM elastic scattering events in dedicated DM detectors. The signal in these scattering events is the recoil of a nucleus or an electron within the detector. The predicted differential rate for nuclear recoils is given by

$$\frac{dR}{dE_{\rm nr}} \;=\; R_0\, \exp\!\left(-\frac{E_{\rm nr}}{E_0}\,\frac{4 m_{\rm DM} m_N}{(m_{\rm DM}+m_N)^2}\right) F^2\,(E_{\rm nr})\;, \tag{5.10}$$

where m_N is the mass of the nucleus, $E_0 \sim \frac{1}{2} m_{\rm DM}\, v^2$ (with $v \sim 230\,{\rm km/s}$) is the mean kinetic energy of the DM particle, $F^2\,(E_{\rm nr})$ is the nuclear form factor. The nominal rate R_0 for is given by

$$R_0 \;=\; \frac{2}{\sqrt{\pi}}\, n_{\rm det}\, \frac{\rho_{\rm DM}}{m_{\rm DM}}\, \sigma\, v\,. \tag{5.11}$$

where $n_{\rm det}$ is the nucleon number density in the detector and σ is either the spin independent or spin dependent cross section for DM-nucleon scattering. Note that due to the small momentum transfer, the DM interacts with the entire nucleus coherently. From the above functional form we learn a few things:

- The total rate decreases exponentially when increasing the detector threshold energy $E_{\rm nr}^{\rm min}$, which is typically O(keV).
- The total rate decreases exponentially when decreasing $m_{\rm DM}$ for $m_{\rm DM} < m_N$.
- The total rate increases linearly when increasing $m_{\rm DM}$ for $m_{\rm DM} \gg m_N$.

In practice, this means we can only use nuclear recoils to probe DM heavier than $\sim$ 5 GeV, and also that direct detection bounds weaken linearly for $m_{\rm DM} \gtrsim 100\,{\rm GeV}$, as can been in Fig 5.4. Above WIMP masses of $\sim$ 5 GeV, the strongest limits are placed by the the liquid xenon (LXe) Time Projection Chambers (TPC) XENON1T, LUX, and PandaX-II. The experiment with the best sensitivity to WIMPs in this mass-range is XENON1T, a LXe TPC with a 2.0 ton target. It excluded the spin-independent DM- nucleon interactions with cross sections above $4.1 \times 10^{47}{\rm cm}^2$ @ 30 GeV and 90% confidence level in a run with a 1 ton $\times$ year exposure [167]. This is much smaller than the cross-section needed to get the right $\Omega_{\rm DM}$ in the early universe, and so it is in major tension with the vanilla WIMP scenario.

In the DM mass range $1.8\,{\rm GeV} \lesssim m_{\rm DM} \lesssim 5{\rm GeV}$, the most competitive bounds are given by electron recoil experiments such as the Liquid-Argon based DarkSide-50, whose electron recoil threshold was as low as 0.1 keV. The limits are weaker than in the nuclear recoil regime due to enhanced background.

Lastly, there has been an extensive effort in the past 5 years to probe light

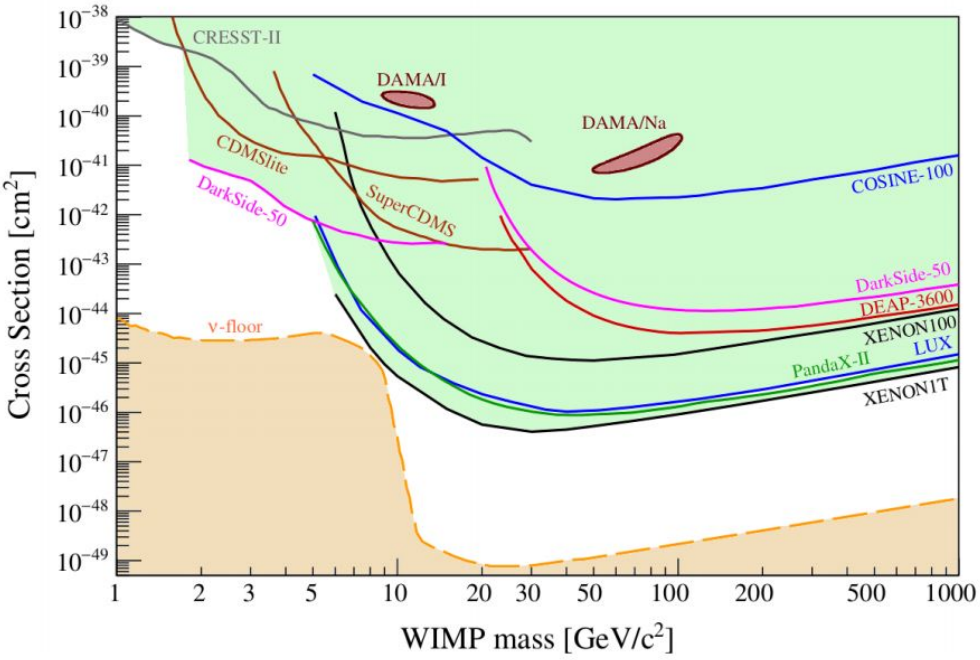

Figure 5.4: The current experimental parameter space for spin-independent WIMP- nucleon cross sections. Only some of the bounds are shown. The space above the lines is excluded at a 90% confidence level. The dashed line limiting the parameter space from below represents the neutrino floor from the irreducible background from coherent neutrino-nucleus scattering (CNNS). This plot is reproduced from [166]

(1 meV $\lesssim m_{\rm DM} \lesssim$ 1 GeV) and ultralight (10^{-22} eV $\lesssim m_{\rm DM} \lesssim$ 1 meV). A partial list of detection concepts for light DM involves DM induced chemical bond breaking, superfluid helium, magnetic bubble chambers, semiconductors and superconductors. Ultra-light scalar DM has a macroscopic Compton wavelength, and so it interacts coherently like a wave. Consequently, the search for ultralight DM focuses on precision tabletop experiments such as atom interferometry, NMR, X-ray, and torsion balance experiments. For excellent reviews of the different detection concepts and their implementations, see [163, 164, 168].

5.3.2 Indirect Detection

Indirect detection is the astrophysical search for DM decay/annihilation signals in the present and in the early universe. Given that the lifetime of DM has to be longer than the age of the universe, and that DM interacts at most weakly with the SM, we expect these decay/annihilation events to be rare, though potentially striking and with low SM backgrounds.

For example, the rate of expected gamma rays from DM annihilation in our galaxy (neglecting redshifting, absorption, etc) is given by (see the review by [169]):

$$\frac{1}{A}\frac{dN_\gamma}{dEdt} = \frac{\langle\sigma v_{\rm rel}\rangle}{m_{\rm DM}^2}\left(\frac{dN_\gamma}{dE}\right)_0 J_{\rm ann}\,, \tag{5.12}$$

where A is the effective area of the observing telescope, $\left(\frac{dN_\gamma}{dE}\right)_0$ is the spectrum of gamma rays obtained for each annihilation event, and $\langle\sigma v_{\rm rel}\rangle$ is the cross section for DM annihilation. The factor

$$J_{\rm ann} \equiv \frac{1}{8\pi}\int dr\, d\Omega\, \rho_{\rm DM}(\vec{r})^2 \tag{5.13}$$

is an astrophysical factor which accounts for the integral of line-of-sight DM density to the source.

Measurements of the CMB provide additional indirect bounds on DM annihilation through the latter's effect on the ionization history of the universe [170]. In Fig. 5.5 we present the current indirect detection bounds from the CMB, the Fermi-LAT [171] observation of the Milky-way dwarf spheroidal galaxies, and the H.E.S.S. Imaging Atmospheric Cherenkov Telescope [172] observation of the Galactic center. Other sources of indirect bounds are from cosmic ray measurement using the AMS-02 detector [173] on the international space station.

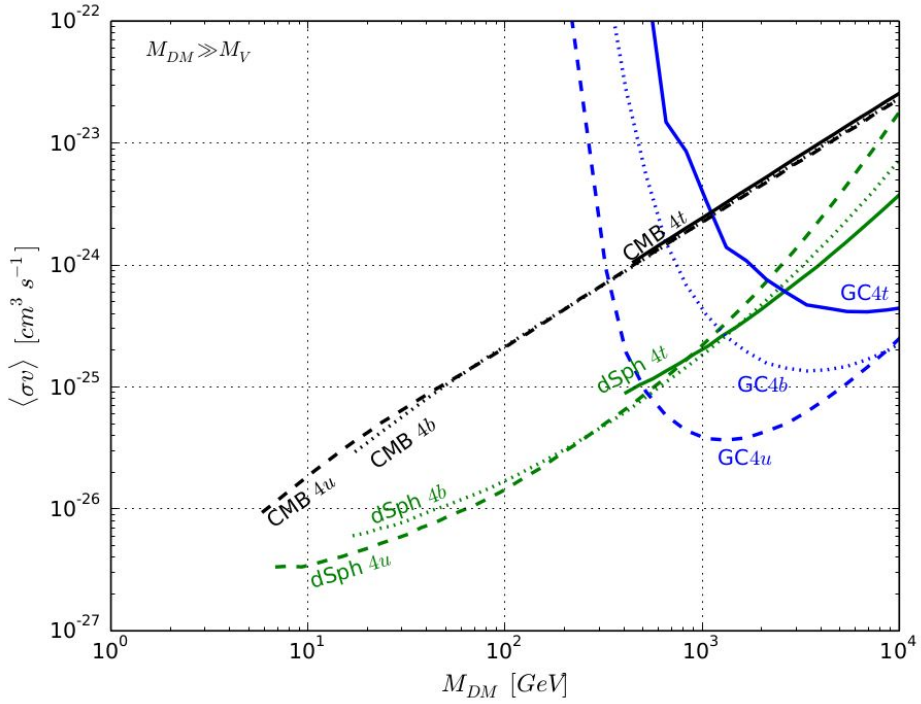

Figure 5.5: 95% C.L. upper limits on the dark matter annihilation cross-section as a function of the dark matter mass for the process DM DM $\rightarrow$ V V , with V decaying into $u\bar{u}$, $b\bar{b}$, $t\bar{t}$ for $M_{\rm DM} \gg M_{\rm V}$, with the V mass being just sufficiently heavier than the decays modes. Reproduced from [174].

5.3.3 Collider Searches

Collider searches look for potential DM particles generated in collider experiments. The modern approach to DM searches at the LHC is using simplified models, most notably the V/AV simplified model in which DM is produced through a vector/axial vector mediator, and the S/PS simplified model, in which the mediator is a scalar/pseudoscalar. The bounds on these simplified models are from several complementary channels, namely the $E_{\rm T}^{\rm miss}$ + X, dijet, di-b-jets, dilepton, and $t\bar{t}$ resonance channels [175]. LHC bounds on the leptophobic V/AV simplified model are shown, from ATLAS (Fig 5.6) and CMS (Fig 5.7). In Fig 5.8, these bounds are shown in comparison to the bounds from

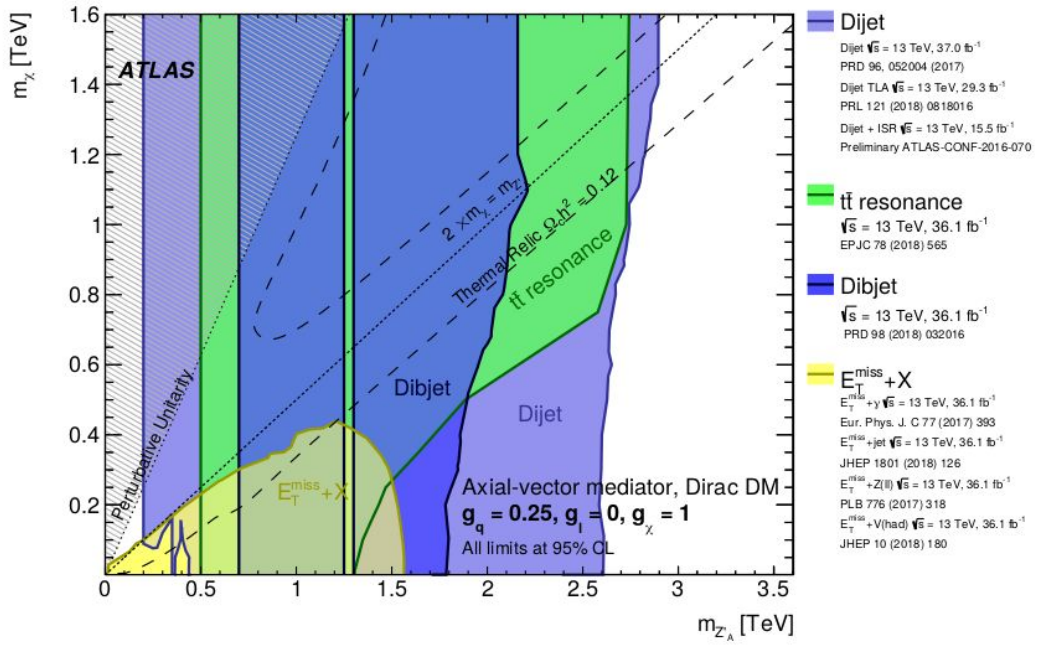

Figure 5.6: Regions in a (mediator-mass, DM-mass) plane excluded at 95% CL by visible and invisible searches, for leptophobic axial-vector mediator simplified model. Reproduced from [175].

spin independent direct detection.

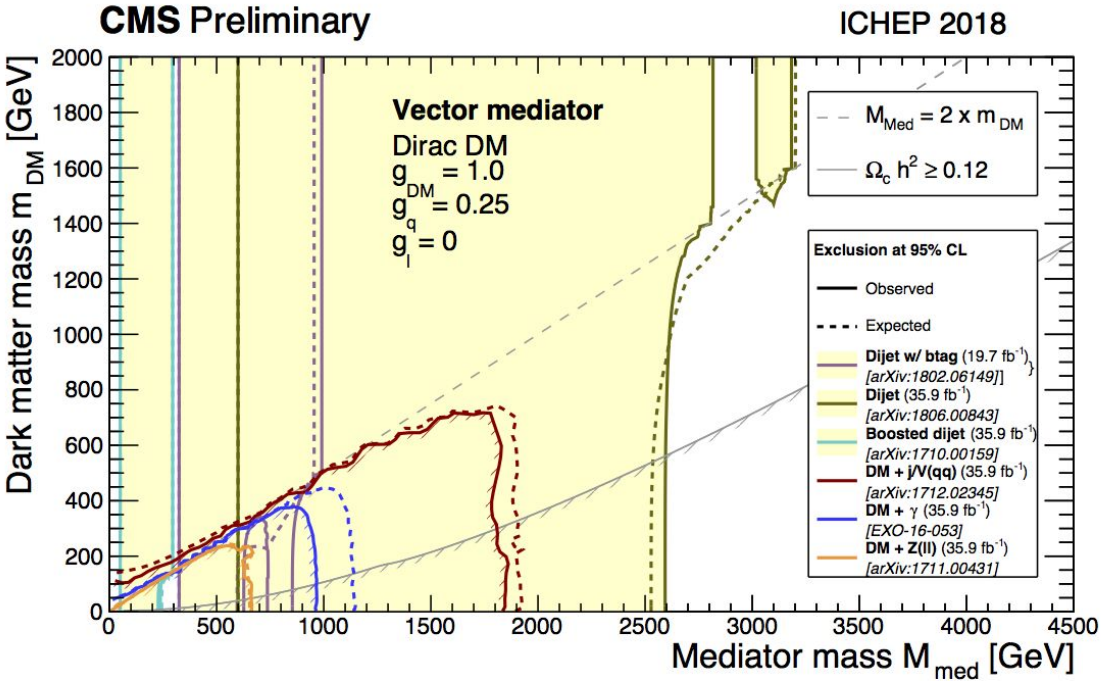

Figure 5.7: 95% CL observed and expected exclusion regions in $m_{\text{Med}}-m_{\text{DM}}$ plane for di-jet searches and different MET based DM searches from CMS in the leptophobic Vector model. The exclusions are computed for a universal quark coupling of $g_q = 0.25$ and for a DM coupling of $g_{\text{DM}} = 1.0$. Reproduced from [176].

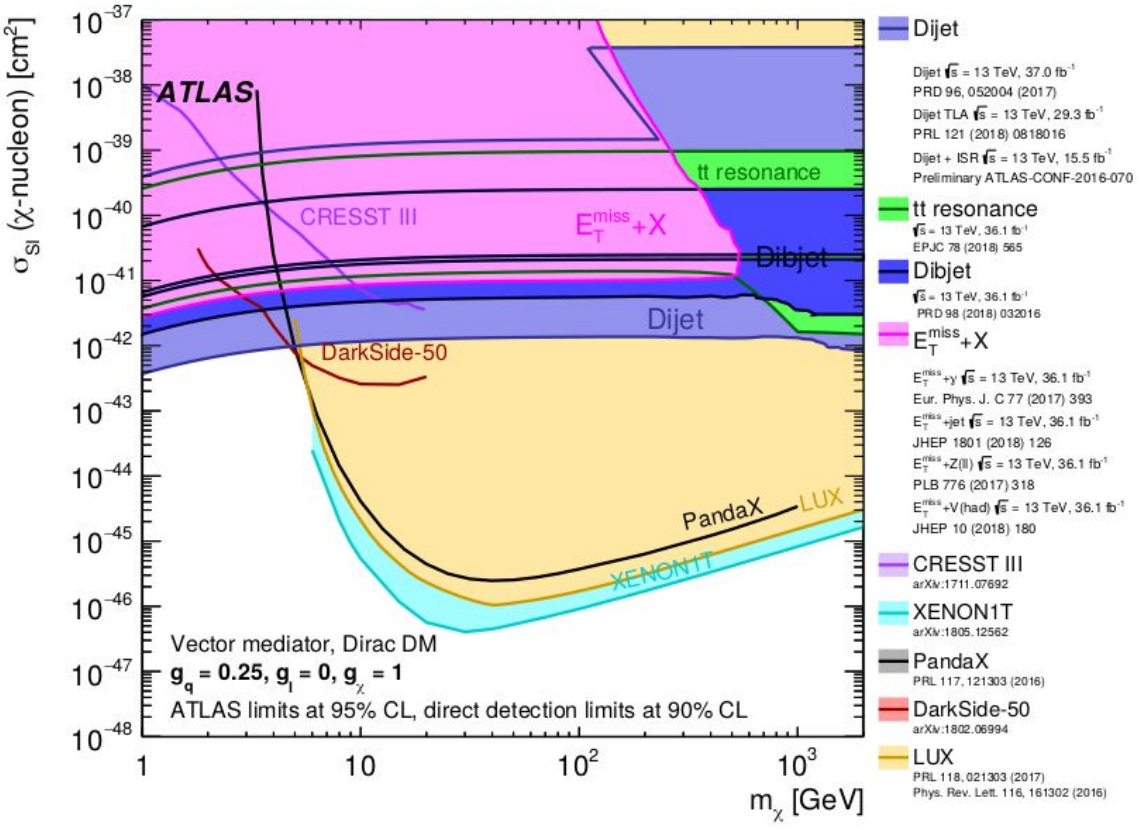

Figure 5.8: A comparison of direct detection SI bounds with the ATLAS bounds on the V/AV simplified model. Reproduced from [175].

5.4 Generic Dark Sectors

In the past 20 years, most of the theoretical and experimental effort has focused on minimal dark sectors. This was in part due to the popularity of the WIMP paradigm, which tied the relic abundance Ω_m to a single weakly interacting particle. However, following the strong direct detection bounds on WIMP DM, there is a resurgence of models involving richer physics in the dark sector. Indeed, given the rich physics observed in the SM, there is no a-priori reason for the dark sector not to have its own gauge symmetry (abelian or non-abelian), or

even a Higgs mechanism.

The consideration of more generic dark sectors could lead to early universe dynamics which is very different from that of a single, weakly interacting particle, and could have a major impact on the relic density. This goes back to the idea of number changing processes in the dark sector [177], and its modern incarnation as the SIMP [178–181] and ELDER [182] models. Two other popular scenarios are asymmetric DM [183–185], in which the relic density in the dark sector is set by a primordial matter-antimatter asymmetry (with or without a link to SM baryogenesis), and freeze-in DM [186], in which an initially empty dark sector is populated by SM decays. Additionally, bound state formation / confinement in the dark sector could have an impact on the relic density of dark matter, [187–196], as is demonstrated in this work.

Searches for generic dark sector physics often involves a mediator - a new particle that couples the dark sector to the SM. Typical mediators are a dark photon which mixes with the SM photon, dark scalar mixing with the SM Higgs, or a dark axion-like particle coupling to the SM. Dark matter coupled to a dark vector or scalar mediator can either annihilate in the early universe to the mediator or directly to the SM, depending on the DM/mediator mass ratio. The parameter space for dark photons is constrained by a combination of collider searches (both LHC and fixed target experiments), astrophysical bounds such as the 1987A supernova bound, and other bounds from 5th force experiments, CMB, late decays. The current bounds are depicted in Figure 5.9.

Finally, a generic dark sector with some self interaction could influence galactic dynamics [197] and even address small scale problems [198–200].

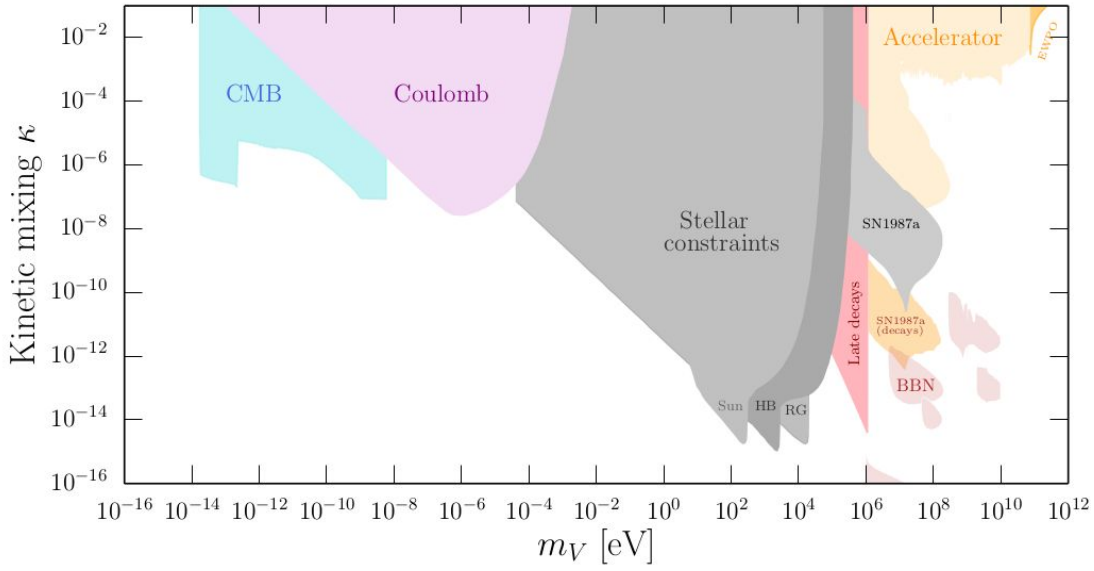

Figure 5.9: Collected constraints on a kinetically mixed vector with mass m_V and kinetic mixing parameter κ of the dark and visible photons. Reproduced from [163].

CHAPTER 6

DARK QUARKONIUM FORMATION IN THE EARLY UNIVERSE

BEYOND THE STANDARD MODEL: COMPOSITE HIGGS AND DARK MATTER

Ofri Telem, Ph.D.

Cornell University 2019

The relic abundance of heavy stable particles charged under a confining gauge group can be depleted by a second stage of annihilations near the deconfinement temperature. This proceeds via the formation of quarkonia-like states, in which the heavy pair subsequently annihilates. The size of the quarkonium formation cross section was the subject of some debate. We estimate this cross section in a simple toy model. The dominant process can be viewed as a rearrangement of the heavy and light quarks, leading to a geometric cross section of hadronic size. In contrast, processes in which only the heavy constituents are involved lead to mass-suppressed cross sections. These results apply to any scenario with bound states of sizes much larger than their inverse mass, such as U(1) models with charged particles of different masses, and can be used to construct ultra-heavy dark-matter models with masses above the naive unitarity bound. They are also relevant for the cosmology of any stable colored relic.

6.1 Introduction

Stable "colored" particles, charged under QCD or a hidden confining gauge group, have been proposed as dark matter (DM) candidates [187, 189, 192, 194, 196, 201–217], and are predicted in various extensions of the Standard Model [218–220]. Even in the simplest models, the cosmological history of colored relics is intriguing, and their present-day abundances have been the subject of some debate. The relic abundance of a heavy colored particle X is sensitive to the two inherent scales in the problem: its mass m_X, and the confinement scale Λ_D. If $m_X \gg \Lambda_D$, the freeze-out of X proceeds via standard perturbative annihilations at temperatures $T \sim m_X/30$. However, at temperatures $T \sim \Lambda_D$, long after the perturbative X–$\bar{X}$ annihilations have shut off, the X relic abundance may be further reduced by interactions of hadronized Xs, whose size is set by $1/\Lambda_D$.

The annihilation process at $T \lesssim \Lambda_D$ was described in a semiclassical approximation in Ref. [219]. At $T \sim \Lambda_D$, most of the Xs are in color-singlet heavy-light hadrons, which we label by H_X. An X-hadron H_X and an $\bar{X}$-hadron $\bar{H}_X$ experience a residual strong interaction whose effective range is $\sim 1/\Lambda_D$, much larger than the Compton wavelength $\sim 1/m_X$, but much smaller than the mean distance between X-hadrons at $T \sim \Lambda_D$. X–$\bar{X}$ annihilation then proceeds via the formation of X–$\bar{X}$ "quarkonia", which subsequently de-excite to the ground state. In the ground state, the X–$\bar{X}$ distance is of order the Compton wavelength, and the pair annihilates into light mesons, (dark) photons, or glueballs. In the following, we use parentheses to denote quarkonium-like states, and refer to the $(X\bar{X})$ states as quarkonia.

The cross section for quarkonia formation was argued in Ref. [219] to be

purely geometric. This certainly holds for the scattering cross section of two H_X hadrons; however, it is less clear that it holds for the quarkonium production cross section, which requires a significant modification of the trajectories of the heavy particles. One semiclassical argument for a mass-suppressed cross section was described in Ref. [220]. To form a bound state, the X and $\bar{X}$ must lose energy and angular momentum. Classically, one can estimate the cross section by modeling the energy loss as Larmor radiation. This is proportional to the acceleration-squared, which scales as Λ_D^4/m_X^2. At $T \sim \Lambda_D$, the Xs are very slow, with speed $v \sim \sqrt{\Lambda_D/m_X}$. Thus it takes a long time for the hadrons to cross a distance $1/\Lambda_D$; however, the total amount of radiation still scales as $m_X^{-3/2}$ and is suppressed by the large X mass.

Our goal in this work is to quantify the cross section for dark quarkonia formation. This is, of course, a strong-coupling problem, so we will employ two simple toy models in which the calculation is tractable. As we will see, the results can be readily interpreted to infer the behavior of the cross section in the case of interest.

We consider a dark SU(N) with two Dirac fermions X and q in the fundamental representation. We denote the SU(N) confinement scale by Λ_D, although much of our discussion applies to real QCD as well. X is heavy, with mass $m_X \gg \Lambda_D$, while q is light, with $m_q \lesssim \Lambda_D$. We denote the color-singlet heavy-light mesons by $H_X \equiv X\bar{q}$ and $\bar{H}_X \equiv \bar{X}q$. The X and $\bar{X}$, as well as their hadrons, are stable by virtue of a flavor symmetry.

We examine two prototypical contributions to quarkonia production in H_X–$\bar{H}_X$ collisions. The first is a radiation process, in which the "brown muck" is merely a spectator. To isolate the contribution of the heavy Xs, we invoke a

dark U(1), under which X is charged while q is neutral. The heavy fermions X and $\bar{X}$ emit radiation in order to bind, and the relevant process is

$$H_X + \bar{H}_X \to (X\bar{X}) + \varphi \qquad \text{[radiation by the } X\text{s]}. \tag{6.1}$$

Here φ is the dark photon. Since the photon is emitted by the heavy X, the cross section for this process can be calculated using non-relativistic QCD (NRQCD) with a simple potential modeling the SU(N) interaction. We use the Cornell potential, with a cutoff at a distance of order $1/\Lambda_D$ to simulate the screening by the brown muck. The resulting cross section is not geometric, but rather m_X-suppressed, in accordance with the simple semiclassical estimate above.

In the second process, the brown muck plays a key role in the interaction, leading to a geometric cross section for quarkonium formation. This happens, for example, when the radiation is emitted by the brown muck itself, which, as a result, exerts a force on the heavy X. While we cannot reliably calculate the cross section in this case, we can nonetheless capture the brown muck dynamics by considering the limit $m_q > \Lambda_D$, in which quarkonium formation can be thought of as a rearrangement of the heavy and light quarks,

$$H_X + \bar{H}_X \to (X\bar{X}) + (\bar{q}q) \qquad \text{[rearrangement]}. \tag{6.2}$$

The cross section for this process can be calculated in analogy with hydrogen-antihydrogen rearrangement into protonium and positronium. As we will see, for $m_q > \Lambda_D$, only the Coulombic states contribute. The result is a geometric cross section, which scales as the square of the Bohr radius $a_q = 1/(\bar{\alpha}_D m_q)$. Thus, quarkonium production is effective at low temperatures not because of confinement *per se*, but because of the large hierarchy between a_q (the size of H_X) and $1/m_X$ (the Compton wavelength). We expect this result to persist as m_q is dialed

back below Λ_D: the quarkonium cross section will continue to scale as the size of H_X, which, in this case, is $1/\Lambda_D^2$.

As we will see, the geometric cross section arises from summing the contributions of many large (i.e., $\sim a_q$-sized) X–$\bar{X}$ bound states, for which the process is exothermic. These states cannot be dissociated, and will de-excite to the ground state, in which the X and $\bar{X}$ annihilate. We will not discuss the cosmology of a specific model in detail, but merely sketch the essentials, following Ref. [219]. Prior to the formation of the H_X and $\bar{H}_X$ mesons, the X particles annihilate and freeze out in the early universe with the standard relic density

$$\Omega_X^{\text{ann}} h^2 \sim \frac{10^{-9}\,\text{GeV}^{-2}}{\left\langle \sigma_X^{\text{ann}} v \right\rangle} \sim \left(\frac{m_X}{10^4\,\text{GeV}}\right)^2 \frac{1}{\alpha_D^2(m_X)}\,. \tag{6.3}$$

Following the second stage of annihilations, the H_X relic abundance is given by

$$\Omega_{H_X}^f \sim \sqrt{\frac{\Lambda_D}{m_X}} \left(\frac{m_X}{30\ \text{TeV}}\right)^2\,. \tag{6.4}$$

Some fraction of Xs remain in hadrons containing multiple Xs, such as baryons. The various final abundances are model dependent and we do not explore them in detail here. Still, the late re-annihilations give a new mechanism for generating the relic abundance of dark matter, which is now a function of the two scales m_X and Λ_D. This opens up many interesting directions to explore. We discuss some of the implications for cosmology in Sec. 6.5. In particular, the models can lead to a long era of matter domination between m_X and Λ_D.

Note that the Xs can hadronize with light quarks q, and the potential between them is screened at large distances. The cosmology of these models is thus somewhat different from quirky models. The presence of light quarks is important for yet another reason: even if there are no photons in the theory, energy loss can proceed via the emission of light pions. In contrast, in models with

a pure SU(N) at low energies, the lightest particles are glueballs, whose mass is $\sim 7\Lambda_D$.

The formalism and the results in this work can be applied more broadly. For example, it is applicable to any confined heavy relic—be it all the dark matter or a component thereof, such as gluinos in split supersymmetry, messengers in gauge-mediated supersymmetry breaking, and so on.

This chapter is structured as follows. The toy model is described in Sec. 6.2. The rearrangement calculation and its results are presented in Sec. 6.3. Section 6.4 focuses on the radiation process from the Xs in which the brown muck is a spectator. In Sec. 6.5 we consider the dynamics of the X–$\bar{X}$ bound states generated by these processes and further implications for cosmology. In the Appendix, we collect some useful results on the properties of the Cornell and linear potentials and their wavefunctions, and discuss the details of the derivation of the cross section used in Sec. 6.4.

6.2 Description of the Toy Model

The minimal particle content in our models consists of two Dirac fermions, $(q, \bar{q})$ and $(X, \bar{X})$, in the fundamental representation of a dark SU(N). In Sec. 6.4, we will assume that X and $\bar{X}$ are also charged under a U(1) gauge symmetry. To describe the X–$\bar{X}$ interaction, we turn to models of quarkonium [221, 222]. The Cornell potential interpolates between the Coulombic QCD potential at small distances and the confining linear potential with string tension Λ_D at large distances:

$$V_{\text{Cornell}}(R) = -C\frac{\alpha_D}{R} + \Lambda_D^2 R\,, \tag{6.5}$$

where R is the distance between X and $\bar{X}$, $C = (C_1+C_2-C_{12})/2$, and C_i (C_{12}) are the quadratic Casimirs of the constituents (bound state). Since X is a fundamental of SU(N) and we require a color-singlet bound state, $C = C_1 = C_2 = (N^2-1)/(2N)$. The deep bound states of the system are then Coulombic, while the shallow states are controlled by the linear potential.

At large distances, the attractive potential is screened by the brown muck surrounding X and $\bar{X}$. In QCD, for example, this distance is roughly the inverse of the string tension $\approx$ 400 MeV (see, e.g., Refs. [223, 224]). In order to capture this screening, the potential is cut off at a distance R_c,[1]

$$V(R) = \begin{cases} -\bar{\alpha}_D \left(\frac{1}{R} - \frac{1}{R_c}\right) + \Lambda_D^2 (R - R_c) + V_0 & \text{for} \quad R < R_c \,, \\ V_0 & \text{for} \quad R \geq R_c \,, \end{cases} \tag{6.6}$$

where $\bar{\alpha}_D = C\alpha_D$, and V_0 is a constant.[2] The cutoff behavior will naturally emerge in the rearrangement calculation of Sec. 6.3, where we work in the calculable limit $m_q \gtrsim \Lambda_D$. For $m_q \gtrsim \Lambda_D$, the attractive potential is cut off at distances of order the Bohr radius of the heavy-light meson,[3]

$$a_q = \frac{1}{\bar{\alpha}_D m_q} \,. \tag{6.7}$$

Thus, for m_q sufficiently large, the problem reduces to a purely Coulombic potential, and we can calculate the cross section in analogy with hydrogen-antihydrogen rearrangement into protonium and positronium.

In Sec. 6.4 we will calculate quarkonia formation via radiation by the Xs. Here the linear part of the potential is important, and the cutoff R_c is introduced

[1] While this option is not pursued here, it may be interesting to use a temperature-dependent cutoff to qualitatively capture the screening effects of the quark-gluon plasma. These cause large X–$\bar{X}$ bound states to "dissolve" at finite temperatures [224–226].

[2] The choice of the constant V_0 is of course a matter of convenience, and we will in fact choose different constants in the rearrangement and radiation calculations.

[3] In this expression, $\bar{\alpha}_D$ should be evaluated at the energy scale of the inverse Bohr radius.

by hand. As we will describe, the choice of R_c will be motivated by a comparison with the masses of B and D mesons in the Standard Model.

We note that, in QCD, the string tension in the confined phase and the dimensional transmutation scale from the running of the QCD gauge coupling are approximately the same [141,224,227], whereas the deconfinement temperature is about a factor of two lower [228]. We will not be concerned with the lightest glueball state because its mass is a factor of about seven larger than the string tension [229].

6.3 The Rearrangement Process

At temperatures below Λ_D, the heavy Xs are mostly found in H_X ($X\bar{q}$) and $\bar{H}_X$ ($\bar{X}q$) mesons. These mesons can further deplete through H_X–$\bar{H}_X$ scattering into ($X\bar{X}$) quarkonia plus light hadrons. For $m_q < \Lambda_D$, the calculation of the cross section for this process requires the full machinery of perturbative NRQCD [230] and is extremely difficult; we will limit ourselves to the case $m_q \gtrsim \Lambda_D$. This puts us firmly in the non-relativistic limit, in which quarkonium production can be thought of as rearrangement of the four partons,

$$H_X + \bar{H}_X \to (X\bar{X}) + (q\bar{q}). \tag{6.8}$$

For $m_X \gg m_q$, the wavefunctions of the system can be calculated in the Born-Oppenheimer approximation, as in hydrogen-antihydrogen rearrangement into protonium and positronium [231–233]. We will closely follow this calculation, applying it to the near-threshold energies of interest.

If the semiclassical arguments in Ref. [219] are correct, the cross section is

expected to be geometric when the temperature is comparable to the binding energy of H_X, with no m_X suppression. We verify this in the following calculation.

6.3.1 Setup

As discussed above, for m_q sufficiently larger than Λ_D, only the Coulombic $(X\bar{X})$ states contribute. We will later comment on the validity of this approach as m_q is taken below Λ_D.

The full interacting Hamiltonian of our system is written as the sum

$$\mathcal{H}_{\text{tot}} = \mathcal{H}_{\text{free}} + \mathcal{H}_{\text{int}}\,, \tag{6.9}$$

where

$$\begin{aligned}
\mathcal{H}_{\text{free}} &= -\frac{1}{m_X}\nabla_R^2 - \frac{1}{2m_q}\nabla_{r_q}^2 - \frac{1}{2m_q}\nabla_{r_{\bar{q}}}^2\,, \\
\mathcal{H}_{\text{int}} &= V_{X\bar{X}}(R) + V_{q\bar{q}}\left(|\boldsymbol{r}_q - \boldsymbol{r}_{\bar{q}}|\right) + \mathcal{H}_{\text{tr}}\,, \\
\mathcal{H}_{\text{tr}} &= V_{q\bar{X}}\left(|\boldsymbol{r}_q + \boldsymbol{R}/2|\right) + V_{\bar{q}X}\left(|\boldsymbol{r}_{\bar{q}} - \boldsymbol{R}/2|\right) - V_{\bar{q}\bar{X}}\left(|\boldsymbol{r}_{\bar{q}} + \boldsymbol{R}/2|\right) - V_{qX}\left(|\boldsymbol{r}_q - \boldsymbol{R}/2|\right)\,.
\end{aligned} \tag{6.10}$$

Here $\boldsymbol{R}$ is the vector from $\bar{X}$ to X and $\boldsymbol{r}_q$, $\boldsymbol{r}_{\bar{q}}$ are the positions of q, $\bar{q}$ relative to the X–$\bar{X}$ center-of-mass (CM), respectively, as shown in Fig. 6.1. The potentials $V_{q\bar{X}}$, $V_{\bar{q}X}$, V_{qX}, $V_{\bar{q}\bar{X}}$, $V_{q\bar{q}}$, and $V_{X\bar{X}}$ are the usual Coulomb potentials (with the relevant sign for same/opposite color quarks taken into account in Eq. (6.10)):

$$V(r) = -\frac{\bar{\alpha}_D}{r}\,. \tag{6.11}$$

Since we assume that X–$\bar{X}$ are in a color-singlet configuration, this factor is the same for the six potentials.

The calculation of the rearrangement cross section involves a subtlety well known to nuclear physicists: the asymptotic in and out states are not eigenstates of the same free Hamiltonian, but rather eigenstates of two different interacting Hamiltonians. This is different from conventional non-relativistic scattering where $\lim_{t\to\pm\infty} \mathcal{H}_{\text{tot}} = \mathcal{H}_{\text{free}}$. In our case, the infinite past Hamiltonian is

$$\mathcal{H}_{\text{in}} \equiv \lim_{t\to-\infty} \mathcal{H}_{\text{tot}} = \mathcal{H}_{\text{free}} + V_{q\bar{X}}\left(|\boldsymbol{r}_q + \boldsymbol{R}/2|\right) + V_{\bar{q}X}\left(|\boldsymbol{r}_{\bar{q}} - \boldsymbol{R}/2|\right) , \tag{6.12}$$

while the infinite future Hamiltonian is

$$\mathcal{H}_{\text{out}} \equiv \lim_{t\to\infty} \mathcal{H}_{\text{tot}} = \mathcal{H}_{\text{free}} + V_{X\bar{X}}\left(R\right) + V_{q\bar{q}}\left(|\boldsymbol{r}_q - \boldsymbol{r}_{\bar{q}}|\right) . \tag{6.13}$$

The scattering cross section is then calculated in the multi-channel formalism. By solving the Lippmann-Schwinger equation for multi-channel scattering (see, e.g., Ref. [234]), we get the simple formula for the cross section:

$$\frac{d\sigma}{d\Omega} = (2\pi)^2 \frac{k_f}{k_i} m_X m_q |\mathcal{M}|^2 , \tag{6.14}$$

where k_f and k_i are the momenta of the final and initial states in the CM frame (see below) and the transition matrix element is

$$\mathcal{M} = 2\pi \left\langle \Psi_f(\boldsymbol{R}, \boldsymbol{r}_q, \boldsymbol{r}_{\bar{q}}) \,\middle|\, \mathcal{H}_{\text{tr}} \,\middle|\, \Psi_i(\boldsymbol{R}, \boldsymbol{r}_q, \boldsymbol{r}_{\bar{q}}) \right\rangle , \tag{6.15}$$

where Ψ_f, Ψ_i are the final- and initial-state wavefunctions and $\mathcal{H}_{\text{tr}} = \mathcal{H}_{\text{tot}} - \mathcal{H}_{\text{out}}$, as can be seen from Eqs. (6.10) and (6.13). Note that in this representation of the cross section, the outgoing states Ψ_f are eigenstates of $\mathcal{H}_{\text{out}}$, while the incoming states Ψ_i are eigenstates of the *full* Hamiltonian $\mathcal{H}_{\text{tot}}$. Below, we discuss these states in more detail.

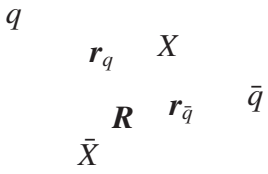

Figure 6.1: Coordinate system used in the calculation of the rearrangement process.

6.3.2 The incoming and outgoing wavefunctions

We wish to express our incoming and outgoing wavefunctions in the factorized form

$$\Psi(\boldsymbol{R}, \boldsymbol{r}_q, \boldsymbol{r}_{\bar{q}}) = \psi^{X\bar{X}}(\boldsymbol{R})\, \psi^{q\bar{q}}(R; \boldsymbol{r}_q, \boldsymbol{r}_{\bar{q}})\,. \tag{6.16}$$

In the final state this factorization is exact, since the outgoing X-onium and q-onium are asymptotically non-interacting. In other words:

$$\mathcal{H}_{\text{out}} = \mathcal{H}_{X\bar{X}} + \mathcal{H}_{q\bar{q}}\,, \tag{6.17}$$

with

$$\begin{aligned} \mathcal{H}_{X\bar{X}} &= -\frac{1}{m_X}\nabla_R^2 + V_{X\bar{X}}(R)\,, \\ \mathcal{H}_{q\bar{q}} &= -\frac{1}{2m_q}\nabla_{r_q}^2 - \frac{1}{2m_q}\nabla_{r_{\bar{q}}}^2 + V_{q\bar{q}}\left(|\boldsymbol{r}_q - \boldsymbol{r}_{\bar{q}}|\right)\,. \end{aligned} \tag{6.18}$$

The final state therefore trivially factorizes as the product of a plane wave for the outgoing $(q\bar{q})$ and the Coulomb bound states $\psi^{X\bar{X}}_{nlm}(R)$ (an eigenstate of $\mathcal{H}_{X\bar{X}}$) and $\psi^{q\bar{q}}_{100}(\boldsymbol{r}_q, \boldsymbol{r}_{\bar{q}})$ (an eigenstate of $\mathcal{H}_{q\bar{q}}$). For concreteness, we assume that the final-state q-onium is in its ground state and the $(X\bar{X})$ is static.

In contrast with the outgoing state, the incoming state is an eigenstate of the full Hamiltonian $\mathcal{H}_{\text{tot}}$, so we naively do not expect it to factorize as in Eq. (6.16). However, we can use the Born-Oppenheimer approximation to express it in this

factorized form,

$$\Psi_i(\boldsymbol{R}, \boldsymbol{r}_q, \boldsymbol{r}_{\bar{q}}) = \psi_i^{X\bar{X}}(\boldsymbol{R})\, \psi_i^{q\bar{q}}(R; \boldsymbol{r}_q, \boldsymbol{r}_{\bar{q}})\,. \tag{6.19}$$

Since we are in the limit $m_X \gg m_q$, this is a very good approximation: at any given X–$\bar{X}$ distance R, q and $\bar{q}$ will quickly adjust their configuration, and their wavefunction $\psi_i^{q\bar{q}}$ can therefore be calculated by integrating out X and $\bar{X}$ and treating them as sources for the light quarks. This gives the energy and wavefunction of the light quarks for a fixed separation R between the heavy Xs as solutions to the eigenvalue problem

$$[\mathcal{H}_{\text{tot}} - \mathcal{H}_{X\bar{X}}]\, \psi_i^{q\bar{q}} = V_{\text{BO}}(\boldsymbol{R})\, \psi_i^{q\bar{q}}\,. \tag{6.20}$$

Substituting this back into the full Schrödinger equation and neglecting derivatives of $\psi_i^{q\bar{q}}$ with respect to the X–$\bar{X}$ coordinates, one obtains the equation for the X–$\bar{X}$ wavefunction,

$$\left[-\frac{1}{2m_X}\nabla_R^2 + V_{X\bar{X}}(R) + V_{\text{BO}}(\boldsymbol{R})\right]\psi_i^{X\bar{X}} = E_i\, \psi_i^{X\bar{X}}\,. \tag{6.21}$$

The effective potential for the X–$\bar{X}$ system is then

$$V_{\text{in}}(\boldsymbol{R}) = V_{X\bar{X}}(R) + V_{\text{BO}}(\boldsymbol{R}) \tag{6.22}$$

with

$$V_{\text{BO}}(\boldsymbol{R}) = \left\langle \psi_i^{q\bar{q}} \,\middle|\, \mathcal{H}_{\text{tot}} - \mathcal{H}_{X\bar{X}} \,\middle|\, \psi_i^{q\bar{q}} \right\rangle\,. \tag{6.23}$$

$V_{\text{BO}}(\boldsymbol{R})$ should interpolate between twice the binding energy of H_X, $2E_b \equiv \bar{\alpha}_D^2 m_q$, at large R, and the q-onium binding energy, $-\bar{\alpha}_D^2 m_q/4$, at small R. Unlike in molecules, for which the Coulombic repulsion of the nuclei must be overcome, here the two heavy particles attract each other, so we do not expect a significant potential barrier. These naive expectations are borne out in the calculation of Ref. [235]. Since $V_{\text{BO}}(\boldsymbol{R})$ does not depend on the initial energy of the system or

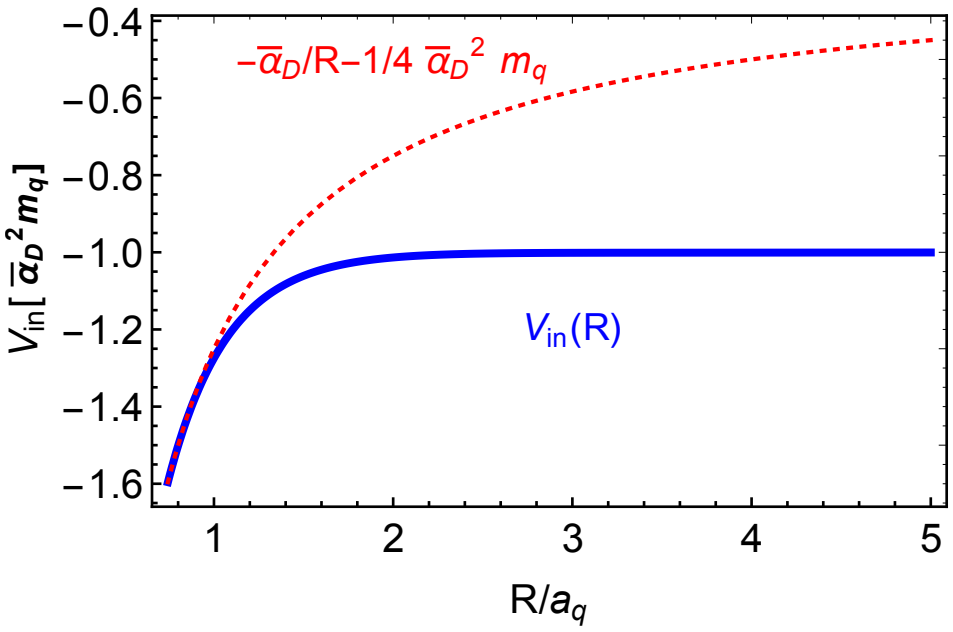

Figure 6.2: The incoming effective potential $V_{\rm in}$ in units of $\bar{\alpha}_D^2 m_q$ for the X–$\bar{X}$ system in the Born-Oppenheimer approximation (blue solid), as a function of X–$\bar{X}$ separation in units of the Bohr radius $a_q = 1/(\bar{\alpha}_D m_q)$. Also shown is the Coulomb potential for the $(X\bar{X})$ quarkonium (red dashed).

on the mass m_X, we can extract $V_{\rm BO}(\boldsymbol{R})$ from Ref. [235]. We plot $V_{\rm in}$ in Fig. 6.2: as expected, the effects of the light quarks captured in $V_{\rm BO}(\boldsymbol{R})$ set in for R of order a_q. Their main effect is to screen the X–$\bar{X}$ interaction at large R; in practice, this happens for $R \sim 2a_q$.

Since $V_{\rm in}(\boldsymbol{R})$ approaches a constant at large R, the X–$\bar{X}$ wavefunction at large distances ($R \geq 4a_q$) is the standard free-particle solution,

$$\Psi_i(\boldsymbol{R}, \boldsymbol{r}_q, \boldsymbol{r}_{\bar{q}}) \xrightarrow{R\geq 4a_q} \sum_l i^l \sqrt{2l+1}\, e^{i\delta_l} \left[\cos\delta_l\, j_l(k_i R) - \sin\delta_l\, n_l(k_i R)\right] Y_{l0}(\theta_R) \psi_i^{q\bar{q}}(\boldsymbol{R}; \boldsymbol{r}_q, \boldsymbol{r}_{\bar{q}})\,. \tag{6.24}$$

The wavefunctions for $R \leq 4a_q$ are found numerically, while their normalization is fixed by matching to Eq. (6.24) at $R = 4a_q$. Some examples for the incoming and outgoing wavefunctions are given in Fig. 6.3.

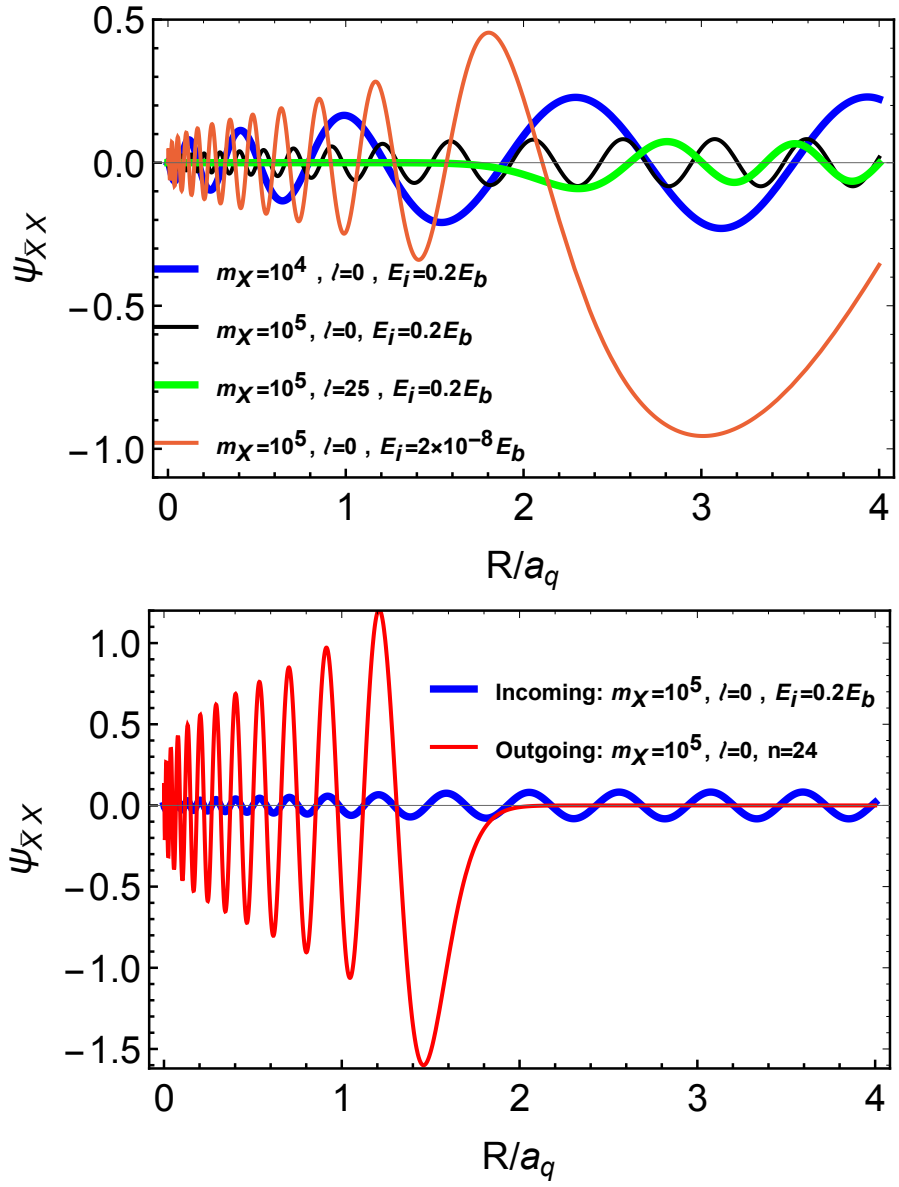

Figure 6.3: Examples of incoming wavefunctions with various m_X, E_i, l (top) and a comparison of an incoming and outgoing wavefunction (bottom). m_X is given in units of the inverse Bohr radius $\bar{\alpha}_D m_q$ and $E_b = \frac{1}{2}\bar{\alpha}_D^2 m_q$ is the H_X binding energy.

6.3.3 The matrix element for rearrangement

Using the factorized incoming and outgoing wavefunctions, the transition matrix element Eq. (6.15) can be written in position space as

$$\mathcal{M} = \int d^3\boldsymbol{R}\, \psi_f^{X\bar{X}*}(\boldsymbol{R})\, \psi_i^{X\bar{X}}(\boldsymbol{R})\, T(\boldsymbol{R})\,, \tag{6.25}$$

where

$$T(\boldsymbol{R}) = \int d^3\boldsymbol{r}_q \, d^3\boldsymbol{r}_{\bar{q}} \; \psi_f^{q\bar{q}*}(\boldsymbol{r}_q, \boldsymbol{r}_{\bar{q}}) \, \mathcal{H}_{\rm tr} \, \psi_i^{q\bar{q}}(R; \boldsymbol{r}_q, \boldsymbol{r}_{\bar{q}}) \, . \tag{6.26}$$

We will assume that the angular part of $T(\boldsymbol{R})$ is constant. This is justified when the $(q\bar{q})$ is in the ground state, and in the short-distance approximation for the plane wave of the $(q\bar{q})$ relative to the $(X\bar{X})$. The second condition is broken when k_f^2 becomes large enough, where we expect an $O(1)$ correction. We neglect this correction in this work, since we are mostly interested in the parametric behavior of this process.

It is easy to see that $T(R)$ is appreciable only for R of order a_q. For $R \gg a_q$, this can be seen by substituting $\mathcal{H}_{\rm tr} = V_{\rm BO}(\boldsymbol{R}) - \mathcal{H}_{q\bar{q}}$ in Eq. (6.26). $\psi_f^{q\bar{q}}$ is an eigenfunction of $\mathcal{H}_{q\bar{q}}$, so one is left with the overlap integral of $\psi_f^{q\bar{q}}$ and the asymptotic $\psi_i^{q\bar{q}}$ at large R. These solve the same Hamiltonian with different eigenvalues: the former is a bound state and the latter is a continuum state. For small R, the initial- and final-state wavefunctions in the integrand do overlap, but $\mathcal{H}_{\rm tr}$ tends to zero.

The full calculation of $T(R)$ is complicated. In fact, the Born-Oppenheimer approximation breaks down for $R \lesssim 0.74 a_q$, where the q and $\bar{q}$ are no longer bound to their respective X (see, e.g., Ref. [233]). Still, we can use this approximation to get a rough estimate of the cross section. In particular, $T(R)$ is independent of the mass m_X in the Born-Oppenheimer approximation, so we can extract $T(R)$ from Ref. [233].[1] The result in the relevant range ($R \sim a_q$) can be

[1] The m_X dependence will enter through higher-order corrections in the effective theory, and will be suppressed by some fractional power of m_X. Here we are only interested in the leading result.

parametrized as

$$T(R) = \begin{cases} \beta\left[E_f + \frac{1}{4}\bar{\alpha}_D^2 m_q - V_{\rm BO}(R)\right] & \text{for} \quad R > 0.74 a_q\,, \\ 0 & \text{for} \quad R \leq 0.74 a_q\,, \end{cases} \tag{6.27}$$

where E_f is the kinetic energy in the final state and β is an $O(1)$ factor determined by matching to the hydrogen-antihydrogen results. Evidently, $T(R)$ depends on the binding energy of the $(X\bar{X})$ quarkonium, $E_b^{X\bar{X}}$, since $E_f = E_i + E_b^{X\bar{X}} - \frac{3}{4}\bar{\alpha}_D^2 m_q$.

6.3.4 Rearrangement results

We calculate the cross section of Eq. (6.14) for different masses m_X and incoming kinetic energies E_i, keeping a_q fixed. In the approximation we use (see Sec. 6.3.3), the angular part of the overlap integral is translated into a selection rule $l_{X\bar{X}} = l_i \equiv l$. The breakdown of the cross section into partial waves—or $(X\bar{X})$ angular momenta—is given in Fig. 6.4 for high incoming kinetic energy $E_i = 0.6 E_b$ and $\bar{\alpha}_D = 1/137$. We see that it vanishes above some maximal l, which corresponds to the classical angular momentum

$$l_{\rm max} \sim k_i a_q = \sqrt{E_i m_X}\, a_q \sim \sqrt{E_i m_X}/m_q\,. \tag{6.28}$$

It is also interesting to examine the branching fraction σ_{nl}/σ_l for some initial partial wave to form an $(X\bar{X})$ quarkonium of definite binding energy. In Fig. 6.5 (left panel), we show this branching fraction for $l = 0, 14$, as a function of the final kinetic energy for two values of the initial kinetic energy $E_i/E_b = 0.6, 0.06$.

We see that quarkonium formation by rearrangement is an exothermic process: the kinetic energy in the final state does not vanish even when the initial

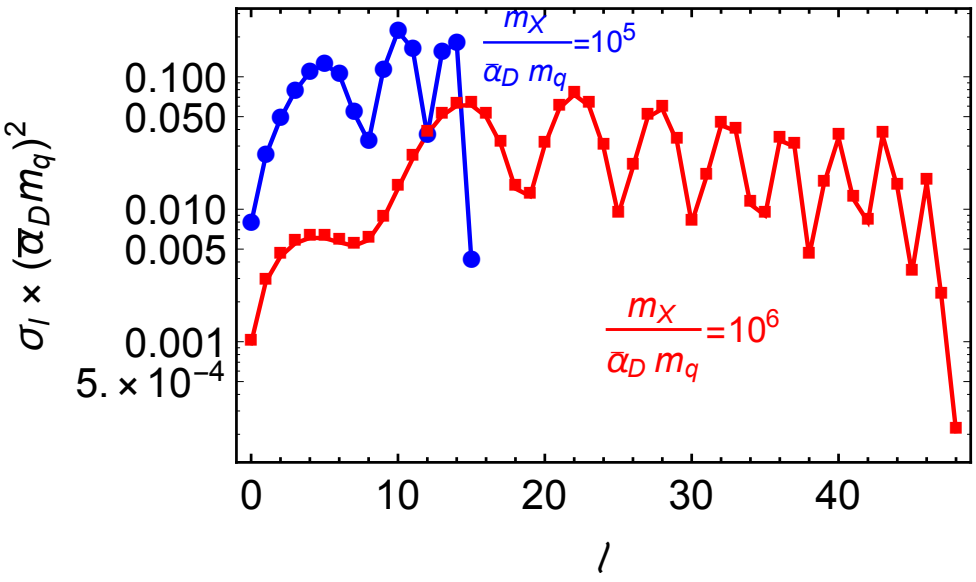

Figure 6.4: The rearrangement cross section for each partial wave l, for two different values of m_X, with $E_i = 0.6E_b$. All partial waves in the incoming state contribute up to a maximal $l \equiv l_{\max} \sim k_i a_q$.

momentum is taken to zero. Therefore the inverse process shuts off at low energies $\lesssim E_b$. Furthermore, only quarkonia with binding energies around E_b are produced at $T \sim E_b$. The cross sections drop to zero for large final-state energies corresponding to $(X\bar{X})$ binding energies above E_b. Thus, deep Coulombic bound states with binding energies $E_b^{X\bar{X}} \sim \bar{\alpha}_D^2\, m_X$ are not formed in the rearrangement process. Correspondingly, the bound states produced are large, with size $\sim a_q$. This behavior is clearly exhibited in Fig. 6.5 (right panel), where we show the cross section as a function of the mean quarkonium radius $R_{X\bar{X}}$.

The total cross section for an initial energy of order the H_X binding energy is plotted in Fig. 6.6 (blue line) as a function of m_X. Indeed, the cross section is geometric, $\sigma \sim a_q^2$, and is independent of m_X to a very good approximation. It is interesting to compare the partial-wave contributions with the unitarity bound,

$$\sigma_l \leq (2l+1)\,\frac{4\pi}{k_i^2}\,. \tag{6.29}$$

We therefore also plot in this figure several individual partial-wave contributions normalized by $2l+1$ (green lines), compared to $4\pi/k_i^2$ (red dashed line). Clearly, for initial-state energies close to the binding energy of H_X, the cross section for each partial wave lies close to the unitarity bound. Summing over all the partial waves up to $l_{\max}$,

$$\sigma = \sum_{l=1}^{l_{\max}} \sigma_l \sim \frac{4\pi}{k_i^2} \sum_{l=1}^{l_{\max}} (2l+1) \sim \frac{4\pi}{k_i^2} l_{\max}^2 \sim 4\pi a_q^2 \,. \tag{6.30}$$

Thus the total cross section is geometric, and scales with the area of the H_X bound state. In the low-temperature limit, we have checked that only s-wave processes are non-vanishing and the cross section scales as

$$\sigma \sim \frac{1}{k_i} a_q \,, \tag{6.31}$$

as demonstrated in Refs. [231, 233].

The above results apply to pure U(1) models. In the context of an SU(N), we have explicitly seen that for m_q above Λ_D, the light quarks truncate the X–$\bar{X}$ attraction for $R \gtrsim a_q$ via $V_{\rm BO}$, long before the linear potential sets in. This justifies neglecting the linear potential in the rearrangement calculation.

We can now turn to the limit of interest, m_q below Λ_D. As we have seen above, the cross section scales with the size of the H_X bound state, $a_q \gg 1/m_X$, thanks to the large number of partial waves contributing. This behavior is not special to the purely Coulombic case. In fact, the Coulombic contribution gives a conservative estimate of the cross section generated by the Cornell potential. Thus we expect a geometric cross section for m_q below Λ_D, with the Bohr radius a_q replaced by $1/\Lambda_D$.

The X–$\bar{X}$ bound states produced via rearrangement at $T \sim E_b$ are of size $\sim a_q$, much larger than the Compton wavelength of X. However, since the process

is exothermic, these X–$\bar{X}$ bound states cannot be dissociated at $T \lesssim E_b$. In the case at hand, since there are light pions (or mesons) in the theory, nothing impedes the relaxation of these states to the ground state, in which the X–$\bar{X}$ pair annihilates.

6.4 The Radiation Process: Spectator Brown Muck

In the rearrangement process described above, the brown muck plays a central role. It is instructive to contrast this with a process in which the brown muck is merely a spectator. As we will see, in this case, the cross section scales with m_X.

To isolate the dynamics of the heavy quarks, we take X to be charged under a dark U(1), while the light quarks are neutral. The relevant bound states are large, of size $\sim 1/\Lambda_D$, and are described by the linear part of the Cornell potential. To calculate $(X\bar{X})$ quarkonium production for $T \lesssim \Lambda_D$, we can therefore neglect the Coulombic part of the potential. This is also consistent with previous studies showing that, for pure U(1) models with no light charged particles, $(X\bar{X})$ bound-state formation gives only mild modifications of the X relic abundance [188,190]. For bound-state formation to deplete the X abundance by orders of magnitude, a new scale is required. In the radiation process considered here, the new scale is Λ_D.

The radiative quarkonium production process is then

$$H_X + \bar{H}_X \to (X\bar{X}) + \varphi\,, \tag{6.32}$$

where φ is a (dark) photon that couples only to X; however, our results below apply more generally to other light particles which can be emitted by X. Unlike

in the previous section, here the light quarks q are relativistic.

We will follow the field-theoretic formalism for computing bound-state formation cross sections with long-range interactions detailed in Ref. [191]. Alternatively, these results can be obtained using the standard non-relativistic QM approach for calculating transition amplitudes, treating the photon as a classical field [193, 236].

The first step is to derive the spectrum and two-particle wavefunctions that describe the bound and scattering states of the X–$\bar{X}$ system. While the light quarks do not actively participate in the radiation process, they screen the heavy Xs at large distances. This is captured by the cutoff R_c in the potential of Eq. (6.6), and leads to a continuum of H_X–$\bar{H}_X$ states with energies above the open H_X–$\bar{H}_X$-production threshold. Roughly speaking, the hadron mass is given by the sum of the heavy constituent masses, with each light quark or gluon contributing about Λ_D to the mass. More precisely,

$$m_{H_X} = m_X + \kappa_{\Lambda_D}\Lambda_D + O(\Lambda_D^2/m_X^2)\,, \tag{6.33}$$

where κ_{Λ_D} is an $O(1)$ constant [237]. The spectrum of bottom and charm mesons in QCD suggests $\kappa_{\Lambda_D}\Lambda_D \sim 600$ MeV, with $\Lambda_D \sim 400$ MeV, so in the following, we set $\kappa_{\Lambda_D} = 1.5$. To estimate the cutoff R_c, we use the fact that the maximal H_X binding energy, $E_b^{\max}$, coincides with the onset of the continuum,

$$2m_X + E_b^{\max} = 2m_{H_X}\,. \tag{6.34}$$

Since the maximal bound state energy of the linear potential is

$$E_b^{\max} = \Lambda_D^2 R_c + \frac{l(l+1)}{m_X R_c^2} \sim \Lambda_D^2 R_c\,, \tag{6.35}$$

we set the cutoff to

$$R_c = \frac{2\kappa_{\Lambda_D}}{\Lambda_D} = \frac{3}{\Lambda_D}\,. \tag{6.36}$$

In summary, the potential we consider is

$$V(R) = \begin{cases} \Lambda_D^2 (R - R_c) & \text{for} \quad R < R_c \,, \\ 0 & \text{for} \quad R \geq R_c \,, \end{cases} \tag{6.37}$$

with R_c given by Eq. (6.36) and V_0 of Eq. (6.6) chosen as zero for convenience. Defining

$$R_0 \equiv \left(\frac{\Lambda_D}{m_X}\right)^{1/3} \frac{1}{\Lambda_D} \,, \qquad E_0 \equiv \left(\frac{\Lambda_D}{m_X}\right)^{1/3} \Lambda_D \,, \tag{6.38}$$

which are the characteristic splittings in energy and size between successive states, the radial part of the wavefunction, χ_{ln}, solves

$$-\chi''_{ln}(x) + V^l_{\rm eff}(x)\chi_{ln}(x) = \epsilon_{ln}\chi_{ln}(x) \,, \tag{6.39}$$

where $x = R/R_0$, $\epsilon_{ln} = E_{ln}/E_0$, and

$$V^l_{\rm eff}(x) = \frac{l(l+1)}{x^2} + x - x_c \tag{6.40}$$

with $x_c = R_c/R_0$.

Using the semiclassical approximation, we can estimate the maximal angular momentum $l_{\rm max}$ of the bound states and the energy $\epsilon_{\rm min}$ of the lowest bound state with a given l. The lowest energy bound state for each l classically corresponds to a minimum of the effective potential; the position $x^l_{\rm min}$ and the energy $V^l_{\rm eff}(x^l_{\rm min})$ of the minimum must satisfy $x^l_{\rm min} < x_c$ and $V^l_{\rm eff}(x^l_{\rm min}) < 0$, which result in

$$l_{\rm max} \simeq \sqrt{\frac{4x_c^3}{27}} \,, \qquad \epsilon_{\rm min} \simeq 3\left(\frac{l}{2}\right)^{2/3} - x_c \,. \tag{6.41}$$

In Appendix 6.A.1, we collect some results for the effective potential and radial wavefunctions for various choices of the parameters.

6.4.1 Radiation results

The cross section for $H_X + \bar{H}_X \to (X\bar{X})_{lmn} + \varphi$ in the CM frame of the initial state is given by

$$v_{\rm rel}\frac{d\sigma_{\boldsymbol{k}\to lmn}}{d\Omega} = \frac{|\boldsymbol{P}_\varphi|}{128\pi^2 m_X^3}\,|\mathcal{M}_{\boldsymbol{k}\to lmn}|^2\,, \tag{6.42}$$

where $\boldsymbol{P}_\varphi$ is the three-momentum of the radiated light state and, assuming that φ is massless,

$$|\boldsymbol{P}_\varphi| = E_k - E_{ln}\,, \tag{6.43}$$

where E_k is the kinetic energy of the initial state. We calculate this cross section in Appendix 6.A. It is useful to write the cross section in terms of dimensionless quantities as

$$v_{\rm rel}\,\sigma_{k\hat{z}\to ln} = \sum_{m=-l}^{l} v_{\rm rel}\,\sigma_{k\hat{z}\to lmn} = \frac{2e_X^2}{m_X^2}\left(\frac{\Lambda_D}{m_X}\right)^{2/3} J_{k,ln}\,, \tag{6.44}$$

where e_X is the U(1) charge of X, $\epsilon_k = E_k/E_0$,

$$J_{k,ln} = (\epsilon_k - \epsilon_{ln})^3\left[(l+1)\left|I_{k,l+1\to ln}\right|^2 + l\left|I_{k,l-1\to ln}\right|^2\right], \tag{6.45}$$

and I is the radial wavefunction overlap integral

$$I_{k,l\pm1\to ln} = \int dx\, x\, \chi^*_{ln}(x)\,\chi_{k,l\pm1}(x)\,. \tag{6.46}$$

We plot $J_{k,ln}$ for several values of l in Fig. 6.7, fixing $m_X/\Lambda_D = 125$ and the initial kinetic energy $E_k/\Lambda_D = 0.05$. As expected, the large, shallow bound states give the largest contributions.

The total thermally-averaged cross section $\langle v_{\rm rel}\sigma\rangle$ (see Appendix 6.A.3) is shown as a function of the temperature in Fig. 6.8 (left panel) for several choices of m_X. We also show $\langle\sigma\rangle$ for the same parameters (right panel). The cross section is clearly dependent on m_X, and decreases as X becomes heavier. In fact, for $T \gtrsim 0.1\Lambda_D$, the scaling is well described by $\langle v_{\rm rel}\sigma\rangle \propto m_X^{-2}$ and $\langle\sigma\rangle \propto (m_X^3\Lambda_D)^{-1/2}$,

which agrees with the semiclassical estimate in Sec. 6.1. Thus, for the high mass region of interest, $m_X \gg \Lambda_D$, this contribution is negligible compared to processes mediated by the brown muck, such as the rearrangement process. We expect this qualitative behavior to persist regardless of the spin of the radiated particles.

6.5 Implications for Cosmology

We have found that, at temperatures below the confinement scale Λ_D, $(X\bar{X})$ bound states are formed with a geometric cross section with no m_X suppression. These bound states are of size $\sim 1/\Lambda_D$, but since the process is exothermic, they cannot be dissociated, and eventually de-excite to the ground state, in which the X–$\bar{X}$ pair annihilates. The rate for this de-excitation process depends mainly on the light degrees of freedom. For the large $(X\bar{X})$ bound states produced, the level splittings are of order $(\Lambda_D/m_X)^{1/3}\Lambda_D$, so we need massless photons or light pions in order to have allowed transitions (as in the models we considered here). In the case where the DM is charged under real QCD, the rate should be sizable, so we expect any $(X\bar{X})$ bound states to quickly decay to light particles.[1]

As a result, the abundance of H_X hadrons is depleted by this second stage of annihilations, down to [219]

$$\Omega^f_{H_X} \sim \sqrt{\frac{\Lambda_D}{m_X}}\left(\frac{m_X}{30\ \text{TeV}}\right)^2 , \tag{6.47}$$

which can be much smaller than the relic density from perturbative X–$\bar{X}$ annihilations earlier in the thermal history.

[1] In models with no light degrees of freedom, as in the case of an adjoint X with no light quarks [205], the lightest degrees of freedom are glueballs of mass $\sim 7\Lambda_D$, and this rate is suppressed by powers of $\bar{\alpha}_D^J$.

There are, however, various different hadronic states (in addition to H_X) in which X can survive [201]. These include other types of single-X hadrons such as baryonic Xq^{N-1} hadrons, double-X states such as baryonic XXq^{N-2}, and up to purely heavy baryons X^N. Thus, in general, our simple toy model can produce multi-component DM with different masses and relic abundances.

We leave a detailed investigation of the parameter space of the models for future study, but note a few qualitative features.[1] The cross section for producing double-X states should be comparable to the quarkonium cross section we calculated, albeit smaller by $O(1)$ factors because of the smaller binding energies in this case. However, for $N > 2$, the double-X hadrons contain some light quark(s), so their size is $1/\Lambda_D$. They can therefore interact quite efficiently with hadrons containing $\bar{X}$ to form bound states containing both X and $\bar{X}$, where X–$\bar{X}$ pairs can quickly annihilate. Meanwhile, they can also interact with H_X hadrons and form triple-X hadrons, and this chain may go on until pure-X (or pure-$\bar{X}$) baryons are formed. All these processes should have geometric cross sections. The pure-X baryons eventually de-excite to the ground state, the size of which is much smaller than $1/\Lambda_D$. Their interactions with other hadrons therefore shut off. As a result, the Xs inside the baryons remain as stable relics, while the other Xs may effectively be annihilated. A systematic analysis necessitates solving the Boltzmann equation with these dynamics, which is beyond the scope of this work. However, it is safe to assume that a sizable fraction of the original Xs can be preserved in a variety of stable hadronic relics.

For DM charged under real QCD, heavy-light hadrons, with size $1/\Lambda_D$, are subject to stringent constraints, but they are efficiently depleted at $T \lesssim \Lambda_D$ as we have shown. In contrast, the relic abundance of X^3 baryons may be just

[1] Many of the relevant processes were described in Ref. [201] for TeV-mass colored relics.

somewhat smaller than the original X relic abundance. Thus the fundamental Xs we considered here may give a different realization of colored DM [196], but whether the models are viable requires a more detailed analysis. Note that the scenario considered in Ref. [196], namely a heavy Dirac adjoint X, is non-generic, in that two Xs can form a stable singlet with no additional light quarks.

In summary, the simple models considered here typically give rise to several components of DM composites of different masses. For certain choices of m_X and Λ_D, these can exhibit self-interactions, transitions between different excited states, and, depending on the coupling to the Standard Model, modified direct and indirect detection cross sections. In some variants of these models, the DM abundance can be significantly depleted at Λ_D, leading to a long era of matter domination between m_X and Λ_D.

6.6 Conclusions

In this work we have considered the cosmological dynamics of bound states that are much larger than their inverse mass, taking as an example $X\bar{q}$ mesons in a confining theory where X is much heavier than q and the confinement scale. We calculated the cross section for quarkonium production from heavy-light meson scattering. The cross section is geometric, and scales with the area of the incident heavy-light mesons. The relic density of heavy-light X-mesons is therefore efficiently diluted with rates much higher than the s-wave unitarity bound due to the participation of many partial waves in the process. We also find that the process is mainly mediated by the effective interaction of the light quarks. In contrast, processes in which only the heavy constituents participate have mass-

suppressed rates. It is amusing to note that if the lifetime of B-mesons were longer, such processes could be experimentally measured.

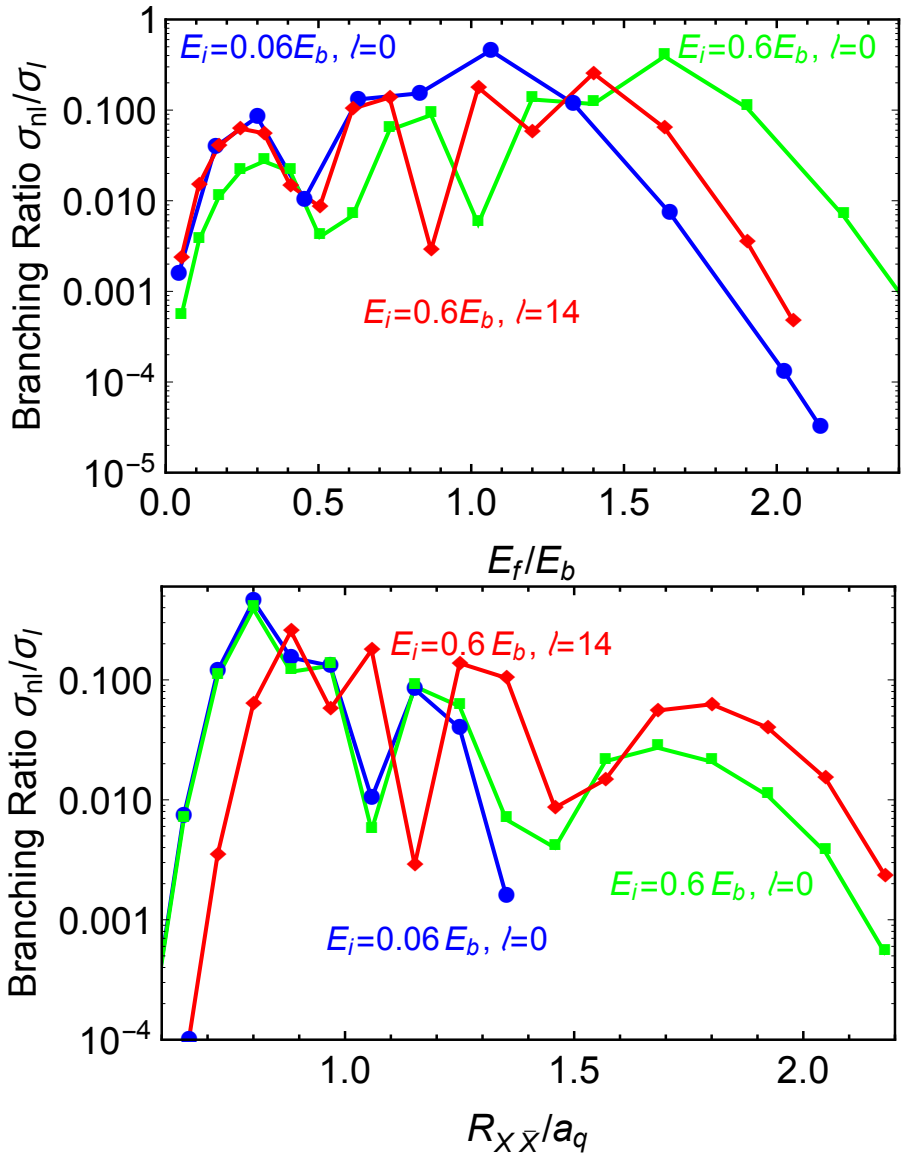

Figure 6.5: The branching fraction σ_{nl}/σ_l for some initial partial waves to form an $(X\bar{X})$ quarkonium of definite n, l (uniquely defined by the x-axis). The results are presented for $m_X = 3 \times 10^4 \bar{\alpha}_D m_q$ and several values of E_i and l. Left panel: The branching fraction as a function of the kinetic energy in the final state. Right panel: The branching fraction as a function of $R_{X\bar{X}}$, the mean radius of the final state.

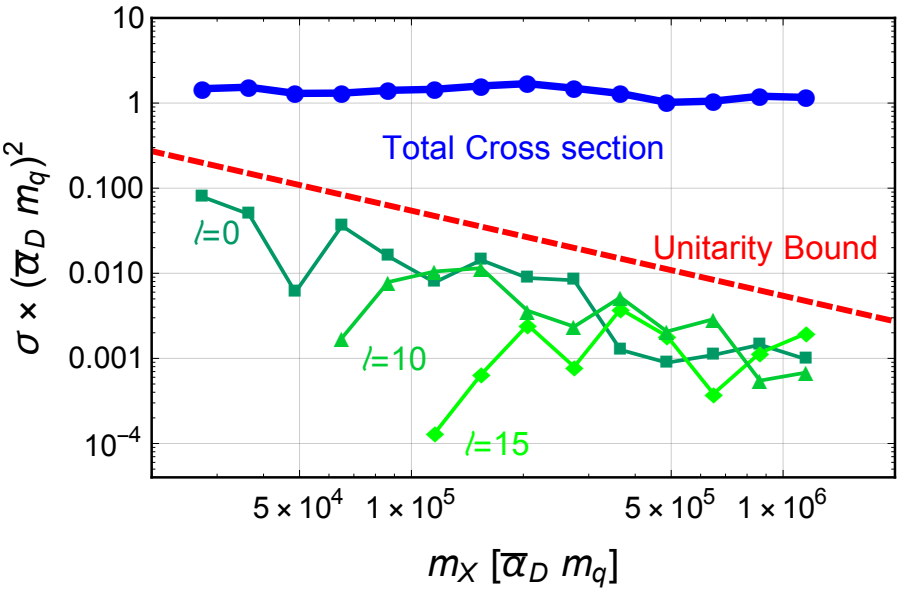

Figure 6.6: The rearrangement cross section. The blue line is the total cross section for an incoming energy $E_i = 0.6E_b$, and is geometric. Several individual partial-wave contributions $\sigma_l/(2l+1)$ are given in green, together with the unitarity bound $4\pi/k_i^2$ (red dashed line) for $l < l_{\max} \sim k_i a_q$.

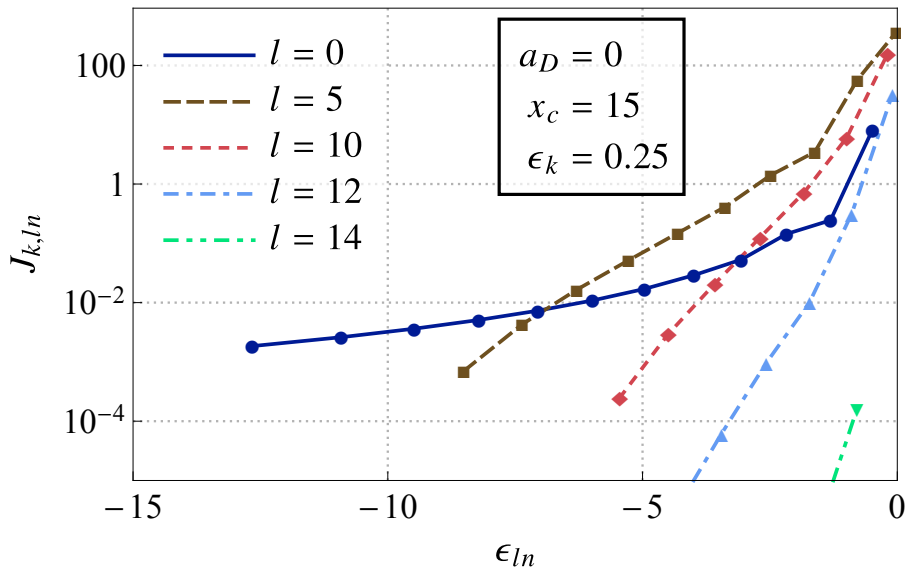

Figure 6.7: $J_{k,ln}$ as a function of ϵ_{ln} for $x_c = 15$ and $\epsilon_k = 0.25$. The lines correspond to different values of l.

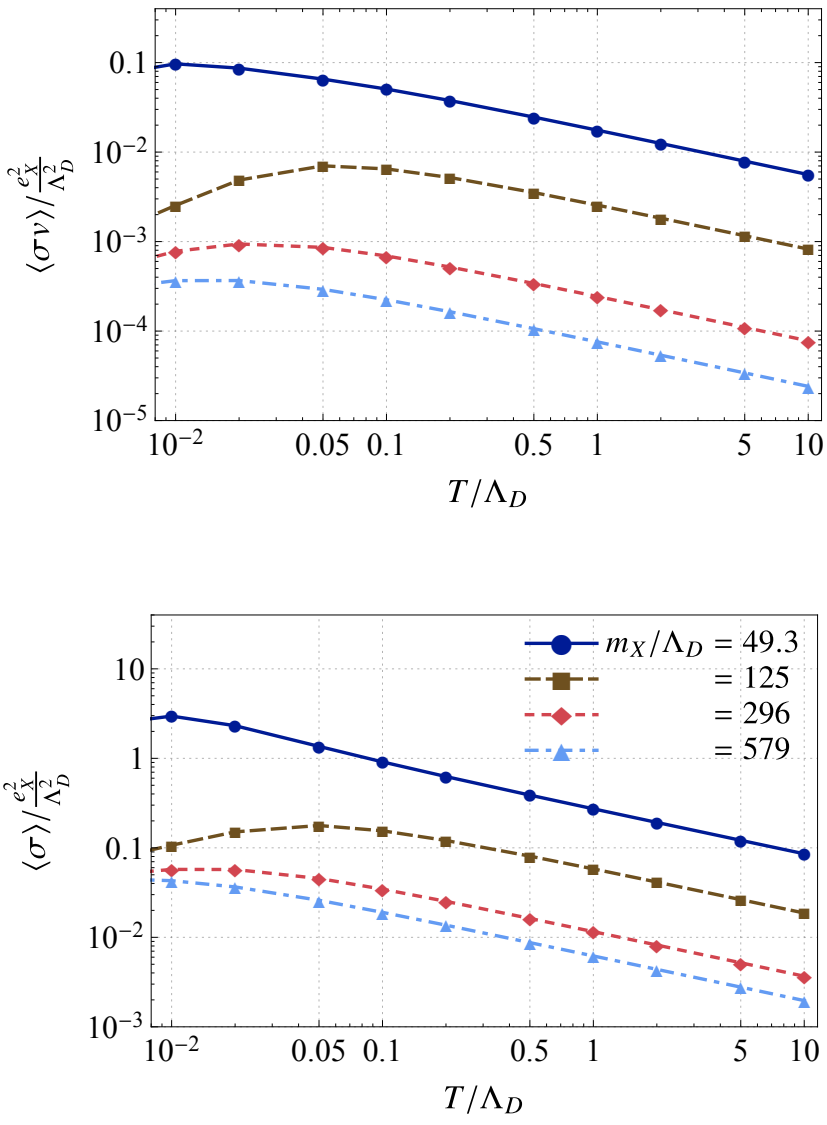

Figure 6.8: Results of thermally-averaged radiative quarkonium production cross section $\langle\sigma v\rangle$ (top panel) and $\langle\sigma\rangle$ (bottom panel) as a function of temperature for different values of m_X/Λ_D.

APPENDIX

6.A Cross Section for Bound-State Formation in the Radiation Process

In this section we summarize the calculation of the bound-state formation cross section via radiation discussed in Sec. 6.4. We also collect here some useful results on the spectrum and wavefunctions of the Cornell and linear potential.

6.A.1 Eigenstates of the Cornell potential

We model the X–$\bar{X}$ attractive interaction by the cutoff Cornell potential of Eq. (6.6), with the cutoff given in Eq. (6.36) and $V_0 = 0$.

The bound states $(X\bar{X})$ are characterized by three integers (l, m, n), where l labels the angular momentum, m labels the angular momentum along the z-axis, and $n \geq 1$. An H_X–$\bar{H}_X$ scattering state is approximated by an X–$\bar{X}$ unbound state, which is characterized by the X–$\bar{X}$ relative momentum $\boldsymbol{k}$, with energy $E_k \approx k^2/m_X$, where $k = |\boldsymbol{k}|$. The reduced mass of both the bound and scattering states is approximately $m_X/2$.

The bound-state wavefunctions can be written as

$$\psi_{lm,n}(R_0\boldsymbol{x}) = \frac{1}{R_0^{3/2}} \frac{\chi_{ln}(x)}{x} Y_{lm}(\Omega_{\boldsymbol{x}}) \,, \tag{6.48}$$

where the dimensionless coordinate x is defined below Eq. (6.39). The

scattering-state wavefunctions can be expanded as

$$\phi_{\boldsymbol{k}}(R_0\boldsymbol{x}) = \sum_{l=0}^{\infty}(2l+1)\phi_{\boldsymbol{k},l}(R_0\boldsymbol{x}) = \sum_{l=0}^{\infty}(2l+1)\frac{\chi_{kl}(x)}{x}P_l(\hat{\boldsymbol{k}}\cdot\hat{\boldsymbol{x}})\,. \tag{6.49}$$

For $\boldsymbol{k}$ along $\hat{z}$ this simplifies to

$$\phi_{k\hat{z},l}(R_0\boldsymbol{x}) = \sqrt{\frac{4\pi}{2l+1}}\frac{\chi_{kl}(x)}{x}Y_l^0(\Omega_{\boldsymbol{x}})\,. \tag{6.50}$$

The radial wavefunctions $\chi_{ln}(x)$ and $\chi_{kl}(x)$ solve

$$-\chi''_{ln\,(kl)}(x) + V^l_{\rm eff}(x)\chi_{ln\,(kl)}(x) = \epsilon_{ln\,(k)}\chi_{ln\,(kl)}(x)\,, \tag{6.51}$$

where

$$\begin{aligned} V^l_{\rm eff}(x) &= \frac{l(l+1)}{x^2} + V(x) \\ &= \frac{l(l+1)}{x^2} + \left[-a_D\left(\frac{1}{x}-\frac{1}{x_c}\right) + (x-x_c)\right]\Theta(x_c-x)\,. \end{aligned} \tag{6.52}$$

Note that this dimensionless problem has only two parameters: x_c and the effective Coulomb strength $a_D \equiv (m_X/\Lambda_D)^{2/3}\bar{\alpha}_D$. The radial wavefunctions are zero at the origin, $\chi_{ln\,(kl)}(0) = 0$, and satisfy the normalization conditions

$$\int_0^\infty \chi_{ln}(x)\chi^*_{ln'}(x)dx = \delta_{nn'}\,, \qquad \int_0^\infty \chi_{kl}(x)\chi^*_{k'l}(x)dx = \frac{\pi}{2k^2}\delta(k-k')\,, \tag{6.53}$$

so that $\langle\psi_{lm,n}|\psi_{l'm',n'}\rangle = \delta_{ll'}\delta_{mm'}\delta_{nn'}$ and $\langle\phi_{\boldsymbol{k}}|\phi_{\boldsymbol{k}'}\rangle = (2\pi)^3\delta^{(3)}(\boldsymbol{k}-\boldsymbol{k}')$.

Figure 6.9 shows $V_{\rm eff}(x)$ in Eq. (6.52) for $x_c = 15$ with $a_D = 7$ (left) and $a_D = 0$ (right). Because of the cutoff, the angular momentum quantum number l of bound states has an upper bound $l_{\rm max}$ given in Eq. (6.41). This is confirmed in the numerical results.[1]

The bound-state energy levels are shown in Fig. 6.10 for a cutoff Cornell (left) and linear (right) potentials. In Ref. [238], the semiclassical approximation

[1] In fact, as one can see in Fig. 6.9, the effective potential for very large l may have a minimum with $V_{\rm eff}(x_0) \geq 0$, and it produces wavefunctions with $\epsilon > 0$ which are mostly confined to the region $x < x_c$.

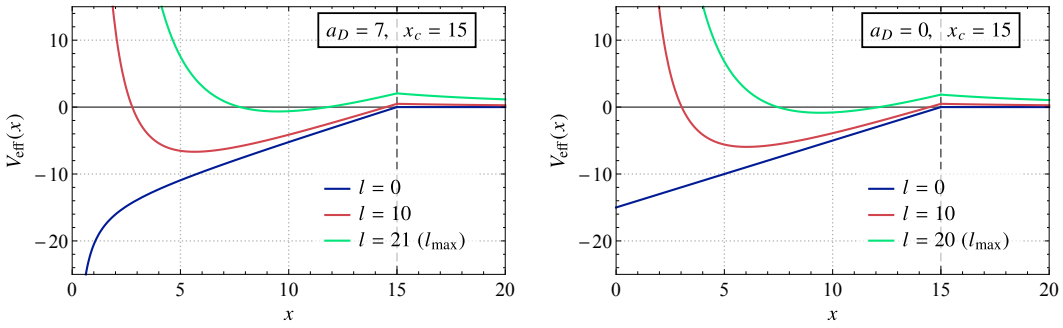

Figure 6.9: The effective potential $V_{\rm eff}(x)$ with $x_c = 15$ ($m_X \simeq 125\Lambda_D$), for three values of l. In the left panel, $a_D = 7$, which corresponds to $\bar{\alpha}_D = 0.3$, while $a_D = 0$ in the right panel. The largest l in each panel corresponds to the upper-bound on l of the bound states. Note that the plots for $l = 0$ correspond to $V(x)$ in Eq. (6.52).

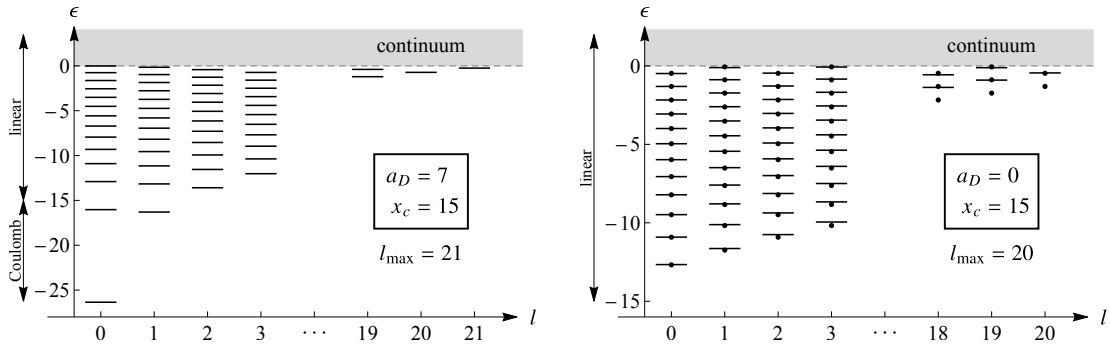

Figure 6.10: The energy spectrum of bound states. Left panel: $a_D = 7$, right panel: $a_D = 0$ (linear). We also show, for the linear potential, the semiclassical results in Eq. (6.55) as the small dots.

is used to obtain the energy levels of the eigenstates of central potentials. Following their discussion, the energy levels under the linear potential are given by

$$E_{ln} - V(0) \approx \left[\frac{3}{2}\pi\left(n + \frac{l}{2} - \frac{1}{4}\right)\right]^{2/3} E_0\,, \tag{6.54}$$

or in our notation, since $V(0) = -R_c\Lambda_D^2 = -x_c E_0$,

$$\epsilon_{ln} \approx \left[\frac{3}{2}\pi\left(n + \frac{l}{2} - \frac{1}{4}\right)\right]^{2/3} - x_c\,. \tag{6.55}$$

We reproduce this result in Fig. 6.10(b). For a Cornell potential (Fig. 6.10(a)),

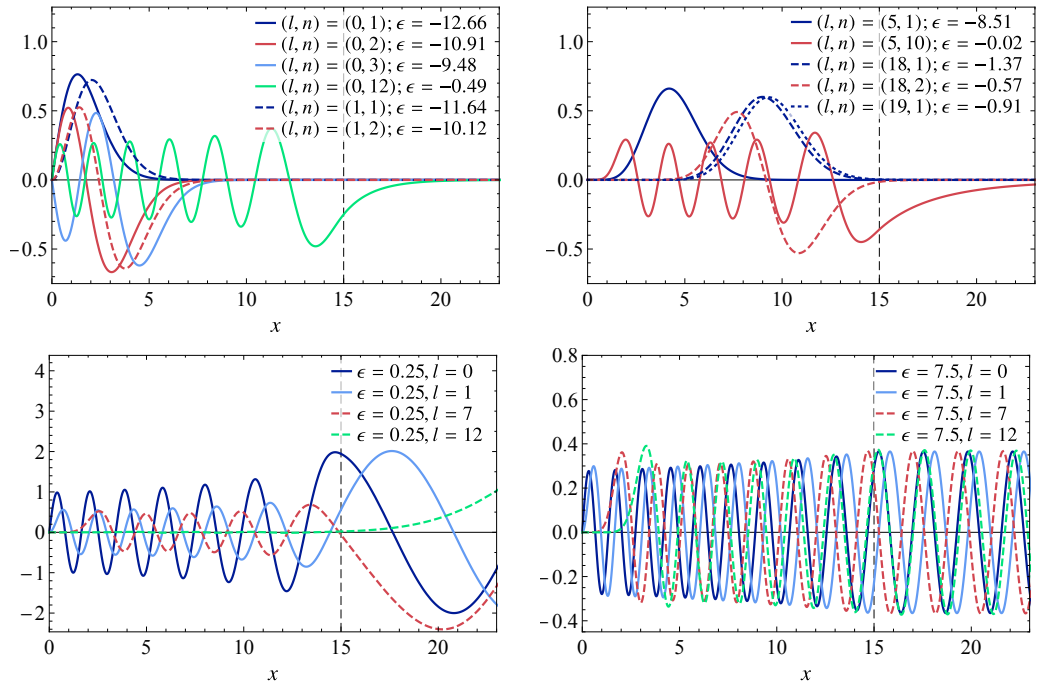

Figure 6.11: Wavefunctions obtained from solving Eqs. (6.51–6.52) with $x_c = 15, a_D = 0$. *Top:* $\chi_{ln}(x)$ for bound states. The left panel contains smaller l (0,1) while the right panel has intermediate and high l (5, 18, 19 = $l_{\max}$), where $(l, n) = (5, 10)$ is the highest-energy bound state. *Bottom:* $\chi_{kl}(x)$ for scattering states. The left panel displays the partial waves of the scattering states with $\epsilon = 0.25$ ($E_k = 0.05\Lambda_D$), while the right panel shows those with $\epsilon = 7.5$ ($E_k = 1.5\Lambda_D$).

deep states are governed by the Coulomb force and therefore obey the well-known Coulombic energy levels

$$\epsilon_{ln} \approx -\frac{a_D^2}{4N^2} - x_c\,, \tag{6.56}$$

where the principal quantum number N is given by $n + l$. For shallower states, the Coulomb force is negligible and the linear potential governs the spectrum.[1]

We show some examples of bound-state and scattering-state wavefunctions

[1]The average size $\langle x\rangle$ of bound states is given by the virial theorem as $\epsilon + x_c = -a_D/(2\langle x\rangle)$ for a Coulombic bound states, i.e., if the effect of the linear term is negligible, and $\epsilon + x_c = 3\langle x\rangle/2$ for bound states in the linear regime.

that solve Eq. (6.51) with the cutoff linear potential (Eq. (6.52) with $a_D = 0$) in the top and bottom rows of Fig. 6.11, respectively. The bound state with $(l, n) = (5, 10)$ is found to be the shallowest bound state, but it should be emphasized that this is an accident due to the cutoff being just above the energy of this state. In general, shallower states with smaller l have wavefunctions that tend to penetrate beyond $x > x_c$. For the scattering states, wavefunctions of states with larger ϵ and smaller l have penetrate further into the region $x < x_c$.

6.A.2 Bound-state formation cross section in the dipole approximation

We calculate the matrix element for the bound-state formation by a vector-mediated interaction,

$$H_X + \bar{H}_X \to (X\bar{X})_{lm,n} + \varphi \tag{6.57}$$

with the X–φ interaction given by

$$\mathcal{L} \ni \left|\left(\partial_\mu - ie_X\varphi_\mu\right) X\right|^2 . \tag{6.58}$$

We follow the approach and notation in Refs. [191, 195]. From now on, we focus on the linear potential and set $a_D = 0$ because, as we will see, the radiative bound-state formation process favors shallow bound states, for which the Coulomb force is negligible.

The bound-state formation cross section is given by [191]

$$(v_{\rm rel}\sigma)^{\rm BSF}_{\boldsymbol{k}} = \sum_{l,m,n}(v_{\rm rel}\sigma)^{\rm BSF}_{\boldsymbol{k}\to lm,n} = \sum_{l,m,n}\int \frac{d\Omega_{\boldsymbol{P}_\varphi}}{4\pi}\frac{|\boldsymbol{P}_\varphi|}{32\,\pi\, m_X^3}\sum_{\rm pol.}\left|\boldsymbol{\epsilon}\cdot\boldsymbol{\mathcal{M}}_{\boldsymbol{k}\to lm,n}\right|^2 \tag{6.59}$$

in the CM frame, where $\boldsymbol{k}$, $\boldsymbol{P}_\varphi$, and $\boldsymbol{\epsilon}$ are the relative momentum of the initial state, the momentum of the radiated light state φ, and its polarization vector,

respectively, and

$$v_{\rm rel} \simeq \frac{|\boldsymbol{k}|}{m_X/2}\,, \qquad |\boldsymbol{P}_\varphi| = E_k - E_{ln}\,; \tag{6.60}$$

E_k is kinetic energy of the initial scattering state. The matrix element is

$$\mathcal{M}^j_{\boldsymbol{k}\to lm,n} = -4e_X\sqrt{m_X}\int\frac{d^3\boldsymbol{p}}{(2\pi)^3}\,p^j\tilde{\psi}^*_{lm,n}(\boldsymbol{p})\left[\tilde{\phi}_{\boldsymbol{k}}\left(\boldsymbol{p}+\frac{\boldsymbol{P}_\varphi}{2}\right)+\tilde{\phi}_{\boldsymbol{k}}\left(\boldsymbol{p}-\frac{\boldsymbol{P}_\varphi}{2}\right)\right], \tag{6.61}$$

where $\tilde{\phi}_{\boldsymbol{k}}(\boldsymbol{p})$ and $\tilde{\psi}_{lm,n}(\boldsymbol{p})$ are the momentum-space equivalents of Eqs. (6.48)–(6.49).

It is convenient to expand the matrix element in partial waves (cf. Eq. (6.49)):

$$\begin{aligned}
\mathcal{M}^j_{\boldsymbol{k}\to lm,n} &= \sum_{l'=0}^{\infty}(2l'+1)\mathcal{M}^j_{\boldsymbol{k},l'\to lm,n}\,,\\
\mathcal{M}^j_{\boldsymbol{k},l'\to lm,n} &= -4e_X\sqrt{m_X}\int\frac{d^3\boldsymbol{p}}{(2\pi)^3}\,p^j\tilde{\psi}^*_{lm,n}(\boldsymbol{p})\left[\tilde{\phi}_{\boldsymbol{k},l'}\left(\boldsymbol{p}+\frac{\boldsymbol{P}_\varphi}{2}\right)+\tilde{\phi}_{\boldsymbol{k},l'}\left(\boldsymbol{p}-\frac{\boldsymbol{P}_\varphi}{2}\right)\right]\\
&= 8ie_X\sqrt{m_X}\int d^3\boldsymbol{r}\,d^3\boldsymbol{r}'\,\psi^*_{lm,n}(\boldsymbol{r})\phi_{\boldsymbol{k},l'}(\boldsymbol{r}')\cos\left(\frac{\boldsymbol{P}_\varphi}{2}\cdot\boldsymbol{r}'\right)\frac{\partial}{\partial r^j}\delta^{(3)}(\boldsymbol{r}-\boldsymbol{r}')\,.
\end{aligned}$$

After partial integration, the derivative acts on $\psi^*_{lm,n}(\boldsymbol{r})$, and the integral over $d^3\boldsymbol{r}'$ is trivial using the delta function. Dotting with the polarization vector and performing another partial integration (the derivative of the cosine is zero as $\boldsymbol{\epsilon}\cdot\boldsymbol{P}_\varphi = 0$) yields

$$\boldsymbol{\epsilon}\cdot\boldsymbol{\mathcal{M}}_{\boldsymbol{k},l'\to lm,n} = 4ie_X\sqrt{m_X}\int d^3\boldsymbol{r}\,\cos\left(\frac{\boldsymbol{P}_\varphi}{2}\cdot\boldsymbol{r}\right)\boldsymbol{\epsilon}\cdot\left[\psi^*_{lm,n}\boldsymbol{\nabla}\phi_{\boldsymbol{k},l'}-\phi_{\boldsymbol{k},l'}\boldsymbol{\nabla}\psi^*_{lm,n}\right], \tag{6.62}$$

where $\psi^*_{lm,n}$ and $\phi_{\boldsymbol{k},l'}$ are functions of $\boldsymbol{r}$. The quantity in brackets above appears in the difference of the Schrödinger equations for the scattering- and bound-state wavefunctions,

$$-\frac{1}{m_X}\boldsymbol{\nabla}\cdot(\psi^*_{lm,n}\boldsymbol{\nabla}\phi_{\boldsymbol{k},l'}-\phi_{\boldsymbol{k},l'}\boldsymbol{\nabla}\psi^*_{lm,n}) = (E_k - E_{nl})\psi^*_{lm,n}\phi_{\boldsymbol{k},l'}\,. \tag{6.63}$$

Using the identity[1]

$$\int d^3\boldsymbol{r}\;(\nabla\cdot\boldsymbol{F})\,\boldsymbol{r} = -\int d^3\boldsymbol{r}\,\boldsymbol{F}\,(\boldsymbol{\nabla}\cdot\boldsymbol{r}) = -\int d^3\boldsymbol{r}\,\boldsymbol{F} \tag{6.64}$$

[1]By assumption, $\boldsymbol{F}$ satisfies appropriate fall-off behavior at large $|\boldsymbol{r}|$ so the boundary term is negligible.

with $\boldsymbol{F} = \psi^*_{lm,n}\boldsymbol{\nabla}\phi_{\boldsymbol{k},l'} - \phi_{\boldsymbol{k},l'}\boldsymbol{\nabla}\psi^*_{lm,n}$ and substituting into Eq. (6.62), we obtain[1]

$$\begin{aligned}\boldsymbol{\epsilon}\cdot\boldsymbol{\mathcal{M}}_{\boldsymbol{k},l'\to lm,n} = 4ie_X\sqrt{m_X}\int d^3\boldsymbol{r}\,(\boldsymbol{\epsilon}\cdot\boldsymbol{r})\Bigg[m_X(E_k - E_{ln})\psi^*_{lm,n}\phi_{\boldsymbol{k},l'}\cos\left(\frac{\boldsymbol{P}_\varphi}{2}\cdot\boldsymbol{r}\right)\\ + \frac{\boldsymbol{P}_\varphi}{2}\cdot(\psi^*_{lm,n}\boldsymbol{\nabla}\phi_{\boldsymbol{k},l'} - \phi_{\boldsymbol{k},l'}\boldsymbol{\nabla}\psi^*_{lm,n})\sin\left(\frac{\boldsymbol{P}_\varphi}{2}\cdot\boldsymbol{r}\right)\Bigg].\end{aligned} \tag{6.65}$$

We are interested in temperatures $T \lesssim \Lambda_D$ for which $\boldsymbol{P}_\varphi \ll m_X$, and thus

$$\boldsymbol{\epsilon}\cdot\boldsymbol{\mathcal{M}}_{\boldsymbol{k},l'\to lm,n} \simeq 4ie_X\sqrt{m_X^3}(E_k - E_{ln})\int d^3\boldsymbol{r}\,(\boldsymbol{\epsilon}\cdot\boldsymbol{r})\psi^*_{lm,n}\phi_{\boldsymbol{k},l'}\cos\left(\frac{\boldsymbol{P}_\varphi}{2}\cdot\boldsymbol{r}\right). \tag{6.66}$$

Also, we can evaluate $\boldsymbol{P}_\varphi\cdot\boldsymbol{r}/2$ as

$$\frac{\boldsymbol{P}_\varphi}{2}\cdot\boldsymbol{r} \le \frac{|\boldsymbol{P}_\varphi|r}{2} = \frac{|E_k - E_{ln}|r}{2} = \kappa_{\Lambda_D}\frac{|E_k - E_{ln}|}{\Lambda_D}\frac{r}{R_c}\,. \tag{6.67}$$

Note that as the integrand contains a bound-state wavefunction, the integral has support only for $r \lesssim R_c$. Also, for $T \ll \Lambda_D$, the overlaps of the bound and scattering states are larger for shallower bound states. Combining these, we can approximate $\boldsymbol{P}_\varphi\cdot\boldsymbol{r}/2 \ll 1$ in order to employ the dipole approximation $\cos(\boldsymbol{P}_\varphi\cdot\boldsymbol{r}/2)\to 1$, which simplifies the cross section to

$$\begin{aligned}(v_{\rm rel}\sigma)^{\rm BSF}_{\boldsymbol{k}} &\to \sum_{l,m,n}\int\frac{d\Omega_{\boldsymbol{P}_\varphi}}{4\pi}\frac{|\boldsymbol{P}_\varphi|}{32\,\pi\,m_X^3}\sum_{\rm pol.}\left|\sum_{l'}(2l'+1)4ie_X\sqrt{m_X^3}(E_k - E_{ln})\boldsymbol{\epsilon}\cdot\boldsymbol{\mathcal{I}}_{\boldsymbol{k},l'\to lm,n}\right|^2\\ &= \sum_{l,m,n}\int\frac{d\Omega_{\boldsymbol{P}_\varphi}}{4\pi}\frac{e_X^2(E_k - E_{ln})^3}{2\pi}\sum_{\rm pol.}\left|\sum_{l'}(2l'+1)\boldsymbol{\epsilon}\cdot\boldsymbol{\mathcal{I}}_{\boldsymbol{k},l'\to lm,n}\right|^2,\end{aligned} \tag{6.68}$$

where the integral of the wavefunctions is defined as

$$\mathcal{I}^j_{\boldsymbol{k},l'\to lm,n} = \int d^3\boldsymbol{r}\,r^j\,\psi^*_{lm,n}\,\phi_{\boldsymbol{k},l'}\,. \tag{6.69}$$

Next, we express the integral in the basis $r^a = (r^+, r^0, r^-)$ defined by

$$r^\pm = \frac{-1}{\sqrt{2}}\left(\pm r^1 + ir^2\right) = r\sqrt{\frac{4\pi}{3}}\,Y_1^{\pm1}(\Omega_{\boldsymbol{r}})\,, \qquad r^0 = r\sqrt{\frac{4\pi}{3}}\,Y_1^0(\Omega_{\boldsymbol{r}})\,. \tag{6.70}$$

[1]This is the form of the matrix element in Refs. [193, 236]; both employ the dipole approximation and the Hamiltonian formulation.

Taking the z-axis parallel to $\hat{\boldsymbol{k}}$, substituting Eq. (6.48) and Eq. (6.50) for the wavefunctions in Eq. (6.69), we obtain

$$\begin{aligned}\mathcal{I}^a_{\boldsymbol{k},l'\to lm,n} &= \frac{4\pi R_0^{5/2}}{\sqrt{3(2l'+1)}} I_{kl'\to ln} \int d\Omega_{\boldsymbol{x}} Y^0_{l'}(\Omega_{\boldsymbol{x}}) Y^a_1(\Omega_{\boldsymbol{x}}) Y^{m*}_l(\Omega_{\boldsymbol{x}}) \\ &= (-1)^m \sqrt{4\pi(2l+1)}\, R_0^{5/2} I_{kl'\to ln} \begin{pmatrix} l' & 1 & l \\ 0 & 0 & 0 \end{pmatrix} \begin{pmatrix} l' & 1 & l \\ 0 & a & -m \end{pmatrix}, \end{aligned} \tag{6.71}$$

$$I_{kl'\to ln} = \int dx\, x \chi^*_{ln}(x) \chi_{kl'}(x)\,, \tag{6.72}$$

where we have expressed the integral over solid angle of three spherical harmonics in terms of Wigner $3j$-symbols

$$\int d\Omega\, Y^{m_1}_{l_1} Y^{m_2}_{l_2} Y^{m_3}_{l_3} = \left[\frac{(2l_1+1)(2l_2+1)(2l_3+1)}{4\pi}\right]^{1/2} \begin{pmatrix} l_1 & l_2 & l_3 \\ 0 & 0 & 0 \end{pmatrix} \begin{pmatrix} l_1 & l_2 & l_3 \\ m_1 & m_2 & m_3 \end{pmatrix}. \tag{6.73}$$

These symbols give the selection rules $l' = |l \pm 1|$ and $m = a$, so that $|m| \leq 1$.

With these results, the sum over m, l', and polarizations in Eq. (6.68) evaluates to[1]

$$\begin{aligned} &\sum_{m=-l}^{l} \sum_{\text{pol.}} \left| \sum_{l'} (2l'+1) \boldsymbol{\epsilon} \cdot \boldsymbol{\mathcal{I}}_{\boldsymbol{k},l'\to lm,n} \right|^2 \\ &= \sum_{m=-l}^{l} \sum_{a=-1}^{1} \left| (2l+3) \mathcal{I}^m_{\boldsymbol{k},l+1\to lm,n} + (2l-1) \mathcal{I}^m_{\boldsymbol{k},l-1\to lm,n} \right|^2 \delta_{am} \\ &= \sum_{m=-1}^{1} \left| (2l+3) \mathcal{I}^m_{\boldsymbol{k},l+1\to lm,n} + (2l-1) \mathcal{I}^m_{\boldsymbol{k},l-1\to lm,n} \right|^2 \\ &= 4\pi R_0^5 \left[(l+1) \left| I_{k,l+1\to ln} \right|^2 + l \left| I_{k,l-1\to ln} \right|^2 \right]. \end{aligned} \tag{6.74}$$

Inserting this into the cross section in Eq. (6.68) and trivially performing the

[1] Note that $\mathcal{I}^a_{k\hat{z},l-1\to lm,n}$ is always zero if $l = 0$.

$d\Omega_{\boldsymbol{P}_\varphi}$ yields

$$
\begin{aligned}
(v_{\rm rel}\sigma)^{\rm BSF}_{\boldsymbol{k}} &= 2e_X^2 R_0^5 \sum_{l,n} (E_k - E_{ln})^3 \left[(l+1) \left| I_{k,l+1\to ln} \right|^2 + l \left| I_{k,l-1\to ln} \right|^2 \right] \\
&= \frac{2e_X^2}{m_X^2} \left(\frac{\Lambda_D}{m_X} \right)^{2/3} \sum_{l,n} J_{k,ln} \,, \qquad (6.75)
\end{aligned}
$$

with $J_{k,ln}$ defined in Eq. (6.45).

6.A.3 Thermally-averaged cross section

Here we briefly describe the procedure to calculate the thermally-averaged cross section, $\langle v_{\rm rel}\sigma \rangle (\beta)$, as a function of the inverse temperature $\beta = T^{-1}$. As in the previous discussion, we denote the momenta of the initial particles as $\boldsymbol{k}_1$, $\boldsymbol{k}_2$.

As we are interested in $T \ll m_X$, the kinetic distributions of H_X and $\bar{H}_X$ are given by the Maxwell-Boltzmann distribution,

$$
f_{\rm MB}(\boldsymbol{p}) = \left(\frac{2\pi\beta}{m} \right)^{3/2} \exp\left(-\frac{\beta |\boldsymbol{p}|^2}{2m_X} \right), \qquad (6.76)
$$

which is normalized so that $\int \frac{d^3\boldsymbol{p}}{(2\pi)^3} f_{\rm MB}(\boldsymbol{p}) = 1$. With this distribution, the thermally-averaged cross section is given by

$$
\begin{aligned}
\langle v_{\rm rel}\sigma \rangle (\beta) &= \int \frac{d^3\boldsymbol{k}_1}{(2\pi)^3} \frac{d^3\boldsymbol{k}_2}{(2\pi)^3} f_{\rm MB}(\boldsymbol{k}_1) f_{\rm MB}(\boldsymbol{k}_2) (v_{\rm rel}\sigma)^{\rm BSF}_{\boldsymbol{k}} \\
&= \left(\frac{2\pi\beta}{m_X} \right)^3 \int \frac{d^3\boldsymbol{K}}{(2\pi)^3} \frac{d^3\boldsymbol{k}}{(2\pi)^3} \exp\left(-\frac{\beta(|\boldsymbol{K}/2|^2 + |\boldsymbol{k}|^2)}{m_X} \right) (v_{\rm rel}\sigma)^{\rm BSF}_{\boldsymbol{k}} \\
&= \sqrt{\frac{16\beta^3}{\pi m_X^3}} \int dk\, k^2\, e^{-\beta k^2/m_X} (v_{\rm rel}\sigma)^{\rm BSF}_{k} \,, \qquad (6.77)
\end{aligned}
$$

where, as before, $\boldsymbol{K} = \boldsymbol{k}_1 + \boldsymbol{k}_2$ and $\boldsymbol{k} = (\boldsymbol{k}_1 - \boldsymbol{k}_2)/2$. We have neglected the dependence of the (non-relativistic) cross section $(v_{\rm rel}\sigma)^{\rm BSF}_k$ on $\boldsymbol{K}$ since $|\boldsymbol{K}| \ll |\boldsymbol{k}|$.

Combining the previous result and also including the final-state effect of φ, we obtain

$$\langle v_{\rm rel}\sigma\rangle(\beta) = \frac{2e_X^2}{m_X^2}\left(\frac{\Lambda_D}{m_X}\right)^{2/3}\int dk\, w(k;\beta)\sum_{l,n}\frac{J_{k,ln}}{1-\exp\left[-\beta(E_k-E_{ln})\right]}\,, \tag{6.78}$$

where we define

$$w(k;\beta) = \sqrt{\frac{16\beta^3}{\pi m_X^3}}\,k^2\,e^{-\beta k^2/m_X}\,, \qquad \int w(k;\beta)dk = 1\,. \tag{6.79}$$

CHAPTER 7

SELF-DESTRUCTING DARK MATTER

BEYOND THE STANDARD MODEL: COMPOSITE HIGGS AND DARK MATTER

Ofri Telem, Ph.D.

Cornell University 2019

We present Self-Destructing Dark Matter (SDDM), a new class of dark matter models which are detectable in large neutrino detectors. In this class of models, a component of dark matter can transition from a long-lived state to a short-lived one by scattering off of a nucleus or an electron in the Earth. The short-lived state then decays to Standard Model particles, generating a dark matter signal with a visible energy of order the dark matter mass rather than just its recoil. This leads to striking signals in large detectors with high energy thresholds. We present a few examples of models which exhibit self destruction, all inspired by bound state dynamics in the Standard Model. The models under consideration exhibit a rich phenomenology, possibly featuring events with one, two, or even three lepton pairs, each with a fixed invariant mass and a fixed energy, as well as non-trivial directional distributions. This motivates dedicated searches for dark matter in large underground detectors such as Super-K, Borexino, SNO+, and DUNE.

7.1 Introduction

Our knowledge of the nature of dark matter (DM) is very limited. Though it accounts for over 80% of the matter in the universe, it is often assumed that the dark sector is minimal, consisting of a single particle that interacts only feebly with the Standard Model (SM). This assumption, which is the most sensible first guess, motivates a set of strategies in our search for DM. In particular, when searching for DM directly, we try to detect the low energy recoil of a nucleus which was struck by a slowly moving DM particle [239]. DM direct detection thus focuses on detectors with thresholds between sub keV and tens of keV.

The current search program is undoubtedly important and must be pursued further. However, we should not let minimality be our only guide. Indeed, considering even slightly non-minimal DM models has led to significant variations in direct detection phenomenology [240–254], including changes in the predicted recoil spectrum, annual modulation, and in the manner in which the DM deposits energy in the detector. These interesting models, however, keep direct detection phenomenology within the purview of low threshold detectors. The reason for this is that the available energy in the problem is at most the kinetic energy in the DM-nucleus or DM-electron system. This energy is of order μv^2, where $v \sim 10^{-3}c$ is the DM velocity, and μ is the reduced mass of the system.

In this work, we consider a drastic departure from this picture and discuss the possibility that DM is capable of leaving not just kinetic energy in the detector, but rather *all* of its mass. This can lead to DM direct detection signals above MeV, allowing to extend the search for DM to detectors with much higher thresholds. In particular, large existing neutrino experiments such as Borex-

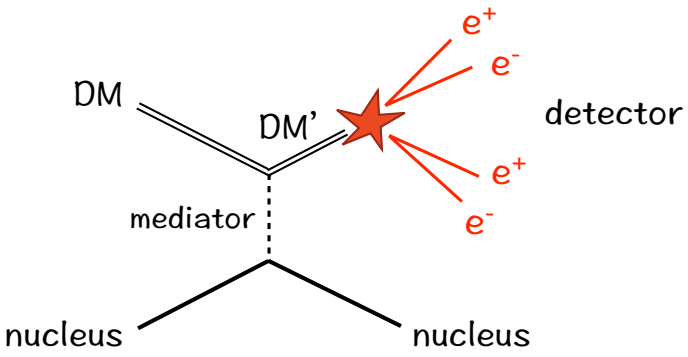

Figure 7.1: A schematic picture of self-destructing DM, where DM denotes the cosmologically long-lived state and DM' denotes the very short-lived one.

ino and Super-Kamiokande, as well as future experiments such as SNO+ and DUNE, can probe self destructing DM models.

A naïve idea to convert the DM rest mass to detectable signal is to consider its down-scattering to a nearly massless state, with the difference in mass converted to recoil energy. This is however unfeasible since it leads to a DM particle that is cosmologically unstable by decaying to this nearly massless state. Instead, we must consider a non-minimal setup in which an interaction of DM with a nucleus triggers a transition from a state that is stable on cosmological timescales to one which is very short-lived. The signal is then not a recoil signal, but rather a subsequent decay of the short-lived state to SM particles. A sketch of this is depicted in Figure 7.1. The crucial ingredients in the story are a cosmologically long lived state and a short lived state, with a possible transition between the two which is induced by the interaction with the Earth. We call this class of DM models self-destructing DM (SDDM for short).

SDDM is not the first class of DM models in which the measured energy is more than just the DM recoil energy. In [245], for example, the DM down-

scatters and converts part of its rest mass to recoil energy. However, in that model the mass splittings considered were still of the same order as the kinetic energy. In [253] the possibility of releasing more than the recoil energy was considered, but with signals still in the domain of low threshold detectors. Other DM models [204, 255–261], are similar to our scenario in that they can be probed at neutrino detectors [262]. Yet, in these models, the dynamics that lead to signals at neutrino detector (a "removal" of a baryon from the detector or a boosted population of DM) is different than the case of SDDM. Lastly, we mention that the axion and other ultralight bosons that can be fully absorbed by a detector may be considered a fully SDDM candidate, but their lightness leads to much lower energy deposition, and thus to very different experimental signatures [263–265].

In the upcoming sections, we present three models which realize the idea of SDDM. These ideas are intended as a proof of principle rather than as complete, well motivated models. In each case, DM is stabilized by a different principle that can be un-done by interactions in the Earth. None of these models is minimal by any means. They are, however, inspired by phenomena that are observed in the visible sector. Particles in the Standard Model find themselves to be either short-lived or meta-stable for a variety of reasons. In many cases different effects, forces, or interactions come into play, balancing one against the other to produce a long- or short-lived state. We are therefore quite liberal in allowing for several particles and interactions. Furthermore, like the visible sector which contains several populations of cosmic relics, we will be open to the possibility that only a subcomponent of DM is self-destructing.

The model building challenge for SDDM is to have a dark matter compo-

nent that is very long-lived, yet capable self-annihilating once it interacts with a nucleus in the Earth. In its long-lived state, this component needs to have a lifetime for more than about 10^{28} sec to satisfy observational constraints [266–268], if it makes up all of DM. Even if we consider only a small sub-component of DM to relax this bound, the state needs to live for more than the age of the universe. In contrast, the short-lived state of our DM component has to decay in much less than 10 seconds, its Earth-crossing time.

The chapter is organized as follows: In Section 7.2 we discuss the cosmological challenges in realizing SDDM, and arrive at an upper bound on the temperature in which it is produced. In Section 7.3 we review the first in our class of SDDM models. In this model, some of the DM consists of excited positronium-like bound states which are stable due to a large angular momentum barrier. Interaction with the matter in the Earth can change the angular momentum of the bound state, rendering it unstable. We then estimate the signal rate of this model in large neutrino detectors and discuss possibilities for its early Universe history. In the second model, presented in Section 7.4, the DM is in a metastable minimum far away from the origin of a bound-state potential. Interaction with the Earth can shake the internal structure and move the system to the global minimum where annihilation is very fast. In our last example, Section 7.5, DM consists of dark baryons. A baryon number violating interaction with matter causes a transition from a dark baryon to a dark meson which can now decay in a detector. In Section 7.6, we discuss the phenomenological signals of our framework in large detectors further in order to motivate more detailed studies. We conclude and provide some further directions for exploration in Section 7.7.

7.2 Survival of SDDM from the early universe

The self-destructing scenario is possible thanks to the high density of matter in the Earth, one which is unprecedented from the perspective of an incoming DM particle. The expected number of DM interactions off of a target with number density n is roughly

$$\langle N \rangle \sim n \langle \sigma v \rangle \Delta t \,, \tag{7.1}$$

where v is the typical relative velocity, σ is the interaction cross section, and Δt is the amount of time spent in this environment. A DM particle with $v \sim 10^{-3} c$ crosses the Earth in about 10 seconds. However, before its short traversal through Earth, it had spent about 10^{16} more time in the low density environment of the galaxy. On the other hand, the number density of atoms in the Earth is about 10^{23} larger than that in the galaxy. As a result, it is reasonable for the expected rate of transitions to an unstable state to be much larger in one Earth-crossing than it is in the preceding Hubble time.

Of course, one should not forget that in the early universe the DM candidate was immersed in a dense thermal bath. Because the density of targets for self-destruction increases early on, there is an upper bound on the temperature above which all SDDM will be destroyed. The probability of destruction is given by $p = n\sigma v \Delta t$. For the case of Super-K, n is the number density of targets in water and Δt is the time interval of dark matter passing through the detector. Assuming that we could observe 100 events in the Super-K detector per year, we could derive the probability of its self-destruction,

$$p \simeq 10^{-20} \left(\frac{m_\chi}{10\,\mathrm{MeV}} \right) \tag{7.2}$$

based on the local dark matter density. We could repeat the calculation for early

universe, where the number density of SM particles is given by $n \sim T^3$, and the Hubble time $\Delta t = H^{-2} \simeq M_{\text{planck}}/T^2$. The destruction of SDDM will be significant at temperatures above

$$T_{\text{survival}} \sim 10\,\text{MeV} \times \left(\frac{10\,\text{MeV}}{m_\chi}\right) \tag{7.3}$$

This implies an upper limit on the temperature for SDDM to be produced in the early universe.

7.3 High angular momentum stabilization

In this model, a component of the DM is a positronium-like bound state which is stabilized by angular momentum conservation. In particular, the self-annihilation of this "dark positronium" is suppressed due to a large angular momentum barrier. An interaction with the Earth allows the dark matter to transition to a lower angular momentum state that has a lifetime which is exponentially shorter.

The dark sector contains light fermions χ and $\bar{\chi}$ which are charged under two broken abelian gauge groups $U(1)_\phi$ and $U(1)_V$. The Lagrangian for this sector takes the form

$$\mathcal{L} = \bar{\chi} i \not{D} \chi - m_\chi \bar{\chi}\chi - \frac{1}{4}\phi^{\mu\nu}\phi_{\mu\nu} + \frac{1}{2}m_\phi^2 \phi_\mu \phi^\mu - \frac{1}{4}V^{\mu\nu}V_{\mu\nu} + \frac{1}{2}m_V^2 V_\mu V^\mu - \frac{\epsilon}{2}V_{\mu\nu}F^{\mu\nu}\,, \tag{7.4}$$

where

$$D_\mu \chi = (\partial_\mu + i g_\phi \phi_\mu + i g_V V_\mu)\chi\,, \tag{7.5}$$

and $\phi_{\mu\nu}$, $V_{\mu\nu}$, and $F_{\mu\nu}$ are the field strengths for ϕ, V and the standard model photon respectively. For simplicity, we assume no kinetic mixing of ϕ to any

of the other gauge bosons. We further define the fine-structure constants, $\alpha_V = g_V^2/(4\pi)$ and $\alpha_\phi = g_\phi^2/(4\pi)$, and the usual $\alpha_{\rm EM} = e^2/(4\pi)$.

We will consider two benchmark models for the lighter of the two gauge bosons, ϕ. One benchmark that is weakly coupled and one that exhibits strong coupling an confinement. Both models will share the same phenomenology of self destruction, but can have difference cosmological histories as discussed in Section 7.3.5.

Weakly coupled model: In this case ϕ is assumed to be a weakly coupled U(1) gauge boson. This field is ϕ is assumed to be light enough to mediate a long range force which leads to $\chi\bar{\chi}$ positronium-like bound states with $n_* \sim 10$ energy levels. On the other hand, ϕ is taken to be too heavy to be emitted on-shell in transitions among energy levels. These constraints give

$$\frac{1}{4}\alpha_\phi^2 m_\chi < m_\phi < \frac{1}{2n_*}\alpha_\phi m_\chi \,. \tag{7.6}$$

We further assume that V is too heavy to play a role in the bound state dynamics, but is light enough to be emitted in the self-annihilation of the $\chi\bar{\chi}$ state, thus

$$\frac{1}{2}\alpha_\phi m_\chi < m_V \lesssim m_\chi \,. \tag{7.7}$$

We assume that $\alpha_V \gtrsim \alpha_\phi$ so that on-shell Vs are produced in a sizable fraction of the annihilation processes. Our last assumption is

$$m_V > 2m_e \,, \tag{7.8}$$

so V could decay into e^+e^- and can be detected easily.

Before proceeding, we comment on some possible alternative weakly coupled models. For example, one could consider a model with a single vector

boson from the dark sector playing the roles of both ϕ and V. However, in this case, Eq. (7.8) with $\alpha_\phi \lesssim 10^{-2}$ and $n_* \sim 10$, and the upper bound in Eq. (7.10) can only be reconciled when $m_\chi \gg 1$ GeV. As we are interested in a wide range of m_χ, as low as the MeV scale, see Section 7.3.2, we keep both ϕ and V in the following discussion. Another possibility is to allow ϕ to also mix with the SM photon, a possibility which, for the most part, affect the signal rate estimated in Section 7.3.2. In addition, there may be other variants of this model where either or both V and ϕ are replaced by light scalars or pseudoscalars or when additional particles are introduced. We focus here on the gauge case for concreteness but other options are considered when the phenomenology is discussed in Section 7.6.

Strongly coupled model: In this case ϕ is assumed to a non-abelian gauge boson which is massless $m_\phi = 0$. In the UV, ϕ is weakly coupled and runs to become strong at some scale Λ_ϕ at which point the theory becomes confining. We will assume that the confinement scale is lower than the mass of χ or any other ϕ-colored state,

$$\Lambda_\phi < m_\chi \tag{7.9}$$

Once produced (at zero temperature), a $\chi\bar{\chi}$ bound state will exhibit quirky dynamics [219]. The $\chi\bar{\chi}$ pair remains bound by a string and will loose energy by emitting glueballs with mass $\sim \Lambda$. Such a bound state will settle in a Coulombic bound state with a Bohr radius of $r_B \sim \alpha_\phi(m_\chi) m_\chi/2$, where $\alpha_\phi(m_\chi)$ is the coupling evaluated at the scale m_χ which is perturbative. The typical energy splittings in this atom-like system are of order $\alpha_\phi^2(m_\chi) m_\chi/4$. We will assume that the gap in the theory, given by the glueball mass Λ_ϕ is such that an on-shell glueball is too heavy to be radiated in transitions among these states. Combining these

requirements, we will consider the region of parameter space

$$\frac{1}{4}\alpha_\phi^2 m_\chi < \Lambda_\phi < m_\chi \,. \tag{7.10}$$

The restrictions on the mass of V will be the same in the weakly coupled model, Equations (7.7) and (7.8).

Though both of these frameworks are quite different in the UV, the bound state dynamics and lifetimes of the various states will be similar. In the next subsection we estimate the various relevant lifetimes using the language of the weakly couple model, though the results apply to both.

7.3.1 Bound state lifetimes

We now consider the lifetimes of the $\chi\bar{\chi}$ bound states. As we show below, states with $\ell \gtrsim 10$ have lifetimes much longer than the cosmological bound on DM lifetime, while S-wave states annihilate very quickly, within the time it traverses the Earth.

In the vacuum, bound states could be destroyed either by direct $\chi\bar{\chi}$ annihilation or by de-excitation to a lower-ℓ state. We begin with an estimate of direct annihilation to Vs. (In the following we also refer to V as the dark photon.) The number of Vs in the final state is denoted by N_V. This number is 2 for bound states that are even under charge conjugation and 3 for odd ones. The leading decay to consider is thus $\Psi_{n,\ell} \to VV$ or $\Psi_{n,\ell} \to VVV$. The amplitude for annihilation into dark photons for the $\Psi_{n,\ell}$ state is proportional to the ℓth derivative of the wave function at the origin. Roughly speaking every derivative result in

an extra power of α_ϕ in the amplitude. Assuming no significant phase space suppression, these decay rates can be estimated by [193],

$$\Gamma_{n,\ell\to V's} \sim \left(\frac{\alpha_\phi}{n}\right)^{2\ell+3} \alpha_V^{N_V} m_\chi \,, \tag{7.11}$$

Annihilation into $\phi\phi$ or into ϕV have a similar power counting. With $m_\chi \sim 1\,\text{GeV}$, and $\alpha_V \sim \alpha_\phi \sim 10^{-2}$ we find that, for example, the inverse width of annihilation of the $\Psi_{n=10,\ell=9}$ state is about 10^{42} seconds, while $\Psi_{n=7,\ell=6}$ lives for about 10^{22} sec. The latter is too short to evade bounds on the lifetime of all of DM, but is safe if that state is a small fraction of the DM.

Next, we consider de-excitation. Since $m_V, m_\phi > \alpha_\phi^2 m_\chi/4$, the de-excitation of $\Psi_{n,\ell}$ to lower states cannot happen via on-shell ϕs or Vs. Rather the leading decay is to three photons through an off shell V or an off shell ϕ, if it couples to the SM. The binding energy difference, of order $\sim \alpha_\phi^2 m_\chi$, is assumed to be too small to emit a pair of e^+e^- for all the parameter space under consideration. There is also the possibility for the off-shell V^* to turn into two neutrinos via its kinetic mixing with the SM Z-boson. The partial rate, in this case, is even more suppressed than the two or three photon final states we are considering.

The de-excitation rate of $\Psi_{n,\ell} \to \Psi_{n-1,\ell-1}$ via off-shell V is approximately

$$\Gamma_{n,\ell\to n-1,\ell-1} \sim \left(\frac{\alpha_\phi}{n^2}\right)^2 \frac{\alpha_V \epsilon^2 \alpha_{\rm EM}}{m_V^4} \frac{\alpha_{EM}^3}{m_e^8} \left(\frac{\alpha_\phi^2 m_\chi}{n^3}\right)^{13} \,, \tag{7.12}$$

where the term in the first parentheses α_ϕ/n^2 is the matrix element for dark photon radiation from the bound states, and the term in the last parentheses $\alpha_\phi^2 m_\chi/n^3$ stands for the difference in binding energy. This dimensionful quantity is raised to the thirteenth power in order to make up the dimension of the rate. For example, with $m_\chi \sim m_V \sim 1\,\text{GeV}$, $\epsilon \sim 10^{-2}$, and $\alpha_V \sim \alpha_\phi \sim 10^{-2}$ we find that the lifetime of the $\Psi_{n=10,\ell=9}$ state is about 10^{41} seconds, making it cosmologically stable. The lifetime is even longer for smaller values of m_χ, or for transitions with $\Delta\ell > 1$.

If ϕ also mixes with the photon, the bound state de-excitation rate via off-shell ϕ can be estimated in a similar way, with the V kinetic mixing parameter and the dark photon mass replaced by those of ϕ. If ϕ is a scalar particle and does not mix with the SM Higgs boson, the de-excitation is even slower because it requires at least three loops and two powers of the kinetic mixing parameter ϵ for it to decay into two SM photons.

We have thus shown that high-ℓ excitations of the $\chi\bar{\chi}$ bound state are cosmologically stable and are a viable candidate to be at least a portion of DM. On the other hand, the bound states with small n and ℓ quantum numbers can decay much faster, into $2V$ or $3V$, depending on its charge-conjugation parity ($C = (-1)^{L+S}$) as discussed above. The amplitude for an S-wave $\chi\bar{\chi}$ bound state to annihilate into $2V$ is proportional to its wave function at the origin, and, neglecting phase space effects, the decay rate is

$$\begin{aligned} \Gamma_{\Psi^{(+)}_{n,0}\to 2V} &= \frac{\alpha_\phi^3 \alpha_V^2 m_\chi}{2n^3}\,, \\ \Gamma_{\Psi^{(-)}_{n,0}\to 3V} &= \frac{2(\pi^2-9)\alpha_\phi^3 \alpha_V^3 m_\chi}{9\pi n^3}\,. \end{aligned} \tag{7.13}$$

Setting $m_\chi = 1\,\text{GeV}$, $\alpha_V = \alpha_\phi = 0.01$, and a DM speed of $v \sim 10^{-3}$ we find the decay length of the ground state to be, $v\tau_{\Psi^{(+)}_{1,0}\to 2V} \sim 4\times 10^{-7}$ cm, or $v\tau_{\Psi^{(-)}_{1,0}\to 3V} \sim 3\times 10^{-4}$ cm, which is a prompt decay. For an S-wave state with $n \leq 10$ the decay is prompt in view of DM or neutrino detectors.

In conclusion, the model has the two desirable ingredients: a cosmologically long lived state and a short lived one that can generate a signal in the detector. The next task is to estimate the rate for transitioning from the long to the short lived states.

7.3.2 Bound state scattering

In this subsection, we demonstrate how collisions of a high-ℓ, long-lived bound state Ψ with a nucleus can induce a transition to a lower ℓ state Ψ' that decays quickly into SM particles. The amplitude for the leading non-relativistic inelastic scattering of a proton with a bound state

$$\Psi(\vec{p}_1) + p(\vec{p}_2) \to \Psi'(\vec{p}_3) + p(\vec{p}_4), \tag{7.14}$$

occurs via t-channel dark photon (V) exchange and it takes the form

$$\mathcal{M}_{\Psi+p\to\Psi'+p} = 4m_\chi F_D(|\vec{q}\,|)\frac{g_V\epsilon e}{|\vec{q}\,|^2 + m_V^2}\bar{u}_p(\vec{p}_4)\gamma^0 u_p(\vec{p}_2)\,. \tag{7.15}$$

Here u_p is the proton spinor, and $F_D(|\vec{q}\,|)$ is the form factor for the $\Psi \to \Psi'$ transition in the presence of a three-momentum $\vec{q} = \vec{p}_3 - \vec{p}_1$ injection,

$$F_D(|\vec{q}\,|) = \int d^3\vec{x}\,\Psi'^*(\vec{x})\Psi(\vec{x})\left[e^{i\vec{q}\cdot\vec{x}/2} - e^{-i\vec{q}\cdot\vec{x}/2}\right]\,. \tag{7.16}$$

In the following we estimate $F_D(|\vec{q}\,|)$ by making the approximation that Ψ and Ψ' are Coulomb-like wave functions. Parity invariance implies that the orbital angular quantum numbers of the initial and final states in Eq. (7.16) must differ by an odd integer.

The differential scattering cross section off a nucleus (with atomic and mass numbers Z, A) takes the approximate form

$$\frac{d\sigma_{\rm scatter}}{d|\vec{q}\,|^2} \simeq \frac{g_V^2\epsilon^2 e^2}{4\pi v^2(|\vec{q}\,|^2 + m_V^2)^2} \times \left|F_D(|\vec{q}\,|)\right|^2 \times Z^2F^2(|\vec{q}|)\,, \tag{7.17}$$

where $v \simeq 10^{-3}$ is the incoming DM bound state velocity. For $F(|\vec{q}|)$, the nuclear form factor, we use the Woods-Saxon form given in [269]. Note that when Ψ' is a deeper bound state than Ψ, both the binding energy difference and the initial

kinetic energy contribute to the momentum transfer, $\vec{q}$. In the small v limit, the upper and lower limit of $|\vec{q}|^2$ take the form

$$\left(|\vec{q}|^2\right)^{\max}_{\min} = 2\mu_{\Psi' A}(m_\Psi - m_{\Psi'}) \pm \mu_{\Psi' A} v \left(\frac{m_\Psi}{m_{\Psi'}}\right) \sqrt{8\mu_{\Psi' A}(m_\Psi - m_{\Psi'})} + O(v^2)\,, \tag{7.18}$$

where the reduced mass $\mu_{\Psi' A}$ is defined as $\mu_{\Psi' A} = m_{\Psi'} m_A/(m_{\Psi'} + m_A)$. For weakly bounded states, we have $m_\Psi \sim m_{\Psi'} \simeq 2m_\chi$ and $m_\Psi - m_{\Psi'} \sim m_\chi \alpha_\phi^2$. The above expansion converges for $\alpha_\phi \gtrsim v$, *i.e.*, when the binding energy release, $m_\Psi - m_{\Psi'} \sim m_\chi \alpha_\phi^2$, dominates over the DM kinetic energy, $\sim m_\chi v^2$. To further simplify the result, we consider the limit $|\vec{q}^2| \ll m_V^2$ and $m_\Psi \ll m_A$, which is the region of interest for this study. In this case, the scattering cross section is approximately,

$$\sigma_{\text{scatter}} \simeq \frac{64\pi\epsilon^2 \alpha_{\text{EM}} \alpha_V \alpha_\phi m_\chi^2}{\pi v m_V^4} \times \left|F_D(|\vec{q}\,|)\right|^2 \times Z^2 F^2(|\vec{q}|)\,, \tag{7.19}$$

with $F_D(|\vec{q}\,|)$ and $F(|\vec{q}\,|)$ evaluated at the typical momentum transfer, $|\vec{q}| \sim m_\chi \alpha_\phi$. Numerically, $F(|\vec{q}|) \simeq 1$ and the typical value of $F_D(|\vec{q}\,|)$ is around 10^{-2} for $\alpha_\phi = 10^{-3} - 10^{-2}$.

Before proceeding to estimate a signal rate, we note that if the lighter vector boson ϕ were allowed to have a kinetic mixing $\epsilon_\phi \phi_{\mu\nu} F^{\mu\nu}$, the scattering rate in Equation (7.19) would have an additional contribution with m_V andϵ replaced by m_ϕ andϵ_ϕ. This contribution can potentially be larger because ϕ is lighter. In this sense the rate estimate in the next subsection, where ϵ_ϕ is set to zero, is conservative.

7.3.3 Signal Rates in Neutrino Detectors

Once a high-ℓ state hits the Earth, it scatters and transitions to a low-ℓ state which is short-lived. Generically, the short-lived state decays promptly to two

or three Vs, both of which can have signals in a large detector. The signal event rate depends primarily on the rate of transitions from long- to short-lived states. It takes the familiar form

$$\Gamma_{\rm signal} = N_T^{(\rm eff)} n_\Psi \langle \sigma v \rangle_{\rm scatter} \ , \tag{7.20}$$

where $N_T^{(\rm eff)}$ is the effective number of target nuclei which is defined below and $\langle \sigma v \rangle_{\rm scatter}$ is the velocity average of the cross section to scatter and transition from the high to the low-ℓ state.

The precise nature of the signal and the effective number of target nuclei depend on the lifetime of the short lived state Ψ' and and the mediator V. It is convenient to define the average decay lengths for these two states

$$L_{\Psi'} = \gamma_{\Psi'} v_{\Psi'} \tau_{\Psi'} \ , \qquad L_V = \gamma_V v_V \tau_V \ , \tag{7.21}$$

where the τs are the respective lifetimes of the two particles, $\gamma_{\Psi'} \approx 1$ and $v_{\Psi'} \sim 10^{-3}$ are the typical boost and velocity of the meta-stable state, while γ_V and v_V are the boost and velocity of V which are set in any given kinematics. In the case of $\Psi' \to 2V$ decay,

$$L_V = c\tau_V \sqrt{m_{\Psi'}^2/4m_V^2 - 1}. \tag{7.22}$$

We can now estimate the effective number of target nuclei $N_T^{(\rm eff)}$. If both decay lengths are shorter than the typical size of the detector, $L_{\Psi'}, L_V < L_{\rm det}$ the calculation is simple. Since neither particle can travel far the transition scattering has most likely happened inside the detector and the number of targets is simply the number of nuclei in the detector

$$L_{\Psi'}, L_V < L_{\rm det} \ : \qquad N_T^{(\rm eff)} \sim n_{\rm det} \, V_{\rm det} \ , \tag{7.23}$$

where $n_{\rm det}$ and $V_{\rm det}$ are the number density of nuclei and the volume of the detector. In this case, the coherence factor in scattering, the Z^2 factor in Eq. (7.19),

should be taken as that of the detector material, be it water, liquid argonne, etc.

In the case that either of the decay lengths is larger than the typical detector size, $L_{\Psi'} > L_{\rm det}$ or $L_V > L_{\rm det}$, the production of Vs is likely to occur elsewhere in the Earth. It is interesting that even in this case, the effective number of target nuclei is parametrically the same as in the short lifetime case. Consider, for example, the case where L_V is much longer than the detector but shorter than the size of the earth, while $L_{\Psi'}$ is short. In this case, we can assume the decay of Ψ' to Vs occurred at the scatter site. The effective number of targets is a sum over Earth nuclei, weighted by the probability that a V decays inside the detector given that is originated near the nucleus in question

$$L_{\rm det} < L_V \lesssim R_\oplus : \qquad N_T^{(\rm eff)} \sim n_\oplus \int_{\oplus \cap L_V} d^3\vec{r}_T \frac{L_{\rm det}^2}{4\pi |\vec{r}_{\rm det} - \vec{r}_T|^2} \frac{L_{\rm det}}{L_V} \sim n_\oplus \, V_{\rm det} \,, \tag{7.24}$$

where the integration limits are

$$|\vec{r}_T| < R_\oplus \quad \text{and} \qquad 0 < |\vec{r}_{\rm det} - \vec{r}_T| < L_V \tag{7.25}$$

in a coordinate system in which the origin is at the center of the Earth. Here we have treated the earth as a sphere of constant density $n_\oplus$. The fraction in the integrand is the suppression due to the small solid angle that the detector subtends, as seen from the scatter site. In the last step, we have used the fact this suppression factor is undone by the fact that the number of target nuclei grows like $|\vec{r}_{\rm det} - \vec{r}_T|^2$ (which will show up as a Jacobian). This effect is similar to the signal rate in [246]. Note that here we do not account for an $O(1)$ geometrical factor, which, for example, comes from the fact that there is more Earth below the detector than above it. The case in which both L_V and $L_{\Psi'}$ are larger than the detector is slightly more convoluted but parametrically similar. Note, that in cases of long lived V and/or Ψ' the coherence factor of Z^2 would be the averaged over the rock, perhaps dominated by iron, but may get contributions from

heavier elements such as lead. In practice, we use a more realistic earth density profile [270] to derive the upper bounds on ϵ.

Though the signal rate does not depend strongly on L_V, the character of the signal does. In the case of a short lived V, $L_V < L_{\rm det}$, both Vs can decay inside the detector and will result in *two* back-to-back or *three* e^+e^- (or $\mu^+\mu^-$, if kinematically allowed) pairs. In the case where $L_V > L_{\rm det}$ it is more likely that just one such pair will be in the detector. In the case where L_V is much longer than the underground depth of the laboratory, there will be more events coming from below than from above. These, and other signal characteristics are discussed in more detail in Section 7.6.

The reach of a particular experiment depends on the detector-specific background rate for the signal in question. Though we expect very little background that mimics our particular signals, we did not delve into these detector-specific details. Instead, we simply estimate the event rates in several detectors as a function of the model parameters. In Fig. 7.2, we show the parameters that lead to 100 events per year in the $\epsilon - m_\chi$ plane. For a weakly-coupled bound state as the SDDM, its mass is related to that of χ, $m_\Psi \simeq 2m_\chi$.

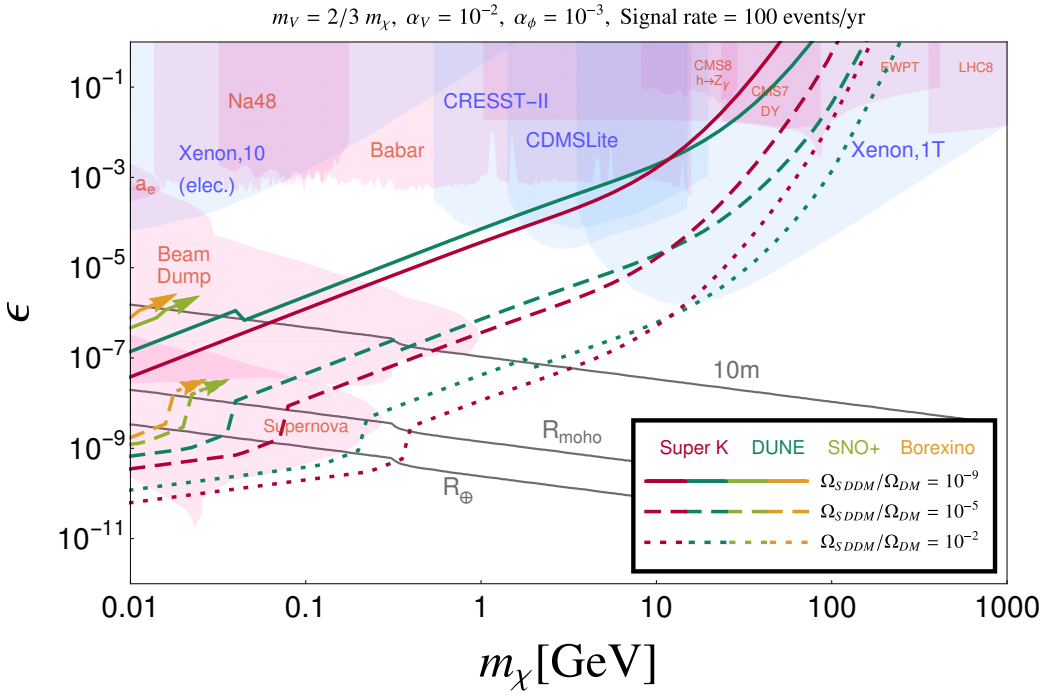

Figure 7.2: Contours that give 100 DM self-destruction events per year in the $\epsilon - m_\chi$ parameter space of the angular momentum model. The other parameters are chosen to be $m_V = 2m_\chi/3$, $\alpha_V = 0.01$, $\alpha_\phi = 0.001$. The colorful thick curves correspond to Super-Kamiokande (red), and DUNE (dark green). Contours for SNO+ (light green), Borexino (orange) are shown as arrows in order to reduce the number of curves with the understanding that they run parallel to that of Super-K. The solid, dashed and dotted curves assume the initial DM bound state is $\Psi_{10,9}$ and comprises 10^{-9}, 10^{-5} and 10^{-2} of the total DM relic density, respectively. The gray curves correspond to constant decay length contours of the dark photon V (see Section 7.6 for their effect on the signal characteristics). The light red and blue shaded regions show the existing experimental constraints from searching for visibly-decaying dark photons and DM direct detection (assuming χ to be the dominant DM), respectively.

The colorful thick curves correspond to the observation of this rate of Ψ' decay events in various neutrino experiments: Super-Kamiokande, SNO+, Borex-

ino and DUNE.[1] In order to reduce the clutter in the plot, we have denoted the limits on the smaller two experiments with arrows, with the understanding that their rate contours run parallel to those of Super-K. The 100-event-per-year contour for ϵ is given by:

$$\epsilon_{100}^2 = \frac{100 \text{ events}}{T_{\text{year}} \times nV \times n_{\chi\bar{\chi}} \langle \sigma v \rangle_{\text{scatter}}^{(\epsilon=1)} \times \text{Br}\,(V \to l^+ l^-)}\,, \tag{7.26}$$

where nV is the effective number of targets, defined by the terms in parentheses in Eqs. (7.23) and (7.24) for $L_V < L_{\text{det}}$ and $L_V > L_{\text{det}}$ respectively. Our result is a rough estimate as we have omitted the $O(1)$ geometry-dependent factor for $L_V > L_{\text{det}}$ and we neglected the density variations in the Earth. The curves in Fig. 7.2 are derived assuming that the initial DM bound state is $\Psi_{10,9}$ and comprises 10^{-9}, 10^{-5} or 10^{-2} of the total DM relic density. For the final state Ψ', we consider all possible S-wave bound states with $n = 1, \ldots, 9$. (Note that this is a conservative assumption as we did not consider the effect of any non-S-wave states.) The model parameters in the plot are set to: $m_V = (2/3)\, m_\chi$, $\alpha_V = 0.01$ and $\alpha_\phi = 0.001$. Since we have used $\alpha_\phi \ll \alpha_V$ the resulting unstable bound state annihilates predominantly into two Vs (and then into SM particles). In the shaded regions, we also show the existing experimental constraints from searching for visibly-decaying dark photons [271–273] as well as direct detection (assuming χ to be the dominant DM). Interestingly, the signals can help to probe a large portion of the parameter space that is not yet accessible otherwise with the existing dark photon searches. This gives a strong motivation for exploring the neutrino experimental data and looking for the existence of DM bound states in nature. Although the current neutrino detectors focus on energy ranges relevant for incoming neutrinos [274–277], they are also sensitive to higher energy ranges and might be used to probe SDDM up to higher masses. We will return to a more

[1] Our signal could also be constrained by the IceCUBE experiment which due to its higher threshold will cover the mass window above tens of GeV.

detailed discussion of the phenomenology of SDDM and some search strategies in Section 7.6.

7.3.4 Challenges in SDDM production in early universe

In Section 7.2 we derived an upper limit on the temperature in which SDDM is produced:

$$T_{\text{survival}} \sim 10\,\text{MeV} \times \left(\frac{10\,\text{MeV}}{m_\chi}\right), \tag{7.27}$$

this leaves two possibilities for the production of SDDM: early universe production below T_{survival} or late time production in our galaxy. Here we explore the challenges in realizing the first option, while in the next section we explore mechanisms for late time production. As we will see, the cosmology of early universe production in this model is challenging and might involve a non-thermal production or other mechanisms.

The difficulty arises from the constraint Eq. (7.10), which implies that the mediator ϕ is heavier than the Rydberg energy, $m_\phi > (\alpha_\phi^2 m_\chi)/4$. This implies that even at zero temperature, an incoming mediator has the potential to dissociate the $\chi\bar{\chi}$ bound states. This fact strongly restricts the production mechanisms of $\chi, \bar{\chi}$ bound states in the early universe. We now discuss several possible production mechanisms. We leave a more dedicated study of these possibilities for a future work.

Thermal freeze out. Consider the case where χ, $\bar{\chi}$, and ϕ are in thermal equilibrium with each other in the early universe. For simplicity, we assume that the dark sector has the same temperature as the SM sector. Around $T \sim m_\chi/25$, the χ and $\bar{\chi}$ particles freeze out by annihilating into ϕs and/or Vs. Assuming $\alpha_\phi \sim \alpha_V$,

their relic abundances satisfy

$$\Omega_\chi = \Omega_{\bar{\chi}} \sim 10^{-4} \left(\frac{\alpha_\phi}{0.01}\right)^{-2} \left(\frac{m_\chi}{1\,\text{GeV}}\right), \qquad \frac{n_\phi}{n_\chi} \sim 10^{14} \left(\frac{\alpha_\phi}{0.01}\right)^{2} \left(\frac{m_\chi}{1\,\text{GeV}}\right)^{-1} . \tag{7.28}$$

After freeze out, $\chi, \bar{\chi}$ bound states could be formed through the process $\chi + \bar{\chi} \to (\chi\bar{\chi}) + \phi$, where $(\chi\bar{\chi})$ is a $\chi\bar{\chi}$ bound state. Since the formation rate is smaller than the Hubble expansion, the resulting bound state relic abundance is given by

$$\Omega_{BS} = \Omega_\chi \frac{R_{BSF}}{H}, \qquad R_{BSF} = n_\chi \sigma_{BSF} , \tag{7.29}$$

where σ_{BSF} is the bound state formation cross section. On the other hand, a bound state could be dissociated by encountering a ϕ particle, $(\chi\bar{\chi}) + \phi \to \chi + \bar{\chi}$. The dissociation cross section σ_{DIS} is related to σ_{BSF} via crossing symmetry. For $T \gtrsim m_\phi$, the two are related by $\sigma_{DIS} \sim (m_\chi/T)^{3/2} \sigma_{BSF}$ [236]. Note that because the ϕ mass is greater than the binding energies, see Eq. (7.10), we must rely on the kinetic energies of $\chi, \bar{\chi}$, dictated by the temperature T, for bound state formation to occur. The dissociation rate for each bound state is then

$$R_{DIS} = n_\phi \sigma v_{DIS} \sim \left(\frac{n_\phi}{n_\chi}\right) \left(\frac{m_\chi}{T}\right)^{\frac{3}{2}} R_{BSF} . \tag{7.30}$$

From Eqs. (7.28) and (7.29), we learn that the probability for a bound state to dissociate satisfies,

$$P_{DIS} = \frac{R_{DIS}}{H} \gtrsim 10^8 \left(\frac{m_\chi}{T}\right)^{\frac{3}{2}} \left(\frac{\alpha_\phi}{0.01}\right)^{4} \left(\frac{m_\chi}{1\,\text{GeV}}\right)^{-2} . \tag{7.31}$$

The above result implies that all bound states are quickly destroyed within a Hubble time as soon as they are produced.

This is a problem since we would like $\Omega_{BS} > 10^{-10}$ for the SDDM to be of experimental interest (see Fig. 7.2). This problem could be cured if we further extend the dark sector with light states which ϕ can annihilate or decay into. The coupling of these light states to ϕ has to be large enough to deplete the ϕ

population and prevent bound-state dissociation. Its coupling to the χ, has to be small enough to not dissociate the bound states themselves.

χ as asymmetric DM. Since χ is much lighter than the weak scale, the thermal production scenario cannot accommodate a situation where χ comprises all the DM relic abundance. It is then tempting to consider the production of χ in an asymmetric scenario. Additionally, in such a scenario one can avoid cosmological constraints on DM annihilation such as the CMB [278]. The problem with this scenario is that the number of $\bar{\chi}$ is exponentially suppressed at late time [279, 280] because the $\chi\bar{\chi}$ annihilation cross section is very large. The exponential suppression of $\bar{\chi}$ would make it even harder to form any $\chi\bar{\chi}$ bound states in the early universe.

Non-thermal history. The thermal freeze out picture we discussed above does not work in its minimal form mainly because it produces many more ϕ particles than χ and $\bar{\chi}$. This problem could be alleviated if the dark sector particles are produced non-thermally, with a suppressed n_ϕ/n_χ ratio compared to Eq. (7.28). Non-thermal production mechanisms include the freeze-in of χ and $\bar{\chi}$ through a small kinetic mixing between V and/or ϕ and the SM photon, or the late decay of some heavier dark sector states. The relic abundance of high-ℓ bound states in these cases is model dependent but it seems plausible that they can still be probed in neutrino detectors.

Additional confining dark force. Another way of efficiently producing the high-ℓ bound states is to replace ϕ by a confining dark force. This implies that χ is colored under a non-abelian dark gauge interaction. In this case, there are no free χ and $\bar{\chi}$ particles at distances larger than the inverse of the dark confinement scale. In that case, it is likely for the high-ℓ $\chi\bar{\chi}$ states to form efficiently [219].

If the dark confinement scale of this gauge interaction is very small, the low-level states are to a good approximation given by a $1/r$ potential. Then, the self-destructing DM scattering, which involves short-distance physics, and the experimental detection discussions in section 7.3.2 still remain valid.

7.3.5 Scenarios for late time SDDM production

We present three possible scenarios for the late time production of SDDM below T_{survival}. This list is by no means exhaustive. These scenarios are: (a) a late time decay of a heavy scalar Φ (b) late time binding in neutron stars (c) dark hydrogen collisions. Below we provide heuristic descriptions of these late time binding scenarios.

Late time decay

In this scenario, we focus on the strongly coupled benchmark presented earlier in Section 7.3. The dark sector contains a confining gauge group (*e.g.*, $SU(N)$) and the elementary particle χ belongs to the fundamental representation of it. For χ production, we introduce a heavy scalar Φ with a Yukawa coupling to χ, $y\bar{\chi}\chi\Phi$. We assume that Φ obtains a small primordial relic abundance in the early universe, making up a subdominant portion of the dark matter energy density. The Yukawa coupling y is taken to be small enough so that the decay of Φ into $\chi, \bar{\chi}$ only occurs at temperatures below T_{survival}, defined in subsection 7.2. This provides a non-thermal production mechanism with a naturally suppressed population of the dark force carriers (the gluons of the dark $SU(N)$ gauge symmetry, or dark glueballs at low energies), which is favored based on

the discussions in the previous subsection. After the decay of Φ, the $\chi, \bar{\chi}$ particles will eventually form bound states when their number density drops below the Λ^{-3}, where Λ is the energy scale for $SU(N)$ confinement. For $m_\chi \gg \Lambda$, this corresponds to the quirky picture [219], and the $(\chi\bar{\chi})$ bound states are expect to first form in the excited states, with large orbital angular momentum, ℓ. These excited states could de-excite by radiating the dark gluons, with $\Delta\ell = 1$ after each radiation. Eventually, after the de-excitations are completed, the resulting $(\chi\bar{\chi})$ bound states will have a wide range of ℓ. As discussed in subsection 7.3.1, the low ℓ states are unstable and will decay away quickly, whereas the high ℓ states are cosmologically long lived and could serve as the SDDM candidate if there exist a dark photon to mediate the interaction between χ and our sector. The states with intermediate values of ℓ could be still decaying today and provide additional indirect detection signals for testing this scenario.

Dark Hydrogen Collisions

In this section, we present a potentially working and calculable model of late time production of SDDM in the galaxy. The starting point is the weakly coupled model presented earlier, in which ϕ is a U(1) gauge boson. To enhance late time production we will make use of the Fermi and Teller mechanism [281] for low energy protonium production. We will sketch the basic picture here, while a more systematic use of the Fermi-Teller mechanism in the dark sector will appear in [282].

In [281], the following protonium production process was considered,

$$H + \bar{p} \rightarrow (p\bar{p}) + e\,. \tag{7.32}$$

It was concluded that its cross section is at least geometric ($\sigma_{\rm FT} \simeq \pi r_b^2$ where

$r_b = (\alpha m_e)^{-1}$ is the Bohr radius of the hydrogen atom), in particular when the incoming antiproton is slow, *i.e.*, $E_K \to 0$. The reason is that for impact parameters $\sim r_b$, the $p\bar{p}$ system can no longer support an e bound state, and the electron is ionized. The condition for generating a bound state is $E_K < -E_B$, the binding energy of the electron. In this case there is a high probability for the $p\bar{p}$ to bind into protonium. As we will see, because the size of the incoming hydrogen (dictating the impact parameter) is much larger than that of the ground state protonium, the generated protonium tends to have high-n and high-l.

We will consider dark matter bound state formation by making analogy to this elegant binding mechanism. We introduce a dark sector containing a dark proton χ and dark electron ψ (much lighter than χ) having opposite charges under a dark $U(1)$ gauge symmetry. In analogy to baryon number, we assume that there is a global symmetry that prevent the decay $\chi \to \psi + \phi/V$ to occur. We assume the dark photon ϕ is massive, but its mass is small enough for the $\chi - \psi$ to bind efficiently. To prevent the dissociation of dark hydrogen in the presence of the relic ϕ, we assume:

$$m_\phi \; < \; \frac{1}{2} E_B \, . \tag{7.33}$$

where $E_B = \frac{1}{2}\alpha_\phi^2 m_\psi$ is the $\chi - \psi$ binding energy. In particular, that means that

$$m_\phi \; < \; \frac{1}{4}\alpha_\phi^2 m_\chi \, , \tag{7.34}$$

in contrast with Eq. 7.10. This means that in this variant of our model the SDDM *will* be able to transition to lower ℓ states and eventually self-annihilate. However, by choosing m_ϕ to be larger than several energy splittings in $(\chi\bar{\chi})$ state, we can make its decay length long enough to observe significant flux on Earth.

In the early universe, the relic abundance of ψ is set by a primordial asymmetry. The $\psi\bar{\psi}$ annihilation cross section is sufficiently large so that all the $\bar{\psi}$

particles have been annihilated away and only ψ particles are around. On the other hand, the relic abundance of χ is symmetric. As the temperature of the dark sector cools below E_B, the dark recombination will occur allowing χ and ψ to capture each other and form hydrogen-like bound states. After the dark recombination, the universe contains a relic abundance of the dark hydrogen and free $\bar{\chi}$ particles.

This is exactly the composition that allows for the Fermi-Teller process to take place in the following evolution of the universe. In particular, we consider the following process to occur in the galaxy today

$$(\chi\psi) + \bar{\chi} \rightarrow (\chi\bar{\chi})_{nl} + \psi\,. \tag{7.35}$$

The cross section for such a process is

$$\sigma_{\rm FT} = \pi\left(\frac{f}{\alpha_\phi m_\psi}\right)^2\,, \tag{7.36}$$

where the factor f was calculated by Bracci et al. [283] for the original Fermi-Teller process and was found to be in the range $2-10$, depending on the collision energy. To be conservative we will assume here that $f \sim 2$.

By energy conservation (assuming zero kinetic energy of the outgoing ψ) it is straightforward to derive that the principle quantum number of the final $(\chi\bar{\chi})$ bound state is

$$n \sim \frac{1}{\sqrt{2(\frac{m_\psi}{m_\chi} - \frac{v^2}{\alpha_\phi^2})}}\,, \tag{7.37}$$

where $v = 10^{-3}$ is the average DM velocity in the galaxy. For example, with the following set of parameters $m_\chi/m_\psi \sim 50$, $\alpha_\phi = 7.5\times10^{-3}$, we can get $n \sim 15$. The maximal angular momentum of the final $(\chi\bar{\chi})$ bound state can be estimated as

$$\ell_{\rm max} = m_\chi v b_{\rm crit} \sim f\frac{m_\chi}{m_\psi}\frac{v}{\alpha_\phi}\,. \tag{7.38}$$

With the same set of parameters, we find that $\ell_{\max} \sim 13$ so that the high-n, high-ℓ $(\chi\bar{\chi})$ bound states can be efficiently formed through this process. These are nothing but our desired SDDM candidates.

Due to the Fermi-Teller process, every point in the galaxy has an average SDDM production rate per volume of

$$\frac{d\Gamma_{\rm SDDM}}{dV} = f_{(\chi\psi)}\, f_{\bar{\chi}} \left(\frac{\rho_{\rm DM}}{m_\chi}\right)^2 r_{\rm SDDM}\, \sigma_{\rm FT}\, v\,, \tag{7.39}$$

where $r_{\rm SDDM}$ is the $O(1)$ fraction of high-l states produced in the rearrangement process, and where $f_{(\chi\psi)}$, $f_{\bar{\chi}}$ are the fractions of $(\chi\psi)$ and $\bar{\chi}$ states in the total DM relic density. Assuming the formed SDDM has a mean free path $d_{(\chi\bar{\chi})}$ (the shortest of its decay length and mean free path for dissociation), most of the SDDM that could reach the earth are formed within a sphere with radius $d_{(\chi\bar{\chi})}$ around the Earth. More precisely, the flux of SDDM coming from all over the galaxy is then

$$\Phi^{\oplus}_{\rm SDDM} = \int d^3 r \frac{d\Gamma_{\rm SDDM}}{dV} \frac{1}{4\pi r^2}\, e^{-r/d_{(\chi\bar{\chi})}}\,, \tag{7.40}$$

where r is the distance to the earth. Assuming that $d_{(\chi\bar{\chi})}$ is smaller than the distance to the end of the Milky-way halo, and that the DM density is a constant $\rho_{\rm DM} \sim 0.3\,{\rm GeV/cm^3}$, we could expect a flux of SDDM

$$\Phi^{\oplus}_{\rm SDDM} \sim 10^4\,{\rm cm^{-2}\,sec^{-1}} r_{\rm SDDM} f_{(\chi\psi)}\, f_{\bar{\chi}} \left(\frac{10\,{\rm GeV}}{m_\chi}\right)^2 \left(\frac{100\,{\rm MeV}}{m_\psi}\right)^2 \left(\frac{0.01}{\alpha_\phi}\right)^2 \left(\frac{d_{(\chi\bar{\chi})}}{1\,{\rm kpc}}\right). \tag{7.41}$$

For the model parameters selected above, m_ϕ can be taken heavy enough such that the SDDM can only de-excite through a forbidden $\Delta\ell = 5$ transition, and so the decay length is much longer than 1 kpc. We still take 1 kpc as our reference value to account for effects that could destroy the SDDM like premature self-destruction, dissociation and inverse rearrangement. The resulting flux is significant, and is comparable to the flux of 1 TeV WIMPs. As we have shown

in Fig. 7.2, our model yields detectable signals even for fluxes a factor of 10^{-7} smaller. The attractive feature of this picture is that the SDDM does not have to be produced in the early universe but rather produced more recently in our galaxy. Therefore, the constraint on its lifetime could be relaxed compared to that estimated in section 7.3.1.

One by product of this late time production mechanism is that the Fermi-Teller process could also generate short lifetime ($\chi\bar{\chi}$) states that potentially lead to indirect detection signals.

Binding in neutron stars

In addition to the production in the early universe, we can consider the more recent production of $\chi\bar{\chi}$ bound states by a late time binding process of relic χ and $\bar{\chi}$. The ϕ particles are sufficiently diluted in the universe today so they no longer play a role in dissociation. Because m_ϕ is larger than the Rydberg energy, the χ and $\bar{\chi}$ in the initial state must have large enough velocities. One might imagine more efficient bound state formation inside neutron stars where χ and $\bar{\chi}$ are gravitationally accelerated. The formed bound states could be liberated if the neutron star belongs to a binary system which inspirals and finally merges [284]. This picture then ties the bound state formation rate to the neutron star merger rate.

7.4 Tunneling stabilization

We now consider a different mechanism to generate the meta-stable state of DM required for the self-destructing phenomenology. The idea is that the long-lived DM state is protected by a potential barrier which keeps the constituents apart, requiring exponentially suppressed tunneling to self annihilate. The same bound state can scatter into a short-lived bound state, where the constituents are localized closer together. This transition can happen through excitation to a de-localized state and a decay to the localized state near the origin.

A key ingredient in this tunneling stabilization mechanism is the existence of a metastable minimum far from the origin, so that the tunneling probability is exponentially small. This happens in nature usually due to an interplay between several forces, both attractive and repulsive. Consider for example the states that can be made of two deuterium atoms. The two atoms can be assembled into a di-deuterium molecule, D_2. The two nuclei of D_2 can, with a very long lifetime, tunnel through the Coulomb barrier to form a Helium-4 atom. Similarly, some common isotopes of table salt, NaCl, can tunnel to become a Nickel atom since they have the same number of protons, neutrons, and electrons. Though these examples are inspiring, they do not quite fulfill our requirements since excited molecular states of D_2 are still very unlikely to fuse into helium. Perhaps real-world examples which are closer to what self-destructing DM requires are super cooled systems in crystals and liquids [285].

To illustrate the main features of tunneling stabilization, we consider a different kind of $\chi\bar{\chi}$ bound state, one which is bounded not by a Coulomb mediator but by a potential $V(r)$ such that r is the relative distance between the χ and $\bar{\chi}$.

We remain agnostic as to the origin of this potential, but one can imagine an effective potential due to several mediators. Furthermore, we consider the case in which $V(r)$ has a global minimum at $r = 0$ and a local minimum at $r = R$, with the two separated by a potential barrier as shown in Fig. 7.3. This potential is reminiscent of a molecular potential, but with the coulomb barrier truncated by hand. We call a potential of this sort a two minima potential. This potential has three kinds of states:

- Long lifetime states centered around the local minimum at $r = R$.
- Short lifetime states centered around the global minimum at $r = 0$.
- excited states above the barrier which are de-localized within the full potential well.

Just like the angular momentum case, the S-wave decay rate of a $\chi\bar{\chi}$ state is proportional to its wavefunction squared at the origin

$$\Gamma_{\chi\bar{\chi}} = 4\pi \frac{\alpha_V^2}{m_\chi^2} \left|\psi_{\chi\bar{\chi}}(0)\right|^2 . \tag{7.42}$$

The states localized at $r = 0$ have significant support at the origin and so their lifetime is very short. In contrast to these, the states localized at $r = R$ have an exponentially small support at the origin and so their lifetime is very long. Additionally, the overlap of the long and short lifetime eigenfunctions is negligible, and so is the rate of spontaneous emission from one to the other. The excited states are unsuppressed at both $r = 0$ and $r = R$ so they quickly either annihilate or spontaneously emit a dark photon and relax to a lower state. When the depth of the global minimum is much larger than the local minimum, the number of short lifetime states is much larger than the number of long lifetime

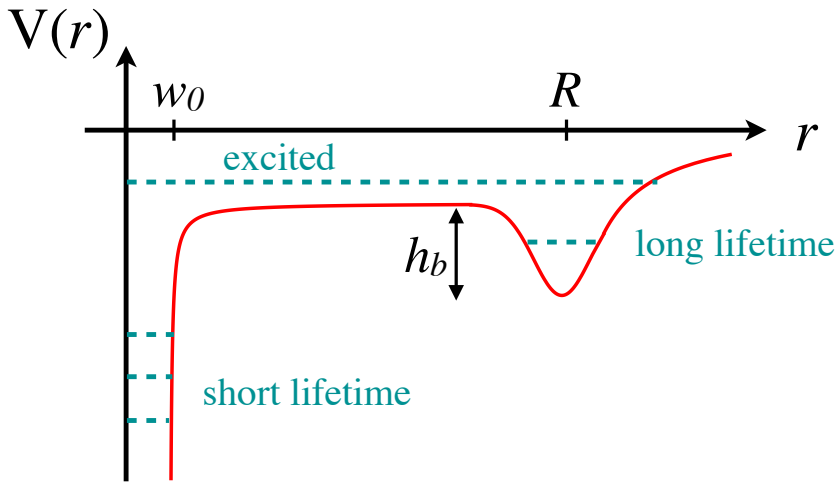

Figure 7.3: An illustration of a two minima potential as described in Section 7.4.

states ($N_{\text{Short}} \gg N_{\text{Long}}$). In that limit, the excited state decays predominantly to short lifetime states, which annihilate instantaneously.

For our SDDM scenario, we envision a fraction of DM is made up of the long-lived state with $\langle r \rangle \sim R$. An interaction of this state with a nucleus on Earth can excite it to the delocalized state, which then proceeds to decay and annihilate as discussed above. The annihilation products, assumed to be dark photons, can then decay in a detector leading to a signal. In the Appendix, we show a toy example which we used to estimate the various rates more quantitatively. We find that the lifetimes of the long, short and excited states scale as

$$\frac{\tau_{\text{Short}}}{\tau_{\text{Long}}} \sim \frac{\tau_{\text{excited}}}{\tau_{\text{Long}}} \sim e^{-2\sqrt{m_\chi h_b} R}, \tag{7.43}$$

where h_b is the height of the potential barrier.

In this work, we do not construct a full model which yields a potential similar to the one in Fig. 7.3. A working model, however, would need to have both

a significant barrier, say with $\sqrt{h_b}R \sim 20$, and excited bound states that can live classically above the barrier. Molecules found in nature have the former, but not the latter.

While we were unable to construct a full model, we do not see any fundamental reason that we will not be able to. We can speculate about ways to modify the molecular picture to make it viable to our model. One way is to add a confining potential that will make the probability to decay into the short lived state significantly. Another idea is to have droplets of a super-cooled dark fluid which make up a part of DM.

7.5 Symmetry stabilization

As a third class of models, we consider bound states in an asymmetric DM scenario, with the DM charged under baryon number. The self-destructing DM picture can be realized when the bound state interacts with SM nuclei.

More specifically, consider a Dirac fermion χ which carries the baryon number q, with $q \neq \pm 1, \pm 1/2$. The exchange of a scalar dark force carrier ϕ (with zero baryon number) allows both χ, χ and $\chi, \bar{\chi}$ to form bound states. Because the $(\chi\chi)$ bound state is stable, we can assume it comprises a significant fraction or even makes up all of the total DM relic abundance today.[1] We also introduce another fermion η which carries non-zero baryon number $1 + 2q$. The assigned baryon quantum numbers above allow a dimension 6 effective interaction between χ, η

[1] With a scalar dark force, it is possible for a large number of χ particles to form stable bound states (also called nuggets) [236, 286–290]. In principle, a similar phenomenon as discussed below could also apply to nuggets. For simplicity, we only consider two-body bound states here.

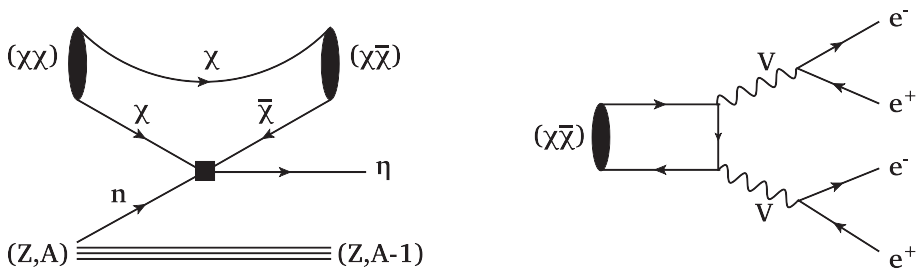

Figure 7.4: *Left*: Feynman diagram for the scattering process $(\chi\chi) + n \to (\chi\bar{\chi}) + \eta$ in the model described in Section 7.5. *Right*: A possible way of destructing the $(\chi\bar{\chi})$ bound state after the scattering.

and the neutron n,

$$\mathcal{L}_{int} = \frac{(\overline{\chi^c}\chi)(\bar{\eta}n)}{\Lambda^2} + \text{h.c.}\,. \tag{7.44}$$

If $2m_\chi < m_\eta + m_p$, the $(\chi\chi)$ bound state is stable. However, when it reaches the detector, the above interaction triggers the following reaction,

$$(\chi\chi) + n \to (\chi\bar{\chi}) + \eta\,, \tag{7.45}$$

as shown by the Feynman diagram in Fig. 7.4 (left). At the "partonic level" in the dark sector, one of the χs participates in the reaction $\chi + n \to \bar{\chi} + \eta$. The other χ is a spectator, and it becomes bounded with the $\bar{\chi}$ in the final state into a $(\chi\bar{\chi})$ bound state. After this reaction, a neutron is removed from the target and the final state particle η can escape away without further interaction. We consider $m_\eta \approx m_n$, and then the cross section for the scattering of a $(\chi\chi)$ ground state into a $(\chi\bar{\chi})$ ground state is,

$$\sigma_{(\chi\chi)+n\to(\chi\bar{\chi})+\eta} \simeq \frac{\mu_{\chi n}^2}{\pi\Lambda^4}\,, \tag{7.46}$$

where $\mu_{\chi n} = m_\chi m_n/(m_\chi + m_n)$, and we make the approximation that the dark form factor, in analogy to Eq. (7.16), is of order 1, when both $(\chi\chi)$ and $(\chi\bar{\chi})$ are in the ground states.

Like the other two scenarios we discuss before, the most striking signal is generated due to the destruction of the unstable $(\chi\bar{\chi})$ state. It can self-annihilate into SM particles via mediators (*e.g.*, a pair of dark photons, see Fig. 7.4 (right)) between the two sectors. The present data from neutrino and DM experiments can be interpreted as constraints on the cutoff scale Λ. As an estimate, if the $(\chi\chi)$ bound state comprises all the DM relic abundance, having 100 events per year from $(\chi\chi) \to (\chi\bar{\chi})$ scattering and the $(\chi\bar{\chi})$ destruction inside the Super-K or DUNE detectors corresponds to a cutoff scale

$$\Lambda \simeq 50\,\mathrm{TeV}\left(\frac{m_\chi}{1\,\mathrm{GeV}}\right)^{1/4} . \tag{7.47}$$

An additional signature predicted in this model besides DM self destruction is the removal of a neutron from a target nucleus. The resulting nucleus is often unstable which leads to additional hadronic activities inside the detectors.

As a necessary condition for this scenario to work, the η particle mass must lie in the following window,

$$m_n - 2m_\chi + BE_{(\chi\chi)} < m_\eta < m_n + KE + BE_{(\chi\chi)} - BE_{(\chi\bar{\chi})} , \tag{7.48}$$

where m_n is the effective neutron mass inside the nucleus, $BE_{(\chi\chi),(\chi\bar{\chi})}$ is the binding energy for the $(\chi\chi), (\chi\bar{\chi})$ bound states, respectively, and KE is the kinetic energy of the incoming $(\chi\chi)$ bound state that enters the detector. The upper bound of the above window is derived for the process $(\chi\chi) + n \to (\chi\bar{\chi}) + \eta$ to be kinematically allowed, and the lower bound is from the requirement of neutron stability against the decay $n \to \eta + (\bar{\chi}\bar{\chi})$. In addition, if $m_\eta \ll m_n$, the final state $\chi, \bar{\chi}$ particles would carry too large a relative momentum for them to remain bounded together. This limitation could be relaxed if the dark force for binding the $(\chi\bar{\chi})$ and $(\chi\chi)$ states is not from the exchange of a scalar ϕ but a confining

non-abelian ($SU(2)$) dark gauge interaction. In this case, there are no free $\chi, \bar{\chi}$ particles and bound states of them always form.

In this model, the new η particle is nearly degenerate in mass with the neutron. There is a potential constraint from neutron star stability as recently noticed in [291]. It is worth noting that here, instead of mixing with the neutron, the η particle couples to the neutron in together with two dark matter particles via a higher dimensional operator. Therefore, as long as the dark matter is heavier than 0.1 GeV, the neutron star bound will not apply.

The idea of DM eliminating a neutron and rendering a nucleon unstable has been discussed previously in [204, 255, 256]. However, in those models, the energy release is completely due to the destruction of a nucleon, yielding a signal very similar to the usual nucleon decay. In contrast, in the model discussed here, as well as the two SDDM models presented in the previous sections, the visible energy is released from $\chi\bar{\chi}$ annihilation into mediators and then into pairs of e^+e^- or $\mu^+\mu^-$. These striking signals are not currently looked at. Furthermore, in these scenarios, it is possible to reconstruct the masses of the DM particle as well as the mediator from the self destruction final states.

7.6 Experimental signatures and Model independent searches

Each one of the different SDDM scenarios presented above has its own unique signature. Still, these different experimental signatures share certain broad brush features. Some of the phenomenology was discussed in the context of the angular momentum model in Section 7.3.3. In this section, we discuss the signal characteristics more broadly. Our aim is not to perform a detailed study

of a specific model but rather, to discuss the general properties of the possible signals and suggest a set of relatively model-independent searches that an experiment can perform.

We assume that the couplings between the two sectors are very small. In that limit, the DM annihilates into mediators that eventually decay to SM particles rather than into the Standard Model directly. The signal characteristics depend on several parameters of the model, and we discuss a few of them below.

Event Rate: The rate of events in a detector is discussed in detailed for a specific model in Section 7.3.3 but will be repeated here for completeness. The rate depends on the scattering cross section $\sigma_{\rm scatter}$ which induces the transition from a long-lived state, Ψ, to a short-lived one, Ψ'. As discussed previously, the rate does not depend strongly on the mediator decay length $L_V \equiv \gamma_V v_V \tau_V$, with τ_V the mediator lifetime. If the mediator is short-lived, $L_V < L_{\rm det}$ the scattering takes place inside the detector, but if it is long-lived it can also happen in the Earth, outside the detector. However, as long as the mediator decay length is within the size of the Earth, the signal rate is largely independent of the mediator lifetime. This is because the $1/r^2$ fall-off in the flux emanating from a particular scatter site is compensated by the r^2 growth in the amount of volume to scatter on. As a result, up to order one geometric factors

$$\text{Rate} \sim n V_{\rm det}\, n_\Psi \langle \sigma v \rangle_{\rm scatter}\,, \tag{7.49}$$

where $V_{\rm det}$ is the volume of the detector, n is the nuclear number density either in the detector or in Earth, depending on whether the mediator is long or short lived. Also, $n_{\chi\bar{\chi}}$ is the number density of long-lived bound states, $\langle \sigma v \rangle_{\rm scatter}$ is the velocity averaged cross section to transition from the long lived DM state to its

short lived counterpart. Note that the atomic number of the scattering nucleus may be different for L_V larger or smaller than the detector size, which may affect the coherence factor in the cross section.

Particle ID: The mass, spin, and couplings of the mediator determine its decay branching fractions. A well motivated mediator is a dark photon which couples to the SM via kinetic mixing. In this case, the mediator has a sizable branching fraction to decay to electrons as well as to muons, charged pions or heavy flavor (whenever the mediator is above the relevant thresholds). A scalar or pseudo-scalar mediator could have a sizable branching fraction to the heaviest particle to which it is kinematically allowed. Di-photons are also an interesting final state, particularly for light (pseudo)scalars.

Event Multiplicity: The decay length of the mediators in the lab frame is

$$L_V = c\tau_V \sqrt{\frac{E_V^2}{m_V^2} - 1}\,. \tag{7.50}$$

For $\Psi' \to 2V$ decay, $E_V = m_{\Psi'}/2$ while for $\Psi' \to 3V$ decay, there is a spectrum for E_V between 0 and $m_{\Psi'}/2$. If this decay length is shorter than the size of the detector, there can be a sizable fraction of the events in which both mediators decay inside the detector. The signature, in this case, is two simultaneous pairs of leptons with opposite reconstructed velocities (since the decaying bound state is non-relativistic), consistent with a single vertex where the bound state decay took place. This is schematically shown in the left panel of Figure 7.5. Such events are expected to have an extremely low background.

Event Kinematics: Each event consists of decays of on-shell mediators pro-

duced via the annihilation $\chi\bar{\chi} \to 2V$ or $3V$ inside the short-lived bound state Ψ'. Consequently, we expect a double or triple lepton pair-production. In the case of $\Psi' \to 2V$ decay, each pair has energy which is half of the dark bound state mass and an invariant mass of m_V,

$$E_{\text{pair}} = \frac{m_{\Psi'}}{2} \qquad \text{and} \qquad m_{\text{pair}} = m_V \,. \tag{7.51}$$

Opening Angle: As the mediators in all of our scenarios are produced boosted, their decay products can't be back-to-back. When the decay products are relativistic, the typical opening angle between the, say, ℓ^+ and ℓ^- in each pair roughly satisfies

$$\cos\theta_{\ell^+\ell^-} \sim 1 - \frac{8m_V^2}{m_{\Psi'}^2} \,, \tag{7.52}$$

in the case of $\Psi' \to 2V$ decay. As long as m_V is not too small, detectors with good angular resolution will be able to distinguish the pair from a single energetic particle. On the other hand, as long as the mediator is not too close to half the bound state mass, the pairs will not be back-to-back and the detector will be able to reconstruct the direction of the mediator velocity.

Event Directionality: When the decay length of the mediator is much larger than the detector, each event will only consist of a single pair. This region of parameter space can be further categorized based on the directional distribution of the mediator velocity. If the decay length is shorter than the depth of the underground laboratory, the events will be isotropic. If on the other hand, the decay length is larger than the laboratory depth, the reconstructed velocities would be primarily coming from below. These two possibilities are also shown

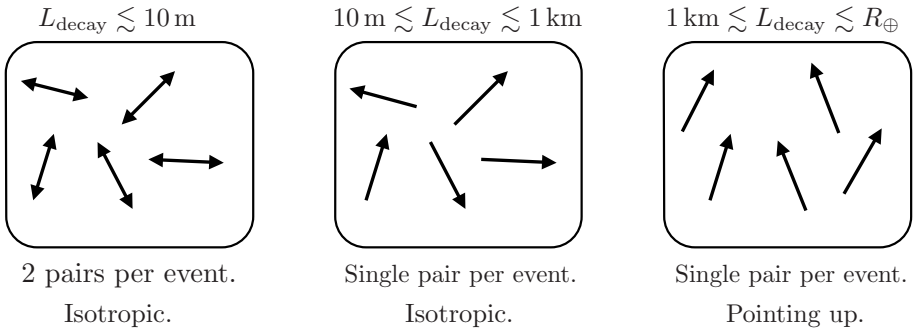

Figure 7.5: A schematic illustration of the expected signals for various decay lengths of the mediator V. In the case of $\Psi' \to 2V$ decay, each black arrow represents a pair of SM particles with a total energy of $m_{\Psi'}/2$, an invariant mass of m_V, and a total momentum pointing in the arrow direction. A double arrow represents two such pairs back-to-back.

schematically in Figure 7.5.

Associated Signals: The transition from the long-lived to the short-lived state could also lead to a visible signal. In this case, if L_V is smaller than the detector size, both the transition and the decay of the mediator(s) can be visible. For example, in the model described in section 7.5, the transition from the long-lived to the short-lived state was associated with the removal of a neutron from a target nucleus which would lead to an additional energy deposit. So long as this process, as well as the decay time of the short live state, are prompt, the mediator velocity would then point back to the transition point. This class of events can also have very low backgrounds.

Simplified Model Searches: Having discussed the signal characteristics, we finally suggest simplified model searches that large detectors can perform. Of course, picking a model and presenting limits in the spirit of Figure 7.2 can cer-

tainly be useful, in the sense that a comparison to other searches can be made. However, a more model independent presentation of the limits, which can then be translated to any model, may also be useful. This is common practice in collider searches, where a limit on a particular final state, say a di-lepton resonance, is presented as a limit on a cross section times a branching fraction rather as a limit on couplings. Other examples are searches for simplified models of, say, supersymmetry, where results are shown as limits on the cross section in the stop-neutralino mass plane using a contour or a color scale.

In the case of SDDM, the signal consists of one or two lepton pairs. The invariant mass of the pairs is set by m_V and the energy is set by $m_{\Psi'}$, see equation (7.51). A useful way to present results is thus to show the limit on the event rate per unit volume in the m_V-$m_{\Psi'}$ plane. To further sophisticate the analysis, this should be repeated for three different assumptions about the decay length L_V which correspond to different angular distributions and multiplicities as shown in Figure 7.5, since each of these options can have a different background rate. In the same way that LHC resonances are searched for in a variety of final states, here too, searches can be carried out for pairs of electrons, muons, photons, pions, etc.

We conclude that the framework of self-destructing DM has a rich phenomenology. The predicted events can have very particular characteristics which in many cases have very low backgrounds. The background rates and rejection efficiencies can be studied systematically for current and future detectors on a phenomenological basis, varying the model parameters $m_{\Psi'}$, m_V and τ_V as well as the decay products (electrons, muons, etc).

7.7 Conclusions

The search for DM is currently at the frontiers of high energy physics. In recent years, great efforts have been made in the direct detection of dark matter, aiming at recoil energies around the keV scale or even lower. This is based on the assumption that the available energy in each dark matter scattering is no larger than its kinetic energy. In this work, we have proposed a novel class of DM models called self-destructing Dark Matter (SDDM), in which the scattering of a DM with the detector (or the Earth) induces its decay to SM particles. The striking new feature of this class of models is the conversion of the entire rest mass of the SDDM to a detectable signal, rather than just its recoil energy. We have demonstrated how large neutrino detectors such as Super-K and DUNE could be at the frontier of the search for SDDM. Additionally, we presented three concrete realizations of SDDM, all of which are based on the DM being a bound state of some dark interaction, with qualitatively different stabilization mechanisms. Finally, we briefly described the broad brush features of the expected detector signals in the SDDM scenario.

There are several directions for further study. More detailed studies of the background to SDDM in large neutrino detectors are required, as well as a closer look at its production in the early universe. Though outside the scope of the current work, SDDM also has potentially interesting indirect signatures. The most striking one is DM decay in the Sun or in Jupiter. In traditional DM models, the DM may be captured in the core of the Sun, yielding an annihilation signal. In our model, however, the DM can simply "self-destruct" in the Sun in a similar manner to Earth. This could yield, *e.g.*, gamma ray or e^+e^- signals for indirect detection experiments [292, 293]. Additional model dependent indirect

signals could arise from DM self destruction induced by DM-DM scattering in the galactic center or in extragalactic sources.

APPENDIX

7.A Estimation of Rates in the Tunneling Model

To estimate the relevant rates in the tunneling stabilization model discussed in section 7.4, we focus on an idealized potential model

$$V(r) = \begin{cases} -h_0 & r < w_0 \\ -h_R + h_b & w_0 < r < w_0 + R \\ -h_R & w_0 + R < r < w_0 + R + w_R \end{cases} \tag{7.53}$$

The results derived in this section, however are quite generic for more realistic two minima potentials with a wide barrier. The potential Eq. (7.53) is depicted in Fig. 7.6 (left) for $h_0 = 50, h_R = 15, w_0 = w_R = 1$ and $h_b = 8, R = 30$, where h_0, h_R, h_b are in units of m_χ and w_0, w_R, R are in units of m_χ^{-1}.

We denote the height and width of the barrier by h_b and R, respectively. The height and width of the potential wells are denoted h_0, w_0 and h_R, w_R for the $r = 0$ and $r = R$ minima. The typical wavefunctions of the relevant states are shown in Fig. 7.6 (right), and their values near the origin are then,

$$\left|\Psi_{\text{Long}}(0)\right|^2 \sim \frac{1}{w_R}\, e^{-2\sqrt{h_b}R}\,, \qquad |\Psi_{\text{Short}}(0)|^2 \sim \frac{1}{w_0}\,, \qquad |\Psi_{\text{excited}}(0)|^2 \sim \frac{1}{R}\,. \tag{7.54}$$

As a result, we have

$$\frac{\tau_{\text{Short}}}{\tau_{\text{Long}}} \sim \frac{\tau_{\text{excited}}}{\tau_{\text{Long}}} \sim e^{-2\sqrt{h_b}R}\,. \tag{7.55}$$

For $2\sqrt{h_b}R \sim 40$, the long lifetime states could be cosmologically stable while the short lifetime ones decay in a second. The rate for spontaneous emission $\Psi_{\text{Long}} \to \Psi_{\text{Short}}$ is

$$\Gamma^{SE}_{L\to S} = \frac{4\alpha_V(\Delta E)^3}{3}\left|\int d^3r\, \Psi^*_{\text{Short}}(r)\, \vec{r}\, \Psi_{\text{Long}}(r)\right|^2 \sim e^{-2\sqrt{h_b}R}\,, \tag{7.56}$$

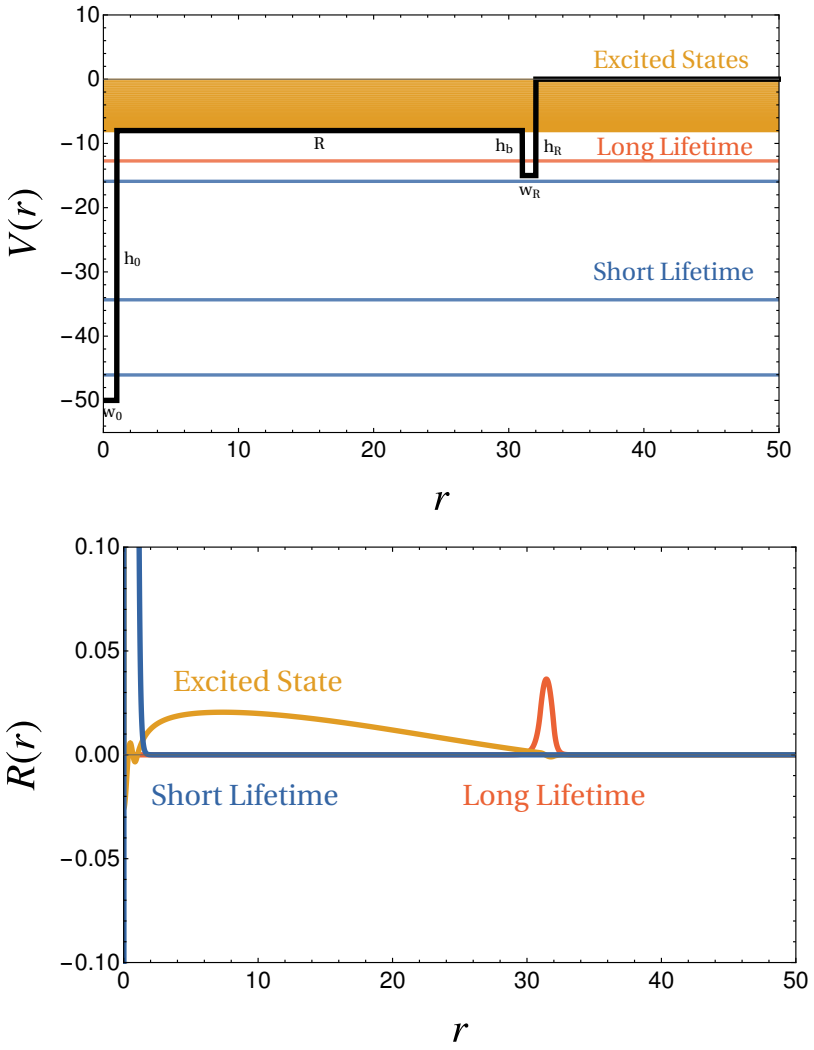

Figure 7.6: An illustration of tunneling Stabilization. *Left*: The potential and energy eigenvalues. *Right*: Sample wavefunctions. The coordinate r is in unit of m_χ^{-1}, the potential energy V is in unit of m_χ and the bound state wavefunctions are in unit of $m_\chi^{3/2}$.

and so the long lifetime states are cosmologically stable. In the above estimate, we assume the energy difference ΔE is large enough for a dark photon to be radiated on-shell in this model.

The cross section for a long lifetime state to hit the Earth and up scatter to an excited state is given by Eqs. (7.16)-(7.17). The form factor $F_D(|\vec{q}|)$ is given

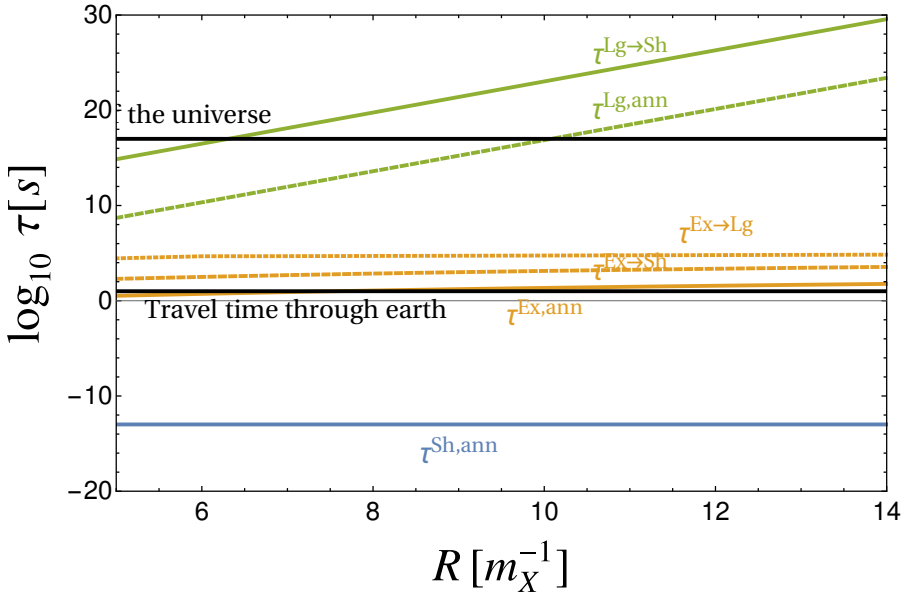

Figure 7.7: Lifetimes for states in the two minima potential as function of the barrier width, for $m_\chi = 0.5\mathrm{GeV}$, $\alpha_V = 10^{-2}$.

by integral between Ψ_{Long} and Ψ_{excited} which, given a large enough momentum transfer, is not exponentially suppressed. Once in the excited state, the total rate for spontaneous emission to short lifetime states is

$$\Gamma^{SE}_{E\to S} = \sum_i \frac{4\alpha_V(\Delta E_i)^3}{3}\left|\int d^3r\,\Psi^*_{\mathrm{Short,i}}(r)\,\vec{r}\,\Psi_{\mathrm{excited}}(r)\right|^2 , \tag{7.57}$$

which is also free from the exponential suppression. For $N_{\mathrm{Short}} \gg N_{\mathrm{Long}}$, the excited states transit exclusively to short lifetime states. A quantitative analysis of the rates in this model is given in Fig. 7.7 for the simple two minima potential Eq. (7.53), with $m_\chi = 0.5\mathrm{GeV}$, $\alpha_V = 10^{-2}$. As we can see in the plot, the only lifetimes that depend significantly on R are the lifetimes of the long lifetime states to annihilate or spontaneously emit a dark photon and transfer to a short lifetime state. This is because the tunneling suppression for these states depends exponentially on R. For $R \gtrsim 12\,m_\chi^{-1}$, the long lifetime states are cosmologically stable, while the short lifetime states annihilate in roughly a picosecond. Interestingly, for this particular configuration, the excited states tend to annihilate

rather than spontaneously emit to either the short or long lifetime states. This is, of course, a completely viable option from the point of view of self-destructing phenomenology.

BIBLIOGRAPHY

[1] S. Rahatlou, *54th Rencontres de Moriond on Electroweak Interactions and Unified Theories: Experimental Summary*. Mar, 2019.

[2] LHCb collaboration, A. A. Alves, Jr. et al., *The LHCb Detector at the LHC*, *JINST* **3** (2008) S08005.

[3] Belle-II collaboration, T. Abe et al., *Belle II Technical Design Report*, 1011.0352.

[4] BaBar collaboration, B. Aubert et al., *The BaBar detector*, *Nucl. Instrum. Meth.* **A479** (2002) 1–116, [hep-ex/0105044].

[5] LHCb collaboration, R. Aaij et al., *Observation of CP violation in charm decays*, 1903.08726.

[6] G. F. Giudice, *The Dawn of the Post-Naturalness Era*, in *From My Vast Repertoire ...: Guido Altarelli's Legacy* (A. Levy, S. Forte and G. Ridolfi, eds.), pp. 267–292. 2019. 1710.07663. DOI.

[7] N. Craig, *PiTP2017 - Naturalness and New Approaches to the Hierarchy Problem*. July, 2017.

[8] S. P. Martin, *A Supersymmetry primer*, hep-ph/9709356.

[9] D. B. Kaplan and H. Georgi, *SU(2) x U(1) Breaking by Vacuum Misalignment*, *Phys. Lett.* **136B** (1984) 183–186.

[10] D. B. Kaplan, H. Georgi and S. Dimopoulos, *Composite Higgs Scalars*, *Phys. Lett.* **136B** (1984) 187–190.

[11] H. Georgi, D. B. Kaplan and P. Galison, *Calculation of the Composite Higgs Mass*, *Phys. Lett.* **143B** (1984) 152–154.

[12] T. Banks, *CONSTRAINTS ON SU(2) x U(1) BREAKING BY VACUUM MISALIGNMENT*, *Nucl. Phys.* **B243** (1984) 125–130.

[13] H. Georgi and D. B. Kaplan, *Composite Higgs and Custodial SU(2)*, *Phys. Lett.* **145B** (1984) 216–220.

[14] M. J. Dugan, H. Georgi and D. B. Kaplan, *Anatomy of a Composite Higgs Model*, *Nucl. Phys.* **B254** (1985) 299–326.

[15] H. Georgi, *A Tool Kit for Builders of Composite Models*, *Nucl. Phys.* **B266** (1986) 274–284.

[16] P. W. Graham, D. E. Kaplan and S. Rajendran, *Cosmological Relaxation of the Electroweak Scale*, *Phys. Rev. Lett.* **115** (2015) 221801, [1504.07551].

[17] N. Arkani-Hamed, T. Cohen, R. T. D'Agnolo, A. Hook, H. D. Kim and D. Pinner, *Solving the Hierarchy Problem at Reheating with a Large Number of Degrees of Freedom*, *Phys. Rev. Lett.* **117** (2016) 251801, [1607.06821].

[18] N. Craig, *CosmoGrav2018 - 21 Increasingly Crazy Approaches to the Hierarchy Problem*. June, 2018.

[19] J. L. Bernal, L. Verde and A. G. Riess, *The trouble with H_0*, *JCAP* **1610** (2016) 019, [1607.05617].

[20] J. S. Bullock and M. Boylan-Kolchin, *Small-Scale Challenges to the ΛCDM Paradigm*, *Ann. Rev. Astron. Astrophys.* **55** (2017) 343–387, [1707.04256].

[21] S. Tremaine and J. E. Gunn, *Dynamical Role of Light Neutral Leptons in Cosmology*, *Phys. Rev. Lett.* **42** (1979) 407–410.

[22] W. Hu, R. Barkana and A. Gruzinov, *Cold and fuzzy dark matter*, *Phys. Rev. Lett.* **85** (2000) 1158–1161, [astro-ph/0003365].

[23] C. Csáki, M. Geller and O. Telem, *Tree-level Quartic for a Holographic Composite Higgs*, *JHEP* **05** (2018) 134, [1710.08921].

[24] C. Csáki, G. Lee, S. J. Lee, S. Lombardo and O. Telem, *Continuum Naturalness*, *JHEP* **03** (2019) 142, [1811.06019].

[25] M. Geller, S. Iwamoto, G. Lee, Y. Shadmi and O. Telem, *Dark quarkonium formation in the early universe*, *JHEP* **06** (2018) 135, [1802.07720].

[26] Y. Grossman, R. Harnik, O. Telem and Y. Zhang, *Self-Destructing Dark Matter*, 1712.00455.

[27] R. Contino, *The Higgs as a Composite Nambu-Goldstone Boson*, in *Physics of the large and the small, TASI 09, proceedings of the Theoretical Advanced Study*

Institute in Elementary Particle Physics, Boulder, Colorado, USA, 1-26 June 2009, pp. 235–306, 2011. 1005.4269. DOI.

[28] B. Bellazzini, C. Csáki and J. Serra, *Composite Higgses*, *Eur. Phys. J.* **C74** (2014) 2766, [1401.2457].

[29] G. Panico and A. Wulzer, *The Composite Nambu-Goldstone Higgs*, *Lect. Notes Phys.* **913** (2016) pp.1–316, [1506.01961].

[30] C. Csáki, S. Lombardo and O. Telem, *TASI Lectures on Non-supersymmetric BSM Models*, in *Proceedings, Theoretical Advanced Study Institute in Elementary Particle Physics : Anticipating the Next Discoveries in Particle Physics (TASI 2016): Boulder, CO, USA, June 6-July 1, 2016*, pp. 501–570, WSP, WSP, 2018. 1811.04279. DOI.

[31] S. R. Coleman and E. J. Weinberg, *Radiative Corrections as the Origin of Spontaneous Symmetry Breaking*, *Phys. Rev.* **D7** (1973) 1888–1910.

[32] K. Agashe, R. Contino and A. Pomarol, *The Minimal composite Higgs model*, *Nucl. Phys.* **B719** (2005) 165–187, [hep-ph/0412089].

[33] C. G. Callan, Jr., S. R. Coleman, J. Wess and B. Zumino, *Structure of phenomenological Lagrangians. 2.*, *Phys. Rev.* **177** (1969) 2247–2250.

[34] D. B. Kaplan, *Flavor at SSC energies: A New mechanism for dynamically generated fermion masses*, *Nucl. Phys.* **B365** (1991) 259–278.

[35] N. Arkani-Hamed and M. Schmaltz, *Hierarchies without symmetries from extra dimensions*, *Phys. Rev.* **D61** (2000) 033005, [hep-ph/9903417].

[36] Y. Grossman and M. Neubert, *Neutrino masses and mixings in nonfactorizable geometry*, *Phys. Lett.* **B474** (2000) 361–371, [hep-ph/9912408].

[37] K. Agashe, G. Perez and A. Soni, *Flavor structure of warped extra dimension models*, *Phys. Rev.* **D71** (2005) 016002, [hep-ph/0408134].

[38] A. D. Medina, N. R. Shah and C. E. M. Wagner, *Gauge-Higgs Unification and Radiative Electroweak Symmetry Breaking in Warped Extra Dimensions*, *Phys. Rev.* **D76** (2007) 095010, [0706.1281].

[39] C. Csáki, A. Falkowski and A. Weiler, *The Flavor of the Composite Pseudo-Goldstone Higgs*, *JHEP* **09** (2008) 008, [0804.1954].

[40] S. Weinberg, *Precise relations between the spectra of vector and axial vector mesons*, *Phys. Rev. Lett.* **18** (1967) 507–509.

[41] A. Pomarol and F. Riva, *The Composite Higgs and Light Resonance Connection*, *JHEP* **08** (2012) 135, [1205.6434].

[42] J. M. Maldacena, *The Large N limit of superconformal field theories and supergravity*, *Int. J. Theor. Phys.* **38** (1999) 1113–1133, [hep-th/9711200].

[43] A. Karch, E. Katz, D. T. Son and M. A. Stephanov, *Linear confinement and AdS/QCD*, *Phys. Rev.* **D74** (2006) 015005, [hep-ph/0602229].

[44] L. Randall and R. Sundrum, *A Large mass hierarchy from a small extra dimension*, *Phys. Rev. Lett.* **83** (1999) 3370–3373, [hep-ph/9905221].

[45] W. D. Goldberger and M. B. Wise, *Modulus stabilization with bulk fields*, *Phys. Rev. Lett.* **83** (1999) 4922–4925, [hep-ph/9907447].

[46] T. Gherghetta and A. Pomarol, *Bulk fields and supersymmetry in a slice of AdS*, *Nucl. Phys.* **B586** (2000) 141–162, [hep-ph/0003129].

[47] R. Contino and A. Pomarol, *Holography for fermions*, *JHEP* **11** (2004) 058, [hep-th/0406257].

[48] C. Csáki, J. Hubisz and P. Meade, *TASI lectures on electroweak symmetry breaking from extra dimensions*, in *Physics in D ¿= 4. Proceedings, Theoretical Advanced Study Institute in elementary particle physics, TASI 2004, Boulder, USA, June 6-July 2, 2004*, pp. 703–776, 2005. hep-ph/0510275.

[49] N. S. Manton, *A New Six-Dimensional Approach to the Weinberg-Salam Model*, *Nucl. Phys.* **B158** (1979) 141–153.

[50] Y. Hosotani, *Dynamical Mass Generation by Compact Extra Dimensions*, *Phys. Lett.* **126B** (1983) 309–313.

[51] I. Antoniadis, K. Benakli and M. Quiros, *Finite Higgs mass without supersymmetry*, *New J. Phys.* **3** (2001) 20, [hep-th/0108005].

[52] M. Kubo, C. S. Lim and H. Yamashita, *The Hosotani mechanism in bulk gauge theories with an orbifold extra space S**1 / Z(2)*, *Mod. Phys. Lett.* **A17** (2002) 2249–2264, [hep-ph/0111327].

[53] G. von Gersdorff, N. Irges and M. Quiros, *Finite mass corrections in orbifold gauge theories*, in *Proceedings, 37th Rencontres de Moriond on Electroweak Interactions and Unified Theories: Les Arcs, France, March 9-16, 2002*, pp. 169–176, 2002. hep-ph/0206029.

[54] C. Csáki, C. Grojean and H. Murayama, *Standard model Higgs from higher dimensional gauge fields*, *Phys. Rev.* **D67** (2003) 085012, [hep-ph/0210133].

[55] C. A. Scrucca, M. Serone and L. Silvestrini, *Electroweak symmetry breaking and fermion masses from extra dimensions*, *Nucl. Phys.* **B669** (2003) 128–158, [hep-ph/0304220].

[56] C. A. Scrucca, M. Serone, L. Silvestrini and A. Wulzer, *Gauge Higgs unification in orbifold models*, *JHEP* **02** (2004) 049, [hep-th/0312267].

[57] G. Cacciapaglia, C. Csáki and S. C. Park, *Fully radiative electroweak symmetry breaking*, *JHEP* **03** (2006) 099, [hep-ph/0510366].

[58] R. Contino, Y. Nomura and A. Pomarol, *Higgs as a holographic pseudoGoldstone boson*, *Nucl. Phys.* **B671** (2003) 148–174, [hep-ph/0306259].

[59] A. Falkowski, *About the holographic pseudo-Goldstone boson*, *Phys. Rev.* **D75** (2007) 025017, [hep-ph/0610336].

[60] A. Falkowski, *Pseudo-goldstone higgs from five dimensions*, in *SUSY 2007 Proceedings, 15th International Conference on Supersymmetry and Unification of Fundamental Interactions, July 26 - August 1, 2007, Karlsruhe, Germany*, pp. 658–661, 2007. 0710.4050.

[61] M. Geller and O. Telem, *Holographic Twin Higgs Model*, *Phys. Rev. Lett.* **114** (2015) 191801, [1411.2974].

[62] C. Csáki, M. Geller, O. Telem and A. Weiler, *The Flavor of the Composite Twin Higgs*, *JHEP* **09** (2016) 146, [1512.03427].

[63] G. Panico, M. Redi, A. Tesi and A. Wulzer, *On the Tuning and the Mass of the Composite Higgs*, *JHEP* **03** (2013) 051, [1210.7114].

[64] R. Contino, L. Da Rold and A. Pomarol, *Light custodians in natural composite Higgs models*, *Phys. Rev.* **D75** (2007) 055014, [hep-ph/0612048].

[65] D. Pappadopulo, A. Thamm and R. Torre, *A minimally tuned composite Higgs model from an extra dimension*, *JHEP* **07** (2013) 058, [1303.3062].

[66] J. Gu, H. Li, Z. Liu, S. Su and W. Su, *Learning from Higgs Physics at Future Higgs Factories*, *JHEP* **12** (2017) 153, [1709.06103].

[67] M. E. Peskin and T. Takeuchi, *Estimation of oblique electroweak corrections*, *Phys. Rev.* **D46** (1992) 381–409.

[68] K. Agashe, R. Contino, L. Da Rold and A. Pomarol, *A Custodial symmetry for $Zb\bar{b}$*, *Phys. Lett.* **B641** (2006) 62–66, [hep-ph/0605341].

[69] R. Barbieri, B. Bellazzini, V. S. Rychkov and A. Varagnolo, *The Higgs boson from an extended symmetry*, *Phys. Rev.* **D76** (2007) 115008, [0706.0432].

[70] B. Keren-Zur, P. Lodone, M. Nardecchia, D. Pappadopulo, R. Rattazzi and L. Vecchi, *On Partial Compositeness and the CP asymmetry in charm decays*, *Nucl. Phys.* **B867** (2013) 394–428, [1205.5803].

[71] ATLAS collaboration, M. Aaboud et al., *Combination of the searches for pair-produced vector-like partners of the third-generation quarks at $\sqrt{s} = 13$ TeV with the ATLAS detector*, 1808.02343.

[72] ATLAS collaboration, M. Aaboud et al., *Search for new phenomena in events with same-charge leptons and b-jets in pp collisions at $\sqrt{s} = 13$ TeV with the ATLAS detector*, 1807.11883.

[73] CMS collaboration, A. M. Sirunyan et al., *Search for vector-like quarks in events with two oppositely charged leptons and jets in proton-proton collisions at $\sqrt{s} = 13$ TeV*, *Submitted to: Eur. Phys. J.* (2018) , [1812.09768].

[74] CMS collaboration, C. Collaboration, *Search for vector-like T or B quark pairs in leptonic final states in 36 fb^{-1} of proton-proton collisions at $\sqrt{s} = 13$ TeV*, .

[75] CMS collaboration, A. M. Sirunyan et al., *Search for single production of vector-like quarks decaying to a top quark and a W boson in proton-proton collisions at* $\sqrt{s} = 13$ *TeV*, *Eur. Phys. J.* **C79** (2019) 90, [1809.08597].

[76] CMS collaboration, A. M. Sirunyan et al., *Search for heavy resonances decaying into two Higgs bosons or into a Higgs boson and a W or Z boson in proton-proton collisions at 13 TeV*, *JHEP* **01** (2019) 051, [1808.01365].

[77] CMS collaboration, A. M. Sirunyan et al., *Search for heavy resonances decaying into a vector boson and a Higgs boson in final states with charged leptons, neutrinos and b quarks at* $\sqrt{s} = 13$ *TeV*, *JHEP* **11** (2018) 172, [1807.02826].

[78] CMS collaboration, A. M. Sirunyan et al., *Search for a heavy resonance decaying into a Z boson and a Z or W boson in 2l2q final states at* $\sqrt{s} = 13$ *TeV*, *JHEP* **09** (2018) 101, [1803.10093].

[79] ATLAS collaboration, M. Aaboud et al., *Search for heavy resonances decaying into a W or Z boson and a Higgs boson in final states with leptons and b-jets in 36* fb^{-1} *of* $\sqrt{s} = 13$ *TeV* pp *collisions with the ATLAS detector*, *JHEP* **03** (2018) 174, [1712.06518].

[80] N. Arkani-Hamed, A. G. Cohen and H. Georgi, *Electroweak symmetry breaking from dimensional deconstruction*, *Phys. Lett.* **B513** (2001) 232–240, [hep-ph/0105239].

[81] N. Arkani-Hamed, A. G. Cohen, E. Katz and A. E. Nelson, *The Littlest Higgs*, *JHEP* **07** (2002) 034, [hep-ph/0206021].

[82] G. F. Giudice, C. Grojean, A. Pomarol and R. Rattazzi, *The Strongly-Interacting Light Higgs*, *JHEP* **06** (2007) 045, [hep-ph/0703164].

[83] C. Csáki, T. Ma and J. Shu, *Maximally Symmetric Composite Higgs Models*, *Phys. Rev. Lett.* **119** (2017) 131803, [1702.00405].

[84] N. Arkani-Hamed, A. G. Cohen and H. Georgi, *(De)constructing dimensions*, *Phys. Rev. Lett.* **86** (2001) 4757–4761, [hep-th/0104005].

[85] T. Gregoire and J. G. Wacker, *Mooses, topology and Higgs*, *JHEP* **08** (2002) 019, [hep-ph/0206023].

[86] Z. Chacko, H.-S. Goh and R. Harnik, *The Twin Higgs: Natural electroweak*

breaking from mirror symmetry, *Phys. Rev. Lett.* **96** (2006) 231802, [hep-ph/0506256].

[87] Z. Chacko, H.-S. Goh and R. Harnik, *A Twin Higgs model from left-right symmetry*, *JHEP* **01** (2006) 108, [hep-ph/0512088].

[88] G. Burdman, Z. Chacko, H.-S. Goh and R. Harnik, *Folded supersymmetry and the LEP paradox*, *JHEP* **02** (2007) 009, [hep-ph/0609152].

[89] N. Craig, S. Knapen and P. Longhi, *Neutral Naturalness from Orbifold Higgs Models*, *Phys. Rev. Lett.* **114** (2015) 061803, [1410.6808].

[90] M. Low, A. Tesi and L.-T. Wang, *Twin Higgs mechanism and a composite Higgs boson*, *Phys. Rev.* **D91** (2015) 095012, [1501.07890].

[91] R. Barbieri, D. Greco, R. Rattazzi and A. Wulzer, *The Composite Twin Higgs scenario*, *JHEP* **08** (2015) 161, [1501.07803].

[92] J. Serra and R. Torre, *Neutral naturalness from the brother-Higgs model*, *Phys. Rev.* **D97** (2018) 035017, [1709.05399].

[93] N. Craig, A. Katz, M. Strassler and R. Sundrum, *Naturalness in the Dark at the LHC*, *JHEP* **07** (2015) 105, [1501.05310].

[94] R. Harnik, K. Howe and J. Kearney, *Tadpole-Induced Electroweak Symmetry Breaking and pNGB Higgs Models*, *JHEP* **03** (2017) 111, [1603.03772].

[95] A. Katz, A. Mariotti, S. Pokorski, D. Redigolo and R. Ziegler, *SUSY Meets Her Twin*, *JHEP* **01** (2017) 142, [1611.08615].

[96] J. Thaler and I. Yavin, *The Littlest Higgs in Anti-de Sitter space*, *JHEP* **08** (2005) 022, [hep-ph/0501036].

[97] C. Csáki, J. Heinonen, M. Perelstein and C. Spethmann, *A Weakly Coupled Ultraviolet Completion of the Littlest Higgs with T-parity*, *Phys. Rev.* **D79** (2009) 035014, [0804.0622].

[98] N. Arkani-Hamed, M. Porrati and L. Randall, *Holography and phenomenology*, *JHEP* **08** (2001) 017, [hep-th/0012148].

[99] R. Rattazzi and A. Zaffaroni, *Comments on the holographic picture of the Randall-Sundrum model*, *JHEP* **04** (2001) 021, [hep-th/0012248].

[100] J. Mrazek, A. Pomarol, R. Rattazzi, M. Redi, J. Serra and A. Wulzer, *The Other Natural Two Higgs Doublet Model*, *Nucl. Phys.* **B853** (2011) 1–48, [1105.5403].

[101] J. F. Gunion and H. E. Haber, *The CP conserving two Higgs doublet model: The Approach to the decoupling limit*, *Phys. Rev.* **D67** (2003) 075019, [hep-ph/0207010].

[102] J. Bernon, J. F. Gunion, H. E. Haber, Y. Jiang and S. Kraml, *Scrutinizing the alignment limit in two-Higgs-doublet models: m_h=125 GeV*, *Phys. Rev.* **D92** (2015) 075004, [1507.00933].

[103] ATLAS collaboration, M. Aaboud et al., *Search for pair production of heavy vector-like quarks decaying to high-p_T W bosons and b quarks in the lepton-plus-jets final state in pp collisions at $\sqrt{s}$ = 13 TeV with the ATLAS detector*, *JHEP* **10** (2017) 141, [1707.03347].

[104] CMS collaboration, A. M. Sirunyan et al., *Search for pair production of vector-like quarks in the $bW\bar{b}W$ channel from proton-proton collisions at $\sqrt{s}$ = 13 TeV*, *Phys. Lett.* **B779** (2018) 82–106, [1710.01539].

[105] G. Cacciapaglia, C. Csáki, J. Galloway, G. Marandella, J. Terning and A. Weiler, *A GIM Mechanism from Extra Dimensions*, *JHEP* **04** (2008) 006, [0709.1714].

[106] C. Csáki, A. Falkowski and A. Weiler, *A Simple Flavor Protection for RS*, *Phys. Rev.* **D80** (2009) 016001, [0806.3757].

[107] M. Redi and A. Weiler, *Flavor and CP Invariant Composite Higgs Models*, *JHEP* **11** (2011) 108, [1106.6357].

[108] R. Barbieri, D. Buttazzo, F. Sala and D. M. Straub, *Flavour physics from an approximate $U(2)^3$ symmetry*, *JHEP* **07** (2012) 181, [1203.4218].

[109] C. Csáki, C. Grojean and J. Terning, *Alternatives to an Elementary Higgs*, *Rev. Mod. Phys.* **88** (2016) 045001, [1512.00468].

[110] C. Csáki and P. Tanedo, *Beyond the Standard Model*, in *Proceedings, 2013 European School of High-Energy Physics (ESHEP 2013): Paradfurdo, Hungary, June 5-18, 2013*, pp. 169–268, 2015. 1602.04228. DOI.

[111] CMS collaboration, A. M. Sirunyan et al., *Search for top quark partners with*

charge 5/3 in the same-sign dilepton and single-lepton final states in proton-proton collisions at $\sqrt{s}$ = 13 TeV, *Submitted to: JHEP* (2018) , [1810.03188].

[112] CMS collaboration, A. M. Sirunyan et al., *Search for single production of vector-like quarks decaying to a top quark and a W boson in proton-proton collisions at $\sqrt{s}$ = 13 TeV*, 1809.08597.

[113] CMS collaboration, A. M. Sirunyan et al., *Search for vector-like T and B quark pairs in final states with leptons at $\sqrt{s}$ = 13 TeV*, *JHEP* **08** (2018) 177, [1805.04758].

[114] ATLAS collaboration, M. Aaboud et al., *Search for pair production of heavy vector-like quarks decaying into hadronic final states in pp collisions at $\sqrt{s}$ = 13 TeV with the ATLAS detector*, *Phys. Rev.* **D98** (2018) 092005, [1808.01771].

[115] CMS collaboration, A. M. Sirunyan et al., *Search for a heavy resonance decaying to a pair of vector bosons in the lepton plus merged jet final state at $\sqrt{s}$ = 13 TeV*, *JHEP* **05** (2018) 088, [1802.09407].

[116] ATLAS collaboration, M. Aaboud et al., *Search for resonant WZ production in the fully leptonic final state in proton-proton collisions at $\sqrt{s}$ = 13 TeV with the ATLAS detector*, *Phys. Lett.* **B787** (2018) 68–88, [1806.01532].

[117] H. Georgi, *Unparticle physics*, *Phys. Rev. Lett.* **98** (2007) 221601, [hep-ph/0703260].

[118] H. Georgi, *Another odd thing about unparticle physics*, *Phys. Lett.* **B650** (2007) 275–278, [0704.2457].

[119] G. Cacciapaglia, G. Marandella and J. Terning, *Colored Unparticles*, *JHEP* **01** (2008) 070, [0708.0005].

[120] G. Cacciapaglia, G. Marandella and J. Terning, *The AdS/CFT/Unparticle Correspondence*, *JHEP* **02** (2009) 049, [0804.0424].

[121] D. Stancato and J. Terning, *The Unhiggs*, *JHEP* **11** (2009) 101, [0807.3961].

[122] A. Falkowski and M. Perez-Victoria, *Electroweak Breaking on a Soft Wall*, *JHEP* **12** (2008) 107, [0806.1737].

[123] A. Falkowski and M. Perez-Victoria, *Holographic Unhiggs*, *Phys. Rev.* **D79** (2009) 035005, [0810.4940].

[124] B. Bellazzini, C. Csáki, J. Hubisz, S. J. Lee, J. Serra and J. Terning, *Quantum Critical Higgs*, *Phys. Rev.* **X6** (2016) 041050, [1511.08218].

[125] O. Aharony, M. Berkooz, D. Kutasov and N. Seiberg, *Linear dilatons, NS five-branes and holography*, *JHEP* **10** (1998) 004, [hep-th/9808149].

[126] A. Giveon and D. Kutasov, *Little string theory in a double scaling limit*, *JHEP* **10** (1999) 034, [hep-th/9909110].

[127] I. Antoniadis, S. Dimopoulos and A. Giveon, *Little string theory at a TeV*, *JHEP* **05** (2001) 055, [hep-th/0103033].

[128] B. Batell, T. Gherghetta and D. Sword, *The Soft-Wall Standard Model*, *Phys. Rev.* **D78** (2008) 116011, [0808.3977].

[129] B. Batell and T. Gherghetta, *Dynamical Soft-Wall AdS/QCD*, *Phys. Rev.* **D78** (2008) 026002, [0801.4383].

[130] J. A. Cabrer, G. von Gersdorff and M. Quiros, *Soft-Wall Stabilization*, *New J. Phys.* **12** (2010) 075012, [0907.5361].

[131] C. Csáki, G. Lee, S. J. Lee and O. Telem, *Phenomenology of Continuum Partners*, *to appear* (2018) .

[132] G. Kallen, *On the definition of the Renormalization Constants in Quantum Electrodynamics*, *Helv. Phys. Acta* **25** (1952) 417.

[133] H. Lehmann, *On the Properties of propagation functions and renormalization contants of quantized fields*, *Nuovo Cim.* **11** (1954) 342–357.

[134] H. Cai, H.-C. Cheng, A. D. Medina and J. Terning, *Continuum Superpartners from Supersymmetric Unparticles*, *Phys. Rev.* **D80** (2009) 115009, [0910.3925].

[135] G. F. Giudice, Y. Kats, M. McCullough, R. Torre and A. Urbano, *Clockwork/linear dilaton: structure and phenomenology*, *JHEP* **06** (2018) 009, [1711.08437].

[136] K. Agashe and R. Contino, *The Minimal composite Higgs model and electroweak precision tests*, *Nucl. Phys.* **B742** (2006) 59–85, [hep-ph/0510164].

[137] R. Contino, P. Creminelli and E. Trincherini, *Holographic evolution of gauge couplings*, *JHEP* **10** (2002) 029, [hep-th/0208002].

[138] CMS collaboration, S. Chatrchyan et al., *Measurement of the ratio of the inclusive 3-jet cross section to the inclusive 2-jet cross section in pp collisions at $\sqrt{s}$ = 7 TeV and first determination of the strong coupling constant in the TeV range*, *Eur. Phys. J.* **C73** (2013) 2604, [1304.7498].

[139] CMS collaboration, V. Khachatryan et al., *Measurement of the inclusive 3-jet production differential cross section in proton–proton collisions at 7 TeV and determination of the strong coupling constant in the TeV range*, *Eur. Phys. J.* **C75** (2015) 186, [1412.1633].

[140] CMS collaboration, V. Khachatryan et al., *Constraints on parton distribution functions and extraction of the strong coupling constant from the inclusive jet cross section in pp collisions at $\sqrt{s}$ = 7 TeV*, *Eur. Phys. J.* **C75** (2015) 288, [1410.6765].

[141] Particle Data Group collaboration, C. Patrignani et al., *Review of Particle Physics*, *Chin. Phys.* **C40** (2016) 100001.

[142] G. Bertone, D. Hooper and J. Silk, *Particle dark matter: Evidence, candidates and constraints*, *Phys. Rept.* **405** (2005) 279–390, [hep-ph/0404175].

[143] Planck collaboration, N. Aghanim et al., *Planck 2018 results. VI. Cosmological parameters*, 1807.06209.

[144] F. Walter, E. Brinks, W. J. G. de Blok, F. Bigiel, R. C. Kennicutt, Jr. et al., *THINGS: The HI Nearby Galaxy Survey*, *Astron. J.* **136** (1985) 2563–2647, [0810.2125].

[145] F. Lelli, S. S. McGaugh and J. M. Schombert, *SPARC: Mass Models for 175 Disk Galaxies with Spitzer Photometry and Accurate Rotation Curves*, *Astron. J.* **152** (2016) 157, [1606.09251].

[146] V. C. Rubin and W. K. Ford, Jr., *Rotation of the Andromeda Nebula from a Spectroscopic Survey of Emission Regions*, *Astrophys. J.* **159** (1970) 379–403.

[147] M. Markevitch, A. H. Gonzalez, L. David, A. Vikhlinin, S. Murray, W. Forman et al., *A Textbook example of a bow shock in the merging galaxy cluster 1E0657-56*, *Astrophys. J.* **567** (2002) L27, [astro-ph/0110468].

[148] D. Clowe, A. Gonzalez and M. Markevitch, *Weak lensing mass reconstruction of the interacting cluster 1E0657-558: Direct evidence for the existence of dark matter*, *Astrophys. J.* **604** (2004) 596–603, [astro-ph/0312273].

[149] D. Clowe, M. Bradac, A. H. Gonzalez, M. Markevitch, S. W. Randall, C. Jones et al., *A direct empirical proof of the existence of dark matter*, *Astrophys. J.* **648** (2006) L109–L113, [astro-ph/0608407].

[150] N. Okabe, T. Futamase, M. Kajisawa and R. Kuroshima, *Subaru Weak-lensing Survey of Dark Matter Subhalos in the Coma Cluster: Subhalo Mass Function and Statistical Properties*, *Astrophys. J.* **784** (2014) 90, [1304.2399].

[151] R. Massey, T. Kitching and J. Richard, *The dark matter of gravitational lensing*, *Rept. Prog. Phys.* **73** (2010) 086901, [1001.1739].

[152] J. M. Kubo, H. Khiabanian, I. P. Dell'Antonio, D. Wittman and J. A. Tyson, *Dark Matter Structures In The Deep Lens Survey*, *Astrophys. J.* **702** (2009) 980–988, [0809.5072].

[153] PLANCK collaboration, P. A. R. Ade et al., *Planck 2013 results. XVI. Cosmological parameters*, *Astron. Astrophys.* **571** (2014) A16, [1303.5076].

[154] PLANCK collaboration, P. A. R. Ade et al., *Planck 2015 results. XIII. Cosmological parameters*, *Astron. Astrophys.* **594** (2016) A13, [1502.01589].

[155] BOSS collaboration, S. Alam et al., *The clustering of galaxies in the completed SDSS-III Baryon Oscillation Spectroscopic Survey: cosmological analysis of the DR12 galaxy sample*, *Mon. Not. Roy. Astron. Soc.* **470** (2017) 2617–2652, [1607.03155].

[156] P. Carter, F. Beutler, W. J. Percival, C. Blake, J. Koda and A. J. Ross, *Low Redshift Baryon Acoustic Oscillation Measurement from the Reconstructed 6-degree Field Galaxy Survey*, 1803.01746.

[157] D. H. Weinberg, M. J. Mortonson, D. J. Eisenstein, C. Hirata, A. G. Riess

and E. Rozo, *Observational probes of cosmic acceleration*, *Physics Reports* **530** (2013) 87 – 255.

[158] DES collaboration, T. M. C. Abbott et al., *Dark Energy Survey year 1 results: Cosmological constraints from galaxy clustering and weak lensing*, *Phys. Rev.* **D98** (2018) 043526, [1708.01530].

[159] DES collaboration, M. A. Troxel et al., *Dark Energy Survey Year 1 results: Cosmological constraints from cosmic shear*, *Phys. Rev.* **D98** (2018) 043528, [1708.01538].

[160] DES collaboration, T. M. C. Abbott et al., *First Cosmology Results using Type Ia Supernovae from the Dark Energy Survey: Constraints on Cosmological Parameters*, *Astrophys. J.* **872** (2019) L30, [1811.02374].

[161] D. Hooper, *Particle Dark Matter*, in *Proceedings of Theoretical Advanced Study Institute in Elementary Particle Physics on The dawn of the LHC era (TASI 2008): Boulder, USA, June 2-27, 2008*, pp. 709–764, 2010. 0901.4090. DOI.

[162] M. Bauer and T. Plehn, *Yet Another Introduction to Dark Matter*, 1705.01987.

[163] T. Lin, *TASI lectures on dark matter models and direct detection*, 1904.07915.

[164] M. Battaglieri et al., *US Cosmic Visions: New Ideas in Dark Matter 2017: Community Report*, in *U.S. Cosmic Visions: New Ideas in Dark Matter College Park, MD, USA, March 23-25, 2017*, 2017. 1707.04591.

[165] E. W. Kolb and M. S. Turner, *The Early Universe*, *Front. Phys.* **69** (1990) 1–547.

[166] M. Schumann, *Direct Detection of WIMP Dark Matter: Concepts and Status*, 1903.03026.

[167] XENON collaboration, E. Aprile et al., *Dark Matter Search Results from a One Ton-Year Exposure of XENON1T*, *Phys. Rev. Lett.* **121** (2018) 111302, [1805.12562].

[168] S. Knapen, T. Lin and K. M. Zurek, *Light Dark Matter: Models and Constraints*, *Phys. Rev.* **D96** (2017) 115021, [1709.07882].

[169] T. R. Slatyer, *Indirect Detection of Dark Matter*, in *Proceedings, Theoretical Advanced Study Institute in Elementary Particle Physics : Anticipating the Next Discoveries in Particle Physics (TASI 2016): Boulder, CO, USA, June 6-July 1, 2016*, pp. 297–353, 2018. 1710.05137. DOI.

[170] D. P. Finkbeiner, S. Galli, T. Lin and T. R. Slatyer, *Searching for Dark Matter in the CMB: A Compact Parameterization of Energy Injection from New Physics*, *Phys. Rev.* **D85** (2012) 043522, [1109.6322].

[171] FERMI-LAT collaboration, W. B. Atwood et al., *The Large Area Telescope on the Fermi Gamma-ray Space Telescope Mission*, *Astrophys. J.* **697** (2009) 1071–1102, [0902.1089].

[172] H.E.S.S. collaboration, F. Aharonian et al., *The h.e.s.s. survey of the inner galaxy in very high-energy gamma-rays*, *Astrophys. J.* **636** (2006) 777–797, [astro-ph/0510397].

[173] AMS collaboration, M. Aguilar et al., *First Result from the Alpha Magnetic Spectrometer on the International Space Station: Precision Measurement of the Positron Fraction in Primary Cosmic Rays of 0.5350 GeV*, *Phys. Rev. Lett.* **110** (2013) 141102.

[174] S. Profumo, F. S. Queiroz, J. Silk and C. Siqueira, *Searching for Secluded Dark Matter with H.E.S.S., Fermi-LAT, and Planck*, *JCAP* **1803** (2018) 010, [1711.03133].

[175] ATLAS collaboration, M. Aaboud et al., *Constraints on mediator-based dark matter and scalar dark energy models using $\sqrt{s} = 13$ TeV pp collision data collected by the ATLAS detector*, 1903.01400.

[176] A. Albert, *ICHEP2018 - Dark Matter searches at CMS*. July, 2018.

[177] E. D. Carlson, M. E. Machacek and L. J. Hall, *Self-interacting dark matter*, *Astrophys. J.* **398** (1992) 43–52.

[178] Y. Hochberg, E. Kuflik, H. Murayama, T. Volansky and J. G. Wacker, *Model for Thermal Relic Dark Matter of Strongly Interacting Massive Particles*, *Phys. Rev. Lett.* **115** (2015) 021301, [1411.3727].

[179] Y. Hochberg, E. Kuflik, T. Volansky and J. G. Wacker, *Mechanism for Thermal Relic Dark Matter of Strongly Interacting Massive Particles*, *Phys. Rev. Lett.* **113** (2014) 171301, [1402.5143].

[180] S.-M. Choi, Y. Hochberg, E. Kuflik, H. M. Lee, Y. Mambrini, H. Murayama et al., *Vector SIMP dark matter*, *JHEP* **10** (2017) 162, [1707.01434].

[181] Y. Hochberg, E. Kuflik and H. Murayama, *Twin Higgs model with strongly interacting massive particle dark matter*, *Phys. Rev.* **D99** (2019) 015005, [1805.09345].

[182] E. Kuflik, M. Perelstein, N. R.-L. Lorier and Y.-D. Tsai, *Phenomenology of ELDER Dark Matter*, *JHEP* **08** (2017) 078, [1706.05381].

[183] D. E. Kaplan, M. A. Luty and K. M. Zurek, *Asymmetric Dark Matter*, *Phys. Rev.* **D79** (2009) 115016, [0901.4117].

[184] K. M. Zurek, *Asymmetric Dark Matter: Theories, Signatures, and Constraints*, *Phys. Rept.* **537** (2014) 91–121, [1308.0338].

[185] K. Petraki and R. R. Volkas, *Review of asymmetric dark matter*, *Int. J. Mod. Phys.* **A28** (2013) 1330028, [1305.4939].

[186] L. J. Hall, K. Jedamzik, J. March-Russell and S. M. West, *Freeze-In Production of FIMP Dark Matter*, *JHEP* **03** (2010) 080, [0911.1120].

[187] F. Chen, J. M. Cline and A. R. Frey, *Nonabelian dark matter: Models and constraints*, *Phys. Rev.* **D80** (2009) 083516, [0907.4746].

[188] J. L. Feng, M. Kaplinghat, H. Tu and H.-B. Yu, *Hidden Charged Dark Matter*, *JCAP* **0907** (2009) 004, [0905.3039].

[189] J. M. Cline, Z. Liu, G. Moore and W. Xue, *Composite strongly interacting dark matter*, *Phys. Rev.* **D90** (2014) 015023, [1312.3325].

[190] B. von Harling and K. Petraki, *Bound-state formation for thermal relic dark matter and unitarity*, *JCAP* **1412** (2014) 033, [1407.7874].

[191] K. Petraki, M. Postma and M. Wiechers, *Dark-matter bound states from Feynman diagrams*, *JHEP* **06** (2015) 128, [1505.00109].

[192] M. Cirelli, P. Panci, K. Petraki, F. Sala and M. Taoso, *Dark Matter's secret liaisons: phenomenology of a dark U(1) sector with bound states*, *JCAP* **1705** (2017) 036, [1612.07295].

[193] H. An, M. B. Wise and Y. Zhang, *Effects of Bound States on Dark Matter Annihilation*, *Phys. Rev.* **D93** (2016) 115020, [1604.01776].

[194] K. Harigaya, M. Ibe, K. Kaneta, W. Nakano and M. Suzuki, *Thermal Relic Dark Matter Beyond the Unitarity Limit*, *JHEP* **08** (2016) 151, [1606.00159].

[195] K. Petraki, M. Postma and J. de Vries, *Radiative bound-state-formation cross-sections for dark matter interacting via a Yukawa potential*, *JHEP* **04** (2017) 077, [1611.01394].

[196] V. De Luca, A. Mitridate, M. Redi, J. Smirnov and A. Strumia, *Colored Dark Matter*, 1801.01135.

[197] J. Fan, A. Katz, L. Randall and M. Reece, *Double-Disk Dark Matter*, *Phys. Dark Univ.* **2** (2013) 139–156, [1303.1521].

[198] M. Rocha, A. H. G. Peter, J. S. Bullock, M. Kaplinghat, S. Garrison-Kimmel, J. Onorbe et al., *Cosmological Simulations with Self-Interacting Dark Matter I: Constant Density Cores and Substructure*, *Mon. Not. Roy. Astron. Soc.* **430** (2013) 81–104, [1208.3025].

[199] A. Kamada, M. Kaplinghat, A. B. Pace and H.-B. Yu, *How the Self-Interacting Dark Matter Model Explains the Diverse Galactic Rotation Curves*, *Phys. Rev. Lett.* **119** (2017) 111102, [1611.02716].

[200] K. K. Boddy, M. Kaplinghat, A. Kwa and A. H. G. Peter, *Hidden Sector Hydrogen as Dark Matter: Small-scale Structure Formation Predictions and the Importance of Hyperfine Interactions*, *Phys. Rev.* **D94** (2016) 123017, [1609.03592].

[201] C. Jacoby and S. Nussinov, *The Relic Abundance of Massive Colored Particles after a Late Hadronic Annihilation Stage*, 0712.2681.

[202] C. F. Berger, L. Covi, S. Kraml and F. Palorini, *The Number density of a charged relic*, *JCAP* **0810** (2008) 005, [0807.0211].

[203] K. Cheung, W.-Y. Keung and T.-C. Yuan, *Phenomenology of iquarkonium*, *Nucl. Phys.* **B811** (2009) 274–287, [0810.1524].

[204] H. Davoudiasl, D. E. Morrissey, K. Sigurdson and S. Tulin, *Hylogenesis: A*

Unified Origin for Baryonic Visible Matter and Antibaryonic Dark Matter, *Phys. Rev. Lett.* **105** (2010) 211304, [1008.2399].

[205] J. L. Feng and Y. Shadmi, *WIMPless Dark Matter from Non-Abelian Hidden Sectors with Anomaly-Mediated Supersymmetry Breaking*, *Phys. Rev.* **D83** (2011) 095011, [1102.0282].

[206] N. Blinov, D. E. Morrissey, K. Sigurdson and S. Tulin, *Dark Matter Antibaryons from a Supersymmetric Hidden Sector*, *Phys. Rev.* **D86** (2012) 095021, [1206.3304].

[207] Y. Bai and P. Schwaller, *Scale of dark QCD*, *Phys. Rev.* **D89** (2014) 063522, [1306.4676].

[208] K. K. Boddy, J. L. Feng, M. Kaplinghat and T. M. P. Tait, *Self-Interacting Dark Matter from a Non-Abelian Hidden Sector*, *Phys. Rev.* **D89** (2014) 115017, [1402.3629].

[209] J. M. Cline and A. R. Frey, *Nonabelian dark matter models for 3.5 keV X-rays*, *JCAP* **1410** (2014) 013, [1408.0233].

[210] K. K. Boddy, J. L. Feng, M. Kaplinghat, Y. Shadmi and T. M. P. Tait, *Strongly interacting dark matter: Self-interactions and keV lines*, *Phys. Rev.* **D90** (2014) 095016, [1408.6532].

[211] L. Forestell, D. E. Morrissey and K. Sigurdson, *Non-Abelian Dark Forces and the Relic Densities of Dark Glueballs*, *Phys. Rev.* **D95** (2017) 015032, [1605.08048].

[212] J. M. Cline, W. Huang and G. D. Moore, *Challenges for models with composite states*, *Phys. Rev.* **D94** (2016) 055029, [1607.07865].

[213] P. Asadi, M. Baumgart, P. J. Fitzpatrick, E. Krupczak and T. R. Slatyer, *Capture and Decay of Electroweak WIMPonium*, *JCAP* **1702** (2017) 005, [1610.07617].

[214] S. P. Liew and F. Luo, *Effects of QCD bound states on dark matter relic abundance*, *JHEP* **02** (2017) 091, [1611.08133].

[215] J. M. Cline, H. Liu, T. Slatyer and W. Xue, *Enabling Forbidden Dark Matter*, *Phys. Rev.* **D96** (2017) 083521, [1702.07716].

[216] L. Forestell, D. E. Morrissey and K. Sigurdson, *Cosmological Bounds on Non-Abelian Dark Forces*, 1710.06447.

[217] A. Berlin, N. Blinov, S. Gori, P. Schuster and N. Toro, *Cosmology and Accelerator Tests of Strongly Interacting Dark Matter*, 1801.05805.

[218] H. Baer, K.-m. Cheung and J. F. Gunion, *A Heavy gluino as the lightest supersymmetric particle*, *Phys. Rev.* **D59** (1999) 075002, [hep-ph/9806361].

[219] J. Kang, M. A. Luty and S. Nasri, *The Relic abundance of long-lived heavy colored particles*, *JHEP* **09** (2008) 086, [hep-ph/0611322].

[220] A. Arvanitaki, C. Davis, P. W. Graham, A. Pierce and J. G. Wacker, *Limits on split supersymmetry from gluino cosmology*, *Phys. Rev.* **D72** (2005) 075011, [hep-ph/0504210].

[221] V. A. Novikov, L. B. Okun, M. A. Shifman, A. I. Vainshtein, M. B. Voloshin and V. I. Zakharov, *Charmonium and Gluons: Basic Experimental Facts and Theoretical Introduction*, *Phys. Rept.* **41** (1978) 1–133.

[222] E. Eichten, K. Gottfried, T. Kinoshita, K. D. Lane and T.-M. Yan, *Charmonium: The Model*, *Phys. Rev.* **D17** (1978) 3090.

[223] QUARKONIUM WORKING GROUP collaboration, N. Brambilla et al., *Heavy quarkonium physics*, hep-ph/0412158.

[224] N. Brambilla et al., *Heavy quarkonium: progress, puzzles, and opportunities*, *Eur. Phys. J.* **C71** (2011) 1534, [1010.5827].

[225] N. Brambilla, M. A. Escobedo, J. Ghiglieri and A. Vairo, *Thermal width and gluo-dissociation of quarkonium in pNRQCD*, *JHEP* **12** (2011) 116, [1109.5826].

[226] N. Brambilla, M. A. Escobedo, J. Ghiglieri and A. Vairo, *Thermal width and quarkonium dissociation by inelastic parton scattering*, *JHEP* **05** (2013) 130, [1303.6097].

[227] C. Simolo, *Extraction of characteristic constants in QCD with perturbative and nonperturbative methods*. PhD thesis, Milan U., 2006. 0807.1501.

[228] M. Teper, *Large N*, *PoS* **LATTICE2008** (2008) 022, [0812.0085].

[229] C. J. Morningstar and M. J. Peardon, *The Glueball spectrum from an anisotropic lattice study*, *Phys. Rev.* **D60** (1999) 034509, [hep-lat/9901004].

[230] N. Brambilla, A. Pineda, J. Soto and A. Vairo, *Effective field theories for heavy quarkonium*, *Rev. Mod. Phys.* **77** (2005) 1423, [hep-ph/0410047].

[231] P. Froelich, S. Jonsell, A. Saenz, B. Zygelman and A. Dalgarno, *Hydrogen-antihydrogen collisions*, *Phys. Rev. Lett.* **84** (May, 2000) 4577–4580.

[232] S. Jonsell, A. Saenz, P. Froelich, B. Zygelman and A. Dalgarno, *Stability of hydrogen-antihydrogen mixtures at low energies*, *Phys. Rev. A* **64** (Oct., 2001) 052712.

[233] S. Jonsell, A. Saenz, P. Froelich, B. Zygelman and A. Dalgarno, *Hydrogen–antihydrogen scattering in the born–oppenheimer approximation*, *J. Phys. B* **37** (2004) 1195.

[234] J. R. Taylor, *Scattering Theory: The Quantum Theory on Nonrelativistic Collisions*. John Wiley & Sons, Inc., June, 1972.

[235] K. Strasburger, *Accurate born–oppenheimer potential energy curve for the hydrogen–antihydrogen system*, *J. Phys. B* **35** (2002) L435.

[236] M. B. Wise and Y. Zhang, *Stable Bound States of Asymmetric Dark Matter*, *Phys. Rev.* **D90** (2014) 055030, [1407.4121].

[237] A. V. Manohar and M. B. Wise, *Heavy quark physics*, vol. 10 of *Cambridge Monographs on Particle Physics, Nuclear Physics and Cosmology*. Cambridge University Press, Mar., 2000.

[238] C. Quigg and J. L. Rosner, *Quantum Mechanics with Applications to Quarkonium*, *Phys. Rept.* **56** (1979) 167–235.

[239] M. W. Goodman and E. Witten, *Detectability of Certain Dark Matter Candidates*, *Phys. Rev.* **D31** (1985) 3059.

[240] D. Tucker-Smith and N. Weiner, *Inelastic dark matter*, *Phys. Rev.* **D64** (2001) 043502, [hep-ph/0101138].

[241] D. P. Finkbeiner and N. Weiner, *Exciting Dark Matter and the*

INTEGRAL/SPI 511 keV signal, *Phys. Rev.* **D76** (2007) 083519, [astro-ph/0702587].

[242] S. Chang, G. D. Kribs, D. Tucker-Smith and N. Weiner, *Inelastic Dark Matter in Light of DAMA/LIBRA*, *Phys. Rev.* **D79** (2009) 043513, [0807.2250].

[243] J. Bramante, P. J. Fox, G. D. Kribs and A. Martin, *Inelastic frontier: Discovering dark matter at high recoil energy*, *Phys. Rev.* **D94** (2016) 115026, [1608.02662].

[244] S. Chang, A. Pierce and N. Weiner, *Using the Energy Spectrum at DAMA/LIBRA to Probe Light Dark Matter*, *Phys. Rev.* **D79** (2009) 115011, [0808.0196].

[245] P. W. Graham, R. Harnik, S. Rajendran and P. Saraswat, *Exothermic Dark Matter*, *Phys. Rev.* **D82** (2010) 063512, [1004.0937].

[246] B. Feldstein, P. W. Graham and S. Rajendran, *Luminous Dark Matter*, *Phys. Rev.* **D82** (2010) 075019, [1008.1988].

[247] R. Essig, J. Kaplan, P. Schuster and N. Toro, *On the Origin of Light Dark Matter Species*, *Submitted to: Physical Review D* (2010) , [1004.0691].

[248] Y. Bai and P. J. Fox, *Resonant Dark Matter*, *JHEP* **11** (2009) 052, [0909.2900].

[249] M. Pospelov and A. Ritz, *Resonant scattering and recombination of pseudo-degenerate WIMPs*, *Phys. Rev.* **D78** (2008) 055003, [0803.2251].

[250] H. An, M. Pospelov and J. Pradler, *Direct constraints on charged excitations of dark matter*, *Phys. Rev. Lett.* **109** (2012) 251302, [1209.6358].

[251] S. Chang, A. Pierce and N. Weiner, *Momentum Dependent Dark Matter Scattering*, *JCAP* **1001** (2010) 006, [0908.3192].

[252] S. Chang, N. Weiner and I. Yavin, *Magnetic Inelastic Dark Matter*, *Phys. Rev.* **D82** (2010) 125011, [1007.4200].

[253] M. Pospelov, N. Weiner and I. Yavin, *Dark matter detection in two easy steps*, *Phys. Rev.* **D89** (2014) 055008, [1312.1363].

[254] K. Kumar, A. Menon and T. M. P. Tait, *Magnetic Fluffy Dark Matter*, *JHEP* **02** (2012) 131, [1111.2336].

[255] H. Davoudiasl, D. E. Morrissey, K. Sigurdson and S. Tulin, *Baryon Destruction by Asymmetric Dark Matter*, *Phys. Rev.* **D84** (2011) 096008, [1106.4320].

[256] J. Huang and Y. Zhao, *Dark Matter Induced Nucleon Decay: Model and Signatures*, *JHEP* **02** (2014) 077, [1312.0011].

[257] K. Agashe, Y. Cui, L. Necib and J. Thaler, *(In)direct Detection of Boosted Dark Matter*, *JCAP* **1410** (2014) 062, [1405.7370].

[258] J. Berger, Y. Cui and Y. Zhao, *Detecting Boosted Dark Matter from the Sun with Large Volume Neutrino Detectors*, *JCAP* **1502** (2015) 005, [1410.2246].

[259] K. Kong, G. Mohlabeng and J.-C. Park, *Boosted dark matter signals uplifted with self-interaction*, *Phys. Lett.* **B743** (2015) 256–266, [1411.6632].

[260] H. Alhazmi, K. Kong, G. Mohlabeng and J.-C. Park, *Boosted Dark Matter at the Deep Underground Neutrino Experiment*, *JHEP* **04** (2017) 158, [1611.09866].

[261] D. Kim, J.-C. Park and S. Shin, *Dark Matter Collider from Inelastic Boosted Dark Matter*, *Phys. Rev. Lett.* **119** (2017) 161801, [1612.06867].

[262] SUPER-KAMIOKANDE collaboration, C. Kachulis et al., *Search for Boosted Dark Matter Interacting With Electrons in Super-Kamiokande*, *Phys. Rev. Lett.* **120** (2018) 221301, [1711.05278].

[263] P. Sikivie, *Experimental Tests of the Invisible Axion*, *Phys. Rev. Lett.* **51** (1983) 1415–1417.

[264] S. Chaudhuri, P. W. Graham, K. Irwin, J. Mardon, S. Rajendran and Y. Zhao, *Radio for hidden-photon dark matter detection*, *Phys. Rev.* **D92** (2015) 075012, [1411.7382].

[265] Y. Hochberg, T. Lin and K. M. Zurek, *Absorption of light dark matter in semiconductors*, *Phys. Rev.* **D95** (2017) 023013, [1608.01994].

[266] A. Arvanitaki, S. Dimopoulos, S. Dubovsky, P. W. Graham, R. Harnik and

S. Rajendran, *Astrophysical Probes of Unification*, *Phys. Rev.* **D79** (2009) 105022, [0812.2075].

[267] A. Arvanitaki, S. Dimopoulos, S. Dubovsky, P. W. Graham, R. Harnik and S. Rajendran, *Decaying Dark Matter as a Probe of Unification and TeV Spectroscopy*, *Phys. Rev.* **D80** (2009) 055011, [0904.2789].

[268] R. Essig, E. Kuflik, S. D. McDermott, T. Volansky and K. M. Zurek, *Constraining Light Dark Matter with Diffuse X-Ray and Gamma-Ray Observations*, *JHEP* **11** (2013) 193, [1309.4091].

[269] G. Jungman, M. Kamionkowski and K. Griest, *Supersymmetric dark matter*, *Phys. Rept.* **267** (1996) 195–373, [hep-ph/9506380].

[270] C. M. Jarchow and G. A. Thompson, *The nature of the mohorovicic discontinuity*, *Annual Review of Earth and Planetary Sciences* **17** (1989) 475–506, [https://doi.org/10.1146/annurev.ea.17.050189.002355].

[271] J. Alexander et al., *Dark sectors 2016 workshop: Community report*, 2016. 1608.08632.

[272] LHCb collaboration, R. Aaij et al., *Search for Dark Photons Produced in 13 TeV pp Collisions*, *Phys. Rev. Lett.* **120** (2018) 061801, [1710.02867].

[273] J. H. Chang, R. Essig and S. D. McDermott, *Revisiting Supernova 1987A Constraints on Dark Photons*, *JHEP* **01** (2017) 107, [1611.03864].

[274] Super-Kamiokande collaboration, E. Richard et al., *Measurements of the atmospheric neutrino flux by Super-Kamiokande: energy spectra, geomagnetic effects, and solar modulation*, *Phys. Rev.* **D94** (2016) 052001, [1510.08127].

[275] SNO+ collaboration, S. Andringa et al., *Current Status and Future Prospects of the SNO+ Experiment*, *Adv. High Energy Phys.* **2016** (2016) 6194250, [1508.05759].

[276] Borexino collaboration, G. Bellini et al., *Measurement of the solar 8B neutrino rate with a liquid scintillator target and 3 MeV energy threshold in the Borexino detector*, *Phys. Rev.* **D82** (2010) 033006, [0808.2868].

[277] DUNE collaboration, R. Acciarri et al., *Long-Baseline Neutrino Facility*

(LBNF) and Deep Underground Neutrino Experiment (DUNE), 1512.06148.

[278] M. S. Madhavacheril, N. Sehgal and T. R. Slatyer, *Current Dark Matter Annihilation Constraints from CMB and Low-Redshift Data*, *Phys. Rev.* **D89** (2014) 103508, [1310.3815].

[279] M. L. Graesser, I. M. Shoemaker and L. Vecchi, *Asymmetric WIMP dark matter*, *JHEP* **10** (2011) 110, [1103.2771].

[280] G. B. Gelmini, J.-H. Huh and T. Rehagen, *Asymmetric dark matter annihilation as a test of non-standard cosmologies*, *JCAP* **1308** (2013) 003, [1304.3679].

[281] E. Fermi and E. Teller, *The capture of negative mesotrons in matter*, *Phys. Rev.* **72** (1947) 399–408.

[282] I. S. L. G. S. Y. T. O. Feng J., Geller M., *To appear*, .

[283] L. Bracci, G. Fiorentini and O. Pitzurra, *PROTONIUM FORMATION IN FLIGHT*, *Phys. Lett.* **85B** (1979) 280–284.

[284] LIGO Scientific, Virgo collaboration, B. P. Abbott et al., *GW170817: Observation of Gravitational Waves from a Binary Neutron Star Inspiral*, *Phys. Rev. Lett.* **119** (2017) 161101, [1710.05832].

[285] F. H. Stillinger, *A topographic view of supercooled liquids and glass formation*, *Science* **267** (1995) 1935–1939, [https://science.sciencemag.org/content/267/5206/1935.full.pdf].

[286] M. B. Wise and Y. Zhang, *Yukawa Bound States of a Large Number of Fermions*, *JHEP* **02** (2015) 023, [1411.1772].

[287] E. Hardy, R. Lasenby, J. March-Russell and S. M. West, *Big Bang Synthesis of Nuclear Dark Matter*, *JHEP* **06** (2015) 011, [1411.3739].

[288] E. Hardy, R. Lasenby, J. March-Russell and S. M. West, *Signatures of Large Composite Dark Matter States*, *JHEP* **07** (2015) 133, [1504.05419].

[289] M. I. Gresham, H. K. Lou and K. M. Zurek, *Nuclear Structure of Bound States of Asymmetric Dark Matter*, *Phys. Rev.* **D96** (2017) 096012, [1707.02313].

[290] M. I. Gresham, H. K. Lou and K. M. Zurek, *Early Universe synthesis of asymmetric dark matter nuggets*, *Phys. Rev.* **D97** (2018) 036003, [1707.02316].

[291] D. McKeen, A. E. Nelson, S. Reddy and D. Zhou, *Neutron stars exclude light dark baryons*, *Phys. Rev. Lett.* **121** (2018) 061802, [1802.08244].

[292] P. Schuster, N. Toro, N. Weiner and I. Yavin, *High Energy Electron Signals from Dark Matter Annihilation in the Sun*, *Phys. Rev.* **D82** (2010) 115012, [0910.1839].

[293] J. L. Feng, J. Smolinsky and P. Tanedo, *Detecting dark matter through dark photons from the Sun: Charged particle signatures*, *Phys. Rev.* **D93** (2016) 115036, [1602.01465].